

Study of Nanostructured Iron Oxides

Thesis submitted for the degree of

Doctor of Philosophy (Science)

in

Physics (Experimental)

by

Arka Chaudhuri

Department of Physics

University of Calcutta

December 2012

Dedicated to my Parents

Acknowledgement

Starting as a fresher at SN Bose Centre, five long years ago, I have been influenced and helped by many people whose contribution towards the culmination of my thesis has been of extreme value to me. I owe my sincere gratitude to each and every one of them. Firstly, I owe my heartfelt gratitude to my thesis supervisor Prof. Kalyan Mandal, for giving me the opportunity to work in his laboratory. It was a great pleasure to conduct research under his supervision. The academic discussions with him were extremely fruitful and motivated me to improve myself continuously.

I would also like to thank Dr. Madhuri Mandal (Madhuri Di) whose guidance in the chemistry related topics of my research was really helpful. I am also grateful to my M.Sc. project supervisor Prof. Sudha Bhoraskar of Dept. of Physics, University of Pune who initiated me to the field of nanoparticles. No word of thanks is apt for Prof. S.K. Date (Adjunct Professor), Dept. of Physics, University of Pune. He was and will always be a source of inspiration for me in this field of Physics in general and Magnetism in particular. It is my privilege and honor to be associated with such a great researcher and human being from my M.Sc. days. Whenever I had any critical questions regarding my Ph.D. topic or any other topic of Physics, I used to call him up on his mobile and he would always patiently give the answer in the simplest possible manner.

I had the pleasure to work with some of the most vibrant group-mates, Dr. Subarna Mitra (Subarna Di), Dr. Suman Das (Suman Da), Dr. Bipul Das (Bipul Da), Dr. Gobinda Gopal Khan (Gogo Da), Debabrata Pal (Debu), Shyam Sundar Ghosh (Shyam), Debasish Sarkar (Deba), Rajasree Das, Ashutosh Singh (Ashu), Arup Ghosh, Rupali Rakshit and Pratapaditya Bej. I owe my heartfelt gratitude to all of them for their kind support throughout my thesis work in various manners. During my initial years in our laboratory, Bipul Da and Debu helped me a lot in settling down and getting used to the rigours and hardships of Ph.D. life. Bipul Da and Madhuri Di taught me all the Lab etiquettes which will stand me in good stead in my future research activities.

I want to specially mention the names of my extremely good friends of SN Bose Centre namely Dr. Pramod Kr. Verma (Pramod), Abhinabh Kr. Mishra and Dhani Nafday for their wonderful companionship. We shared a very good camaraderie with each other. I was always cheerful under their company. They provided much needed advice and support during the tough times encountered by me during my tenure.

I would also like to thank the Director of our Institute Prof. Arup Kr. Roychaudhuri for allowing me to do some measurements in his laboratory. The lab assistants of our centre during my tenure were very prompt in carrying out the different experimental characterizations of my samples. I am extremely thankful to them. I am grateful to all the staff members of our centre for their unconditional support and help in the hour of need. I thank the entire S.N. Bose family for making me feel at home and making my stay memorable. Participation in the different cultural programmes, football, cricket, badminton, volleyball, rejuvenated me and in a way helped me to do my research work with renewed vigour.

God's greatest gift to a man is his parents. I would like to express my gratitude to my parents (Baba, Ma), my brother (Angshu), my aunt (Pishi) for their pains and sacrifices throughout this long tenure. Without their blessings and encouragement this thesis would not have been possible.

Finally I want to thank Department of Science and Technology (DST) India and SN Bose National Centre for Basic Sciences for providing me the fellowship.

Arka Chaudhuri

Kolkata, India

December 2012

LIST OF PUBLICATIONS

1. **A. Chaudhuri**, M. Mandal and K. Mandal, “Preparation and study of NiFe₂O₄/SiO₂ core-shell nanocomposites”, **J. of Alloys and Compounds**, **487**, (2009), 698.
2. **A. Chaudhuri**, S. Mitra, M. Mandal and K. Mandal, “Nanostructured Bismuth Ferrites Synthesized by Solvothermal Process”, **Journal of Alloys and Compounds**, **491**, (2010), 703.
3. D.Pal, M.Mandal, **A,Chaudhuri**, B. Das, D. Sarkar, K.Mandal,” Micelles Induced High Coercivity in Single Domain Cobalt ferrite Nanoparticles”, **J. Appl. Phys.** 108, (2010)124317.
4. **A. Chaudhuri**, K. Mandal,”Enhancement of Ferromagnetic and dielectric properties of Lanthanum doped Bismuth Ferrite nanostructures”, **Materials Research Bulletin**, **47**(2012)1057.
5. **A.Chaudhuri**, K. Mandal, “Study of structural, ferromagnetic and ferroelectric properties of nanostructured Barium doped Bismuth Ferrite” Communicated.
6. **A. Chaudhuri**, K. Mandal, “Synthesis and magnetic properties of monodisperse CoFe₂O₄ nanoparticles by a simple hydrothermal technique” Communicated.
7. **A. Chaudhuri**, K. Mandal, S. Pati and D. Das ”Solvothermal Synthesis of nanostructured Nickel Ferrite and their magnetic properties” Communicated.
8. **A. Chaudhuri**, K. Mandal “Magnetolectric properties of CoFe₂O₄ :BaTiO₃ core-shell nanocomposites” Under preparation.

Contents

1	Introduction	1
1.1	Magnetic Nanoparticles.....	1
1.1.1	Domain Theory.....	2
1.1.2	Superparamagnet.....	2
1.1.3	Hysteresis loss and Coercivity.....	4
1.2	Iron Oxides.....	6
1.2.1	Orthoferrite.....	6
1.2.2	Hexaferrites.....	7
1.2.3	Spinel Ferrites.....	7
1.2.4	Different Spinel Ferrites.....	10
1.3	Multiferroics.....	14
1.3.1	Bismuth Ferrite.....	18
1.4	Magnetoelectric Effect.....	23
1.4.1	Piezoelectricity.....	23
1.4.2	Magnetostriction.....	24
1.4.3	Product property of Magnetoelectric effect.....	24
1.5	Motivation of Thesis.....	25
1.6	Objective of Thesis.....	27
1.7	Organization of Thesis.....	28
2	Experimental Techniques	37
2.1	Preamble.....	37
2.2	Mechanism of nanoparticle formation.....	37
2.3	Synthesis Techniques.....	41
2.3.1	Chemical co-precipitation method.....	41
2.3.2	Hydrothermal synthesis.....	43

2.3.3	Sol-gel synthesis.....	45
2.3.4	Micelles and Reverse micelles.....	48
2.4	Experimental techniques.....	49
2.4.1	X ray diffraction.....	49
2.4.2	Scanning Electron Microscope.....	52
2.4.3	Fourier Transform Infra-Red Spectroscopy.....	56
2.4.4	Transmission Electron Microscope.....	58
2.4.5	Vibrating Sample Magnetometer.....	62
2.4.6	Superconducting Quantum Interference Device.....	63
2.4.7	Differential Thermal Analysis.....	64
2.4.8	Thermogravimetric Analysis.....	65
2.4.9	Mossbauer Spectroscopy.....	66
2.4.10	AC susceptibility set-up.....	67
2.4.11	PE loop tracer.....	70
2.4.12	Dielectric properties measurement set-up.....	72
2.4.13	Magnetoelectric co-efficient measurement.....	74
2.4.14	Gas sensing set-up.....	77
3	Synthesis and study of NiFe₂O₄/SiO₂ core-shell nanocomposites	80
3.1	Preamble.....	80
3.2	Synthesis of NiFe ₂ O ₄ and NiFe ₂ O ₄ :SiO ₂ core shell.....	81
3.3	Results and Discussions.....	82
3.3.1	Variation of Magnetization with applied field in a superparamagnet.....	86
3.3.2	Zero field cooled and field cooled dc magnetic measurements.....	94

3.3.3	Dynamic properties of NiFe ₂ O ₄	97
3.4	Magnetic properties of nanostructured NiFe ₂ O ₄ synthesized by solvothermal technique and its application for Gas sensing.....	102
3.4.1	Synthesis of nanostructures of NiFe ₂ O ₄ by the solvothermal technique.....	102
3.4.2	Gas Sensing properties of NiFe ₂ O ₄	105
3.5	Conclusions.....	107
4	Synthesis of single domain CoFe₂O₄ nanoparticles and study of the influence of micelle on its magnetic properties	110
4.1	Preamble.....	110
4.2	Synthesis of nonagglomerated CoFe ₂ O ₄ nanoparticles.....	111
4.3	Synthesis of micelle coated CoFe ₂ O ₄ nanoparticles.....	111
4.4	Results and Discussions.....	112
4.4.1	Magnetic properties.....	115
4.4.2	Magnetic relaxation.....	124
4.5	Conclusions.....	126
5	Synthesis and study of nanostructured Bismuth Ferrites	130
5.1	Preamble.....	130
5.2	Experimental.....	131
5.3	Results and Discussions.....	132
5.3.1	Structural properties.....	132
5.3.2	Magnetic properties.....	139

5.3.3	Dielectric properties.....	146
5.4	Conclusions.....	161
6	Magnetoelectric properties in CoFe₂O₄/BaTiO₃ core shell nanocomposites	164
6.1	Preamble.....	164
6.2	Experimental.....	165
6.2.1	Synthesis of CoFe ₂ O ₄	165
6.2.2	Synthesis of CoFe ₂ O ₄ :BaTiO ₃ core shell.....	165
6.3	Results and Discussions.....	168
6.4	Conclusions.....	175
7	Conclusion of the thesis	177

Chapter 1

1 Introduction

1.1 Magnetic Nanoparticles

Nanotechnology refers to the creation and uses of materials having at least one dimension of the order of 100 nanometers. The properties of nanoparticles are significantly different from those of bulk particles. Over the years scientists took immense interest in studying nanoparticles because of its fascinating properties subject to its variable sizes. They found that suitable control of the properties of nanometer scale structures can lead to new science as well as new devices and technologies [1,2].

Out of all different kinds of nanoparticles magnetic nanoparticles are of great interest for researchers from a wide range of disciplines, including magnetic fluids [3], catalysis [4,5], biotechnology/biomedicine [6], magnetic resonance imaging [7,8], data storage [9], environmental remediation [10,11], protein separation [12], cancer therapy [13], hyperthermia [14] and a host of other applications. While a number of suitable methods have been developed for the synthesis of magnetic nanoparticles of various different compositions, successful application of such magnetic nanoparticles in the areas listed above is highly dependent on the stability of the particles under a range of different conditions. The particles for these applications must be as small as possible (~nm). When the size of these particles goes below a critical value, (typically around 10–20 nm) each nanoparticle becomes a single magnetic domain. They show superparamagnetic behavior when the temperature is above the so-called blocking temperature. Such individual nanoparticles have a large constant magnetic moment and behave like a giant paramagnetic atom with a fast response to applied magnetic fields with negligible remanence (residual magnetism) and coercivity (the field required to bring the magnetization to zero). These features make superparamagnetic nanoparticles very attractive for a broad range of biomedical applications. Before describing superparamagnetism we must understand the Domain theory.

1.1.1 Domain Theory

The ferromagnetic or ferrimagnetic sample is actually composed of small regions called magnetic domains, within each of which the local magnetization is saturated but not necessarily parallel. Domains are small (1-100's microns), but much larger than atomic distances. Domains constitute a fundamental concept in magnetism. Domain walls are interfaces between regions in which the magnetization has different directions. Within the wall, the magnetization must gradually change direction from that in one domain to that in the other domain. Domain walls have a finite width (on the order of 100 nm) and surface energy that is determined principally by exchange and magnetocrystalline energy. The number of domains for a given grain size depends on the magnitudes of the exchange, magnetocrystalline and saturation magnetization. The magnetic behavior can be subdivided on the basis of grain size into three ranges. 1) MD: multidomain 2) SD: single domain 3) SPM: Superparamagnetic [15,16,17].

For large sizes the particles are multi-domain. They are bulk-like with increasing size. The mechanism of magnetization reversal is domain wall nucleation and motion for the multi-domain case.

As the grain size decreases, a critical size will be reached where the grain can no longer accommodate a wall. Below this critical size, the grain contains a single domain (SD). This critical size is shown by the peak in coercivity versus grain size curve in Fig. 1.1. An SD grain is uniformly magnetized to its saturation magnetization. SD grains are magnetically hard and have high coercivities and remanence. The critical size for SD behavior depends on several factors including the saturation magnetization and the shape of the grain.

1.1.2 Superparamagnet

As particle size continues to decrease within the SD range another critical threshold is reached, at which remanence and coercivity go to zero. When this happens, the grain becomes superparamagnetic even at temperatures below the Curie or the Neel temperature (for antiferromagnet). In superparamagnets temperature destroys the magnetic ordering and the atomic moment is replaced by the particle moment [15,16,17].

An SD particle of volume V has a uniform magnetization directed along the easy axis of magnetization. If V is small enough or the temperature is high, thermal energy ($k_B T$) will be

sufficient to overcome the anisotropy energy separating the (+) and (-) magnetization states and cause a spontaneous reversal of magnetization. This fluctuation tends to randomize the moments of the nanoparticle unless a magnetic field is applied. At this point, the rate at which the particles will randomly reverse direction becomes significant. Normally coupling forces in ferromagnetic materials cause the magnetic moments of neighbouring atoms to align, resulting in very large internal magnetic fields. This is what distinguishes ferromagnetic materials from paramagnetic materials. At temperatures above the Curie temperature (or the Neel temperature for antiferromagnetic materials), the thermal energy is sufficient to overcome the coupling forces, causing the atomic magnetic moments to fluctuate randomly. Because there is no longer any magnetic order, the internal magnetic field no longer exists and material exhibits paramagnetic behavior. For superparamagnetic particles, the net magnetic moment in zero field, will average to zero. In an applied field, there will be a net statistical alignment of magnetic moments. This is analogous to paramagnetism, except now the magnetic moment is not that of a single atom, but of a SD particle. Hence, the term superparamagnetism, which denotes a much higher susceptibility than that for simple paramagnetism. The basis of superparamagnetism can be summarized by a double potential well as shown in the left part of Fig. 1.1.

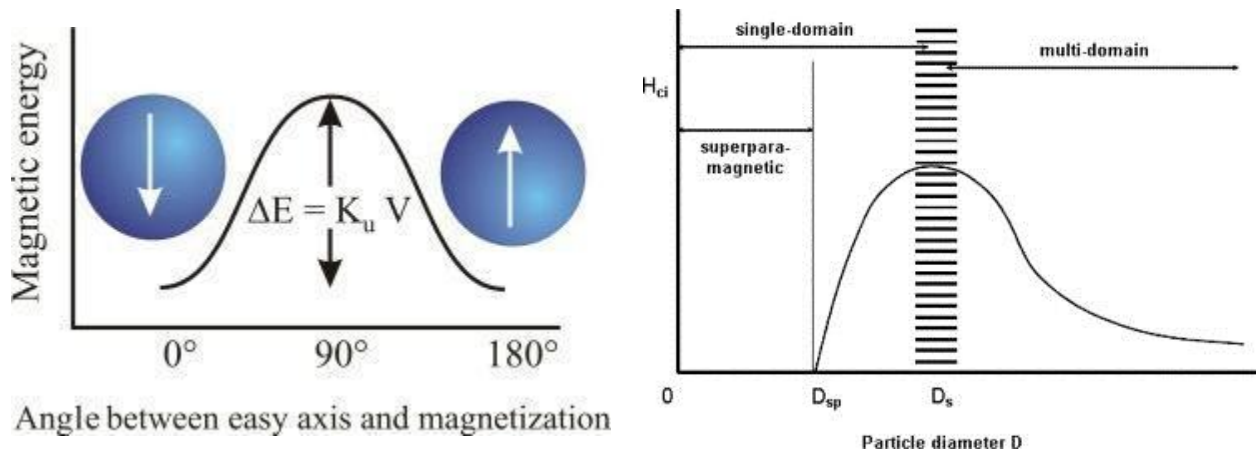


Fig. 1.1: Left figure is representing the schematic representation of energy barrier for magnetization reversal and the right figure is showing coercivity H_c versus particle diameter D curve. The magnetic behavior can be subdivided on the basis of particle diameter into three ranges.

As seen from left part of Fig. 1.1 the two states of magnetization of a uniaxial magnetic particle are separated by an energy barrier, KV , where K is the anisotropy energy density and V is the

particle volume. If the thermal energy $k_B T$ becomes comparable to the barrier height there is an increased probability of the magnetization reversing. In response to a change in the applied field or temperature, an ensemble of SPM particles will approach an equilibrium value of magnetization with a characteristic relaxation time, represented by Arrhenius-Néel equation [18]

$$f = f_0 e^{\frac{-KV}{k_B T}} \quad (1.1)$$

Where, f_0 is the attempt frequency (10^9 - 10^{12} sec^{-1}), K is the anisotropy constant, V is particle volume, k_B is Boltzmann constant and T is absolute temperature. The exponential nature of the relaxation time on V and T makes it possible to define a blocking temperature, T_B (at constant volume), or blocking volume V_B , (at constant temperature) at which the magnetization goes from an unstable condition ($1/f_0 \ll t$) to a stable condition ($1/f_0 \gg t$). Superparamagnetism is identified by three characteristics of magnetization curves. A superparamagnetic magnetization curve has zero coercivity and remanence, existence of T_B below which ferromagnetic order reappears and magnetization curves superimpose when plotting as H/T above T_B .

1.1.3 Hysteresis loss and Coercivity

The properties of magnetic materials vary in a wide spectrum. Magnetic hysteresis loop is most common way to represent the bulk properties of a magnetic material. It is a plot of magnetization M as a function of applied magnetic field H . For an ideal magnetic material the loop has a two-fold rotational symmetry. Its lack of ability to retrace the magnetization curve is related to the existence of magnetic domains in the material. Once the magnetic domains are reoriented, it takes some energy to turn them back again. This property of a magnetic material is useful in magnetic memory devices. Magnetic anisotropy yields easy magnetization directions corresponding to local energy minima and energy barriers that separate the easy directions in a single domain particle. On an atomic scale, the barriers are easily overcome by thermal fluctuations, but on nanoscale or macroscopic length scales excitations are usually too weak to overcome the barriers. This is observed as magnetic hysteresis. From the first quadrant the saturation magnetization, M_s can be measured. Most of the useful information, however, can be derived from the second quadrant of the loop. The maximum value of the product of M and H is called the maximum energy product, $(MH)_{MAX}$ and is a measure of the maximum amount of useful work that can be performed by the magnet. $(MH)_{MAX}$ is used as a figure of merit for

permanent magnet materials. Coercivity H_c can be measured from the hysteresis loop and it is the necessary reverse magnetic field to reduce the magnetization to zero. It is the measure of how strong a magnet can resist an external magnetic field. Magnetic materials can be divided according to the coercivity into hard magnetic materials (high coercivity, high remanence) and soft magnetic materials (low coercivity, low remanence). Both are widely used in media applications, an intermediate coercivity is needed for proper writing and stability of the data. Remanence M_r is also determined from the hysteresis loop. It is the remaining magnetization when the field is reduced to zero after magnetizing a magnetic material.

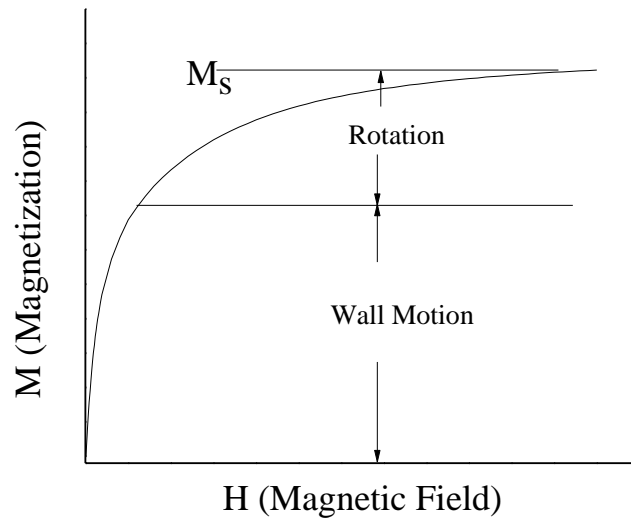


Fig. 1.2: Magnetization processes.

Domains and the magnetization process

During the magnetization process domain wall motion is the main process upto about the knee of the magnetization curve. From there to saturation rotation predominates. In this region work must be done against the anisotropy forces and a rather large increase in H is required to produce a relatively small increase in M . This division of the magnetization curve is rather arbitrary because wall motion and rotation are not sharply divisible processes [17]. When magnetization occurs entirely by domain rotation, we expect the process to be reversible, with the same M vs H curve followed in both increasing and decreasing fields. Domain wall motion in real materials is irreversible, leading to different curves for increasing and decreasing fields.

In the regime of single domain particle magnetization reversal occurs by rotation of the magnetization by the application of external magnetic field. For considering a random distribution of non-interacting single domain particles with uniaxial anisotropy, Stoner and Wohlfarth in their works theoretically determined the coercivity along the anisotropy axis to be

$$H_c = \frac{2K}{M_s} \quad (1.2)$$

where K is the anisotropy constant and M_s is the saturation magnetization. Considering the effect of thermal fluctuation, the coercivity as a function of particle size D is given by [15],

$$H_c(D) = 0.5H_k \left[1 - \left(\frac{D_p}{D} \right)^{\frac{3}{2}} \right] \quad (1.3)$$

where, H_k is the anisotropy field of the material in question, D is particle diameter, D_p is superparamagnetic particle size.

1.2 Iron Oxides

Out of the magnetic nanoparticles Iron Oxides form a very important class of materials having manifold applications. Iron Oxides are chemical compounds composed of Fe and O such as Iron (II) Oxide (Wüstite, FeO), Iron (III) Oxide (Hematite, Fe₂O₃), Iron (II, III) Oxide (Magnetite, Fe₃O₄) and their derivatives. Among the various Iron Oxides ferrites form a very important class of material. Ferrites are classified into three main categories:- Orthoferrites, Hexaferrites and Spinel Ferrites.

1.2.1 Orthoferrite

Orthoferrites are a class of chemical compounds with the formula RFeO₃ (where R is one or more rare-earth elements). Orthoferrites have an orthorhombic crystal structure with a space group Pbnm and mostly are weakly ferromagnetic [19]. At the Néel temperature T_N the subsystem of iron ions orders into a slightly canted antiferromagnetic structure with antiferromagnetic moment G and a weak ferromagnetic moment F . The rare-earth ion subsystem acquires magnetization m due to an interaction with the iron subsystem. The orthoferrites are particularly interesting because of the presence of an antisymmetric exchange interaction which

involves the vector cross product of neighboring spins as opposed to the usual scalar product. In the absence of this interaction, the orthoferrites would be antiferromagnetic. Its presence leads to a small canting of the sublattices, making the orthoferrites “weak” ferromagnets with $4\pi M_s = 100$ G. Another interesting feature of these materials is the fact that some of them exhibit a transition as a function of temperature, in which the direction of the antiferromagnetically ordered spins and consequently also of the net magnetization rotates by 90° .

The combination of high magnetic resonance frequencies with very large magneto-optical effects makes the orthoferrites interesting objects for study of laser-induced dynamics. Orthoferrites are transparent, and can modify the polarization of a beam of light under the control of a magnetic field (Faraday rotation). This makes them potentially useful as optical sensors and actuators for use in optical communications [20]. They were also once used as the magnetic material in bubble memory.

1.2.2 Hexaferrites

Hexaferrite is the term given to those kinds of ferrites which have hexagonal structures [21]. They have long been used for permanent magnets and are of interest for microwave applications. At higher frequencies, ferrites with substantially higher magnetic anisotropy are required. In those regions Hexaferrites are very useful because of its high anisotropy. Example is the Ba M-type (or BaM) hexaferrite, $\text{BaFe}_{12}\text{O}_{19}$.

1.2.3 Spinel Ferrites

Spinel Ferrites are non-conductive, highly resistive, highly magnetically permeable, ferrimagnetic ceramic compounds. Because of its high resistivity ferrites have very low eddy current losses. Hence it can be used at very high frequencies. These properties also afford them unique value in microwave devices that require strong coupling to electromagnetic signals and often non-reciprocal behavior. They have contributed greatly to technological applications [22,23] because of their room temperature ferromagnetic and insulating properties. Ferrite cores are used in electronic inductors, transformers, and electromagnets where the high electrical resistance of the ferrite leads to very low eddy current losses. They are commonly seen as a lump in a computer cable, called a ferrite bead, which helps to prevent high frequency electrical noise (radio frequency interference) from exiting or entering the equipment. Early computer

memories stored data in the residual magnetic fields of hard ferrite cores, which were assembled into arrays of core memory. Ferrite powders are used in the coatings of magnetic recording tapes. Ferrite particles are also used as a component of radar-absorbing materials or coatings used in stealth aircraft and in the absorption tiles lining the rooms used for electromagnetic compatibility measurements. Most common radio magnets, including those used in loudspeakers, are ferrite magnets. Ferrite magnets have largely displaced Alnico magnets in these applications. It is a common magnetic material for electromagnetic instrument pickups. Because of its manifold applications we have chosen spinel ferrites as our material of research.

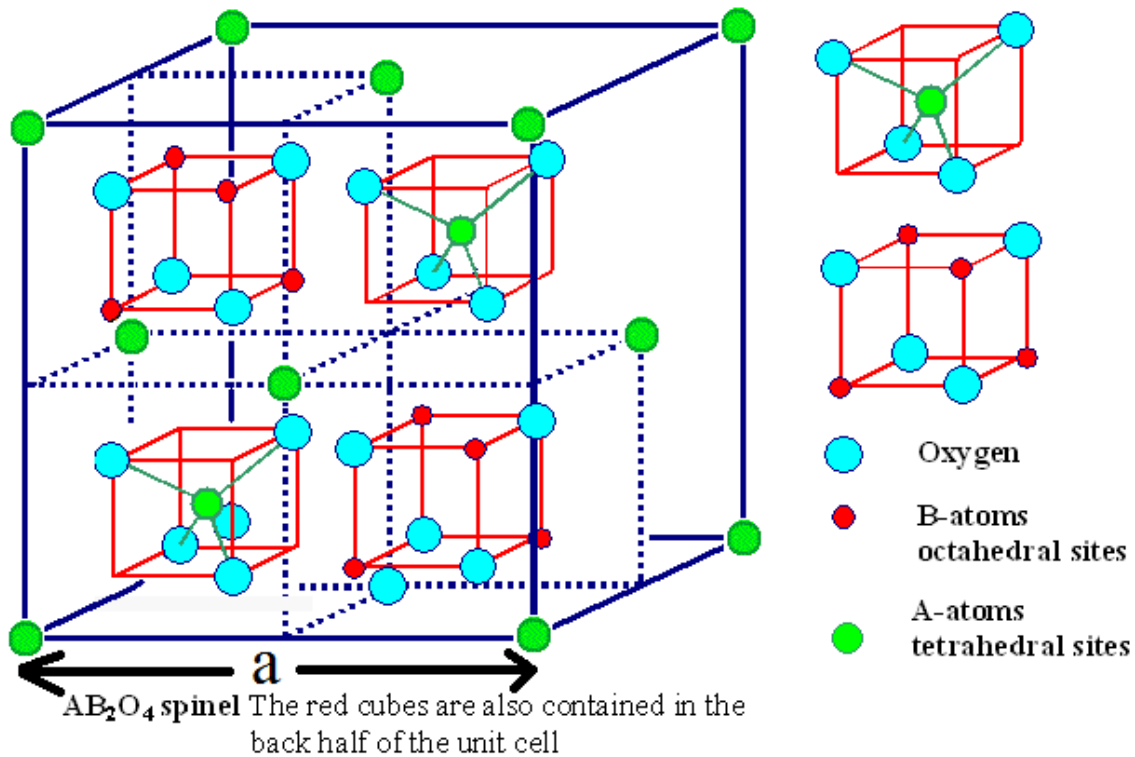


Fig. 1.3: The AB_2O_4 structure of spinel. The unit cell consists of alternate octahedral and tetrahedral structures as shown in the left diagram. The quadrants are also shown.

The chemical formulae of spinel ferrite is :- $MOFe_2O_3$ where M represents one or more divalent metal ions such as Mn, Fe, Co, Ni, Zn, Mg etc. The spinel ferrites have same crystallographic structure as the mineral spinel $MgAl_2O_4$ determined by Bragg [24,25]. Space group of spinel ferrites are cubic, $O_h^7 - F3dm$.

Atomic positions are the following:

8-fold position, 8- metal cations in (a) i.e.

$$0,0,0, \frac{1}{4}, \frac{1}{4}, \frac{1}{4}$$

16-fold position, 16 metal ions in (d), i.e.

$$\frac{5}{8}, \frac{5}{8}, \frac{5}{8}, \frac{5}{8}, \frac{7}{8}, \frac{7}{8}, \frac{7}{8}, \frac{7}{8}, \frac{5}{8}, \frac{7}{8}, \frac{7}{8}, \frac{7}{8}, \frac{5}{8}$$

32-fold position, 32 oxygen ions in (e), i.e.

$$uuu, u\bar{u}\bar{u},$$

$$\frac{1}{4}-u, \frac{1}{4}-u, \frac{1}{4}-u, \frac{1}{4}-u,$$

$$\frac{1}{4}+u, \frac{1}{4}+u,$$

$$\bar{u}\bar{u}\bar{u}, \bar{u}\bar{u}u,$$

$$\frac{1}{4}+u, \frac{1}{4}-u, \frac{1}{4}+u, \frac{1}{4}+u, \frac{1}{4}+u, \frac{1}{4}-u \text{ with the translations}$$

$$+ \left(\text{ooo}, \text{o} \frac{1}{2} \frac{1}{2}, \frac{1}{2} \text{o} \frac{1}{2}, \frac{1}{2} \frac{1}{2} \text{o} \right) u = \frac{3}{8}$$

Within the cubic closed-packed array of anions, the structure holds two types of interstices: octahedral and tetrahedral. Eight formulae units make up a unit cell of spinel, containing a total of 64 tetrahedral interstices and 32 octahedral interstices between the anions [26,27]. In each unit cell for each oxygen atom, there is one interstitial atom surrounded by an octahedral arrangement of oxygen atoms and two interstitial sites similarly surrounded by corresponding tetrahedral arrangement of the same. Among 64 tetrahedral sites only eight tetrahedral sites and among 32 octahedral sites only 16 octahedral sites are occupied in an unit

cell. In order to present a simpler picture the cubic lattice can be considered to be divided into two different groups, consisting of four cubes as shown in Fig. 1.3, with edge length $a/2$, known as octants. In two adjacent octants each of the small cubes contains four oxygen ions. In one of these octants the oxygen ions lie along the main diagonal and are half way from the divalent cations in the corner sites. For the other type of octant the oxygen ions lie along the main diagonal but in this case lie half toward the divalent metal cations in the corners.

There is a metal ion at the centre in the 8a position, which lies in the centre of a tetrahedron of oxygen ions (tetrahedral or A-site). In the right octant there are four metal cations in the 16d position, each surrounded by six oxygen ions (octahedral or B sites). Each A ion has 12 nearest neighbours of B type and each B ion has six nearest neighbours of the tetrahedral ions. Shortest distance between A and B sites i.e. r_{AB} is $(a/8)\sqrt{11}=0.414a$ and shortest distances between A-A sites i.e. r_{AA} and that for B-B sites i.e. r_{BB} are respectively, $(a/4)\sqrt{3}=0.432a$ and $(a/4)\sqrt{2}=0.353a$.

1.2.4 Different Spinel Ferrites

The spinel structure must contain eight divalent and sixteen trivalent iron cations distributed among eight tetrahedral and sixteen octahedral interstices in the unit cell. It is therefore reasonable to conclude that the divalent ions occupy tetrahedral and the trivalent iron ions occupy octahedral interstices, an arrangement which fully satisfies the requirement of lattice symmetry. Such a cationic distribution in a spinel ferrite is referred to as ‘Normal Spinel’ structure. Example of normal spinel ferrites are $ZnFe_2O_4$, $CdFe_2O_4$.

It was shown, however, by Barth and Posnjak [28] in 1932 that symmetry requirements are also met by another arrangement in which half of the trivalent iron ions occupy tetrahedral interstices and the octahedral interstices being filled by the divalent metal ions and the other half of the trivalent iron ions, distributed at random. This kind of arrangement is called inverse spinel. Examples of inverse spinel are $NiFe_2O_4$, $CoFe_2O_4$, $CuFe_2O_4$. We are interested in these inverse spinels mainly $NiFe_2O_4$ and $CoFe_2O_4$.

Nickel Ferrite

Nickel Ferrite ($NiFe_2O_4$) is a non-corrosive, non-toxic, soft ferromagnetic material. $NiFe_2O_4$ proved to be a good catalyst for the benzylation of toluene with benzoyl chloride [29]. It has a

peculiar and extraordinary gas sensing capabilities towards low concentration of chlorine gas in air [30]. NiFe_2O_4 is also used as a highly reproducible humidity sensor with a fairly good linearity [31]. Nanosized NiFe_2O_4 is a novel material for the detection of liquefied petroleum gas in air [32]. It is observed by Baea et al. [23] that solid state NiFe_2O_4 nanoparticles showed very promising self-heating temperature rising characteristics, high biocompatibility and suitable magnetic and structural properties for a hyperthermia agent application. In addition it was revealed that the maximum self-heating temperature of solid state NiFe_2O_4 nanoparticles is easily controlled in the biological safety and physiological tolerance ranges [23]. NiFe_2O_4 is also a promising material for microwave and magnetic device applications [33].

However, an unavoidable problem associated with magnetic nanoparticles like Iron Oxides is their intrinsic instability over longer periods of time. Such small particles tend to form agglomerates to reduce the energy associated with the high surface area to volume ratio of the nanosized particles. Moreover, bare nanoparticles are chemically highly active and are easily oxidized in air, resulting generally in loss of magnetism and dispersibility. For many applications it is thus crucial to develop protection strategies to chemically stabilize the naked magnetic nanoparticles against degradation during or after the synthesis. These strategies comprise grafting of or coating with organic species, including surfactants or polymers, or coating with an inorganic layer, such as silica or carbon. It is noteworthy that in many cases the protecting shells not only stabilize the nanoparticles, but can also be used for further functionalization, for instance with other nanoparticles or various ligands, depending on the desired application. The rich and well documented biocompatible chemistry of silica colloids may allow for practical implementation of magnetic nanoparticles in magnetically guided drug delivery, tumor targeting, and magnetically assisted chemical separation of cells and/or proteins [34]. Particularly, the silica shell provides a chemically inert surface for the nanoparticulate system in biological systems. Moreover, it greatly improves the hydrophilicity of the oxide magnetic nanoparticles [34]. Among the various types of oxide magnetic particles, ferrites belong to a unique class since they have the advantage of having high resistivity in a wide frequency range as well as low production cost. NiFe_2O_4 is one such soft ferrite whose nanoparticles in core/shell form can have applications in magnetic recording media, ferrofluids, catalysts and microwave absorbents.

With this motive we have prepared the NiFe_2O_4 nanoparticles by co-precipitation technique, coated them with SiO_2 employing the Stöber process and studied their magnetic properties in details. Some research has been done on Fe, Fe/Ni, FePt, Fe_3O_4 , CoFe_2O_4 , MnFe_2O_4 nanoparticles coated with SiO_2 or embedded in SiO_2 matrix [34 - 37]. But the coating of SiO_2 on NiFe_2O_4 has not been properly explored yet. Zhang et al. [34] have reported the use of reverse micelle microemulsion method with the surfactant polyoxyethylene (5) nonylphenyl ether (Igepal CO-520) to prepare silica-coated CoFe_2O_4 and MnFe_2O_4 nanoparticles. We were successful in synthesizing perfect spherical core shell nanoparticle by a more simple chemical synthesis called the Stöber process. M. Ammar et al. [37] have also coated SiO_2 on $\text{Fe}_{29.5}\text{Ni}_{70.5}$ nanoparticles. They have proposed that coating by an insulating shell like SiO_2 on the surface of a soft magnetic nanoparticle like $\text{Fe}_{29.5}\text{Ni}_{70.5}$ confers to the material a high permeability independent of the frequency, even in the gigahertz range. Such materials are typically suited for applications in telecommunications. Since NiFe_2O_4 is also a very good soft magnetic material, we have proceeded in coating SiO_2 on NiFe_2O_4 to make it applicable in telecommunications. NiFe_2O_4 being a ferrite has high frequency applications [33]. Hence we have also analyzed the ac hysteresis loops of these NiFe_2O_4 nanoparticles at different frequencies by a home-made set up. We have also explored the LPG sensing properties of different nanostructures of NiFe_2O_4 prepared by the hydrothermal technique. This has been discussed in Chapter 3 of this thesis.

Cobalt Ferrite

CoFe_2O_4 has received enormous attention for its high magnetocrystalline anisotropy, high coercivity (H_C), moderate saturation magnetization (M_s), large magnetostrictive co-efficient along with good mechanical hardness and chemical stability [38]. Again CoFe_2O_4 nanoparticles have many biomedical applications like Magnetic Resonance Imaging (MRI) [7,8], ferrofluids [3], cancer therapy [13], hyperthermia [14], catalysis [4,5]. But for the fruitful realization of these applications the particles must have a narrow size distribution, high magnetization values, and no agglomeration. So far various synthesis routes have been devised for the synthesis of nanoparticles like co-precipitation [39,40], sol-gel technique [41], hydrothermal [42], microemulsion [43], forced hydrolysis [44]. But the problem in these processes is that the particles become agglomerated with very poor size distribution which greatly restricts their applications [45]. To address these concerns, Li et al. adopted a general liquid–solid–solution

(LSS) phase transfer and separation method [46]. This strategy is based on a general phase transfer mechanism occurring at the interfaces of the liquid, solid, and solution phases present during the synthesis. Through this general method, Li et al. successfully synthesized Fe_3O_4 doped with Co, which has coercivity about 250 Oe at room temperature [47]. However, the synthesis of non-agglomerated CoFe_2O_4 nanoparticles with a superparamagnetic behavior at room temperature is quite challenging. We have synthesized non-agglomerated superparamagnetic CoFe_2O_4 nanoparticles with high saturation magnetization of 50 emu/g. These particles can be very useful in biological applications. This has been discussed in Chapter 4 of this thesis.

The particles with small size and high coercivity have potential in data storage devices such as audio and videotape and high-density digital recording disks. The coercivity of magnetic nanoparticles depends on several parameters such as particle size and its distribution, shape, anisotropy, strain, surface spins, interaction between the particles etc. [48-51]. From last decades intensive research is going on in these topics. But there is no clear evidence to state which property is most responsible. Till now, it is believed that the coercivity of fine particles is mainly influenced by particle size. With the decrease in particle size, H_C increases and below a critical diameter (as shown in Fig. 1.1), the particles become single domain, and in this size range H_C reaches maximum [48]. On further decrease in size, the H_C decreases and the particles reach a super-paramagnetic state. A number of efforts have been made to increase the coercivity of cobalt ferrite nanoparticles. B. H. Liu et al. [49] have reported a high coercivity of 5.1 kOe for mechanically milled CoFe_2O_4 powder and explained it on the basis of high density of defects and high level of strain induced by milling. A high coercivity of 4.65 kOe is obtained for CoFe_2O_4 nanoparticles of diameter 40 nm synthesized by seed-mediated growth dominant precipitation and modified oxidation methods [50]. They have discussed such a high coercivity from the viewpoint of particle size and have suggested that the critical size of single-domain CoFe_2O_4 nanoparticles is 40 nm. Also in [51] change of H_C with particle size has been reported. A high coercivity of 1.2 kOe for single domain CoFe_2O_4 nanoparticle of critical diameter ~40nm has also been reported in [51]. Apart from these results, a highest coercivity of 1.215 kOe at room temperature (RT) was reported for 25 nm particles [52] which is almost half of the most reported value of critical diameter. Hence from many references we see that coercivity is not constant for

a fixed size and critical diameter also differ. Hence size is not only a crucial point, there are some other parameters too influencing magnetic property in case of nanoparticles. We have synthesized CoFe_2O_4 nanoparticles by wet chemical route using micelles as capping agent and obtained a high coercivity of ~ 4.4 kOe at room temperature (RT) for the as synthesized particles of diameter ~ 16 nm. The size 16 nm is much smaller than the reported critical diameter of single domain particles so far. In our research work, we have found micelles as capping agent playing an important role to enhance the coercivity for cobalt-ferrite nanoparticles. We have checked also the role of particle size in enhancement of coercivity by annealing the sample at different temperatures. Here we see annealing the sample at 350°C the coercivity decreases abruptly to ~ 350 Oe from 4.4 kOe (H_C for as made samples). This is an unusual result from the critical diameter point of view as this temperature (350°C) cannot change the particle size. Therefore we presume in our system, there might be some other parameters such as surface anisotropy, inter-particle interaction etc. which are responsible for this high H_C and we have discussed those parameters in Chapter 4 of this thesis.

1.3 Multiferroics

Some of the iron oxides show two or more ferroic properties simultaneously, such as ferroelectricity, ferromagnetism, ferroelasticity, ferrotoroidicity. They are called Multiferroics. Typical multiferroics belong to the group of the perovskite transition metal oxides, and include rare-earth manganites and ferrites like TbMnO_3 , HoMn_2O_5 , LuFe_2O_4 , BiFeO_3 , GaFeO_3 , BiMnO_3 [53,54,55,56]. These materials offer a wide opportunity for potential applications in ferroelectric memories, spintronics, storage devices, sensors, actuators and other applications [57-60] where both electric and magnetic polarizations can be coupled giving enough opportunity for manipulating devices.

We will first give a brief description of the different ferroic properties.

- (i) **Ferroelectric materials** possess a spontaneous polarization that is stable and can be switched hysteretically by an applied electric field.
- (ii) **Antiferroelectric materials** possess ordered dipole moments that cancel each other completely within each crystallographic unit cell.
- (iii) **Ferromagnetic materials** possess a spontaneous magnetization that is stable and can be switched hysteretically by an applied magnetic field.

(iv) **Antiferromagnetic materials** possess ordered magnetic moments that cancel each other completely within each magnetic unit cell.

(v) **Ferroelastic materials** display a spontaneous deformation that is stable and can be switched hysteretically by an applied stress.

(vi) **Ferrotoroidic materials** possess a stable and spontaneous order parameter that is taken to be the curl of a magnetization or polarization. By analogy with the above examples, it is anticipated that this order parameter may be switchable. Ferrotoroidic materials have evaded unambiguous observation. Ferrimagnetic materials differ from antiferromagnets because the magnetic moment cancellation is incomplete in such a way that there is a net magnetization that can be switched by an applied magnetic field.

The Maxwell equations that relate electric and magnetic fields, charge density and current density show that magnetic and electric interactions couple to each other. The formal equivalence of the equations of electrostatics and magnetostatics explains numerous similarities in the theory of ferroelectrics and ferromagnets, for instance their behavior in external fields and domain structures.

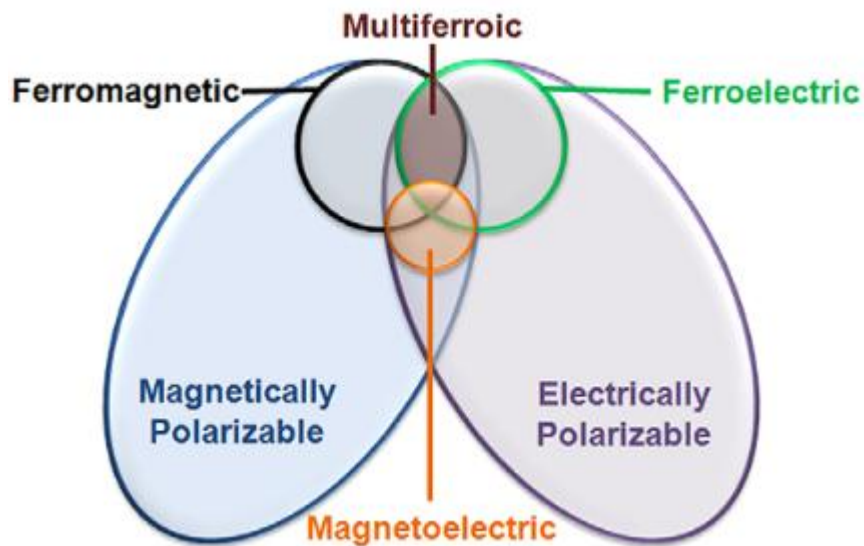


Fig. 1.4: The relationship between multiferroic and magnetoelectric materials. Ferromagnets (ferroelectrics) form a subset of magnetically (electrically) polarizable materials such as paramagnets and antiferromagnets (paraelectrics and antiferroelectrics). The intersection (grey area) represents materials that are multiferroic. Magnetoelectric coupling (orange area) is an independent phenomenon that can, but need not, arise in any of the materials that are both magnetically and electrically polarizable. In practice, it is likely to arise in all such materials, either directly or via strain.

These similarities are unexpected because of the different origins of ferroelectricity and magnetism in solids. Magnetism appears in materials which have incomplete d orbitals whereas ferroelectricity originates from atomic shifts that break inversion symmetry in a crystal. Moreover ferroelectric polarization appears in materials with distorted asymmetric crystal structures, whereas ferromagnetism requires a symmetric structure. Thus the multiferroic compounds (single phase) are scarce, especially ferromagnetic ferroelectric multiferroic compounds as shown in Figure 1.4.

Each multiferroic property is closely linked to symmetry. The primary ferroic properties can be characterized by their behavior under space and time inversion. Space inversion for example will reverse the direction of polarization P while leaving the magnetization M invariant. Time reversal, in turn, will change the sign of M , while the sign of P remains invariant [61]. Magnetoelectric multiferroics require simultaneous violation of space and time inversion symmetry. In BiFeO_3 , for example, off-centering of ions gives rise to an electric polarization, while at a lower temperature additional magnetic ordering breaks time-reversal symmetry.

Table 1.1: Spatial-inversion and time-reversal symmetry in ferroics

Characteristic symmetry	Spatial-inversion symmetry?	Time-reversal symmetry?
Ferroelastic	Yes	Yes
Ferroelectric	No	Yes
Ferromagnetic	Yes	No
Multiferroic	No	No

The phenomenological description of magnetoelectrics and multiferroics is based on the series expansion of the free energy in powers of the magnetic and electric fields [62-64]. We consider here the free energy density

$$dF = -SdT - P.dE_0 - M.dB_0 \quad (1.4)$$

written in S.I. units, where S is the entropy, T the temperature, P , and M the electric polarization and magnetization, E_0 and $B_0 = \mu_0 H_0$, the external electric and magnetic fields, where $\mu_0 = 4\pi \times$

$10^{-7} \text{ VsA}^{-1}\text{m}^{-1}$ is the free space permeability. The thermodynamic potential F is constructed such that it does not include the electric and magnetic energies existing in the absence of the system. For a single-phase multiferroic, at constant temperature and up to quadratic order in the electric and magnetic fields, [62,64,65].

$$-F(E_0, B_0) = P_s E_0 + M_s B_0 + \frac{\epsilon_0}{2} \sum_{ij} \chi_{ij}^e E_{0i} E_{0j} + \frac{1}{2\mu_0} \sum_{ij} \chi_{ij}^m B_{0i} B_{0j} + \frac{1}{\mu_0} \sum_{ij} \alpha_{ij} E_{0i} B_{0j} + \dots \quad (1.5)$$

where P_s and M_s are spontaneous electric and magnetic polarizations; χ^e and χ^m are the electric and magnetic susceptibility tensors; α is the linear magnetoelectric coupling tensor; and ϵ_0 is the free space permittivity. (For simplicity, we assume uniform fields and polarizations; in the general case, integrations over the volume of the sample need to be carried out.) α describes the onset of an induced electric (magnetic) polarization upon application of a magnetic (electric) field. In the general case, one may take α to be a function of the electric and magnetic fields, in analogy to the electric permittivity or the magnetic permeability of polarized materials. From equation (1.5), it follows that in order to fulfill time reversal and space inversion symmetries, the presence of the last term implies that the crystal must be invariant under inversion reflection [63]. This requirement implies that magnetic order is a necessary condition to the presence of a linear magnetoelectric effect [66,62].

A multiferroic that is ferromagnetic and ferroelectric is liable to display large linear magnetoelectric effects. This follows because ferroelectric and ferromagnetic materials often (but not always) possess a large permittivity and permeability respectively, and α_{ij} is bounded by the geometric mean of the diagonalized tensors χ^e and χ^m such that [67]:

$$\alpha_{ij} \leq (\epsilon_0 \mu_0 \chi_{ii}^m \chi_{jj}^e)^{\frac{1}{2}} \quad (1.6)$$

Equation (1.6) is obtained from equation (1.5) by forcing the sum of the last three terms to be greater than zero, that is, ignoring higher-order coupling terms. It represents a stability condition on χ^e and χ^m , but if the coupling becomes so strong that it drives a phase transition to a more stable state, then α_{ij} , χ^e and χ^m take on new values in the new phase. It is to be noted that a large χ^e is not a prerequisite for a material to be ferroelectric (or vice versa); and similarly ferromagnets do not necessarily possess large χ^m . For example, the ferroelectric KNO_3 possesses a small $\epsilon=25$ near its Curie temperature of 120°C [68], whereas paraelectric SrTiO_3 exhibits $\epsilon >$

50,000 at low temperatures [69]. Therefore large magnetoelectric couplings need not arise in, or be restricted to, multiferroic materials.

Nonlinear coupling. Most materials have small values of either χ^e and χ^m or both, so the linear magnetoelectric effect will also be small, given that permittivity and permeability appear as a product in equation (1.6).

Indirect coupling. So far, our discussion of linear and higher-order magnetoelectric coupling has ignored the effects of strain. Such effects could be significant or even dominant. For example, the inclusion of piezomagnetism (magnetostriction) would generate cross terms in equation (1.5) that are proportional to strain and vary linearly (quadratically) with H_i . Analogous expressions would arise from piezoelectricity or electrostriction (described in 1.4.1). Furthermore, mixed terms involving products of strain, H_i and E_j have been predicted [70]. In two-phase materials, magnetic and electrical properties are strain-coupled by design in the quest for large magnetoelectric effects. The strength of this indirect coupling is not restricted by equation (1.6), and enhancements over single-phase systems of several orders of magnitude have been achieved [71].

1.3.1 Bismuth Ferrite (BiFeO_3)

BiFeO_3 is perhaps the most commonly studied multiferroic material, in part because of its large ferroelectric and magnetic ordering temperatures, $T_C = 1123$ K, $T_N = 643$ K. At room temperature, bulk BiFeO_3 adopts a rhombohedrally distorted perovskite structure with Bi ions present in the cube edges, Fe present in the body centre (1/2,1/2,1/2) and Oxygen present in the face centre (1/2,1/2,0); as shown in Fig. 1.5. It belongs to the space group $R3c$ (or C_6^{3V}). The hexagonal unit-cell (as shown in Fig. 1.6 (a).) parameters are $a = b = 5.587$ Å and $c = 13.867$ Å [72] with $\alpha = \beta = 90^\circ$ and $\gamma = 120^\circ$ [73,74].

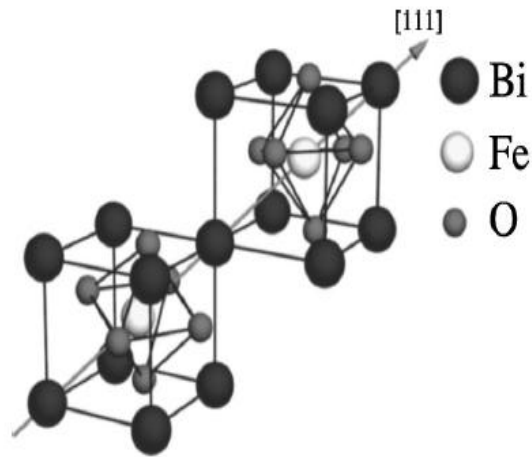


Fig. 1.5: Crystal Structure of BiFeO_3 [Image taken from C. Ederer, N. Spaldin PRB 71(060401) (R) (2005)]

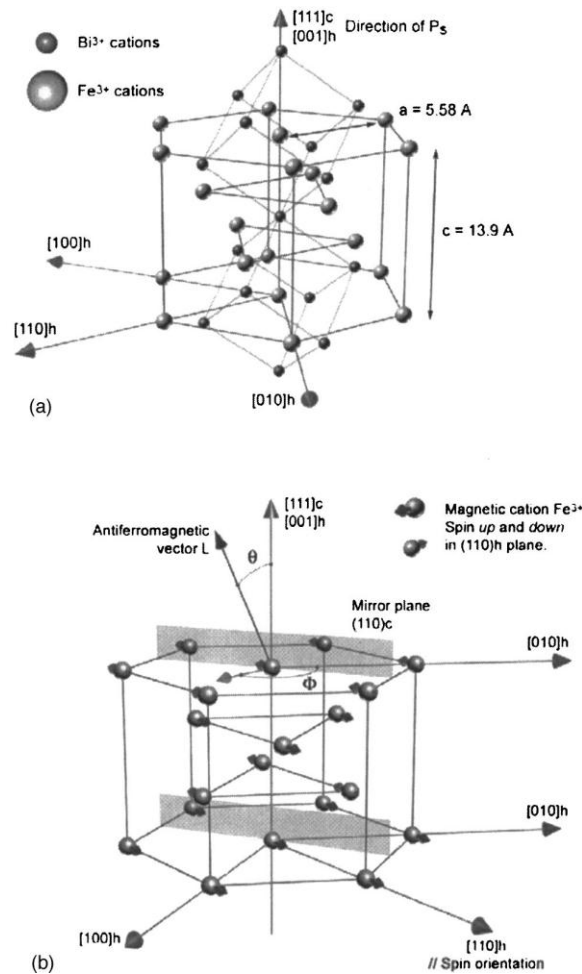


Fig.1.6.(a) Crystal lattice of BiFeO_3 , illustrating rhombohedral units and hexagonal cell. The direction of spontaneous polarization is illustrated in this figure. (b) Hexagonal representation of spin structure of BiFeO_3 . Both the antiferromagnetic order and spin rotation planes are shown in this figure. (image taken from PHYSICAL REVIEW B **69**, 064114 ~2004)

The ferroelectricity in BFO originates from the A-site cation (Bi^{3+}) which has a stereochemically active $6s^2$ lone-pair. It causes the Bi 6p (empty) orbital to come closer in energy to the O 2p orbitals. This leads to hybridization between the Bi 6p and O 2p orbitals and drives the off-centering of the cations towards the neighboring anion resulting in ferroelectricity along the threefold pseudocubic $[111]_c$ direction [75]. This centrosymmetric distortion is polar, and results in a spontaneous polarization (P_s), as illustrated in Fig. 1.6 (a). The large remnant polarization was initially reported in thin films, but has recently been demonstrated in both ceramics [76] and high quality single crystals [77,78].

The local short-range magnetic ordering of BiFeO_3 is G-type antiferromagnet [79,80]. The spin is provided by the transition-metal cation Fe^{3+} . Each Fe^{3+} spin is surrounded by six antiparallel spins on the nearest Fe neighbours. Figure 1.6 (b) shows the hexagonal representation of the spin structure of BiFeO_3 . In this structure the hexagonal $[001]_h$ direction is equivalent to the pseudocubic $[111]_c$, about which axis there is a threefold rotation; and about the hexagonal $[110]_h$, there is a mirror plane. Thus along the $[001]_h/[111]_c$, BiFeO_3 has antiferromagnetic order, as illustrated in Fig. 1.6 (b). Due to the structural distortion, the arrangement of the neighbouring spins is in fact not perfectly antiparallel. The canted spins induce a weak magnetic moment that couples with the ferroelectric polarization.

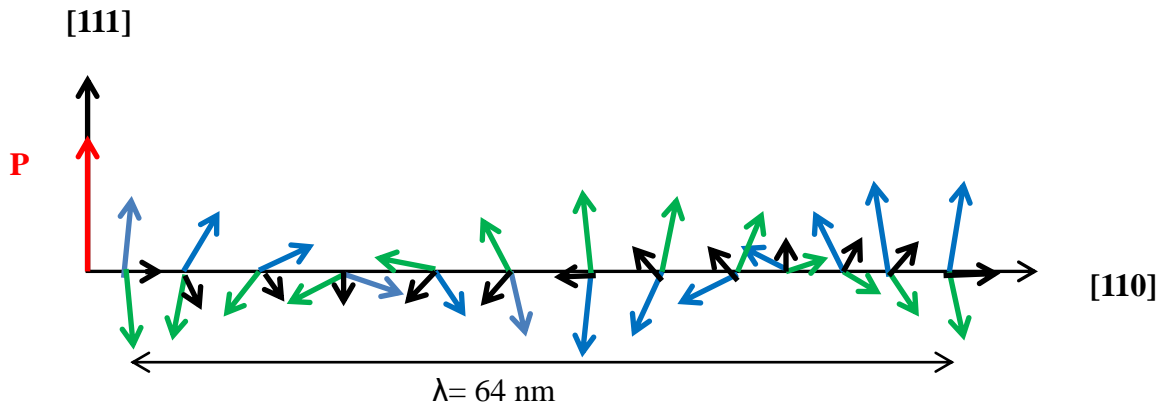


Fig. 1.7: Schematic representation of the spin cycloid. The canted antiferromagnetic spins (blue and green arrows) give rise to a net magnetic moment (black arrows) that is spatially averaged out to zero due to the cycloidal rotation. The spins are contained within the plane defined by the polarization vector (red) and the cycloidal propagation vector (black).

Superimposed on this canting, however, is also a long-range superstructure proposed and verified by Sosnowska et al. (1982) [81,82]. It consists of an incommensurate spin cycloid of the antiferromagnetically ordered sublattices. The cycloid has a very long repeat distance of 62–64

nm as shown in Fig. 1.7 and a propagation vector along the $[110]_h$ direction [83,84]. This leads to the cancellation of the magnetization. The linear magneto-electric effect is allowed by the average $R3c$ space group but at the same time is excluded by the spin cycloid.

Hence, inspite of being a multiferroic material, Bismuth Ferrite has some problems like cancellation of macroscopic magnetization due to the spin cycloid, difficulties in imparting strong ferroelectric behavior and piezoelectric properties because of the low electrical resistivity; which restricts its applications.

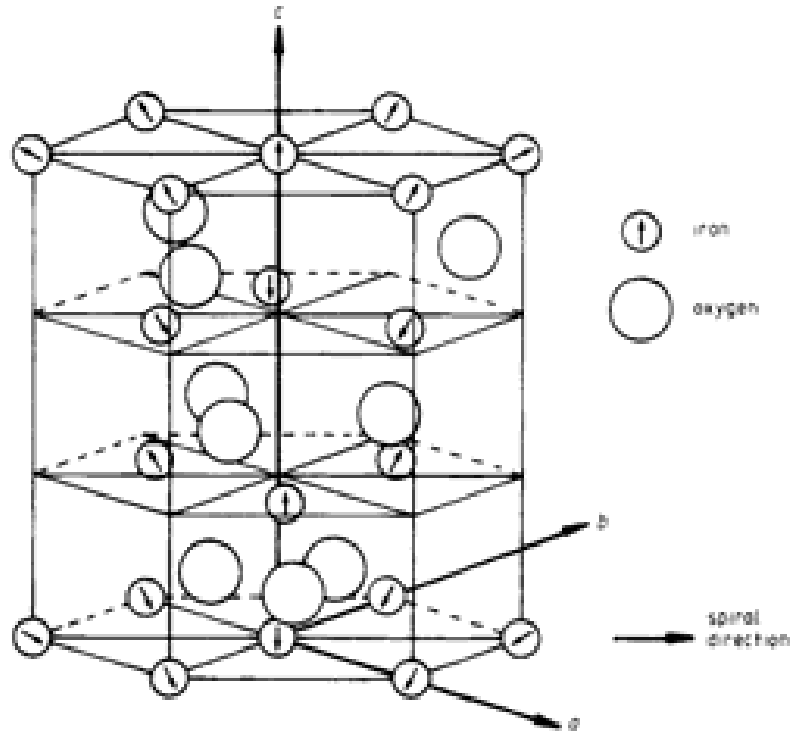


Fig. 1.8: The part of the BiFeO_3 lattice with only iron and oxygen ions shown. The arrows indicate the Fe^{3+} moment direction [22].

It is therefore of interest to try and destroy the space-modulated spin cycloid. Various methods have been used for this purpose. Many researchers have doped various rare earth, transition, alkaline earth metals in the A as well as B sites [85-90]. The application of a magnetic field of 20T has been shown to induce a transition to a homogeneous AF state and to restore a non-zero magnetization [91,92]. Making BiFeO_3 in thin film form also leads to a homogeneous AF spin structure [93,94]. Low level substitutions of rare earth ions (La, Dy,...) for bismuth have an interesting effect: the introduction of rare earth cations in BiFeO_3 seems to increase the

magnetocrystalline anisotropy [95-97] thus making the cycloidal spin structure energetically unfavourable. It can then be destroyed by a magnetic field lower than in pure BiFeO₃. However, much of the work on the La doping effect in bismuth ferrite reported so far has usually focused on the thin films and bulk samples. As the thin film performance highly depends on the film thickness and the strain formed due to lattice mismatch between the film and the substrate, it is always hard to distinguish the genuine effect of element substitution from strain effect. Bulk La doped BiFeO₃ material, prepared by solid state reaction, has the problems of non-stoichiometry and impurities. In order to overcome this problem we have tried to synthesize Lanthanum doped BFO in the nanocrystalline form and explore the changes taking place.

Valency of Bismuth is 3+ whereas that of Barium is 2+. Hence incorporating Barium in the Bismuth site will require charge compensation. This may result in the formation of Fe⁴⁺ or oxygen vacancies; the former may distribute statistically with Fe³⁺ in the octahedron in BBFO and lead to a net magnetization and ferromagnetism [98]. With this goal we have also doped Barium in the Bismuth site. Many work has been done in Barium doped BFO in bulk form. Ong et al. [99] have synthesized Ba doped BFO by the solid state method and have obtained a high magnetization and ferroelectricity. Change in the morphology with change in doping concentration has not been investigated so far for Ba doped BFO.

Synthesis of nanostructures of Bismuth Ferrite of different morphology can also break the spin cycloid if the dimension of the particle be comparable to that of the spin cycloid. Producing different morphology can induce a distortion in the spin cycloid structure leading to its breakage. With this in mind we have chosen hydrothermal route to synthesize BFO nanoparticles because particles formed in hydrothermal synthesis have varied shapes (discussed in Chapter 2). As far as our knowledge is concerned; synthesis and characterization of nanostructures of bismuth ferrite have rarely been done. The only work on different nanostructures of BFO so far is by Goodenough et al. [100]. They have synthesized various structures of BFO by changing the solvothermal conditions. But their particle size was much bigger of the order of μm . Jimin et al. have synthesized plate shaped BFO having diameter $1\mu\text{m}$ and thickness 300 nm by changing the concentration of the surfactant [101]. We have synthesized nanoparticles ranging from 80 nm to 600 nm by changing the temperature and solvent of solvothermal synthesis. In Chapter 5, we have discussed in details about the synthesis

of various nanostructures of BFO, Lanthanum doped BFO and Barium doped BFO by the hydrothermal route.

1.4 Magnetoelectric Effect

Single phase multiferroics do not solve the problem completely since in a single phase it is very difficult to obtain both the ferromagnetism and ferroelectricity simultaneously. Magnetoelectric composites consisting of piezoelectric and magnetostrictive phases are more suited for scientific applications.

1.4.1 Piezoelectricity

The piezoelectric effect is a phenomenon whereby mechanical stress or strain leads to reorientation of electric dipoles through a material, inducing a spontaneous change in the charge polarization. All ferroelectrics exhibit the piezoelectric effect (although all piezoelectrics are not necessarily ferroelectric). The piezoelectric effect may be formally described by the following set of equations, which provide a relationship between the electric displacement D , the electric field E , and the stress and strain, T and S respectively [102]:

$$D = \epsilon_T E + d_{33} T \quad (1.7)$$

$$S = d_{33} E + s_E T \quad (1.8)$$

where ϵ_T is the dielectric constant and d_{33} is the piezoelectric constant. s_E is the material's compliance in the presence of a constant electric field. This constant describes the stress strain relationship for a material and is based on the material's Young's modulus and Poisson's ratio [103]. From the equations above, it can be seen that any increase or decrease in stress (T) or strain (S) on the material will lead to an increase or decrease in electric displacement (D) and in the material's electric field (E). These relations also predict the existence of the converse piezoelectric effect, whereby a piezoelectric material physically changes shape when an external

electric field E is introduced. This altered shape is a result of an increase in stress T and strain S on the material due to the electric field change.

1.4.2 Magnetostriction

Not surprisingly, there exists a magnetic parallel to a piezoelectric, referred to as a magnetostrictive material. For a piezoelectric, reorientation of the material's net electric polarization causes the structure to physically change shape. Equivalently, when a magnetostrictive material is subject to an external magnetic field, the magnetic field alters the shape of the material. Practically all ferromagnets (and ferrimagnets) are magnetostrictive. At room temperature, cobalt is the most magnetostrictive pure element [104]. A magnetostrictive material alters its shape as a result of two phenomena. First, the magnetic dipoles spin about their axis in order to reorient to match the external magnetic field. Second, the force felt by the external field causes the domain walls to migrate. These changes that occur on the level of individual dipoles and on the scale of domain walls both contribute to the shape change [104].

1.4.3 Product property of ME effect

The ME effect in composite materials is known as a product tensor property, first proposed by van Suchtelen in 1972 [105]. According to the original definition, the composite ME effect is a result of the product of the magnetostrictive effect (magnetic/mechanical effect) in the magnetic phase and the piezoelectric effect (mechanical/electrical effect) in the ferroelectric phase,

$$ME\ effect = \frac{Magnetic}{Mechanical} * \frac{Mechanical}{Electric} \quad (1.9)$$

The application of a magnetic field in the magnetostrictive phase will induce a strain in it which in turn will induce a strain in the piezoelectric phase resulting in the generation of ferroelectricity. The ME effect obtained in composites is more than a hundred times that of single-phase ME materials. In 1978, Boomgaard [106] outlined the conceptual points inherent to the ME effect in composites. These can be summarized as (i) two individual phases should be in equilibrium (ii) mismatching between grains should not be present (iii) magnitude of the magnetostriction coefficient of piezomagnetic or magnetostrictive phase and magnitude of the piezoelectric coefficient of the piezoelectric phase must be greater (iv) accumulated charge must not leak through the piezomagnetic or magnetostrictive phase and (v) deterministic strategy for

poling of the composites. CoFe_2O_4 is highly magnetostrictive. BaTiO_3 is also highly piezoelectric. Hence their composite will act as a very good magnetoelectric composite. At present various composites have been reported such as $\text{Ni}(\text{Co},\text{Mn})\text{Fe}_2\text{O}_4\text{-BaTiO}_3$, $\text{CoFe}_2\text{O}_4\text{-BaTiO}_3$, $\text{NiFe}_2\text{O}_4\text{-BaTiO}_3$, $\text{LiFe}_5\text{O}_8\text{-BaTiO}_3$, $\text{CoFe}_2\text{O}_4\text{-Bi}_4\text{Ti}_3\text{O}_{12}$ etc. [107-116]. But most of them were bulk composites. Duong et al. [117] have synthesized core shell $\text{CoFe}_2\text{O}_4\text{:BaTiO}_3$ core shell nanocomposites. They have obtained very high magnetoelectric co-efficient of $3.4 \text{ mVcm}^{-1}\text{Oe}^{-1}$. We have explored the possibilities of increasing magnetoelectric effect by making core shell nanocomposites. Corral-Flores et al. [118] have produced nanostructures of core shell $\text{CoFe}_2\text{O}_4\text{:BaTiO}_3$. But they have not shown the magnetoelectric co-efficient measurements. We have prepared a home-made set-up for measuring the magnetoelectric co-efficient. We have not only shown the magnetoelectric co-efficient of the core shell nanocomposites but also proved that the magnetoelectric coupling in the core shell nanocomposite is much more than that in the mixture of two phases. This has been discussed in Chapter 6. Our motivation behind preparing core shell was to enhance the coupling between the two phases. In composites the particles are present in an agglomerated state with an irregular distribution. This increases the conductivity of the sample and hence the ferroelectric property is not manifested in it fully. This problem can be overcome by preparing core shell nanoparticles. We have proved the enhancement of the magnetoelectric co-efficient of the core shell composite by comparing their magnetoelectric co-efficient with that of a mixture of the two constituents.

1.5 Motivation of Thesis

An unavoidable problem associated with magnetic nanoparticles like Iron Oxides is their intrinsic instability over longer periods of time. Such small particles tend to form agglomerates to reduce the energy associated with the high surface area to volume ratio of the nanosized particles. Moreover, naked nanoparticles are chemically highly active and are easily oxidized in air, resulting generally in loss of magnetism and dispersibility. For many applications it is thus crucial to develop protection strategies to chemically stabilize the naked magnetic nanoparticles against degradation during or after the synthesis. These strategies comprise grafting of or coating with organic species, including surfactants or polymers, or coating with an inorganic layer, such as silica or carbon. It is noteworthy that in many cases the protecting shells not only stabilize the nanoparticles, but can also be used for further functionalization, for instance with other

nanoparticles or various ligands, depending on the desired application. With this goal in mind we have coated NiFe_2O_4 with SiO_2 and prepared core shell nanostructures. Ferrites also have very good high frequency applications. Hence we have studied the high frequency hysteresis behavior of the NiFe_2O_4 nanoparticles. NiFe_2O_4 also have good gas sensing properties. Hence we have prepared NiFe_2O_4 of two different morphology and studied the gas sensing behavior with the change of morphology.

Nanoparticles also have a problem of agglomeration and this prevents its full application in biomedical purposes. Hence preparation of non-agglomerated magnetic nanoparticles is of huge importance in the context of biomedical applications. Different researchers have prepared non-agglomerated ferrite nanoparticles by different methods. We have synthesized non-agglomerated CoFe_2O_4 nanoparticles having very small size of ~ 7 nm by the hydrothermal technique using strong capping agents. CoFe_2O_4 also have high magnetocrystalline anisotropy and hence are highly coercive and hence can be used in recording devices. If we can prepare nanoparticles which have high coercivity then that can be very useful since huge information can be stored within very less space. But nanoparticles below ~ 20 nm becomes superparamagnetic i.e. have zero coercivity. Many researchers have tried to enhance the coercivity of CoFe_2O_4 nanoparticles and have given different reasons for the enhancement of coercivity. We have synthesized single domain CoFe_2O_4 nanoparticles of ~ 16 nm in diameter and have obtained a huge coercivity of ~ 4.4 kOe. After detailed analysis we have concluded that the micelles are playing the main role in the enhancement of coercivity. These single domain nanoparticles having high coercivity can be extremely useful in memory storage devices.

BiFeO_3 is a multiferroic. But at room temperature it does not show its multiferroic properties. There is a spin cycloid structure of wavelength ~ 62 nm. Because of this structure the macroscopic magnetization is cancelled. In addition Bi is stereochemically active because of the lone pair of electrons. Hence BiFeO_3 has very low resistance and high leakage characteristics. It is therefore of interest to try and destroy the space-modulated spin cycloid and stabilize Bismuth. Synthesis of nanostructures can be a solution to this problem since nanoparticles of diameter < 62 nm will not have the problem of spin cycloid. Doping of various elements like rare earth, transition, alkaline-earth in the Bi site and the Fe site can overcome this problem since due to doping some distortion might take place which will break the spin cycloid Doping of rare earth

elements in the Bi site can stabilize the structure and reduce the leakage current since rare earth elements are extremely stable elements. This motivated us to dope Lanthanum as well as Barium in the Bi site separately and study its magnetic and dielectric properties in details.

Single phase multiferroics do not solve the problem completely since in a single phase it is very difficult to obtain both the ferromagnetism and ferroelectricity simultaneously. Magnetoelectric composites consisting of piezoelectric and magnetostrictive phases are more suited for scientific applications. In composites the particles are present in an agglomerated state with an irregular distribution. This increases the conductivity of the sample and hence the ferroelectric property is not manifested in it fully. This problem can be overcome by preparing core shell nanoparticles. CoFe_2O_4 is highly magnetostrictive and BaTiO_3 is highly piezoelectric. Hence we have synthesized core shell nanocomposites of $\text{CoFe}_2\text{O}_4/\text{BaTiO}_3$.

1.6 Objective of this work

- To synthesize NiFe_2O_4 and $\text{NiFe}_2\text{O}_4:\text{SiO}_2$ core shell nanocomposites and variation of the size of the nanoparticles.
- To study the size dependent dc magnetic properties of the coated and uncoated particles and also the ac hysteresis loops of the same at different frequency.
- To synthesize NiFe_2O_4 nanoparticles of different morphology and study its gas sensing properties.
- To synthesize non-agglomerated CoFe_2O_4 nanoparticles from capping agents, Olyl Amine, Sodium Oleate and variation of the particle size by varying the concentration of the capping agents.
- To study the size dependent dc magnetic properties of the same.
- To synthesize micelle (TX 100) coated single domain CoFe_2O_4 nanoparticles having high coercivity and detailed study of their magnetic behavior.
- To synthesize various nanostructures of Bismuth Ferrite and study of their magnetic and dielectric properties.

- To separately dope Lanthanum and Barium in the Bismuth site of Bismuth Ferrite and enhance its multiferroic property.
- To synthesize core shell $\text{CoFe}_2\text{O}_4:\text{BaTiO}_3$ nanocomposites and a mixture of the two.
- To measure the magnetoelectric co-efficient of both of them and show that the magnetoelectric co-efficient of the core shell composite structure is more than that of the mixed structure.

1.7 Organization of the thesis

The work done in this thesis has been discussed in six chapters and the details discussed in each chapter are discussed below:

Chapter 1 gives an introduction about the different kinds of iron oxides their properties and applications. A review on the work done so far on iron oxides (ferrites and multiferroics) has been discussed. The motivation behind this work has been justified and the main objectives of this thesis are outlined.

Chapter 2 describes the chemistry and synthesis techniques used for synthesizing the nanoparticles and also the different characterization techniques used for characterization of the nanoparticles. The home-made AC susceptibility set up and Magnetoelectric co-efficient (ME) set up is described in details.

Chapter 3 presents the study on NiFe_2O_4 and $\text{NiFe}_2\text{O}_4:\text{SiO}_2$ core shell nanocomposites. The procedure of synthesizing $\text{NiFe}_2\text{O}_4:\text{SiO}_2$ core shell nanocomposites is described in details. The annealing temperature has been varied to produce particles of different sizes (4 nm – 32 nm). Superparamagnetic behavior is observed for particles upto ~14 nm in diameter. The Langevin function used to explain paramagnetism was found to describe well the magnetization behavior of the samples ~14 nm in diameter consisting of weakly interacting single domain particles in the superparamagnetic state. The ZFC FC curves show an increase in the blocking temperature with increase in particle size. The blocking temperature also decreases for the core shell particles. The AC hysteresis loops of the samples measured in a frequency range of 30 Hz – 650 Hz show an

increase in coercivity with the increase of frequency of the applied field. This is attributed to the decrease in relaxation time. NiFe₂O₄ nanoparticles of different morphology has been synthesized by the solvothermal technique. The change in the magnetic properties with the change in morphology has been investigated. Their gas sensing properties were studied in the presence of LPG gas.

Chapter 4 presents the study of non-agglomerated CoFe₂O₄ and micelle (TX 100) coated CoFe₂O₄ nanoparticles. Non-agglomerated CoFe₂O₄ nanoparticles were synthesized by the hydrothermal technique using Olyl Amine and Sodium Oleate as capping agents. Different particle size has been obtained by changing the concentration of the capping agents. The change in the magnetic properties with the change in particle size has been studied in details. TX 100 coated CoFe₂O₄ nanoparticles were synthesized by a wet chemical route. A set of particles were obtained by annealing the as synthesized particles at different temperatures. The size of the as synthesized particles as obtained from XRD and TEM measurements was found to be ~16 nm. But a very interesting result has been found showing that the as synthesized particles had a very high coercivity of 4.4 kOe. The particles were found to be single domain from the linear fitting of the coercivity versus $T^{1/2}$ plot. The reason behind this unusually high coercivity has been investigated.

Chapter 5 deals with the synthesis and characterization of different nanostructures of BiFeO₃ and doped BiFeO₃. BiFeO₃ is a multiferroic material. But due to the arrangement of the spins in a spin cycloid like structure having wavelength of 62 nm, the magnetization is cancelled. Hence the multiferroic properties are not manifested in BiFeO₃. This drawback can be overcome either by preparing nanostructures or by doping in the Bismuth or the Iron site. We have synthesized various nanostructures (spindle, tile, cylindrical and hexagonal) of BiFeO₃. It is observed that the magnetic and the dielectric properties are best for the tile shaped sample. Lanthanum as well as Barium has been doped in the Bismuth site separately. It is observed that with doping the morphology of the particles also changes. In both cases there is enhancement of the dielectric constant and magnetization. The change is of bigger magnitude in case of Barium doping because of the bigger ionic radius (1.42 Å) of Barium compared to Bismuth (1.03 Å). ESR spectra analysis has been done which shows the breakage of spin cycloid due to doping.

Chapter 6 presents the study of magnetoelectric effect in $\text{CoFe}_2\text{O}_4:\text{BaTiO}_3$ core shell nanocomposites synthesized by the sol gel technique. A mixture of the two phases has also been prepared. The magnetoelectric co-efficient measurement set-up has also been indigenously developed. It is observed that the magnetoelectric co-efficient is 11 times more than that in the mixture. The dielectric constant measured in the presence of 1 Tesla field also proves the same.

References

- [1] Handbook of Nanophase Materials, A.N. Goldstein, ed., (Marcel Dekker Inc., New York, 1997).
- [2] The Chemistry of Nanomaterials, C.N.R. Rao, A. Müller and A.K. Cheetham, eds., (Wiley-Vch Verlag GmbH & Co. KGaA, New York, 1997), Vol.1.
- [3] S. Chikazumi, S. Taketomi, M. Ukita, M. Mizukami, H.Miyajima, M. Setogawa, Y. Kurihara, J. Magn. Magn. Mater., **65**, 245 (1987).
- [4] A.-H. Lu, W. Schmidt, N. Matoussevitch, H. BPNnermann, B.Spliethoff, B. Tesche, E. Bill, W. Kiefer, F. SchVth, Angew. Chem. **116**, 4403 (2004); Angew. Chem. Int. Ed. **43**, 4303 (2004).
- [5] S. C. Tsang, V. Caps, I. Paraskevas, D. Chadwick, D. Thompsett, Angew. Chem. **116**, 5763 (2004); Angew. Chem. Int. Ed. **43**, 5645 (2004).
- [6] A. K. Gupta, M. Gupta, Biomaterials **26**, 3995 (2005).
- [7] S. Mornet, S. Vasseur, F. Grasset, P. Verveka, G. Goglio, A. Demourgues, J. Portier, E. Pollert, E. Duguet, Prog. Solid State Chem. **34**, 237 (2006).
- [8] Z. Li, L. Wei, M. Y. Gao, H. Lei, Adv. Mater. **17**, 1001 (2005).
- [9] T. Hyeon, Chem. Commun. (2003) 927.
- [10] D. W. Elliott, W.X. Zhang, Environ. Sci. Technol. **35**, 4922 (2001).
- [11] M. Takafuji, S. Ide, H. Ihara, Z. Xu, Chem. Mater. **16**, 1977 (2004).
- [12] Hongwei Gu, Keming Xu, Chenjie Xu and Bing Xu Chem. Commun., **9**, 941 (2006).
- [13] M. Sincai, D. Ganga, D. Bica, L. Ve'ka's, J. Magn. Magn. Mater. **225**, 235 (2001).
- [14] P. Pradhan, J. Giri, G. Samanta, H.D. Sarma, K.P. Mishra, J.Bellare, R. Banerjee, D. Bahadur, J. Biomed. Mater. Res. Part B Appl. Biomater. **12**, 81B (2007).
- [15] Advanced Magnetic Nanostructures, D. Sellmyer and R. Skomski, eds., (Springer, New York, 2006).
- [16] E. Roduner, Nanoscopic Materials (RSC Publishing, Cambridge, UK, 2006).
- [17] B.D. Cullity, Introduction to magnetic materials (Addison-Wesley, Reading, Massachusetts, 1972), p.385.
- [18] L. Néel, Ann. Geophys. **5**, 99 (1949).
- [19] <http://www.en.Wikipedia.org> (Accessed in 2012).
- [20] Didosyan, Hauser, Reider, Nicolics, *Sensors and Actuators on Orthoferrites*, IEEE 2004

- [21] <http://www.en.Wikipedia.org> (Accessed in 2012).
- [22] V. Zaspalis, V. Tsakaloudi, E. Parazoglou, M. Kolenbrander, R. Guenther and P.V.D. Valk, *J. of Electroceramics* **13**, 585 (2004).
- [23] S. Baea, S. W. Lee, and Y.T. Ann *Appl. Phys. Lett.* **89**, 252503 (2006).
- [24] W.H. Bragg, *Nature* **95**, 561 (1915).
- [25] W.H. Bragg, *Phil. Mag.* **30**, 305 (1915).
- [26] K.E. Sickafus, J.M. Wills and N.W. Grimes, *J. Am. Ceram. Soc.* **82**, 3279 (1999).
- [27] D. Bacorisen, R. Smith, J.A. Ball, R.W. Grimes, B.P. Uberuaga, K.E. Sickafus and W.T. Rankin, *Nuclear Instruments and Methods in Physics Research B* **250**, 36 (2006).
- [28] T.F.W. Barth and E. Posnjak *Crystallography* **82**, (1932) 325.
- [29] C.G. Ramankutty and S. Sugunan, *Appl. Catal. A* **218**, 39 (2001).
- [30] C.V.G. Reddy, S.V. Manorama and V.J. Rao, *Sens. Actuators B* **55**, 90 (1999).
- [31] H. Arai and T. Seiyama in *Sensors: A Comprehensive Survey*, W. Gopel, J. Hesse and J.N. Zamel, eds., (Wiley-VCH, New York, 1991), Vol. 3.
- [32] L. Satyanarayana, K.M. Reddy and S.V. Manorama, *Mater. Chem. & Phys.* **82**, 21 (2003).
- [33] K.J. Button, *PTGMITT National Symposium Digest* **63**, 167 (1963).
- [34] C.R. Vestal and Z.J. Zhang *Nano Letters* **3**, (2003) 1739
- [35] H. Zeng , S.Sun , J.Li ,Z.L Wang and J.P. Liu *Appl.Phys. Lett.* **79**, (2001) 1501
- [36] C.Lin , C.Wang and I.H Chen *J. Appl. Phys.* **99**, (2006) 08N707.
- [37] M. Ammar , F. Mazaleyrat , J.P Bonnet , P. Audebert ,A. Brosseau ,G. Wang and Y. Champion *Nanotechnology* **18**, (2007) 285606.
- [38] M. Gharagozlou, *Journal of Alloys and Compounds.***486**, (2009) 660.
- [39] S.Y. Zhao, D.K. Lee, C.W. Kim, H.G. Cha, Y.H. Kim, Y.S. Kang, *Bull. Korean Chem. Soc.* **27**, 237 (2006).
- [40] Z.F. Zi, Y.P. Sun, X.B. Zhu, Z.R. Yang, J.M. Dai, W.H. Song, *J. Magn. Magn. Mater.* **321**, 1251 (2009).
- [41] Niederberger, M. *Acc. Chem. Res.* **40**, 793 (2007).
- [42] B. Baruwati, M.N. Nadagouda, R.S. Varma, *J. Phys. Chem. C* **112**, 18399 (2008).
- [43] Y. Lee, J. Lee, C.J. Bae, J.G. Park, H.J. Noh, J.H. Park, T. Hyeon,*Adv. Funct. Mater.* **15**, 503 (2005).

- [44] N. Hanh, O.K. Quy, N.P. Thuy, L.D. Tung, L. Spinu, *Physica B* **327**, 382 (2003).
- [45] S. Bhattacharyya, J.P. Salvetat, R. Fleurier, A. Husmann, T.Cacciaguerra, M.L. Saboungi, *Chem. Commun.* **38**, 4818 (2005).
- [46] X. Wang, J. Zhang, Q. Peng, Y.D. Li, *Nature* **437**, 121 (2005).
- [47] X. Liang, X. Wang, J. Zhuang, Y.T. Chen, D.S. Wang, Y.D. Li, *Adv. Funct. Mater.* **16**, 1805 (2006).
- [48] B. D. Cullity, *Fine particles and thin films: Introduction To Magnetic Material*; Addison-Wiseley Publishing company: London, (1972) 385.
- [49] B. H. Liu, J. Ding, Z. L. Dong, C. B. Boothroyd, J. H. Yin, J. B. Yi, *Phys. Rev B* **74**, 184427 (2006).
- [50] C. N. Chinnsamy, B. Jeyadevan, K. Shinoda, K. Tohji, D. J. Diayaprawira, M. Takahashi, R. J. Joseypphus, A. Narayanasamy, *Appl. Phys. Lett.* **83**, 2862 (2003).
- [51] C. P. Bean, *J. Appl. Phys.* **26**, 1381 (1955).
- [52] V. Kumara, A. Ranaa, M.S.Yadav, R.P. Pant, *J. Magn. Magn. Mater.* **320**, 1729 (2008).
- [53] J.P. Rivera, *Ferroelectrics* **161**, 165 (1994).
- [54] B.I. AlShin and D.N. Astrov, *So. Phys. – JETP* **17**, 809 (1963).
- [55] G.T. Rado, *Phys. Rev. Lett.* **13**, 335 (1964).
- [56] T. Watanabe and K. Kohn, *Phase Trans.* **15**, 57 (1989).
- [57] R. Ramesh, N.A. Spaldin, *Nat. Mater.* **6**, 21 (2007).
- [58] S.-W. Cheong, M. Mostovoy, *Nat. Mater.* **6**, 13 (2007).
- [59] C.-L. Jia, N. Nagaranjan, J.Q. He, L. Houben, T. Zhao, R. Ramesh, K. Urban, R.Waser, *Nat. Mater.* **6**, 64 (2007).
- [60] P. Muralt, *Nat. Mater.* **6**, 8 (2007).
- [61] <http://www.en.Wikipedia.org> (Accessed in 2012).
- [62] L. D. Landau and E. M. Lifshitz , *Electrodynamics of Continuous Media , Course of Theoretical Physics*, **8** , Pergamon Press,(1960).
- [63] G. T. Rado and V. J. Folen , *J. Appl. Phys.* **33S**, 1126 (1962).
- [64] G. T. Rado, *Phys. Rev.* **128**, 2546 (1962).
- [65] R. E. Newnham , *Am. Mineralogist* **59**, 906 (1974).
- [66] G. A. Smolenskii and I. E. Chupis , *Sov. Phys. Usp.* **25**, 475 (1982).

- [67] W. F. Brown, R. M. Hornreich, & S. Shtrikman, Phys. Rev. **168**, 574 (1968).
- [68] A. Chen, & F. Chernow, Phys. Rev. **154**, 493 (1967).
- [69] M. A. Saifi, & L. E. Cross, Phys. Rev. B **2**, 677 (1970).
- [70] H. Grimmer, Acta Crystallogr. A **48**, 266 (1992).
- [71] J. Ryu, A. Va'squez Carazo, K. Uchino, & H.-E. Kim, Jpn. J. Appl. Phys. **40**, 4948 (2001).
- [72] K. Y. Yun, D. Ricinshi, T. Kanashima, M. Noda, and M. Okuyama, Jpn. J. Appl. Phys. **43**, L647 (2004).
- [73] F. Kubel and H. Schmid, Acta Cryst. B **46**, 698 (1990).
- [74] J. D. Bucci, B. Robertson, and W. J. James, J. Appl. Cryst. **5**, 187 (1972).
- [75] K. Y. Yun, M. Noda, M. Okuyama, H. Saeki, H. Tabata and K. Saito, J. Appl. Phys. **96**, 3399 (2004).
- [76] V. V. Shvartsman, W. Kleemann, R. Haumont and J. Kreisel, Appl. Phys. Lett. **90**, 172115 (2007).
- [77] D. Lebeugle, D. Colson, A. Forget, and M. Viret, Appl. Phys. Lett. **91**, 022907 (2007).
- [78] D. Lebeugle, D. Colson, A. Forget, M. Viret, P. Bonville, J. F. Marucco, and S. Fusil, Phys. Rev. B **76**, 024116 (2007).
- [79] A. M. Kadomtseva, Y. F. Popov, A. P. Pyatakov, G. P. Vorob'ev, and D. Viehland, Phase Transitions **79**, 1019 (2006).
- [80] J. F. Scott, J. Magn. Mater. **321**, 1689 (2009).
- [81] I. Sosnowska, T. Peterlin-Neumaier and E. Steichele, J. Phys. C: Sol. State Phys. **15**, 4835 (1982).
- [82] I. Sosnowska, M. Loewenhaupt, W. I. F. David, and R. M. Ibberson, J. Phys. C: Sol. State Phys. **117**, 180 (1992).
- [83] D. Lebeugle, D. Colson, A. Forget, M. Viret, A. M. Bataille, A. Gukasov, Phys. Rev. Lett. **100**, 227602 (2008).
- [84] <http://www.en.Wikipedia.org> (Accessed in 2012).
- [85] V. R. Palkar, Darshan C. Kundaliya, S. K. Malik, and S. Bhattacharya, Phys. Rev. B **69**, 212102 (2004).
- [86] R.K. Mishra, D. K. Pradhan, R.N.P. Choudhary, and A. Banerjee, J. Magn. Mater. **320**, 2602 (2008).

- [87] V. A. Khomchenko, D. A. Kiselev, J. M. Vieira, L. Jian, A. L. Kholkin, A. M. L. Lopes, Y. G. Pogorelov, J. P. Araujo, and M. Maglione, *J. Appl. Phys.* **103**, 024105 (2008).
- [88] B. Kundys, A. Maignan, C. Martin, N. Nguyen, and C. Simon, *Appl. Phys. Lett.* **92**, 112905 (2008).
- [89] P. Fischer, M. Polomska, I. Sosnowska, and M. Szymanski, *J. Phys. C: Solid St. Phys.*, **13**, 1931 (1980).
- [90] J. R. Teague, R. Gerson and W. J. James *Solid State Commun.* **8**, 1073 (1970).
- [91] A. Kadomtseva, A. Zvezdin, Y. Popov, A. Pyatakov, and G. Vorob'ev, *JETP Lett.* **79**, 571 (2004) and references therein.
- [92] Yu. F. Popov, A.M. Kadomtseva, A.K. Zvezdin, G.P. Vorob'ev, and A.P. Pyatakov, in *Magnetoelectronic Phenomena in Crystals*, ed. M. Fiebig (Kluwer Academic Publishers, Dordrecht, 2004).
- [93] Y. H. Chu et al., *Nature Materials* **7**, 478 (2008).
- [94] F. Bai, J. Wang, M. Wuttig, J. F. Li, N. Wang, A. Pyatakov, A. K. Zvezdin, L. E. Cross, D. Viehland, *Appl. Phys. Lett.* **86**, 182905 (2005)
- [95] G. P. Vorob'ev, A. K. Zvezdin, A. M. Kadomtseva, Yu. F. Popov, V. A. Murashov, and Yu. P. Chernenkov, *Phys. Solid State* **37**, 1329 (1995)
- [96] S.R. Das, R.N.P. Choudhary, P. Bhattacharya, R.S. Katiyar, *J. Appl. Phys.* **101**, 034104 (2007).
- [97] Y.H. Lin, Q. Jiang, Y. Wang, C.W. Nan, L. Chen, J. Yu, *Appl. Phys. Lett.* **90**, 172507 (2007).
- [98] Meiya Li, Min Ning, Yungui Ma, Qibin Wu and C K Ong, *J. Phys. D: Appl. Phys.* **40**, 1603 (2007).
- [99] Ong et al. *Appl. Phys. Lett.* **88**, 212907 (2006).
- [100] J.T. Han, Y. H. Huang, X.J. Wu, C.L. Wu, W. Wei, B. Peng, W. Huang and J. B. Goodenough *Adv. Mater.* **18**, 2145 (2006).
- [101] Jimin et al. *J Mater Sci* **42**, (2007) 6824.
- [102] A. Preumont, *Mechatronics: Dynamics of Electromechanical and Piezoelectric Systems*, 2nd ed. (Springer, Netherlands, 2006) 98.
- [103] S.W. Tsai and H.T. Hahn, *Introduction to Composite Materials* (Technomic Publishing

Company, Inc., Lancaster, PA , 1980).

[104] C.B. Carter and G.M. Norton, *Ceramic Materials: Science and Engineering* (Springer, New York, 2007) 607.

[105] J. van Suchetelene, Philips Res. Rep. **27**, 28 (1972).

[106] J. van den Boomgaard and R.A.J. Born, *J. Mater. Sci.*, **13**, 1538 (1978).

[107] J. Van, *Philips Res. Rep.*, **27**, 28 (1972).

[108] J. van den Boomgaard, A.M.J.G. Van Run and J. Van Suchetelene, *Ferroelectrics*, **10**, 295 (1976).

[109] J. van den Boomgaard, D.R. Terrell, R.A.J. Born, and H.F.J.I. Giller, *J. Mater. Sci.*, **9**, 1705 (1974).

[110]. A.M.J.G. Van Run, D.R. Terrell, and J.H. Scholing, *J. Mater.Sci.*, **9**, 1710 (1974).

[111]. T.G. Lupeiko, I.V. Lisnevskaya, M.D. Chkheidze, and B.I. Zvyagintsev, *Inorg. Mater.*, **31**, 1139 (1995).

[112] T.G. Lupeiko, I.B. Lopatina, S.S. Lopatin, and I.P. Getman, *Neorg. Mater.*, **27**, 2394 (1991).

[113] C. Spezzani, M. Fabrizioli, P. Candeloro, E.D. Fabrizio, G. Panaccione, and M. Sacchi, *Phys. Rev. B* **69**, 224412 (2004).

[114] T.G. Lupeiko, I.B. Lopatina, I.V. Kozyrev, and L.A. Derbaremdiker, *Neorg. Mater.*, **28**, 632 (1991).

[115] Yu. I. Bokhan and V.M. Laletin, *Inorg. Mater.*, **32**, 634 (1996).

[116] T.G. Lupeiko, S.S. Lopatin, I.V. Lisnevskaya, and B.I. Zvyagintsev, *Inorg. Mater.* **30**, 1353 (1994).

[117] G. V. Duong and R. Groessinger, *J. Magn. Magn. Mater.* **316**, e624 (2007).

[118] Corral-Flores et al. *Acta Materialia* **58**, 764 (2010).

Chapter 2

2 Experimental Techniques

2.1 Preamble

In this chapter, we elaborate on the various synthesis techniques to synthesize the Iron Oxide nanostructures along with the various characterization techniques that are used during the investigations presented in this thesis work.

The morphological and phase characterizations of the samples are done using Scanning Electron Microscope (SEM), Field Emission Scanning Electron Microscope (FESEM), Transmission Electron Microscope (TEM), High Resolution Transmission Electron Microscope (HRTEM), Energy Dispersive X Ray Analysis (EDAX), Selected Area Electron Diffraction (SAED) and X Ray Diffraction (XRD). The magnetic characterizations are carried out employing Vibrating Sample Magnetometer (VSM), Superconducting Quantum Interference Device (SQUID), Mössbauer Spectroscopy. The phase transition of the sample was studied by the Differential Thermal Analysis (DTA), Differential Scanning Calorimetry (DSC). The dielectric and ferroelectric characterization of the sample was studied by Impedance analyzer and Polarization vs. Electric Field loop tracer respectively. The magnetoelectric coefficient was measured by the dynamic method by a set up designed in our laboratory.

2.2 Mechanism of nanoparticle formation

The formation of nanoparticles usually takes place via nucleation and growth stages. We calculate the free-energy changes associated with the process of homogeneous nucleation. The overall excess free energy, ΔG , between a small solid particle of a solute and the solute in solution is equal to the sum of excess surface free energy, ΔG_s , that is, the excess free energy between the surface of the particle and the bulk of the particle, and the volume excess free energy, ΔG_v , that is, the excess free energy between a very large particle and the solute in the

solution. ΔG_s is a positive quantity, the magnitude of which is proportional to square of the particle size (r^2). In a supersaturated solution, ΔG_v is a negative quantity proportional to r^3 . Thus we have

$$\Delta G = \Delta G_s + \Delta G_v = 4\pi r^2 \gamma + 4\pi r^2 \frac{\Delta G_v}{3} \quad (2.1)$$

where ΔG_v is the free energy change per unit volume and γ is the interfacial tension between the developing crystallite surface and the supersaturated solution. The two terms on the right hand side have opposite signs and depend differently upon r . Therefore the free energy of formation, ΔG , passes through a maximum, as shown in Figure 2.1. This maximum value ΔG_{crit} , corresponds to the critical nucleus, r_c , and for a spherical cluster can be obtained by setting

$$\frac{dG}{dr} = 8\pi r \gamma + 4\pi r^2 \Delta G_v = 0 \quad (2.2)$$

Therefore,

$$r_c = \frac{-2\gamma}{\Delta G_v} \quad (2.3)$$

where ΔG_v is a negative quantity. From Equations 2.1 and 2.3 we get:

$$\Delta G_{crit} = \frac{16\pi\gamma^3}{3(\Delta G_v)^2} = \frac{4\pi\gamma r_c^2}{3} \quad (2.4)$$

So ΔG_{crit} is the energy barrier that a nucleation process must overcome and r_c represents the minimum size of a stable spherical nucleus. A nucleus smaller than r_c will dissolve into the solution to reduce the overall free energy, whereas a nucleus larger than r_c is stable and continues to grow bigger.

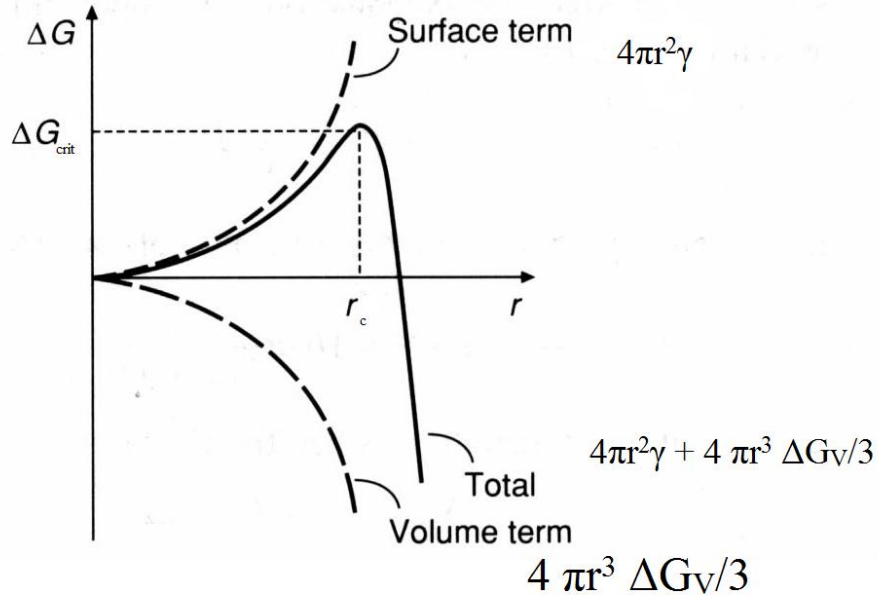


Fig. 2.1: Free-energy diagram for nucleation processes, which explains the existence of a critical nucleus.

It can also be shown that the rate of nucleation is

$$J = A \exp \left[\frac{-16\pi\gamma^3 v^3}{3k_B^3 T^3 (\ln S)^2} \right] \quad (2.5)$$

Where v is the molar volume, and S is the ratio of solution concentration to that of equilibrium saturation concentration at a given temperature, and is given by

$$\ln S = \frac{2\gamma v}{k_B T r} \quad (2.6)$$

Thus we see that temperature (T), degree of supersaturation (S) and interfacial tension (γ) are the three main variables which govern the rate of nucleation. The crystal structure, size and morphology of grown particles depends on the system and reaction parameters. The shapes of the crystallites occur either in order to minimize the surface energy of the particles or because of the kinetics of the growth. If kinetics dominates then the shape is determined by the rate at which the different crystal faces grow. If the particles are formed in thermal equilibrium, their shape or crystal habit results from minimizing the surface energy.

Since nuclei grow via molecular addition, at times the concentration drops below the critical level and nucleation stops. Yet the particles continue to grow by molecular addition until the equilibrium concentration of the precipitated species is reached. At this stage, the smaller particles grow more rapidly than the larger particles. This is because the free energy driving force is larger for smaller particles than for larger ones if the particles are slightly larger than the critical size. Nearly monodisperse size distribution can be obtained at this stage by either stopping the reaction (nucleation and growth) quickly or by supplying reactant source to keep a saturated condition during the course of the reaction. On the other hand, when the particles are depleted due to particle growth, Ostwald ripening occurs, where the larger particles continue to grow, and the smaller ones get smaller and finally dissolve. Because the supersaturation ratio (S) decreases now and the corresponding critical nuclei size (r_c) increases, any particles smaller than this new critical size will dissolve. If the reaction is quickly stopped at this stage, the particles will have a broad size distribution, which is featured by a distribution centering two size regimes, a bigger one and a smaller one and the critical size now at this saturation is in between. Once the reaction (mainly the growth of the particles) goes into this stage, it is difficult to get monodisperse particles unless the reaction is extended to long enough times to completely deplete the supersaturation and the smaller nuclei. In addition to the growth by molecular addition where soluble species deposit on the solid surface, particles can grow by aggregation with other particles and this is called secondary growth. After the particles grow to a stable size they will grow by combining with smaller unstable nuclei and not by collisions with other stable particles. Nanoparticles are small and are not thermodynamically stable for crystal growth kinetically. To finally produce stable nanoparticles, these nanoparticles must be arrested during the reaction either by adding surface protecting agents, such as organic ligands or inorganic capping materials [1] or, by placing them in an inert environment such as an inorganic matrix or polymers [2]. The nanocrystal (NC) dispersions are stable if the interaction between the capping groups and the solvent is favorable, providing an energetic barrier to counteract the van der Waals and magnetic (magnetic materials) attractions between nanoparticles. To help arrest these nanoparticles, different solvents are also used to change the solubility or the reaction rate [3].

In general, when synthesizing nanoparticles from solution, nucleation is very fast, and subsequent growth occurs by two primary mechanisms: coarsening (also known as Ostwald

ripening) and growth involving aggregation. Coarsening processes involve the growth of larger crystals at the expense of smaller crystals [4].

Because the chemical potential of a particle increases with decreasing particle size, the equilibrium solute concentration near a small particle is higher than near a large particle, as described by the Gibbs-Thompson equation. The resulting concentration gradients lead to the transport of solute from small particles to larger particles. This mode of growth may result in the formation of faceted particles if it occurs near equilibrium and there is sufficient difference in the surface energies of the different crystallographic faces. Crystal growth by aggregation can occur by a range of mechanisms, producing particle assemblies built from randomly oriented to highly oriented nanoparticles. Epitaxial aggregation is an important mode of crystal growth. Primary particles may aggregate in an oriented fashion to produce a larger single crystal, or they may aggregate randomly and reorient, recrystallize, or undergo phase transformations to produce larger single crystals. Aggregation-growth mechanisms provide a route for the incorporation of defects, such as edge and screw dislocations, in stress-free and initially defect-free nanocrystalline materials.

2.2 Synthesis Techniques

2.2.1 Chemical co-precipitation method

Chemical co-precipitation method is extensively used in industry and research work to synthesize complex oxides. With this method high quality ceramic powder of higher compositional homogeneity, better stoichiometry, fine particle size and unagglomerated particles required for practical applications can be synthesized. The co-precipitation technique used in our laboratory is shown in Figure 2.2. At the first stage of chemical co-precipitation starting salts are dissolved in aqueous medium. The solution is then mixed with a solution of dissolved precipitating agent such as ammonium hydroxide or sodium hydroxide or oxalic acid. The final crystalline oxide is obtained by firing the precipitates at a higher temperature. Precipitation temperature can be in the range of 0°C to 80°C. A significant role is played by colloidal chemistry in the precipitation of powder from solution. The main controlling factor in this

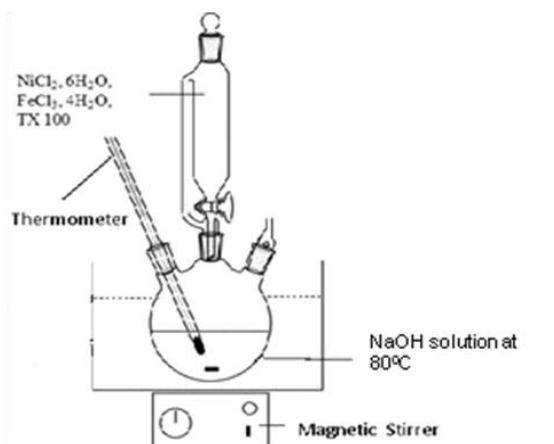


Fig. 2.2: Co-precipitation technique

method that causes individual particles to bond to form larger agglomerates is interparticle force. The agglomeration rate is largely dependent on the rate of particle collisions per unit time caused by Brownian motion, thermal convection and shear forces (caused by stirring). The balance of these forces determines whether particles adhere once they come into contact. If there is a net attractive force of Van der Waal type (which includes dipole-dipole, dipole–non-dipole, non-dipole-non-dipole interactions) the particles will bond to form agglomerate. Van der Waal force decreases sharply with distance. Another force plays an important role that is surface charge or zeta potential. These surface charges are generated by the non-stoichiometric adsorption or desorption of an ionic species near the surface of the particle or through chemical reactions with the surface and the aqueous media. Adjusting the pH the formation of these surface charges can be controlled. There is a point at which no surface charges exist on the particles i.e. net charge is zero, which is defined as the isoelectric point [5].

Mean particle size and distribution width increases with solution temperature and titration rate but decreases with high pH value. The processing parameters affect not only the particle diameter and the width but also the morphology of the particles. Titration method and nature of starting reagents affect the crystalline form of the end product.

2.2.2 Hydrothermal Synthesis

Hydrothermal synthesis is a technology for crystallizing materials and chemical compounds directly from aqueous solution by adept control of thermodynamic (temperature, pressure and chemical composition) and non-thermodynamic (stirring etc.) variables. Hydrothermal synthesis is a technology for crystallizing materials and chemical compounds directly from aqueous solution by adept control of thermodynamic (temperature, pressure and chemical composition) and non-thermodynamic (stirring etc.) variables. This method exploits the solubility almost of all inorganic substances in water at elevated temperatures and pressures and subsequent crystallization of dissolved material from the fluid. Water at elevated temperatures plays an essential role in the precursor material transformation because the vapor pressure is much higher. The properties of the reactants like their solubility and reactivity change at high temperatures. As a result of these changes more parameters are obtained whose calculated change leads to high quality nanoparticles which is not possible at lower temperatures. The particles are obtained in hydrothermal synthesis by the dissolution and crystallization mechanism. The chamber where the reaction takes place is called the autoclave. The schematic diagram of an autoclave is shown in Fig. 2.3.

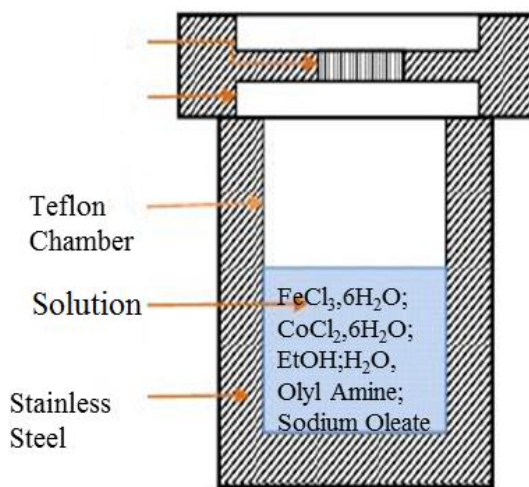


Fig. 2.3: Schematic diagram of an autoclave

It consists of a Stainless steel chamber which encloses a Teflon chamber. The precursor solution is poured into the Teflon chamber in such a way that 80% of it is filled. The autoclave is heated in order to create two temperature zones. A convective motion starts where the water below gets heated and ascends and the cold water from the top descends. The nutrient dissolves in the hotter zone and the saturated aqueous solution in the lower part is transported to the upper part by convective motion of the solution. This continues for a very long time until the entire solution is in equilibrium i.e. the temperature remains same everywhere. The supersaturation is achieved by reducing the temperature in the crystal growth zone. The cooler and denser solution in the upper part of the autoclave descends while the counter flow of solution ascends. The solution becomes supersaturated in the upper part as the result of the reduction in temperature and crystallization sets in. During the synthesis of nanocrystals, parameters such as water pressure, temperature, reaction time and the respective precursors-product system can be tuned to maintain a high simultaneous nucleation rate and narrow size distribution. Nanocrystals prepared according to this method usually have high crystallinity, varied shapes and poor size distribution [6].



Fig.2.4: The Home fabricated Stainless Steel chamber and the Teflon chamber where all the synthesis were done.

There are many theories which describe the mechanism of formation of different nanostructures. We have discussed below about some of these.

Oriented-Attachment Model

Oriented attachment occurs when particles join at specific dimensionally similar crystallographic phases. This coarsening mechanism mainly involves the reduction of surface tension through the elimination of surfaces via attachments that are constrained only in two dimensions of the interface [7-9]

Selective-Adsorption Model

According to this model a mixture of surfactants is required for anisotropic crystal growth. This surfactant mixture provides selective adsorption of surfactants at different crystallographic faces of the growing crystals and results in modification of surface free energy of individual crystallographic faces leading to different crystallographic growth along these planes. The difference in growth along different crystallographic faces is responsible for shape anisotropy in such a crystal [10].

Thermodynamic Theory

The most widely cited classical model for shape control of crystals is given by the Gibbs-Curie-Wulff theorem [11]. This theory suggests that the shape of the crystal is determined by the surface free energy of individual crystal faces. The final crystal shape is determined in a way such that the total free energy of the system is minimized. This theory has been successful in explaining most of the morphological control of crystals [12].

2.2.3 Sol-Gel synthesis

Sol-gel synthesis is a form of nanostructure synthesis. The sol-gel process refers broadly to room temperature solution routes for preparing oxide materials. This process involves the preparation of nanostructures materials by forming colloidal suspensions called sol and then to irreversible gel by the process of hydrolysis and polymerization of metal alkoxide precursors of silica, alumina, titania etc. Finally the gel is dried and it shrinks to rigid oxide forms. Before going into the details of this process we introduce some definitions as listed below

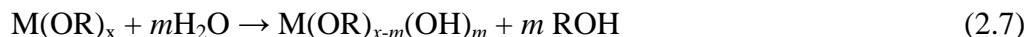
Colloid: A colloid is a suspension in which dispersed phase is so small (1-100 nm) that gravitational forces are negligible. Short-range forces like Vander Waals attraction and surface charges dominate the interactions among the particles. Inertia of the dispersed phase is small enough to exhibit Brownian motion [13].

Sol: A sol is a stable suspension of colloidal solid particles within a liquid. In this case forces of dispersion are greater than the force of gravity. Solvent used to disperse stably the colloidal particles of a sol is either water or a solution composed mostly of water. Other solvents like alcohol can be used.

Gel: A gel is a porous three dimensionally interconnected solid network that expands in a stable fashion throughout a liquid medium and is only limited by the size of the container. Nature of gel depends on the coexistence between the solid network and the liquid medium. In this case liquid is present between the mesh of the solid network that composes the gel, it does not flow out spontaneously and is in thermodynamic equilibrium with the solid network. If the liquid phase is mostly composed of alcohol then the gel is called alcogel. If most of the liquid is removed, the brittle solid obtained is either called a xerogel or aerogel, depending on the drying method. If the solid network is made up of colloidal sol particles the gel is called colloidal. The sol-gel process includes four steps: hydrolysis, polycondensation, drying and thermal decomposition.

Step I: Hydrolysis

At the first step liquid metal alkoxide precursor $M(OR)_x$, is mixed with water and acid or base, where R is CH_3, C_2H_5, C_3H_7 and acid or base is used as a catalyst. Then hydrolysis takes place through acid catalyzed or base catalyzed processes. This is shown in the following reaction



where if m is up to x , the reaction is total hydrolysis,

Step II: Condensation

Condensation reactions can be water condensation or may be alcohol condensation. Condensation reactions may also be acid catalyzed or base catalyzed. In both the cases the reaction proceeds via a rapid formation of a charged intermediate product by reaction with a proton or hydride ion followed by either a water condensation



or an alcohol condensation



A slow attack occurs on the intermediate by a second neutral silicon species. Linkage of additional tetrahedral occurs as a polycondensation reaction and eventually results in a MO_2

network. The water and alcohol expelled from the reaction remain in the pores of the network. When sufficient interconnected $-M-O-M-$ bonds are formed they respond collectively as colloidal particles or sol.

Step III: Gelation

When links formation takes place among the sol particles in such a way that a giant spinning cluster is formed across the container, then gelation takes place. The initial gel has a high viscosity but low elasticity.

Following gelation, further cross linking and chemical insertion of isolated sol particles into the spanning cluster continues, leading to an increase in elasticity of the sample. In gelation process polycondensation reaction continue to occur within the gel network as long as the neighbouring silanol groups in a newly formed gel are close enough to react. This increases the connectivity of the network and its factual dimension.

Step IV: Aging, Coarsening and Ripening

After gelation, aging occurs through physical and chemical changes. Aging usually improves the properties of the material. The effect of this process is a stiffening and shrinkage of the sample. Shrinkage occurs because new bonds are formed where there were previously only weak interactions among surface hydroxyl and alkyl groups. This shrinkage leads to eviction of liquid from the pores of the gel, so the gel sample gradually changes its appearance from homogenous gel to transparent shrunken solid monoliths immersed in liquid. This process is known as syneresis.

The coarsening and ripening are the processes deeply involved in the process of aging. In these processes, material dissolves from the surface of larger particles and deposits on the narrow neck like linking part, which join particles to each other. The surface of an individual particle has a positive radius of curvature (r_+). Whereas the narrow neck between particles altogether has a smaller negative radius of curvature (r_-) (Fig. 2.5). A pressure gradient exists across a curved interface between two media, and this leads to the difference in solubility in the two regions of the material. Small particles will have higher solubility, whereas the regions of negative surface curvature will have low solubility and will tend to accumulate material. This will strengthen the solid and leads to some change in pore sizes and shapes of the material.

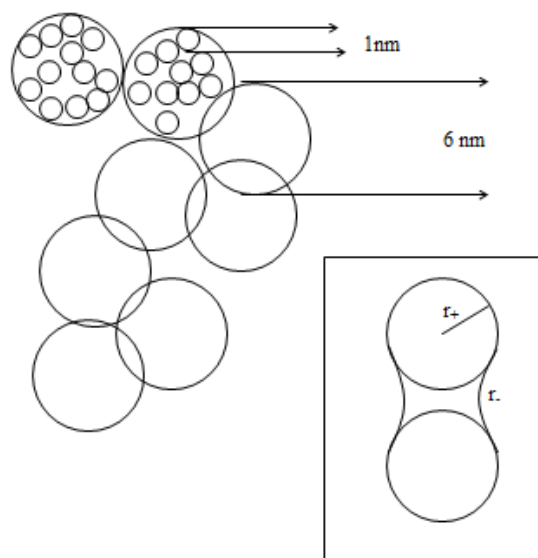


Fig. 2.5: Schematic representation of the primary and secondary particles in silica alkoxide gel. Inset figure shows the radii of curvature of the particles and necks.

Step V: Drying and Densification

Once a solution is condensed into a gel, solvent removal must be carried out. Drying is the process of removal of solvent. Heating the gel at high temperature causes densification of the gel. In this process pores are eliminated and the density of the gel ultimately becomes equivalent to fused quartz or fused silica.

We have prepared $\text{NiFe}_2\text{O}_4:\text{SiO}_2$ and $\text{CoFe}_2\text{O}_4:\text{BaTiO}_3$ core shell nanocomposite by the sol-gel technique.

2.2.4 Micelles and Reverse Micelles

Reverse micelles are another method in controlling the cluster growth. In this process a small region of physical space is defined by a micelle and required materials are precipitated within this defined region. The micellar reagent acts more like a physical boundary to hold the nanoparticles than acting as surface capping agent that are used very popularly to confine the nanoparticles. When the surfactant concentration exceeds the critical micelle concentration (cmc) in water, micelles are formed as aggregates of surfactant molecules. Above the cmc, the physical state of the surfactant molecules changes radically, and additional surfactant exists as aggregates or micelles. In normal micelles, the hydrophobic hydrocarbon chains of the surfactants are oriented toward the interior of the micelle, and the hydrophylic groups of the

surfactants are in contact with the surrounding aqueous medium. The micelles exist only as a small amount of solubilized hydrophobic or hydrophilic material as illustrated in Fig. 2.6.

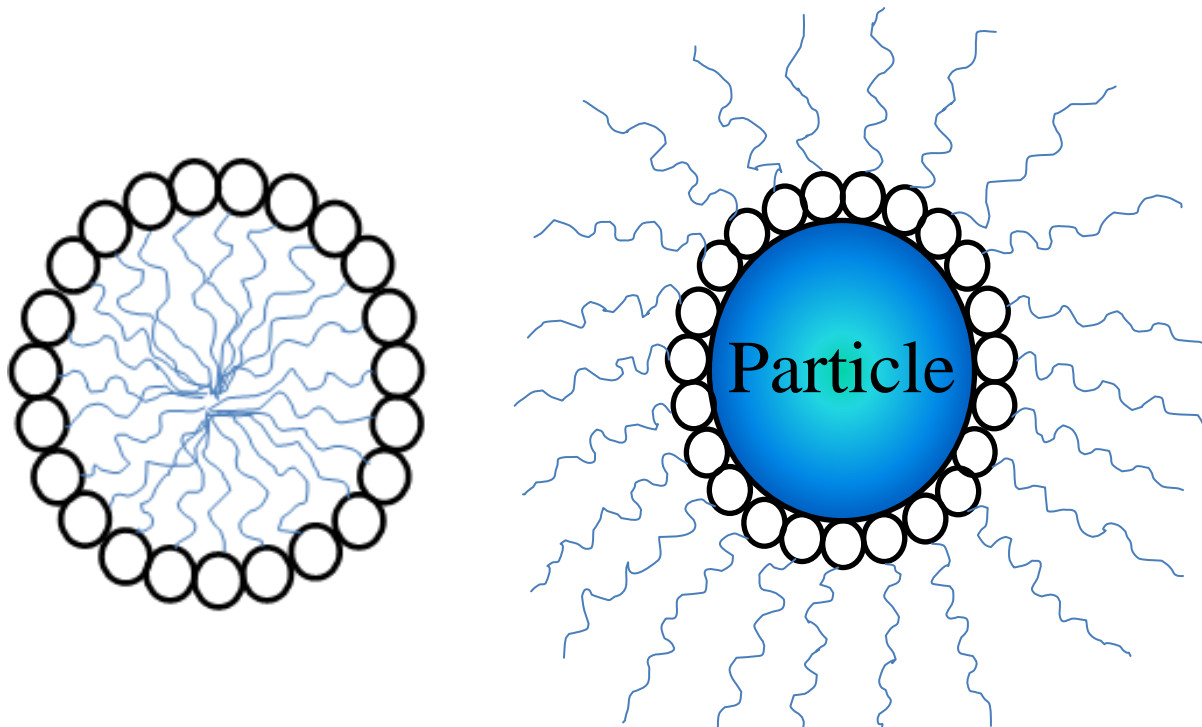


Fig.2.6: Schematic diagram of micelle and reverse micelle.

The solubilization process can be modified, (more precisely, enhanced) if the concentration of surfactant is changed further (ie. increased). The droplet size can be increased to a dimension that is much larger than the monolayer thickness of the surfactant because the inside pool of water or oil is enlarged. As the surfactant concentration increases further, micelles can be deformed and can change into different shapes, which makes it possible to synthesize different nanoparticle shapes [7,11]. Examples of micelles are Triton X-100 (Polyoxyethylene Octyl Phenyl Ether), CTAB (Cetyl Trimethyl Ammonium Bromide), SDS (Sodium Dodecyl Sulphate) etc.

2.3 Experimental Techniques

2.3.1 X-Ray Diffraction

X-ray crystallography relies on the dual wave/particle nature of x-rays to discover information about the structure of crystalline materials. X-ray powder diffraction is a common technique for the study of crystal structures and atomic spacing.

The physics and mathematics describing the generation of monochromatic X-rays and the diffraction of those X-rays by crystalline powders are very complex. However in precise, X-rays are generated by a cathode ray tube, filtered to produce monochromatic radiation, collimated to concentrate, and directed toward the sample [14]. X-rays can be considered waves of electromagnetic radiation which is about 1 Å (10^{-10} m). This is about the same size as an atom. Upon incidence on crystalline sample, atoms within the sample elastically scatter the X-ray waves, primarily through the atom's electrons. The regular array of scatterers (electrons) within a crystalline sample produces a regular array of outgoing spherical waves of scattered X-rays. Although these waves cancel one another out in most directions through destructive interference, they add constructively in a few specific directions, determined by Bragg's law:

$$2d \sin \theta = n\lambda \quad (2.10)$$

Here d is the spacing between diffracting planes, θ is the incident angle, n is any integer, and λ is the wavelength of the beam. These diffracted X-rays are then detected, processed and counted. By scanning the sample through a range of 2θ angles, all possible diffraction directions of the lattice should be attained due to the random orientation of the powdered material. Conversion of the diffraction peaks to d -spacings allows identification of the elements/compound present in the sample because each element/compound has a set of unique d -spacings. Experimental diffraction patterns can be compared to those in the JCPDS (Joint Committee on Powder Diffraction Standard) database for phase identification or may be with some other standard data base. Each crystallographic plane has three indices h, k, l . Hence with the help of the data base JCPDS each plane can be indexed with different hkl .

Powder diffractometers come in two basic varieties: θ - θ in which the X-ray tube and detector move simultaneously or a θ - 2θ in which the X-ray tube is fixed, and the specimen moves at $\frac{1}{2}$ the rate of the detector to maintain the θ - 2θ geometry. Our X-ray PAnalytical system is a θ - 2θ system. In both systems the geometry shown in the diagram in Fig.2.7 is maintained during data collection.

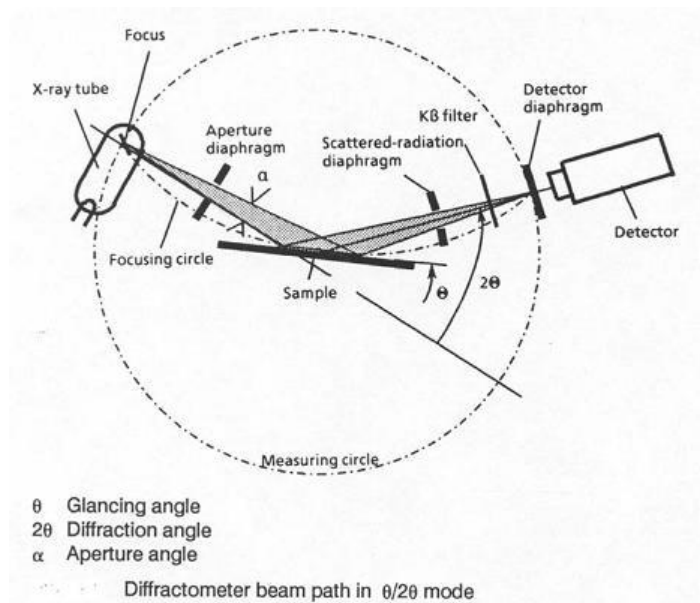


Fig.2.7: X-ray Diffraction optics used in $\theta/2\theta$ mode.

The angles and intensities of diffractions are recorded electronically using a detector, electronics and specialized software resulting in a plot of 2θ (horizontal axis) vs. intensity (vertical axis) for the specimen.

Crystallite size and Scherrer formulae

One of the most vital applications of XRD analysis is to determine the crystallite size in nanocrystalline materials. The finite size of the crystallite results in a broadening of the diffraction peaks or Bragg peaks in the XRD spectra. Inhomogeneous lattice strains because of variation in lattice constants from one crystallite to another and structural faults will also result in the broadening of the diffraction peaks. A simple treatment of finite size broadening results in Scherrer's equation [14,15]

$$D = \frac{K\lambda}{\beta \cos \theta} \quad (2.11)$$

Where D is the average crystallite dimension perpendicular to the reflecting phase, λ is the X-ray wavelength, θ is the Bragg angle, and β is the finite size broadening, K is a constant close to unity that is related both to the crystallite shape and to the way β is defined as the full width at half maximum intensity. Eq. 2.11 can be used to obtain a rough estimate of the crystallite size when there are no inhomogeneous strains and when particle size distribution is narrow. However the accuracy of the size determination is hampered by the mathematical nature of this

relationship and relatively precise measurements are possible only if the size is small. This is because if the size is large then a small inaccuracy in the breadth measurement can cause a large shift in the result. Fig. 2.8 shows a typical XRD pattern obtained for CoFe_2O_4 nanoparticle's.

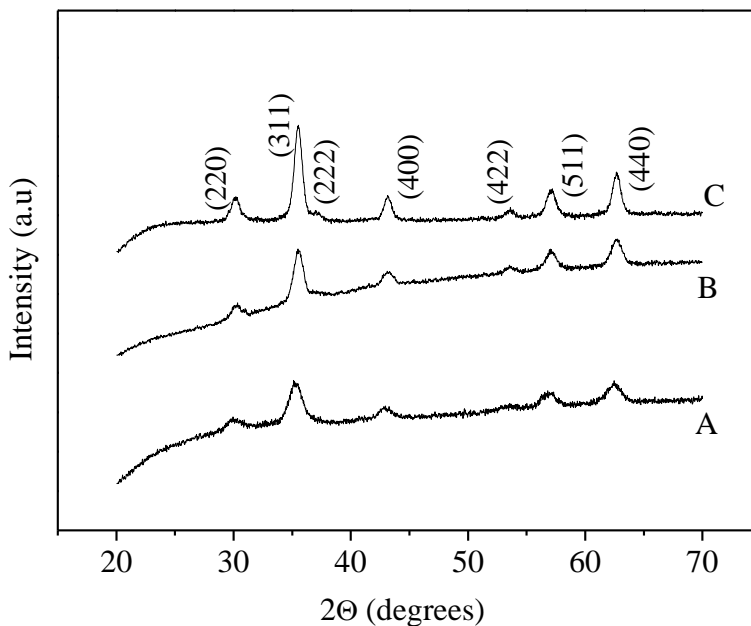


Fig. 2.8: XRD of the CoFe_2O_4 nanoparticles

2.3.2 Scanning Electron Microscope (SEM)

The basic steps involved in all Electron Microscopes (EM) are the following: A stream of electrons is formed in high vacuum (by electron guns). This stream is accelerated towards the specimen (with a positive electrical potential) while it is confined and focused using metal apertures and magnetic lenses into a thin, focused, monochromatic beam. The sample is irradiated by the beam and interactions occur inside the irradiated sample, affecting the electron beam. These interactions and effects are detected and transformed into an image. The above steps are carried out in all EM's regardless of type.

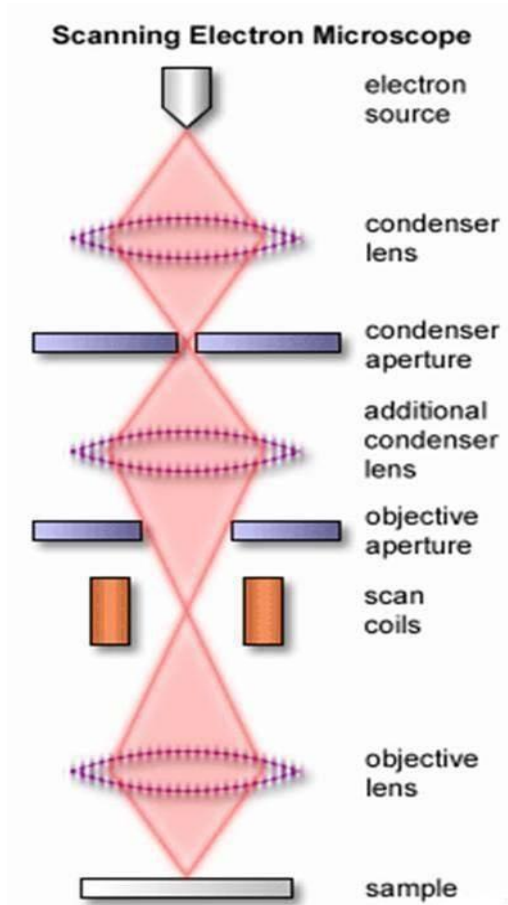


Fig.2.9: Schematic diagram of SEM shows the parts of the microscopes.

In SEM, the electron beam is thermoionically emitted from an electron gun fitted with a tungsten filament cathode and focused in vacuum into a fine probe that is rastered over the surface of the specimen. The electron beam passes through scan coils and objective lens that deflect horizontally and vertically so that the beam scans the surface of the sample. SEM works on a voltage between 2 to 50kV and its beam diameter that scans the specimen is 5 nm-2 μm . Other types of electron emitters include lanthanum hexaboride (LaB_6) cathodes and field emission guns (FEG) [16]

which may be of the cold-cathode type using tungsten single crystal emitters or the thermally-assisted Schottky type, using emitters of zirconium oxide. When the primary electron beam interacts with the sample, the energy exchange between the electron beam and the sample results deceleration of incident electrons through the energy dissipation and produces a variety of signals. These signals include secondary electrons, backscattered electrons, diffracted backscattered electrons, characteristic

X-rays, visible light (cathodo-luminescence) and heat. Secondary and backscattered electrons are conventionally separated according to their energies [17]. Detectors of each type of electrons are placed in the microscope in proper positions to collect them. Backscattered electrons (BSE) consist of high-energy electrons originating in the electron beam, that are reflected or back-scattered out of the specimen interaction volume by elastic scattering interactions with specimen atoms.

Since heavy elements (high atomic number) backscatter electrons more strongly than light elements (low atomic number), and thus appear brighter in the image, BSE are used to detect contrast between areas with different chemical compositions. The most common imaging mode collects low-energy (<50 eV) secondary electrons that are ejected from the k-orbitals of the specimen atoms by inelastic scattering interactions with beam electrons. Due to their low energy, these electrons originate within a few nanometers from the sample surface. The secondary electrons give an idea about the morphology of the surface.

A field-emission cathode in the electron gun of a SEM (FESEM) provides narrower probing beams at low as well as high electron energy, resulting in both improved spatial resolution and minimized sample charging and damage. The sample preparation include a thin gold coating on the sample (mainly for electrically non conducting samples) to avoid static charge accumulation during SEM imaging.

Emission of secondary electrons by inelastic scattering of incident electrons produces the SEM micrograph of the sample. Due to the very narrow electron beam, SEM micrographs have a large depth of field yielding a characteristic three-dimensional appearance useful for understanding the surface structure of a sample.

Whereas, characteristic X-rays produced by inelastic collisions of the incident electrons with electrons in discrete orbitals (shells) of atoms in the sample are used for elemental analysis. The process is known as energy dispersive X-ray spectroscopy (EDS). When the electron beam bombards the sample, electrons are ejected from the atoms comprising the sample's surface. An electron from a higher shell fills a resulting electron vacancy and an X-ray is emitted to balance the energy difference between the two electrons. The wavelengths and hence energies of the X-rays are characteristics of the electron shell energies and the spectrum of X-rays can be used to identify different elements.

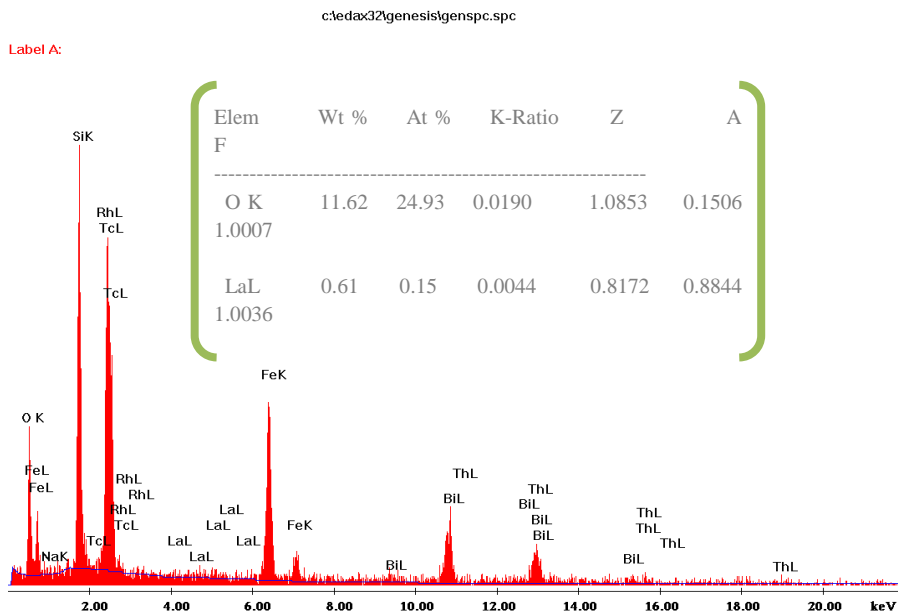
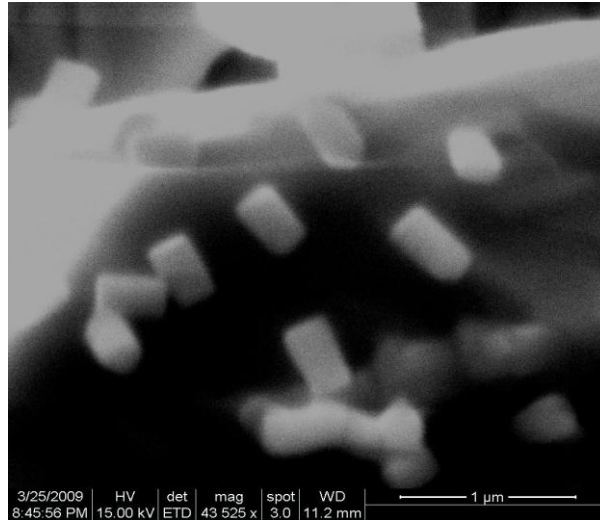


Fig.2.10: SEM image and EDAX of BFO.

It is possible to measure the amount of different elements from the spectrum. The EDAX detector measures the number of emitted X-rays versus their energy. The X rays emitted from the sample atoms are characteristic in energy and wavelength to not only the element of the parent atom but also which shells lose electrons and which shells replaces them. The SEM image of Lanthanum doped Bismuth Ferrite sample is shown in Figure 2.10.

2.3.3 Fourier Transform Infrared Spectroscopy (FTIR)

Fourier Transform Infrared spectroscopy (FTIR) is a powerful tool for identifying types of chemical bonds in a molecule by producing an infrared absorption spectrum that is like a molecular fingerprint. The infrared portion of the electromagnetic spectrum is divided into three regions: the near, mid and far infra-red named after their relation to the visible spectrum.

The far infrared (approx. $400\text{-}10\text{ cm}^{-1}$) lying adjacent to the microwave region has low energy and may be used for rotational spectroscopy. The mid-infrared (approx. $4000\text{-}400\text{ cm}^{-1}$) may be used to study the fundamental vibrations and associated rotational-vibrational structure, whilst the higher energy near-IR ($14000\text{-}4000\text{ cm}^{-1}$) can excite overtone or harmonic vibrations. Molecular bonds vibrate at various frequencies depending on the elements and the type of bonds. For any given bond there are several specific frequencies at which it can vibrate. According to quantum mechanics these frequencies correspond to the ground state (lowest frequency) and several excited states (higher frequencies). One way to cause the frequency of a molecular vibration to increase is to excite the bond by having it absorb light energy. Infrared spectroscopy works because chemical bonds have specific frequencies at which they vibrate corresponding to energy levels. The resonant frequencies or vibrational frequencies are determined by the shape of the molecular potential energy surfaces, the masses of the atoms and eventually by the associated vibronic coupling. In order for a vibrational mode in a molecule to be IR active, it must be associated with changes in the permanent dipole. In particular in the Born-Oppenheimer and harmonic approximations i.e. when the molecular Hamiltonian corresponding to the electronic ground state can be approximated by a harmonic oscillator in the neighbourhood of the equilibrium molecular geometry, the resonant frequencies are determined by the normal modes corresponding to the molecular electronic ground state potential energy surface. Nevertheless the resonant frequencies can be in a first approach related to the strength of the bond, and the mass of the atoms at either end of it. Thus the frequency of vibrations can be associated with a particular bond type.

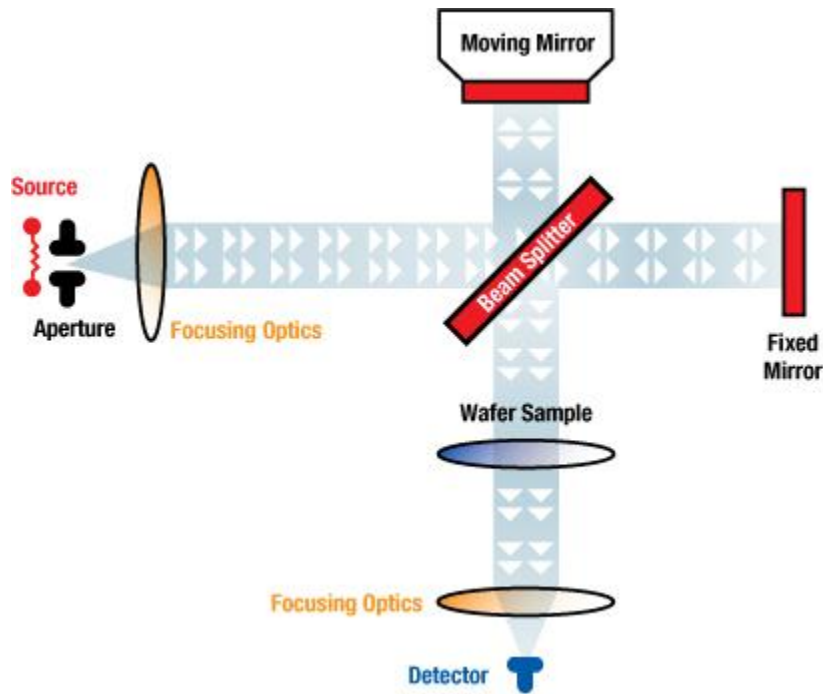


Fig.2.11. FTIR schematic diagram.

The basic components of an FTIR are shown schematically in Figure 2.11. The infrared source emits a broad band of different wavelength of infrared radiation. The IR source used in the Temet GASMET FTIR CR-series is a SiC ceramic at a temperature of 1550 K. The IR radiation goes through an interferometer (beam splitter) that modulates the infrared radiation. The interferometer performs an optical inverse Fourier transform on the entering IR radiation. The modulated IR beam passes through the gas sample where it is absorbed to various extents at different wavelengths by the various molecules present. Finally the intensity of the IR beam is detected by a detector, which is a liquid-nitrogen cooled MCT (Mercury-Cadmium-Telluride) detector in the case of the Temet GASMET FTIR CR-series. The detected signal is digitised and Fourier transformed by the computer to get the IR spectrum of the sample gas.

Simple diatomic molecules have only one bond which may stretch. More complex molecules have many bonds and vibrations can be conjugated leading to infrared absorptions at characteristic frequencies that may be related to chemical groups. The atoms in a CH₂ group commonly found in organic compounds can vibrate in six different ways, symmetrical and asymmetrical stretching, scissoring, rocking, wagging and twisting. The FTIR of NiFe₂O₄ and SiO₂ coated NiFe₂O₄ are shown in Figure 2.12. and will be analyzed in Chapter 3.

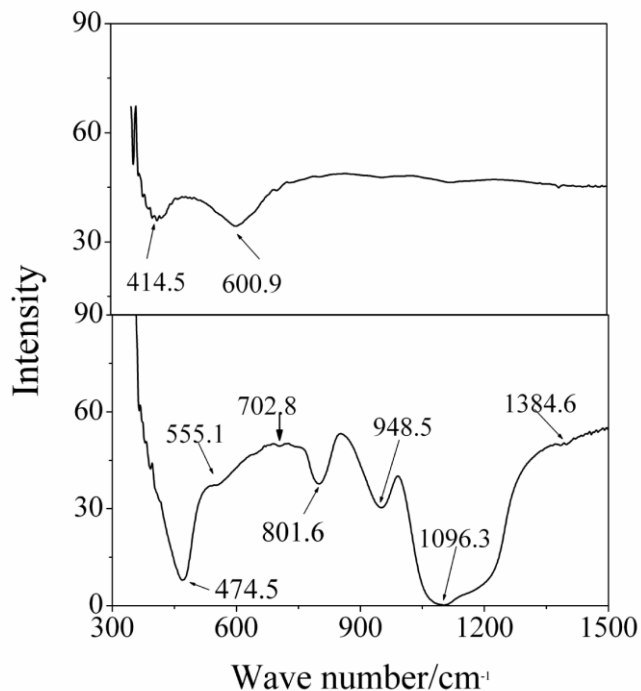


Fig.2.12. FTIR of NiFe₂O₄ and SiO₂ coated NiFe₂O₄.

2.3.4 Transmission Electron Microscope (TEM)

In this imaging technique a beam of electrons is focused onto a specimen causing an enlarged version of the sample to appear. A technical explanation of typical TEM is shown below in figure 2.13 [18].

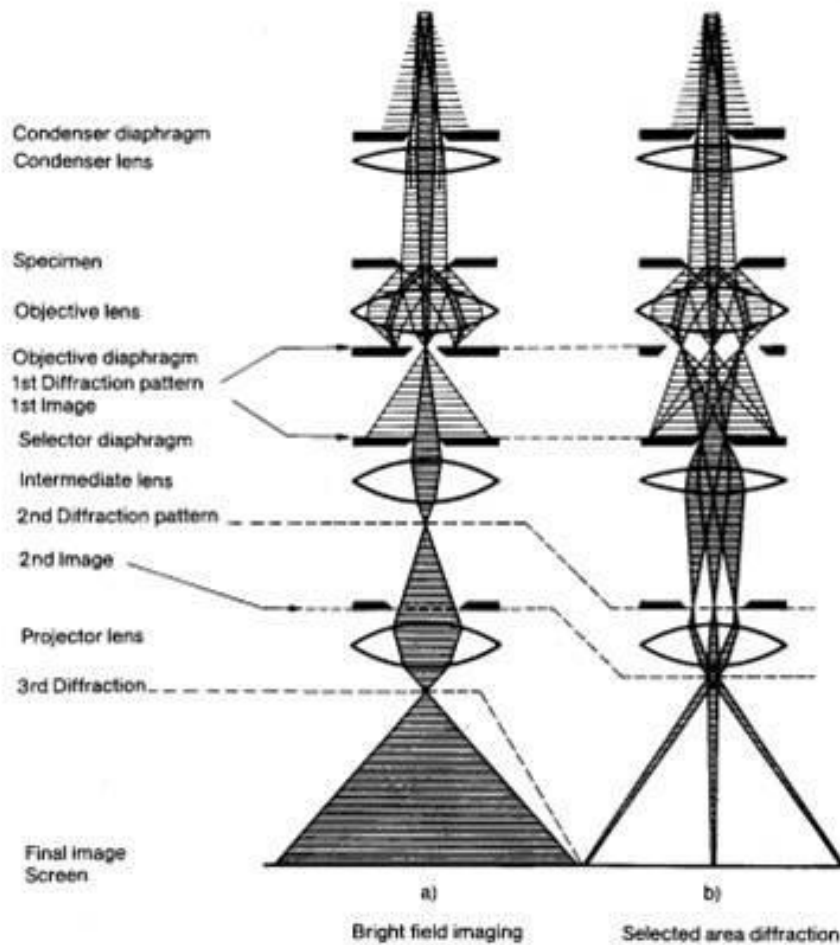


Fig.2.13. Schematic diagram of electron optics of a TEM

At the top there is an electron gun, producing a stream of monochromatic electrons. This stream is focused into a thin, small, coherent beam by the use of condenser lens. The first lens (usually controlled by the ‘spot size knob’) largely determines the ‘spot size’; the general size range of the final spot that strikes the sample. The second lens usually controlled by the ‘intensity or brightness knob’ actually changes the size of the spot on the sample; changing it from widespread spot to pin point beam. The beam is restricted by the condenser aperture, knocking out high angle electrons (those far from the optic axis, the dotted line down the center). The beam strikes the specimen and parts of it are transmitted. The transmitted portion is focused by the objective lens into an image. The image strikes the phosphor image screen and light is generated allowing the user to see the image. Areas of the specimen that are thicker will have fewer transmitted unscattered electrons and so will appear darker, conversely the thinner areas

will have more transmitted electrons and thus will appear lighter. This mode of operation to create contrast in image is known as bright field imaging mode.

In case of crystalline sample, the electron beam undergoes Bragg scattering and disperses electrons into discrete locations in the back focal plane as shown in Fig.2.14 below. The desired Bragg reflections can be selected by specific placement of objective apertures at back focal plane. Thus only parts of the sample that are causing the electrons to scatter to the selected reflections will end up projected onto the imaging apparatus producing diffraction contrast. Another part of the incident electrons are scattered (deflected from their original path) by atoms in the specimen in an elastic fashion (no loss of energy).

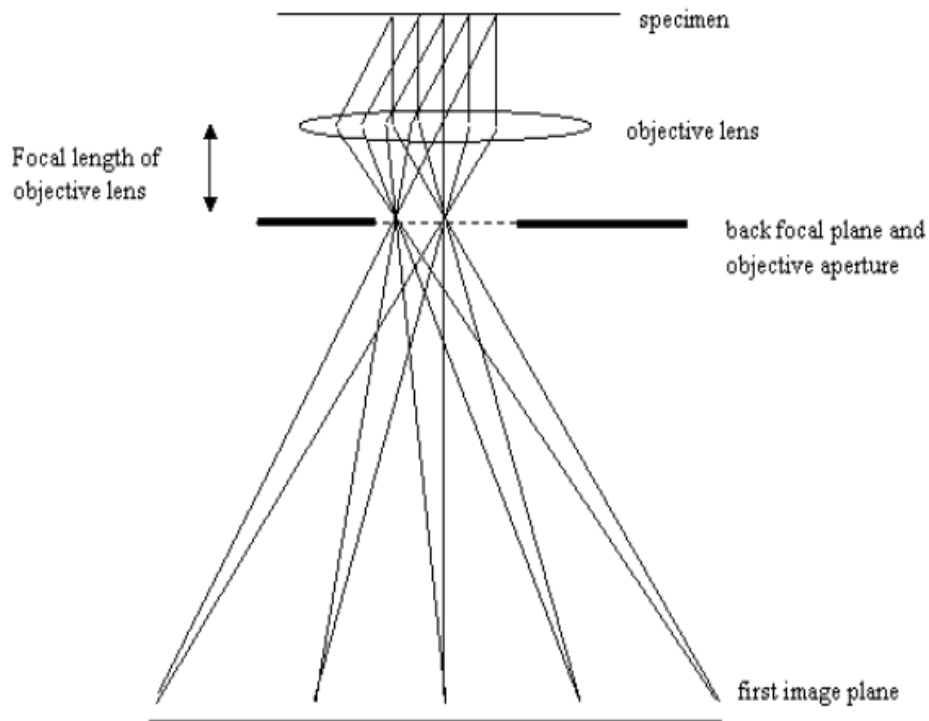


Fig. 2.14: Schematic diagram of image forming by E-beam

These scattered electrons are then transmitted through the remaining portions of the specimen. All electrons follow Bragg's Law and are scattered according to

$$2d \sin \theta = n\lambda \quad (2.12)$$

Where λ is the wavelength of the rays, θ is the angle between the incident rays with respect to the surface of the crystal and d is the spacing between layers of atoms. All incident electrons have the same energy (thus wavelength) and enter the specimen normal to its surface. All incident electrons that are scattered by the same atomic spacing will be scattered by the same angle. These scattered electrons can be collated using magnetic lenses to form a pattern of spots; each spot corresponding to a specific atomic spacing (a plane). This pattern can then yield information about the orientation, atomic arrangements and phases present in the area being examined. The TEM image and SAED pattern of Lanthanum doped BFO is shown in Figure 2.15.

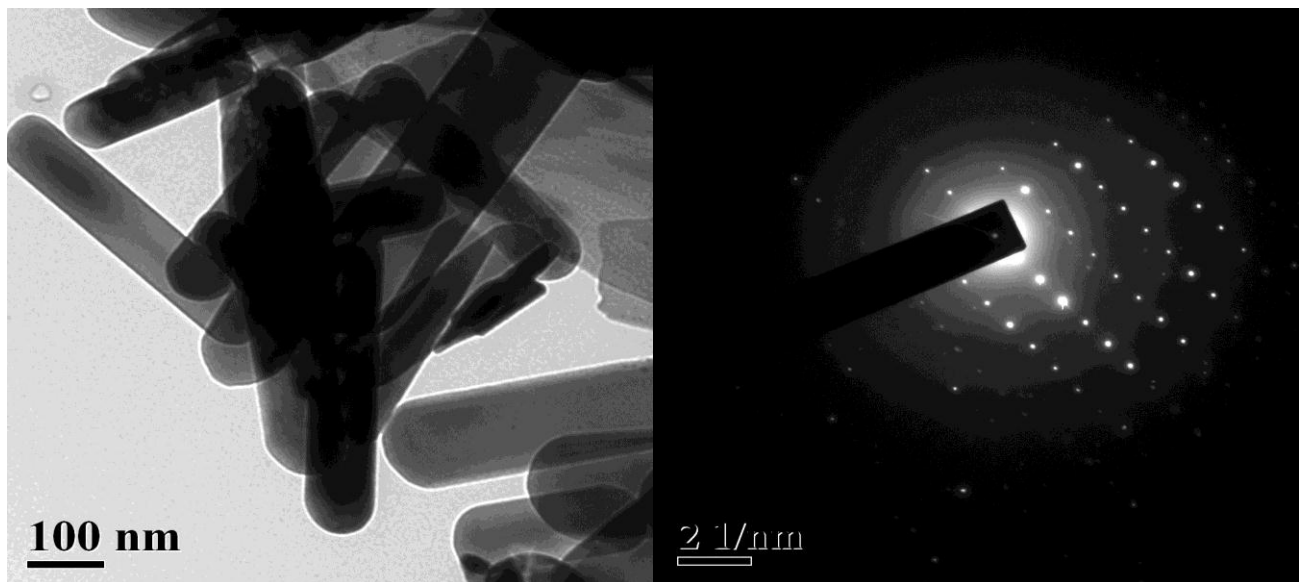


Fig. 2.15: TEM and SAED pattern of Lanthanum doped BFO

In order to take microscopic images of nanoparticles (NPs), we place them on carbon grids that are specially made for TEM imaging purpose [18]. Standard TEM grid has typical diameter of ~ 3.05 mm with a thickness and mesh size ranging from a few to 100 μm . Pretreatments of the NPs are done before placing them on carbon grid. The NPs, were dispersed in ethyl alcohol and the solution was ultrasonicated to detach the magnetic particles from each other. After sonication, we drop the ethyl alcohol solutions containing NPs on the TEM grids using micropipette. Proper pretreatment is necessary to get good quality images of nanostructures.

2.3.5 Vibrating Sample Magnetometer (VSM)

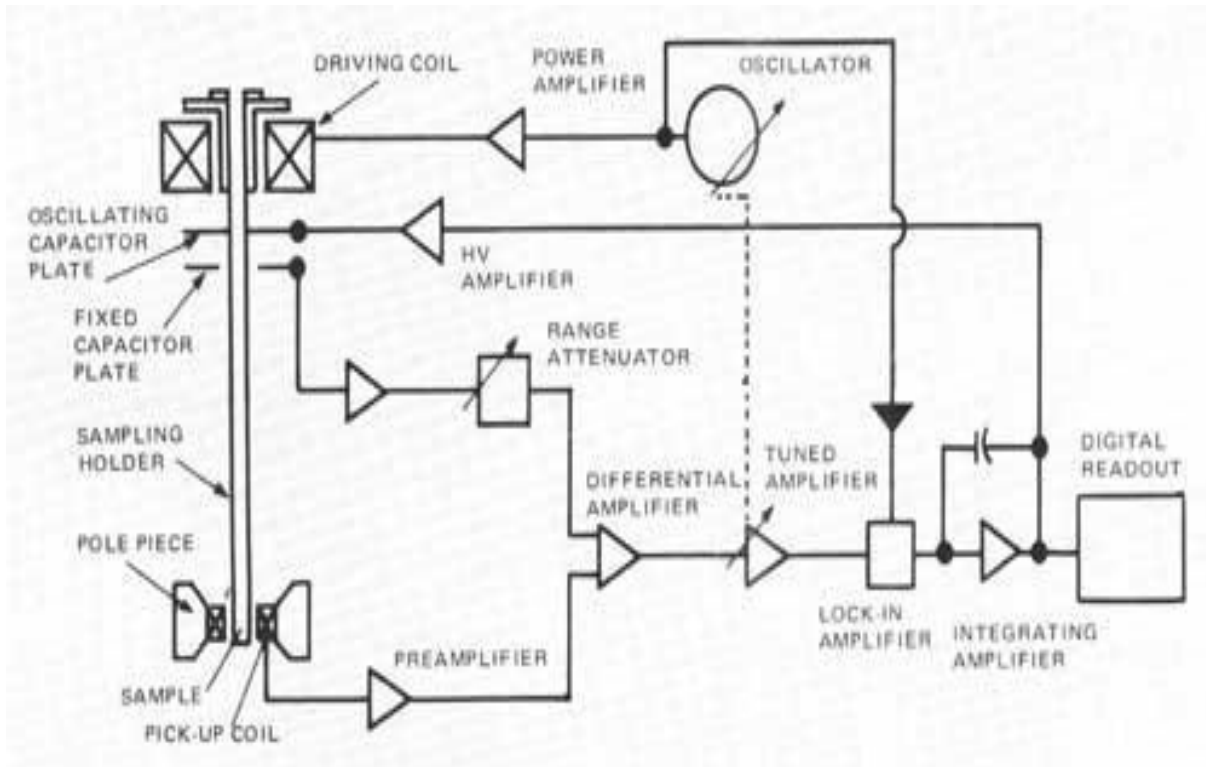


Fig. 2.16: Schematic diagram of VSM

In a VSM, the sample is subjected to a sinusoidal motion (of frequency ν) and the corresponding voltage is induced in suitably located stationary pickup coils. The electrical output signals of these pick up coils have the same frequency ν . Its intensity is proportional to the magnetic moment of the sample, the vibration amplitude and the frequency ν . The schematic diagram of the set-up is shown in Fig. 2.16. The sample to be measured is centered in the region between the poles of an electromagnet which can generate a uniform magnetic field H_0 . A thin vertical nonmagnetic sample rod (made of plastic/quartz) connects the sample holder with a transducer assembly located above the magnet. The transducer converts a sinusoidal signal as drive signal (generated by an oscillator/amplifier circuit) into a sinusoidal vertical vibration of the sample rod. The sample is thus subjected to a sinusoidal motion in the magnetic field H_0 .

Pickup coils made of copper and mounted on the poles of the magnet which pick up the signal resulting from the motion of the sample. However, though the pick-up coil signal at the

vibration frequency ν is proportional to the magnitude of the moment of the sample, it is also proportional to the vibration amplitude and frequency. Thus the moment readings taken simply by measuring the amplitude of the signal are subject to errors due to variation in amplitude and frequency of vibration. In order to avoid this difficulty, a nulling technique is introduced employing a vibrating capacitor for generating a reference signal that varies with moment, vibration amplitude and frequency in the same manner as the signal from the pickup coils. When these two signals are processed in an appropriate manner, it is possible to eliminate the effects of vibration amplitude and frequency shifts. In that case, one obtains readings that vary only with the moment of the sample.

The VSM in our laboratory (Lakeshore model) has maximum magnetic field generating capability of 2.1 T without cryogenic system and 1.76 T can be achieved with LN₂/LHe dewar between the coils. The moment versus temperature or temperature dependent hysteresis loops can be measured using a cryogenic system (Liq. N₂) that can operate within a temperature range of 80 to 400 K with temperature stability of ± 0.2 K controlled by a temperature controller (331, Lakeshore) and temperature resolution of 0.001 K. Noise level of 1.25 μ emu (RMS value) in moment measurement can be achieved using the system [19].

2.3.6 Superconducting Quantum Interference Device (SQUID)

SQUID is the most sensitive and effective device available till now to detect magnetic moment/field. The working principle of the SQUID is based on two fundamental principles of superconductivity [3,20]. One is quantization of magnetization flux in a superconducting ring and the other one is the Josephson effect. Superconducting electron pairs i.e. the Cooper-pairs can tunnel through a thin layer of insulator into another superconductor. Josephson effect can be understood from the propagation of electron waves. If the insulating layer between two superconductors is thin enough the electron wave in one superconductor can penetrate the insulating layer and overlap with the electron wave in the other superconductor. Consequently the cooper pairs tunnel through the insulating junction. Let us consider a SQUID consisting of two identical Josephson junctions. The total supercurrent is divided into I_a and I_b which tunnel through the junction a and b respectively. Hence,

$$I = I_a + I_b \quad (2.13)$$

When a magnetic field is applied a magnetic flux ϕ goes through the superconducting loop and induces a persistent current J . The induced current adds onto I_a while it gets subtracted from I_b . When the current waves flow through the junctions their phases shift by δ_a and δ_b respectively. That is

$$I_a = I_0 \sin \delta_a \quad (2.14)$$

$$I_b = I_0 \sin \delta_b \quad (2.15)$$

Where I_0 is the maximum allowable current flowing through the junction. Magnetic flux going through a superconducting loop is quantized. Hence there is interference between I_a and I_b after passing the junctions.

When a magnetic moment is kept in the loop containing a Josephson junction, an emf is induced in the loop, which induces a current with a frequency decided by the Josephson equations. The SQUID detects the change in currents or frequency to deduce the magnetic moment of the sample.

There are two types of SQUIDs, DC or AC. The MPMS SQUID works on the principle of DC SQUID, consisting of two Josephson junctions connected in parallel so that the electrons tunneling through the junctions demonstrate quantum interference depending upon the magnetic field within the loop. The MPMS SQUID is capable of providing magnetic fields in the range ± 70 kOe with field ramp possible as high as 700Oe/s and sample temperature ranging from 1.8 K to 400 K. Sensitivity is 1×10^{-8} emu at zero magnetic field and 5×10^{-8} emu at 70 kOe with 4 seconds data averaging.

2.3.7 Differential Thermal Analysis (DTA)

In DTA one measures the difference in temperature between a sample and a thermally inert reference as the temperature is raised. The plot of this differential provides information on exothermic and endothermic reactions taking place in the sample. The technique is routinely applied in a wide range of studies such as identification, quantitative composition analysis, phase diagrams, hydration-dehydration, thermal stability, phase transitions, melting points [21].

A DTA consists of a sample holder comprising thermocouples, sample containers and a ceramic or metallic block; a furnace; a temperature programmer; and a recording system. The key feature is the existence of two thermocouples connected to a voltmeter. One thermocouple is placed in an inert material such as Al_2O_3 , while the other is placed in a sample of the material under study. As the temperature is increased, there will be a brief deflection of the voltmeter if the sample is undergoing a phase transition. This occurs because the input of heat will raise the temperature of the inert substance, but be incorporated as latent heat in the material changing phase.

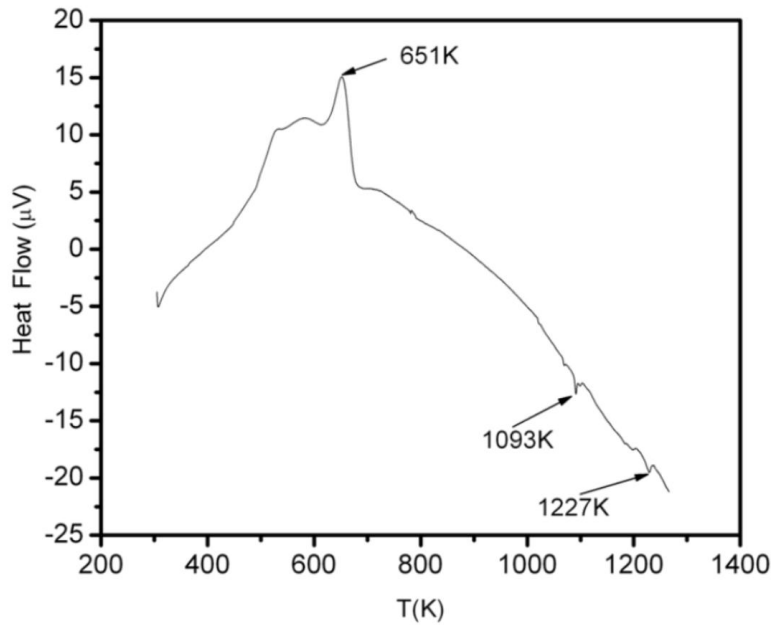


Fig. 2.17: DTA plot of Bismuth Ferrite sample

2.3.8 Thermogravimetric Analysis (TGA)

It measures changes in weight of a sample with increasing temperature. The TGA measures the weight loss of a material from a simple process such as drying or from complex chemical reactions that liberate gases such as structural water release, structural decomposition, carbonate decomposition, sulphur oxidation and fluoride oxidation. The TGA also measures the weight gain of a material from a simple process such as rehydration or from more complex surface reactions from reactive gas atmospheres [21]. The DTA plot of Bismuth Ferrite is shown in Figure 2.18.

2.3.9 Mossbauer Spectroscopy

Mössbauer spectroscopy is a spectroscopic technique based on the Mössbauer effect. This effect, discovered by Rudolf Mössbauer in 1957, consists of the recoil-free, resonant absorption and emission of gamma rays in solids. In its most common form, Mössbauer absorption spectroscopy, a solid sample is exposed to a beam of gamma radiation, and a detector measures the intensity of the beam transmitted through the sample. The atoms in the source emitting the gamma rays must be of the same isotope as the atoms in the sample absorbing them. If the emitting and absorbing nuclei were in identical chemical environments, the nuclear transition energies would be exactly equal and resonant absorption would be observed with both materials at rest. The difference in chemical environments, however, causes the nuclear energy levels to shift in a few different ways, as described below. Although these energy shifts are tiny (often less than a micro-electron volt), the extremely narrow spectral linewidths of gamma rays for some radionuclides make the small energy shifts correspond to large changes in absorbance. To bring the two nuclei back into resonance it is necessary to change the energy of the gamma ray slightly, and in practice this is always done using the Doppler effect. During Mössbauer absorption spectroscopy, the source is accelerated through a range of velocities using a linear motor to produce a Doppler effect and scan the gamma ray energy through a given range. A typical range of velocities for ^{57}Fe , for example, may be ± 11 mm/s (1 mm/s = 48.075 neV) [22]. In the resulting spectra, gamma ray intensity is plotted as a function of the source velocity. At velocities corresponding to the resonant energy levels of the sample, a fraction of the gamma rays are absorbed, resulting in a drop in the measured intensity and a corresponding dip in the spectrum.

The number, positions, and intensities of the dips (also called peaks; dips in transmitted intensity are peaks in absorbance) provide information about the chemical environment of the absorbing nuclei and can be used to characterize the sample.

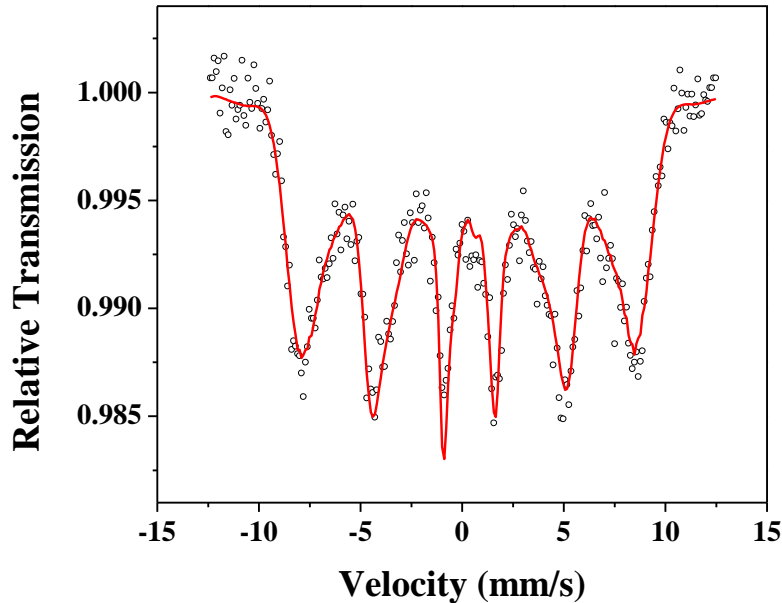


Fig. 2.18: Mössbauer spectra of a NiFe_2O_4 nanoparticle

Room temperature Mössbauer measurements were carried out in a standard PC based set-up consisting of a 1024 channel MCA card, working in the constant acceleration mode. A 10 mCi ^{57}Co in Rh matrix was used as the source. The system was calibrated with a high purity iron foil of thickness $12\mu\text{m}$. A least squares fitting program LGFIT2 was used to fit the experimental data. The Mössbauer spectra of a NiFe_2O_4 nanoparticle is shown in figure 2.18.

2.3.10 AC susceptibility set up

AC hysteresis loop is commonly measured by the mutual inductance between two coils, one a primary coil (in our case a solenoid) for generating the ac magnetic field and the other a pick up coil used as secondary. Usually the secondary is a set of two oppositely wound identical coils so as to give a zero net signal when there is no sample. Samples are placed near the central zone of the primary coil in order to achieve a uniform magnetic field [23,24]. In the AC measurement, the moment of the sample is actually changing in response to an applied ac field, allowing the dynamics of the magnetic system to be studied.

Fig. 2.19 shows the block diagram of the experimental set-up for measuring ac hysteresis loop. The coils were located coaxially within a long solenoid producing a homogenous field along the length of the sample. The flux in presence of the sample is measured with an integrating

fluxmeter (Walker Scientific MF-3D). The MF-3D is a precision electronic integrating fluxmeter which measures the magnetic flux coupling within a coil or loop of wire.

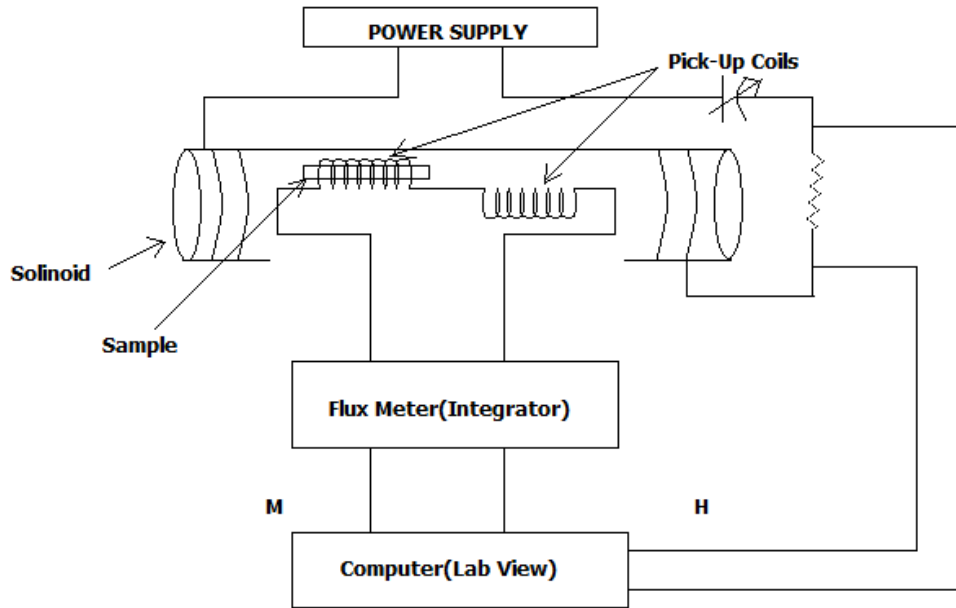


Fig. 2.19: Schematic diagram of the experimental set-up for measuring ac hysteresis loop

It integrates the volt-second signals induced across a coil, by the flux coupling to the coil. The output is representative of the change in flux coupling during the integrating period. Each magnetic line (Maxwell), in linking a conductor induces in it a 10^{-8} volt-second impulse. For a coil of N turns, the signal input received is $N\Phi$ Maxwell-turns or $N\Phi 10^{-8}$ volt-seconds. Therefore the induced voltage in presence of the sample is

$$V = N \frac{d\Phi}{dt} 10^{-8} \quad (2.16)$$

The flux can be expressed as AM where A is the area of the coil in which a magnetization M is experienced and the input impulse becomes $NAM 10^{-8}$ volt-seconds.



Fig. 2.20: Photograph of the experimental set-up for measuring hysteresis loops.

By virtue of the heavy feedback employed in the integrator, its input impedance appears as the resistance value set in on the decade dial. A current, $\frac{NAM}{R} 10^{-8}$ ampere-seconds flows in this resistor and is constrained by the feedback to flow solely into the integrating capacitor which is free to move in voltage only at the output terminal. From the relationship, voltage equals charge (ampere-seconds) divided by capacitance, we obtain the output voltage (in volts)

$$V = \frac{N\Phi}{RC} 10^{-8} = \frac{NAM}{RC} 10^{-8} \quad (2.17)$$

The value of R (Ω) is 100 times the setting of the decade dial and the value of C (farad) is 10^{-7} , 10^{-6} or 10^{-5} depending on the range selected. This integrated voltage which is proportional to the magnetization of the sample was recorded as a function of the voltage proportional to the magnetic field produced by the uniform solenoid. These voltages corresponding to M and H are recorded in two respective Digital Multimeters (Agilent, 34401A) and then plotted in the computer using a Pico Analog to Digital convertor (ADC-212). We have formed a LCR circuit so that at series resonance high current is obtained by changing the capacitance. At series

resonance the inductive reactance (ωL) and inductive capacitance ($1/\omega C$) becomes equal. Hence the effect of the inductance is nullified and high current is obtained. MH curve of the sample is finally obtained after calibrating the values of these voltages. Fig.2.20 shows the photograph of the home-made experimental set-up for measuring hysteresis loops. The AC hysteresis loop of NiFe_2O_4 sample is shown in Fig. 2.21.

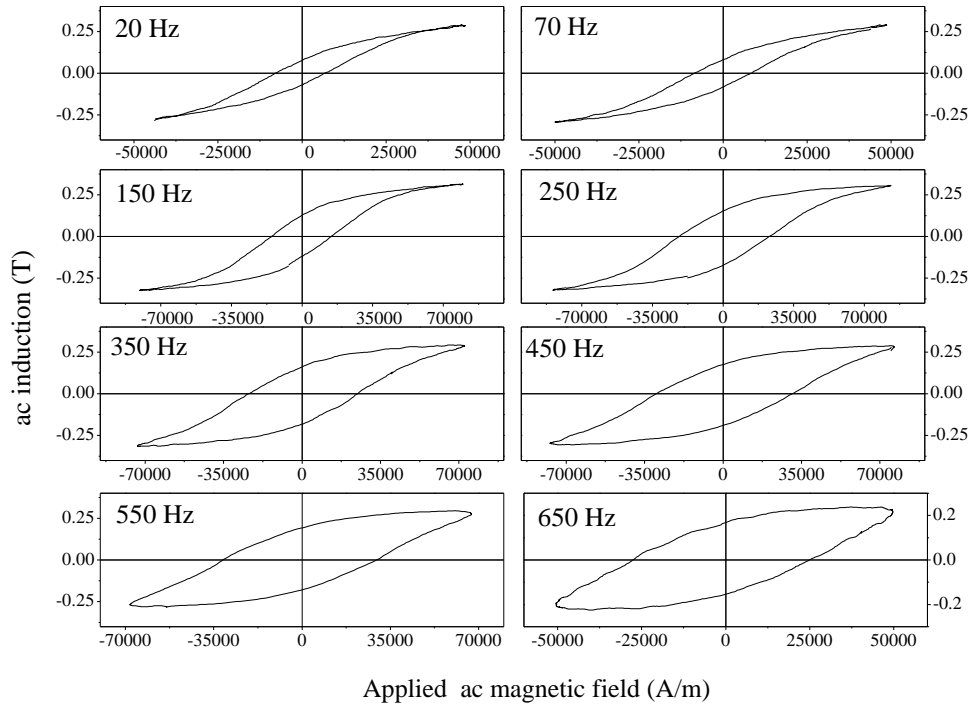


Fig. 2.21: Hysteresis loops obtained from our home made set up

2.3.11 P.E Loop Tracer

The Polarization vs Electric Field hysteresis loop is measured by a Sawyer Tower circuit which is shown in Figure 2.22. This Sawyer Tower circuit is the basic operation circuit of a PE loop tracer [25]. AC current is passed in the circuit consisting of two capacitors C_s and C_i connected in series. s stands for sample (Ferroelectric in Fig. 2.22) and i for internal (Reference capacitor in fig. 2.22). Since the capacitors are connected in series, the charge on the known (C_i) and unknown capacitors (C_s) will be same. C_i is selected from the PE main screen as shown in Fig. 2.24. The load resistance should be selected as default value of 10 K Ω .

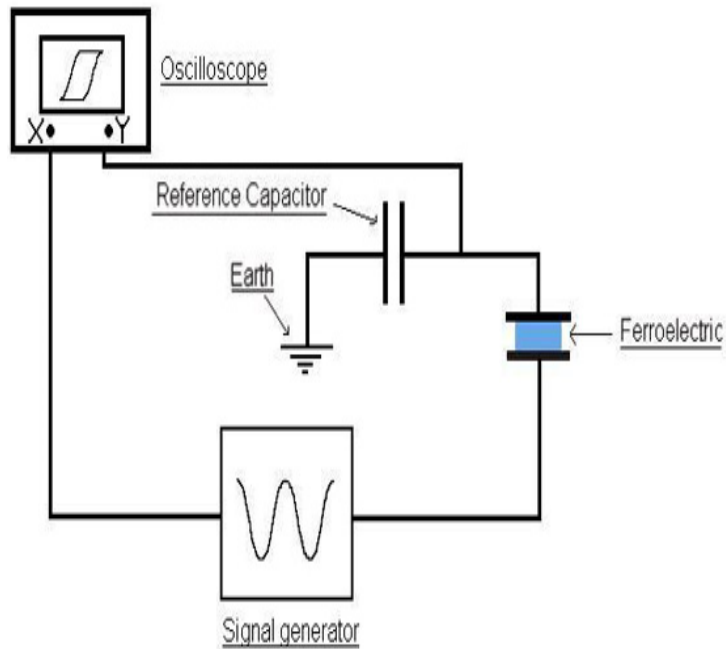


Fig 2.22. Sawyer Tower circuit

$$Q_s = Q_i \quad (2.18)$$

$$C_s * V_s = C_i * V_i \quad (2.19)$$

Also total voltage

$$V_t = V_s + V_i \quad (2.20)$$

V_t is the total voltage which we are applying and V_i is measured manually.

Now in equation (2.19) we know V_s , C_i and V_i . We can calculate C_s . Finally multiplying C_s with V_s we will have Q_s . Now Q_s divided by the sample area gives the polarization. The P vs E hysteresis loop of Barium doped Bismuth Ferrite sample is shown in Figure 2.23.

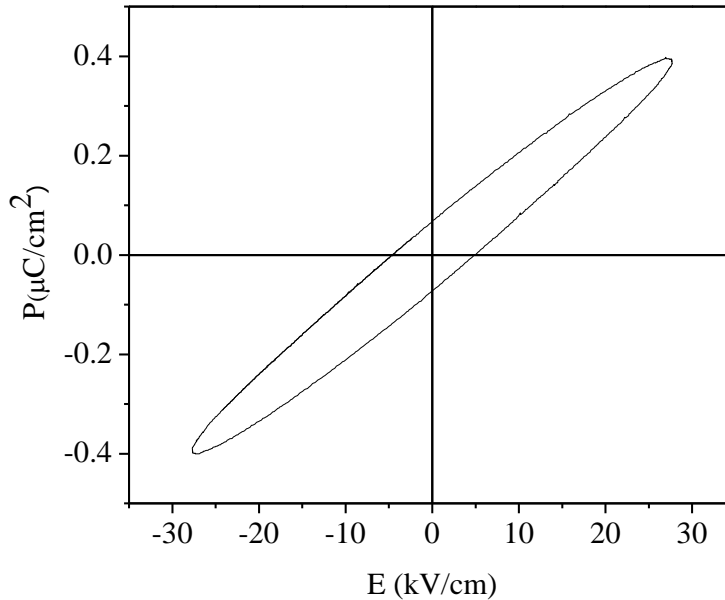


Fig. 2.23: PE hysteresis loop

2.3.12 Dielectric properties measurement setup

An LCR meter (Inductance (L), Capacitance (C), and Resistance (R)) is a piece of electronic test equipment used to measure the inductance, capacitance and resistance of a component. In the simpler versions of this instrument the true values of these quantities are not measured; rather the impedance is measured internally and converted for display to the corresponding capacitance or inductance value. That is why it has been named Impedance Analyzer. Readings will be reasonably accurate if the capacitor or inductor device under test does not have a significant resistive component of impedance. More advanced designs measure true inductance or capacitance, and also the equivalent series resistance of capacitors and the Q factor of inductive components.

The Impedance Analyzer, is interfaced with the computer and the data (capacitance and Dissipation factor) is collected as a function of temperature at different frequencies. The electroded samples were used to take the measurements.



Fig. 2.23: The Agilent 4294A Impedance Analyzer used in our laboratory

Dielectric constant was measured from the formulae

$$\epsilon = \frac{Cd}{A\epsilon_0} \quad (2.21)$$

where ϵ is the dielectric constant or relative permittivity of the sample, C is the capacitance in Farad (F), d is the thickness of the pellet in meters (m), A is the area of the pellet in square meters (m^2), $\epsilon_0 =$ permittivity of free space in farad per meter (8.85×10^{-12} F/m). We have discussed the technique of measuring dielectric constant and dielectric loss in details in Chapter 5. We have also measured AC conductivity, Real part of Impedance Z , Imaginary part of impedance Z'' by impedance analyzer which has been discussed in Chapter 5.

Usually the device under test (DUT) is subjected to an AC voltage source [26,27]. The meter measures the voltage across and the current through the DUT. From the ratio of these the meter can determine the magnitude of the impedance. The phase angle between the voltage and current is also measured in more advanced instruments; in combination with the impedance, the equivalent capacitance or inductance, and resistance, of the DUT can be calculated and

displayed. The meter must assume either a parallel or a series model for these two elements. The most useful assumption, and the one usually adopted, is that LR measurements have the elements in series (as would be encountered in an inductor coil) and that CR measurements have the elements in parallel (as would be encountered in measuring a capacitor with a leaky dielectric). We have also measured the temperature dependence of capacitance, Impedance, Conductivity etc. by our impedance analyzer by placing the sample in an oven. The home-made set-up is shown in the figure 2.23. The dielectric constant vs. frequency plot of Lanthanum doped BFO with temperature is shown in Figure 2.24.

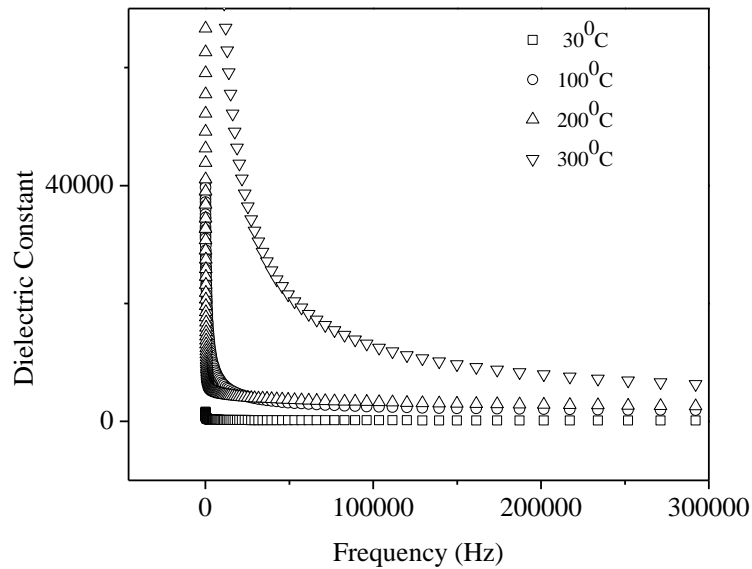


Fig. 2.24 : The dielectric constant vs frequency plot of Lanthanum doped BFO sample

2.3.13 Magnetoelectric Co-efficient measurement

Magnetoelectric co-efficient is the measure of the strength of the magnetoelectric coupling in a magnetoelectric substance. The experiment setup to measure the ME effect using lock-in technique is shown in Fig. 2.25. The DC magnetic bias field up to 10 kOe is produced by an electromagnet. The time-varying DC magnetic field is achieved by a constant current power supply (Model: DPS-175) with the current varying from 0 - 3A. To measure the DC field, a Hall probe (Scientific Equipments Roorkee Model DGM-102) is employed. Additionally, an AC magnetic field up to 20 Oe with frequencies from 1 Hz to 10 kHz is superimposed onto the DC field. The AC field is produced by a Helmholtz coil (100 turns with a diameter of 50 mm), which

is driven by an AC current generated by a Lock in Amplifier (Stanford Research systems Model SR830 DSP) with input resistance and capacitance of $10\text{M}\Omega$ and 25 pF , respectively.

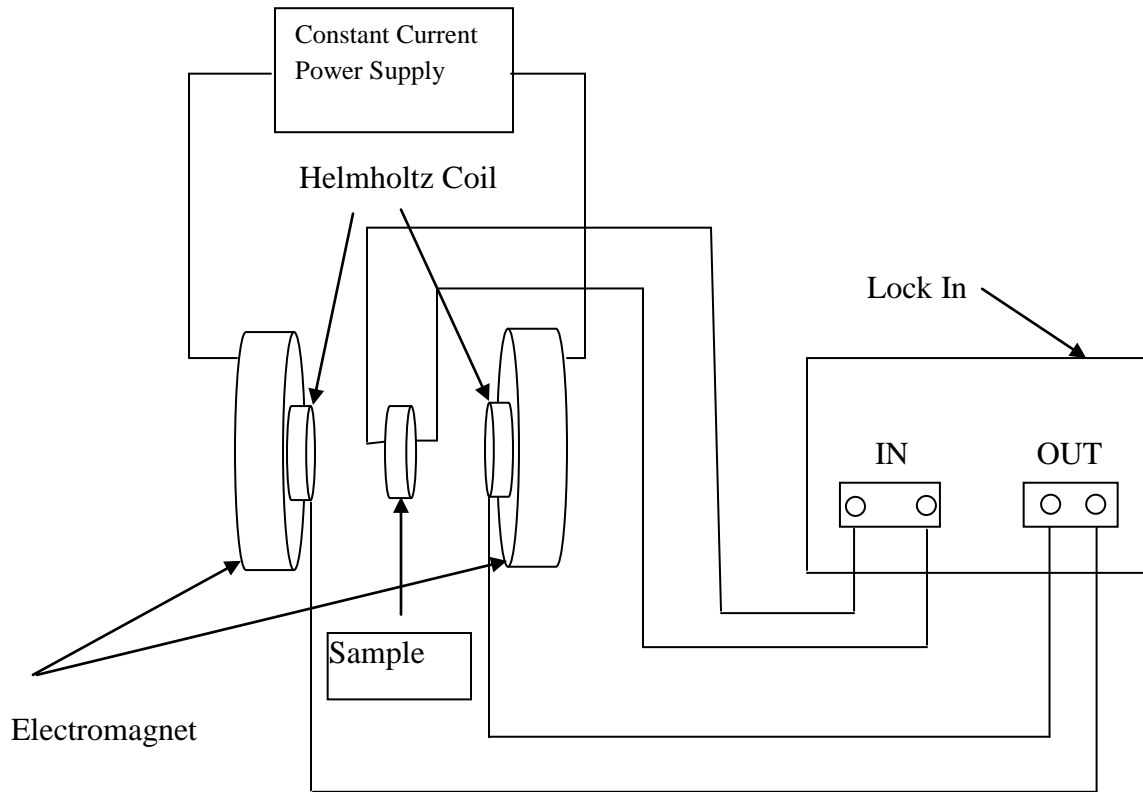


Fig.2.25: Schematic diagram of magnetolectric coefficient measurement set up



Fig.2.26: Home-made magnetolectric coefficient measurement set up

The amplitude of the AC field is also measured by the Hall Probe. The sample is placed in between the pole pieces of the electromagnet with its surface perpendicular to the field direction. The ME signal was measured using a lock-in amplifier. This signal is actually the emf induced in the sample because of the time varying ac field in the Helmholtz coil. This signal changes with the change in the dc field.

The ME coefficient is approximated as (described in Chapter 6)

$$\alpha_{ME} = \frac{dE}{dH} \quad (2.22)$$

$$= \left(\frac{1}{t} \right) \frac{dV}{dH}$$

$$= \frac{V_{out}}{h_0 t} \quad (2.23)$$

where V_{out} is the ac magnetoelectric voltage appearing across the sample surface (measured by the lock-in), h_0 is the amplitude of the ac magnetic field, and t is the thickness of the sample [28,29]. The α_{ME} vs H_{DC} of $CoFe_2O_4:BaTiO_3$ core shell sample is shown in Figure 2.27.

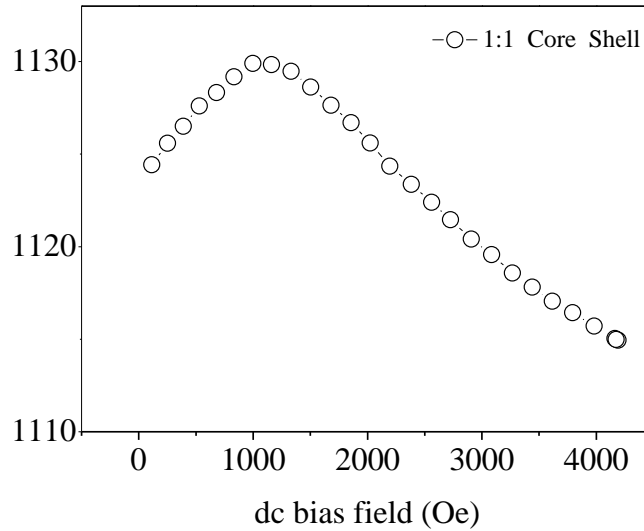
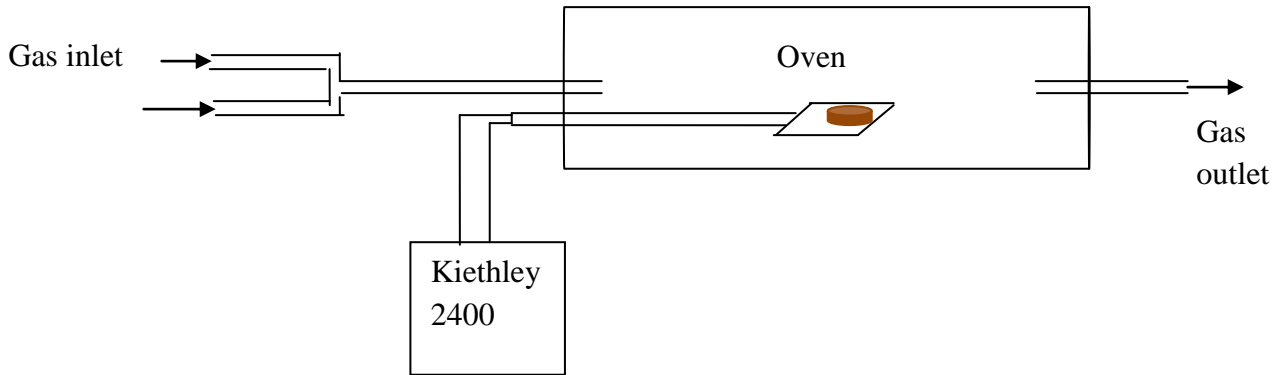


Fig.2.26: Magnetoelectric coefficient measurement vs. dc bias field of $CoFe_2O_4:BaTiO_3$ core shell sample

2.3.14 Gas Sensing set up

The sensing property was measured by two probe method. The schematic diagram of the set-up is shown in Fig. 2.27.



2.27: Schematic representation of the Gas sensing measurement

First, the pellet of the samples was prepared at the pressure of 7.5 ton/cm^2 . Then the LPG sensing properties were measured at different temperature with two Au contacts on the top surface of the pellet of 3 mm radius at a bias voltage of 5 volts. The sensing property was measured using a mixture of Ar and O_2 gas in the ratio 4:1. Then LPG gas of concentration 1000 ppm was passed [30]. The change in the current was recorded by a Keithley source meter (Model: 2400).

References

- [1] C.B. Murray, C.R. Kagan and M.G. Bawendi, *Annu. Rev. Mater. Sci.* **30**, 545 (2000).
- [2] Z. L. Wang, Y. Liu and Z. Zhang *Handbook of Nanophase and Nanostructured Materials* (Kluwer Academic, Beijing 100085, China, 2000), Vol. 3.
- [3] X. Peng, J. Wickham and A.P. Alivisatos, *J. Am. Chem. Soc.* **120**, 5343 (1998).
- [4] R.L. Penn, G. Oskam, T. J. Strathmann, P.C. Searson, A.T. Stone and D.R. Veblen “Epitaxial Assembly in Aged Colloids” *J.Phys. Chem. B* **105**, 2177-2182 (2001).
- [5] Z.L. Wang, Y. Liu and Z. Zhang *Handbook of Nanophase and Nanostructured Materials* (Kluwer Academic, Beijing 100085, China, 2000), Vol. 3.
- [6] H. Bethe, *Ann. Physik* **3**,133 (1929).
- [7] S. Kumar and T. Nann *Small* **2**, 316329 (2006).
- [8] R.L. Penn and J.F. Bannfield, *Am. Mineral.* **83**, 10771082 (1998).
- [9] Z.Tang, N.A. Kotov and M. Giersig, *Science* **297**, 237240 (2002).
- [10]L. Manna, E.C. Scher and A.P. Alivisatos, *J.Am. Chem. Soc.***122**, 1270012706 (2000).
- [11] C. Burda, X. Chen, R. Narayanan and M.A. El-Sayed, *Chem. Rev.* **105**,1025 (2005).
- [12] J. Mullin, *Crystallization*, 4th ed. (Butterworth Heinemann, Boston, 2001).
- [13] J.D. Wright and N.A.J.M. Sommerdijk, *Sol Gel Materials, Chemistry and Applications* (Taylor & Francis, London, 2001), p. 16.
- [14] Cullity, B. D., Stock, S. R., *Elements of X-ray Diffraction*, 3rd Edition, Prentice Hall (2001).
- [15] T. Okubo, M.Watanabe, K. Kusakabe and S. Morooka *J.Mater. Sc.* **25**, 4822 (1990).
- [16] T.R. Groves, H.C. Pfeiffer, T.H. Newman, and F.J. Hohn, *J. Vac. Sci. Technol. B*, **6(6)**, 2028 (1988).
- [17] C. Richard Brundle, Charles A. Evans Jr, Shaun Wilson. *Encyclopedia of materials characterization*, Butterworth-Heinemann publications, 1992.
- [18] ProSciTech, Australia.
- [19] J. H. E. Griffiths, *Nature* **158**, 670 (1946).
- [20] “SQUID magnetometer,”<http://www.hyperphysics.phy-tr.gsu.edu/hbase/solids/squid.htm> (Accessed in 2012).
- [21] R.F. Speyer, *Thermal Analysis of Materials* (Marcel Dekker, Inc., New York, 1994).

- [22] "Mossbauer Spectroscopy" <http://www.en.Wikipedia.org> (accessed in 2012).
- [23] Q. Design, "Introduction to Ac Susceptibility," <http://www.qdusa.com> (Accessed in 2012).
- [24] A. Bajpai and A. Banerjee Rev. Sci. Instrum. **68**, 11(1997).
- [25] PE loop tracer manual, Marine India, Accessed in 2012.
- [26] Agilent 4294A Precision Impedance Analyzer, Operation Manual, Accessed in 2012.
- [27] J. Wu and J. Wang J. of App. Phys. **105**, 124107 (2009).
- [28] G. V. Duong, R. Groessinger and R. S. Turtelli IEEE Transactions on Magnetics, **42**, 10, (2006).
- [29] G.V. Duong, R. Groessinger, M. Schoenharta, D. Bueno-Basques J. of Magn. and Magn. Mater. **316**, 390 (2007).
- [30] C. Xiangfeng, J. Dongli, Z. Chenmou Sensors and Actuators B **123**, 793 (2007).

Chapter 3

3 Synthesis and study of NiFe₂O₄/SiO₂ core-shell nanocomposites

3.1 Preamble

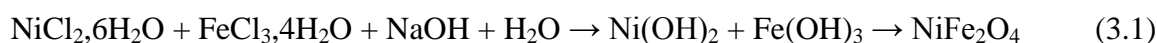
Presently oxide magnetic nanomaterials are of extreme significance to the society because of their manifold applications in high density magnetic storage media [1], high frequency devices [2], magnetically assisted drug delivery [3], cell isolation [4], MRI contrast agents [5], immobilization of proteins and enzymes [6], biosensors [7] and so on. But most of these applications require the magnetic particles to be coated with a nonmagnetic and biologically compatible substance since nanoparticles themselves are very reactive and agglomerate easily [8]. Magnetic nanoparticles for in vivo biomedical use must be small enough to avoid detection by the immune system, to be circulated through the blood stream and should be stable enough to remain in the body for a sufficient time [9]. Coating them with a biologically compatible substance will make them suitable for specific applications. Among the various types of oxide magnetic particles, ferrites belong to a unique class since they have the advantage of high resistivity in a wide frequency range as well as low production cost [10]. NiFe₂O₄ is one such ferrite whose nanoparticles in core/shell form can have applications in magnetic recording media, ferrofluids, catalysts and microwave absorbents [11].

In this work we have prepared the NiFe₂O₄ nanoparticles by co-precipitation technique, coated them with SiO₂ employing the Stöber process and studied their magnetic properties in details. Some research has been done on Fe, Fe/Ni, FePt, Fe₃O₄, CoFe₂O₄, MnFe₂O₄ nanoparticles coated with SiO₂ or embedded in SiO₂ matrix [12 - 15]. But the coating of SiO₂ on NiFe₂O₄ has not been properly explored yet. We have measured the Ac hysteresis loops of the NiFe₂O₄ samples. We have also synthesized NiFe₂O₄ nanoparticles of different morphology by the hydrothermal technique and studied the variation of its magnetic and gas sensing properties with morphology.

3.2 Synthesis of NiFe₂O₄ and NiFe₂O₄:SiO₂ core shell

To prepare NiFe₂O₄ nanoparticles by co-precipitation technique, a solution of NiCl₂, 6H₂O and FeCl₃, 4H₂O, mixed in stoichiometric ratio, was prepared in double distilled water [16]. TX 100 was added as a surfactant. The resulting mixture was added drop by drop to a preheated NaOH solution (5 N) at 80°C. As a result of this hydroxides of Nickel and Iron are coprecipitated. The reaction was carried out for one hour with continuous stirring. The solution was brought to room temperature and washed with distilled water. The obtained precipitate was dried and termed as sample A. It was annealed for 10 hours at 400°C (Sample B), 500°C (Sample C) and 700°C (Sample D).

The coprecipitation technique is shown in the following equation.



Each of these samples was coated with silica following the conventional Stöber method [17]. In a typical procedure, 6 ml of the NiFe₂O₄ suspension in ethanol was ultrasonicated for 1 hour. This solution was then added to a solution of 60 ml ethanol, 3 ml ammonium hydroxide (30 wt%). After stirring for around 15 min, 1.5 ml of tetraethyl orthosilicate was added drop by drop to the solution. The reaction was then allowed to proceed for 12 hrs at room temperature under continuous stirring. After stirring for 12 hrs, silica was formed on the surface of ferrite nanoparticles through hydrolysis and condensation of TEOS. Double distilled water was used throughout the synthesis. The uncoated samples A, B, C, D coated with SiO₂ were denoted as A1, B1, C1 and D1 respectively.

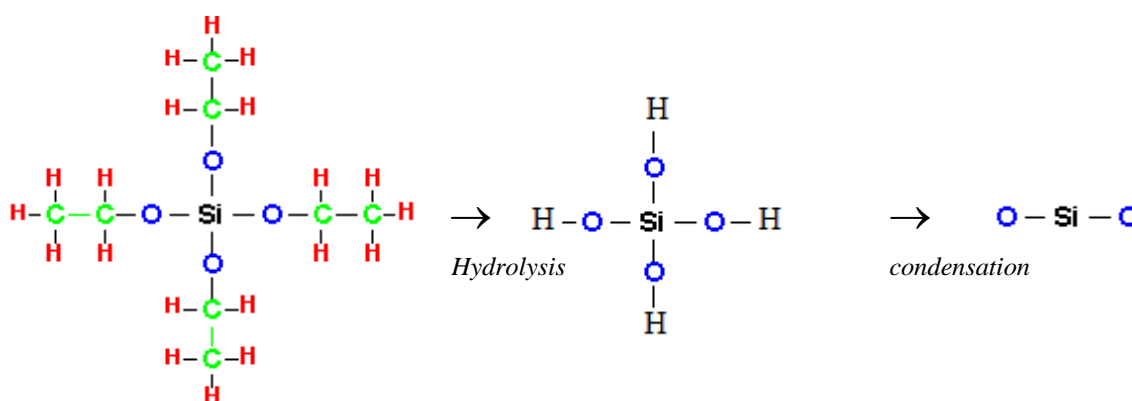


Fig. 3.1: Molecular structure of Tetraethyl Orthosilicate

The Stöber process reaction is shown in the following equation



Ammonia was used as a catalyst in this reaction. With the increase or decrease of the concentration of ammonia the rate of hydrolysis and condensation increases and decreases respectively.

The crystal structure of uncoated annealed samples was verified by an x-ray diffractometer (PANalytical). The stretching frequency of the SiO_2 coated samples was obtained from the Fourier Transform Infra Red Spectroscopy (JASCO FTIR-6300). The morphology of the uncoated and coated samples was studied with the help of a Transmission Electron Microscope (JEOL) and Field Emission Scanning Electron Microscope (JEOL). A Vibrating Sample Magnetometer (VSM Lake Shore Cryotronics) was used to study the magnetic properties of the samples at various temperatures down to 80K.

3.3 Results and Discussions

The x-ray diffraction patterns of samples A, B, C and D are shown in Fig.3.2. All the observed peaks confirmed the formation of spinel NiFe_2O_4 . The peaks became sharper with the increase in annealing temperature.

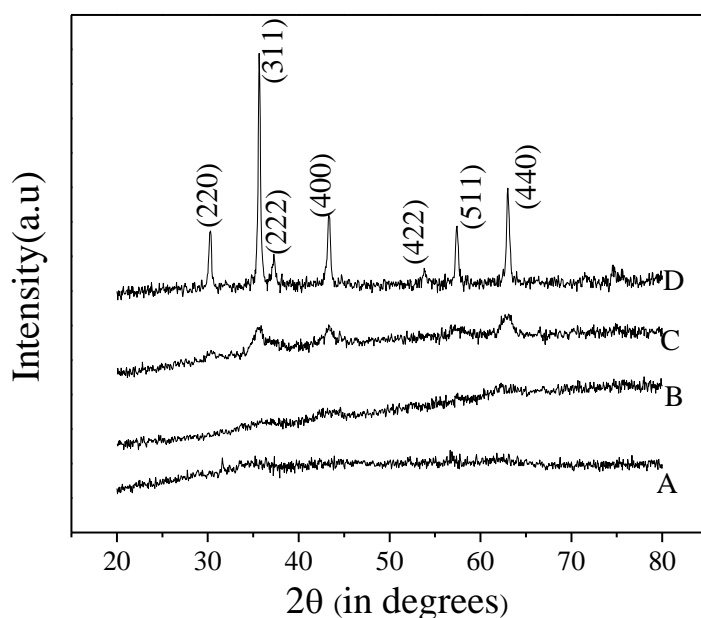


Fig. 3.2: XRD of Uncoated NiFe_2O_4 nanoparticles (samples A, B, C and D).

This proved that the particle size increases with the increase in annealing temperature. The average crystallite size was calculated using the Scherrer formulae as discussed in Chapter 2. The crystallite size of the uncoated samples was found to vary from ~ 4.0 nm (for sample A) to ~ 32 nm (for sample D) as mentioned in Table-3.1.

Table 3.1: Particle size of uncoated NiFe₂O₄ nanoparticles determined from XRD study

Sample name	Heat treatment	Average particle size from XRD (nm) with standard deviation
Sample A	Before heat treatment	4.0 (0.3)
Sample B	400°C / 10 hours	6.0 (0.4)
Sample C	500°C / 10 hours	14.0 (1.0)
Sample D	700°C / 10 hours	32.0 (2.5)

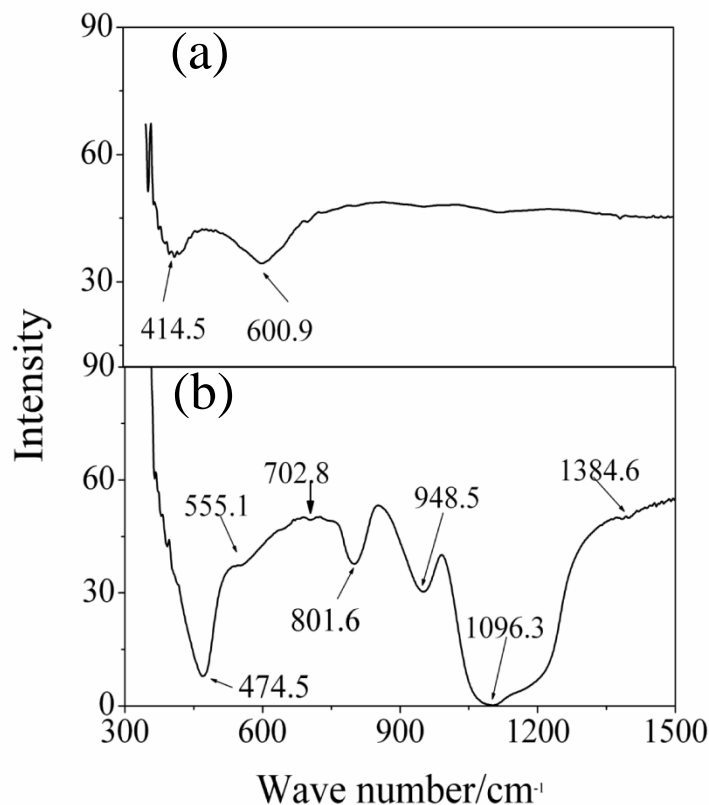


Fig. 3.3: FTIR spectra of sample C and C1

The Fourier Transform Infrared spectra of the uncoated (Sample C) and Silica coated nickel ferrite nanoparticles (Sample C1) are shown in Fig.3.3. The spectra of the uncoated sample (Fig 3.3(a)) show absorption peaks at 411.38 cm⁻¹ and 600.98 cm⁻¹ which

can be associated with the characteristic Ni-O stretching modes in NiFe₂O₄ phase. The spectra of the silica coated sample C1 (Fig. 3.3(b)) showed a number of peaks at 471.42, 555.16, 797.69, 948.58 and 1096.31 cm⁻¹ [18]. The broad absorption at 1096.31 cm⁻¹ is due to ≡Si-O-Si≡ of the SiO₄ tetrahedron. The absorption at 948.58 cm⁻¹ is due to the contribution from Si-O-H stretching vibration and Si-O-Fe vibration. A faint band at 555.16 cm⁻¹ is composed of Fe-O stretching band in Fe-O-Si bonds. The absorption at 797.69 cm⁻¹ is due to the Si-O-Si symmetric stretching and that at 471.42 cm⁻¹ is for Si-O-Si or O-Si-O bending mode.

The size and morphology of the uncoated and coated (core-shell) samples were studied in details using FESEM and HRTEM. Fig.3.4 (a) shows the HRTEM micrograph of sample C and 3.4 (b) shows its SAED pattern. Its particle size distribution is shown in Fig.3.5. The SAED pattern shows that the particles formed are polycrystalline in nature. The particle size distributions obtained from TEM micrograph follow log-normal distribution [19]. The lognormal distribution function is described by P (D) is the log-normal distribution function of diameter D and is given by,

$$P(D) = \frac{1}{Ds\sqrt{2\pi}} e^{-\frac{(\ln \frac{D}{D_0})^2}{2s^2}} \quad (3.3)$$

where D₀ = most probable diameter

s = parameter determining width of distribution and also a fitting parameter

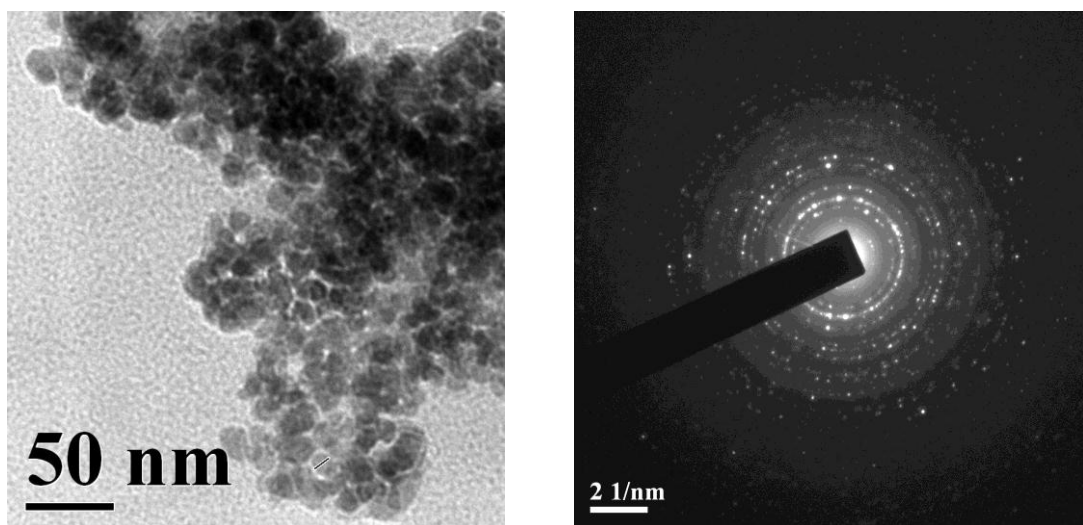


Fig. 3.4 (a): HRTEM image of sample C along with SAED **(b)** Its SAED pattern

The most probable particle size (~13.7 nm) obtained by fitting lognormal distribution function to the experimental data are close to the average crystallite size (~ 14 nm) estimated from XRD study.

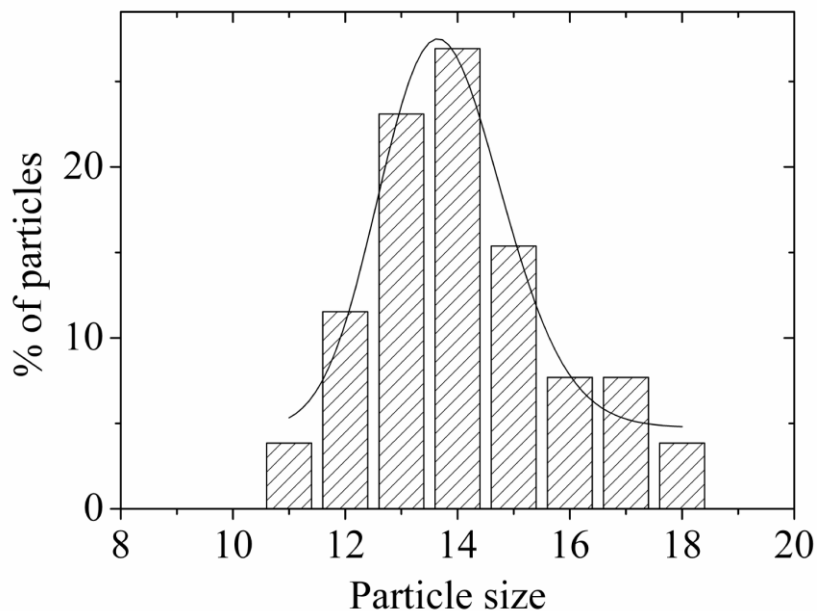


Fig.3.5: Size distribution of sample C fitted with log-normal distribution function.

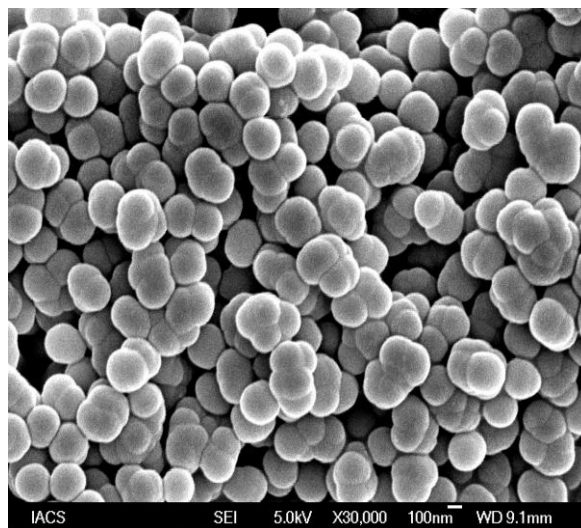


Fig.3.6: FESEM image of sample C1

The FESEM and HRTEM micrograph of sample C1 (SiO_2 coated sample C) is shown in Fig.3.6 and 3.7 respectively. The figures show that the particles are almost spherical and composed of NiFe_2O_4 as core and SiO_2 as shell. Though the core diameter varies within 50 –

80 nm, the shell thickness is almost the same (~20nm) for all the particles. These micrographs indicate that the core of a coated particle is composed of several uncoated particles.

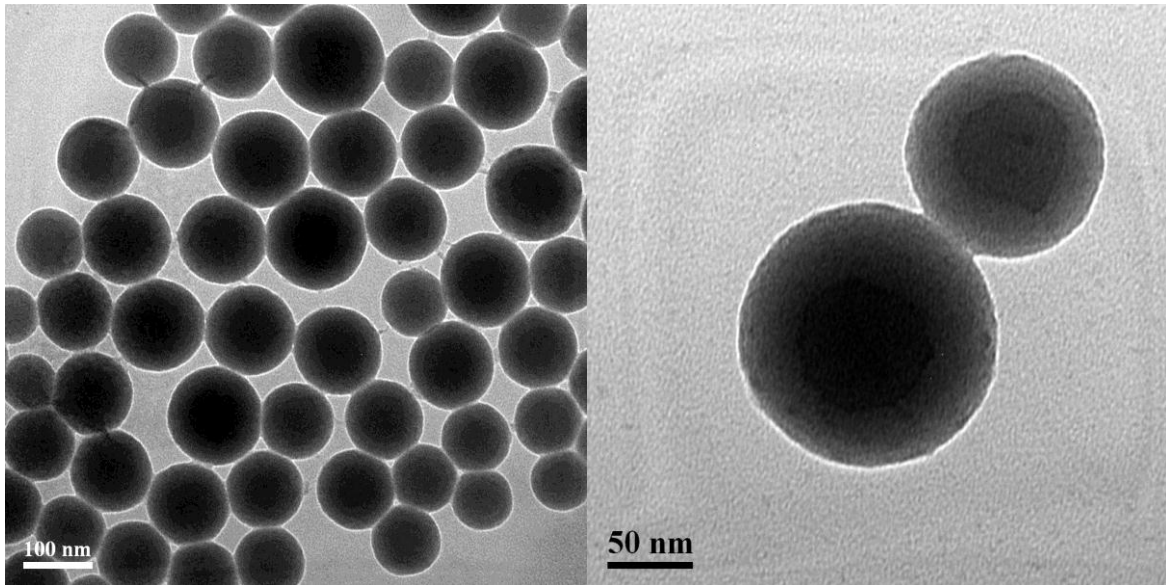


Fig.3.7: HRTEM image of sample C1

3.3.1 Variation of Magnetization with applied field in a superparamagnet

The room temperature hysteresis loops of all the coated and uncoated samples are shown in Fig. 3.8 and 3.9 respectively.

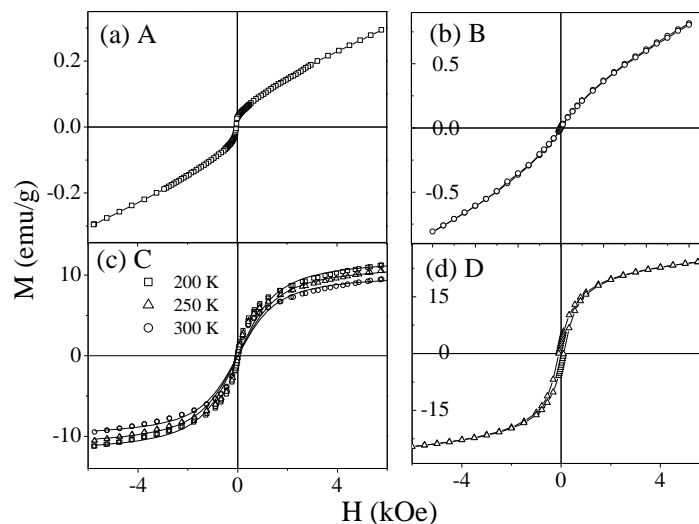


Fig.3.8: Magnetic Hysteresis loops of samples A,B and D at room temperature and that of sample C at 200, 250 and 300 K with theoretical fitting using Eq.(3.5).

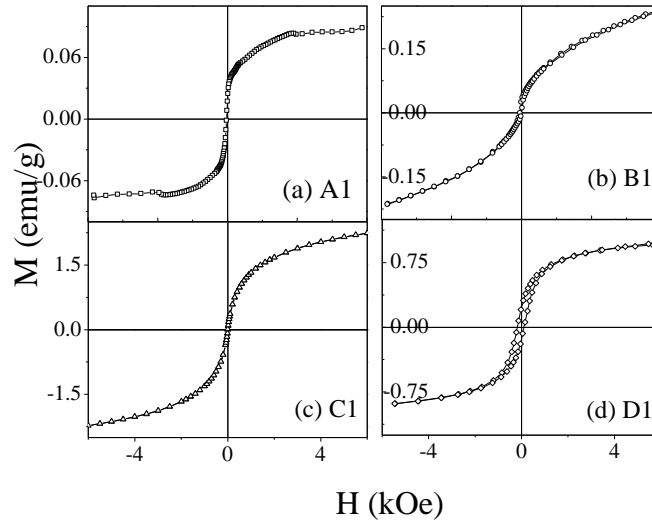


Fig. 3.9: Magnetic Hysteresis loops of samples A1, B1, C1 and D1 at room temperature.

The uncoated samples A, B and C as well as the coated samples A1, B1 and C1 do not show any measurable coercivity, H_c and remanence, M_r indicating the superparamagnetic behavior (described in Chapter 1) at room temperature. But the samples D and D1 exhibit ferromagnetic hysteresis loss with substantial H_c . D1 shows slightly higher H_c (~145 Oe) compared to that of its uncoated counterpart D (~100 Oe). This can be attributed to the higher anisotropy due to larger size of the coated single domain nanoparticles (D1). The saturation magnetization of the samples increases with the increase in annealing temperature.

In superparamagnetic state, the temperature and field dependence of the measured global magnetization $M(T,H)$ and susceptibility $\chi(T,H)$ are similar to those of a classical paramagnet if the atomic moment is replaced by the particle moment. In this state, the magnetic moment of a sample containing N non-interacting particles can be described by the relation [20]

$$M(H) = N\mu_p L\left(\frac{\mu_p H}{k_B T}\right) \quad (3.4)$$

where the Langevin function, $L = \coth(\mu_p H / k_B T) - (k_B T / \mu_p H)$ and each particle have the magnetic moment, $\mu_p = M_s V_p$, M_s and V_p being the bulk saturation magnetization and particle volume respectively. Considering the log-normal distribution function, $P(D)$ for particle size distribution, the average magnetic moment of the sample of mass m and containing N particles of different sizes could be written as [21]

$$M(H) = \int_0^{\infty} xN\mu_p L\left(\frac{\mu_p H}{k_B T}\right) P(D) dD \quad (3.5)$$

where x is the volume fraction of ferrite in the sample, $P(D)$ is the log-normal distribution function of diameter D .

M vs. H experimental data of sample C at three different temperatures 200, 250 and 300K (above its blocking temperatures) have been plotted in Fig.3.8(c) and fitted with Eq.(3.5). At superparamagnetic state the theoretical curve fits the experimental data very well and the most probable size ~ 12.32 nm obtained from the fitting is close to that obtained from the XRD measurement.

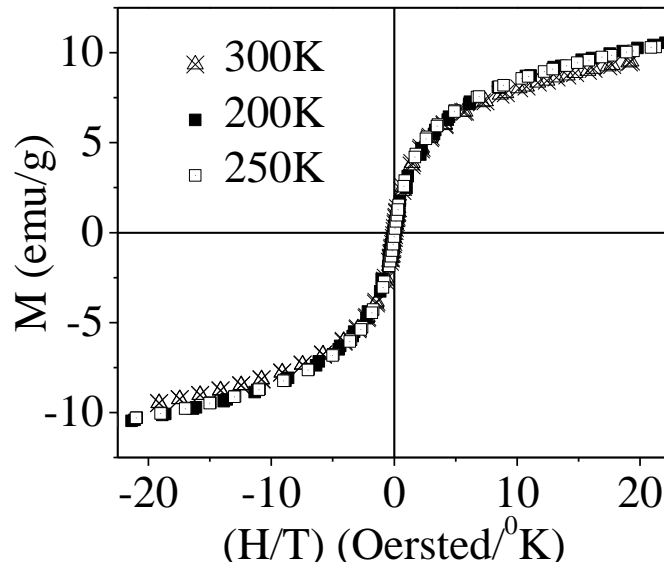


Fig. 3.10: M vs. H/T curves of C at 200, 250 and 300K

M vs. H graphs of sample C at different temperatures are replotted as M vs H/T in Fig.3.10 and they are found to merge with each other further confirming their superparamagnetic nature. This occurs as for all the curves, at a particular field, magnetization M acquires different values because of difference in the measuring temperature, as clear from Fig. 3.8 (c). Hence in these cases the only variable is the temperature at a particular field for a particular sample. As a result when all the curves are scaled with H/T , it is expected that all the curves should coincide with each other which is confirmed for our sample.

At a finite temperature and in absence of any magnetic field, the ferromagnetically aligned magnetic moments within these single-domain particles fluctuate between their two energetically degenerate ground states on a time scale given by [22,23]

$$\tau = \tau_0 \exp\left(\frac{K_{eff}V_p}{k_B T}\right) \quad (3.6)$$

where τ is the relaxation time, τ_0 , a constant estimated to be between 10^{-9} and 10^{-13} and $K_{eff}V_p$, the total anisotropy energy E_A of the particle. In case of $k_B T > K_{eff}V_p$, no hysteresis is observed if the characteristic time of the measuring instrument, τ_m is higher than τ . This is the reason for not observing any measurable coercivity in some samples (Fig.3.8 and 3.9). The blocking temperature T_B of a particle is the temperature at which $\tau = \tau_m$, the measurement time of the instrument. For $\tau < \tau_m$ the system behaves as a superparamagnet. For $\tau > \tau_m$ the system behaves as a ferromagnet.

The temperature dependence of coercivity can be studied for the samples from the hysteresis measurements. In order to find out the temperature dependence of coercivity let us consider an assembly of uniaxial particles with easy axes parallel to z-axis. The assembly is initially saturated in the +z-direction. An external field H is applied along -z direction. Hence each particle moment makes an angle θ with the +z-direction. The total energy per particle is given by [24],

$$E = V(K \sin^2 \theta + HM_s \cos \theta) \quad (3.7)$$

The energy barrier for the reversal is the difference between the maximum and minimum values of E. Hence for extremum of E we have,

$$\begin{aligned} \frac{\delta E}{\delta \theta} &= 2KV \sin \theta \cos \theta - HM_s V \sin \theta = 0 \\ &\simeq \sin \theta = 0 ; \cos \theta = \frac{HM_s}{2K} \end{aligned} \quad (3.8)$$

$HM_s/2K$. Putting the value $\theta=0$ in Eq. 3.7, we have $E = VHM_s$ and putting the value of $\cos\theta$ from above equation again to Eq. 3.7, we have,

$$\begin{aligned}
E &= KV \left[1 - \left(\frac{HM_s}{2K} \right)^2 \right] + \frac{V(HM_s)^2}{2K} \\
&= KV \left[1 + \left(\frac{HM_s}{2K} \right)^2 \right]
\end{aligned} \tag{3.9}$$

The energy barrier for reversal is the difference between the maximum and minimum values of E and is given by,

$$\begin{aligned}
\Delta E &= KV \left[1 + \left(\frac{HM_s}{2K} \right)^2 \right] - HM_s V \\
&= KV \left[1 + \left(\frac{HM_s}{2K} \right)^2 - 2.1 \cdot \frac{HM_s}{2K} \right] \\
&= KV \left[1 - \frac{HM_s}{2K} \right]^2
\end{aligned} \tag{3.10}$$

Hence the anisotropy energy barrier which has to overcome in order to achieve magnetization changes in a magnetic material can be reduced by the application of external field. Particles with size larger than the critical diameter D_c , will not thermally reverse within the measurement time window say 100 second. But when the field is applied, the energy barrier will be reduced to $25 k_B T$, which is evident from Arrhenius law $\tau = \tau_0 \exp(KV/k_B T)$, where τ is the relaxation time, τ_0 is the attempt frequency for non-interacting single domain particles, K is anisotropy constant, V is the volume of the particle and $KV = E$ is the anisotropy energy. Considering relaxation time $\tau = 100$ sec., $\tau_0 = 10^{-9}$ sec., we have $KV = 25 k_B T$ and this will allow thermally activated reversal in 100 sec. This field will be the coercivity H_c and is given by,

$$\begin{aligned}
\Delta E &= KV \left[1 - \frac{HM_s}{2K} \right]^2 = 25 k_B T \\
H_c &= \frac{2K}{M_s} \left[1 - \left(\frac{25 k_B T}{KV} \right)^{\frac{1}{2}} \right]
\end{aligned} \tag{3.11}$$

When V becomes very large or $T \rightarrow 0$, $H_c \rightarrow 2K/M_s$, $2K/M_s$ is the coercivity when the field is unaided by thermal energy. If we denote this limiting value of H_c as $H_c(0)$, then above equation becomes,

$$H_c = H_c(0) \left[1 - \left(\frac{25k_B T}{KV} \right)^{\frac{1}{2}} \right] \quad (3.12)$$

For uniaxial particles of constant size the blocking temperature T_B above which the magnetization is stable can be expressed as, $T_B = \frac{KV}{25k_B}$. Hence equation (3.12) can be written as [25]

$$H_c = H_c(0) \left[1 - \left(\frac{T}{T_B} \right)^{\frac{1}{2}} \right] \quad (3.13)$$

For an assembly of monodispersed, non-interacting, ferro or ferrimagnetically ordered single domain particles, the temperature dependence of coercivity, $H_c(T)$ can be expressed by the above Eq. 3.12. The coercivity H_c increases with the decrease in temperature following Eq.3.13.

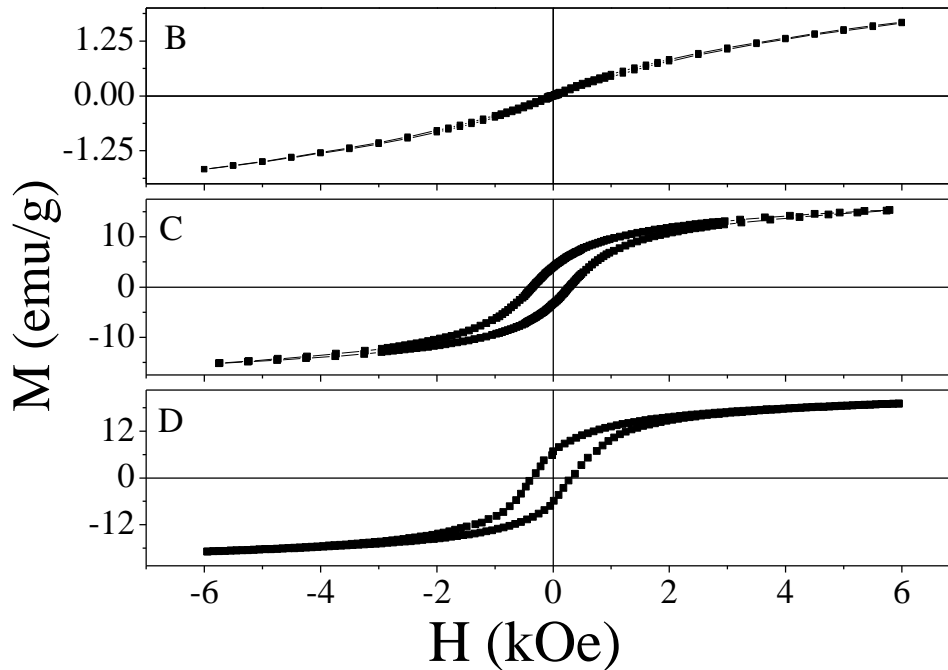


Fig. 3.11 (a): MH loop of B,C and D at 80K

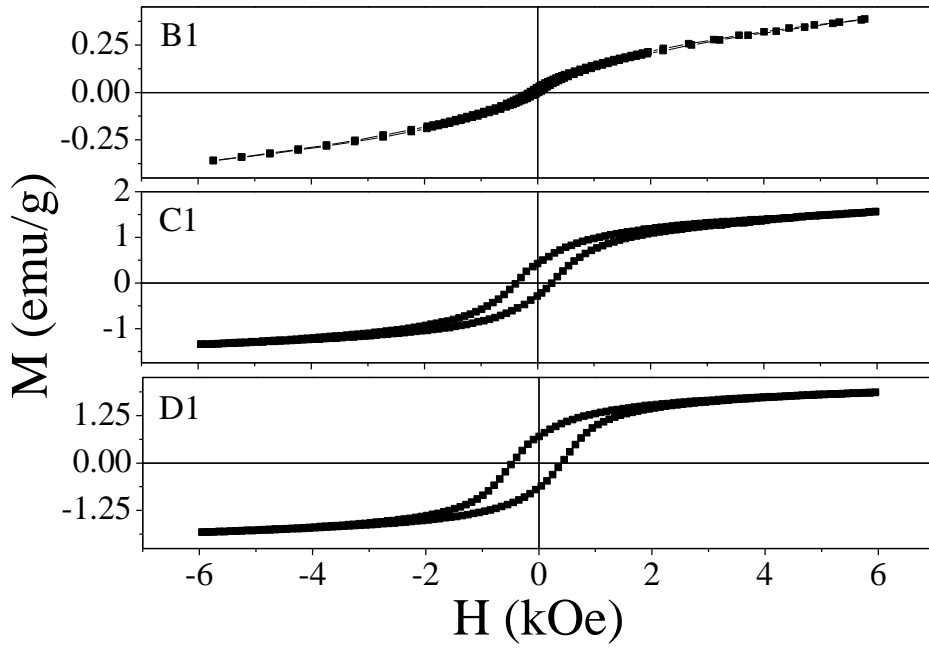


Fig. 3.11 (b): MH loop of B1,C1 and D1 at 80K

The hysteresis loops of sample B, C, D and B1, C1, D1 at 80K are plotted in Fig. 3.11 (a) and 3.11 (b).

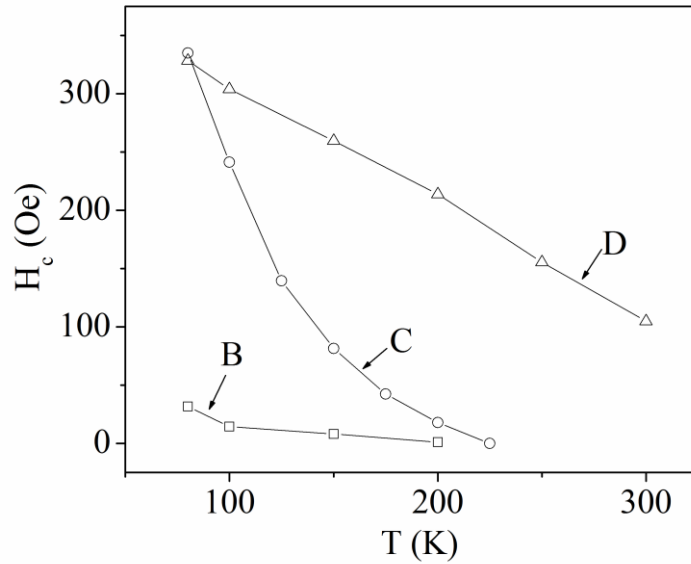


Fig.3.12: Coercive field H_c vs. Temperature, T of sample B, C and D

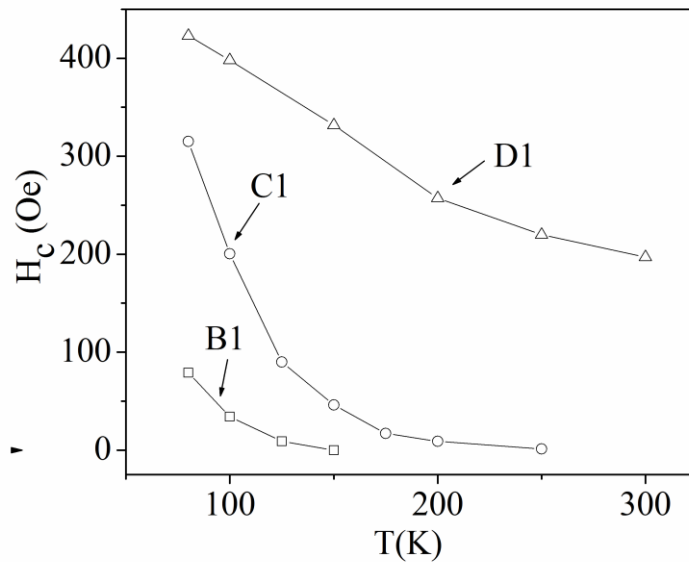


Fig.3.13: Coercive field H_c (T) vs. Temperature, T of sample B1, C1 and D1

Temperature dependence of coercivity H_c of uncoated and coated samples is shown in Fig.3.12 and Fig.3.13 respectively. For all samples, the coercivity H_c increases with the decrease in temperature. Experimental values of $H_c(T)$ are plotted against $T^{1/2}$ in Fig. 3.14 and 3.15. Though in case of uncoated samples, the linearity is observed to some extent, a large deviation is observed for coated samples around their T_B . As both the uncoated and coated particles are present in an agglomerated state the interaction between them might be the reason for the deviation from linearity.

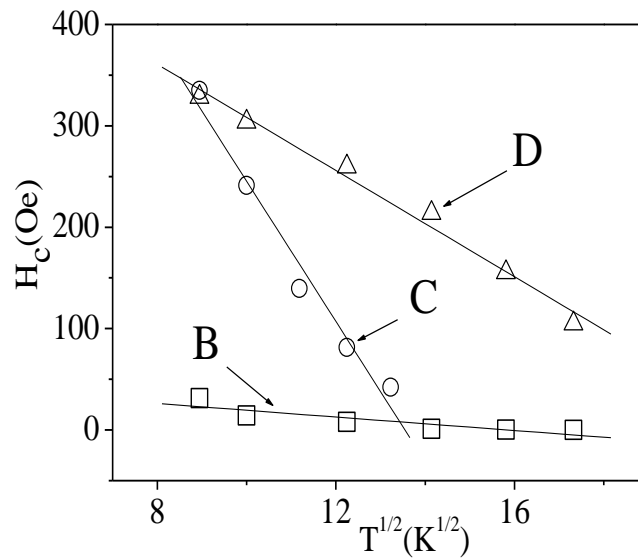


Fig.3.14: H_c (T) vs. $T^{1/2}$ plot of B, C and D.

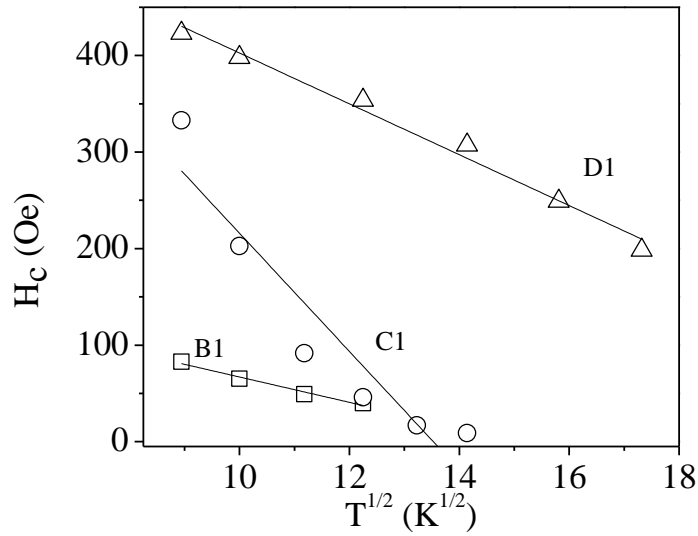


Fig.3.15: $H_c(T)$ vs. $T^{1/2}$ plot of B1, C1 and D1.

3.3.2 Zero field cooled and field cooled dc magnetic measurements

If the sizes of the particles are reduced to a few nanometers they become single domain particles. At a finite temperature and in absence of any magnetic field, the ferro/ferrimagnetically aligned magnetic moments within these single domain particles fluctuate between their two energetically degenerate ground states on a time scale given by Arrhenius law. The blocking temperature T_B of a particle is the temperature at which relaxation time $\tau = \tau_m$, the measurement time of the instrument. The magnetic moment relaxation time τ decreases with the increase in sample temperature. For $T > T_B$, the particles rapidly achieve thermal equilibrium during the measurement time as $\tau < \tau_m$ and the system behaves as a superparamagnet (SPM). On the other hand, at $T < T_B$ the particles are said to be blocked, i.e. their magnetic moments remain at a fixed direction during a single measurement

as $\tau > \tau_m$. Above T_B if all the particles have same volume V , the magnetization of that collection of single domain particles are very similar to that of paramagnetic particles with a large moment i.e. they are superparamagnetic particle.

In order to carry out the zero field cooled (ZFC) magnetic measurement, sample temperature is reduced from room temperature down to 80 K in absence of a magnetic field. The dc magnetization is measured during heating heating the sample in presence of a magnetic field of 100 Oe. For field cooled measurements (FC) sample temperature is reduced from 300K in presence of a field of 100 Oe down to 80 K. DC magnetization is measured during heating the sample in presence of a dc field of 100 Oe. In presence of a low magnetic field FC-ZFC temperature dependent magnetization curves show irreversibility below certain temperature for nanometric samples, which is a signature of superparamagnetism. The experimental data of ZFC and FC magnetization (with $H=100$ Oe) against temperature are plotted in Fig.3.16 and Fig.3.17 for samples A, B, C and A1, B1, C1 respectively. The magnetic signal from samples A and A1 at 100 Oe were very small compared to the sensitivity of our VSM and therefore their results are not presented here.

The ZFC curve shows a peak at a temperature, beyond which they merge with the FC curve. The ZFC peak broadens with the increase in particle size due to wider particle size distributions and more interactions among the particles. For a single nanoparticle, ZFC magnetization increases with T as the small thermal fluctuations help orienting the direction of magnetization towards the field direction [26]. Beyond a certain temperature T_B , called blocking temperature, the thermal energy is more than the anisotropy energy and because of the random thermal fluctuations, magnetization decreases with the increase in temperature. As a particle size distribution is present within a sample, a broad peak is observed instead of a sharp peak near T_B . For FC measurement, magnetization continuously decreases with the increase in T . In this case, the magnetization was initially oriented along the direction of H and higher thermal fluctuations at higher T reduces the component of magnetization along the

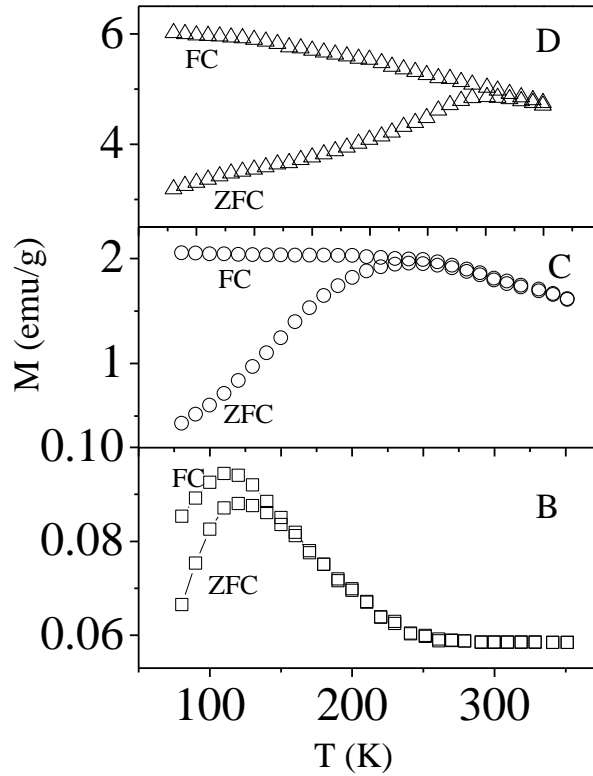


Fig.3.16: Zero field cooled (ZFC) and field cooled (FC) magnetization ($H = 100$ Oe) vs. temperature curves of samples B, C, D.

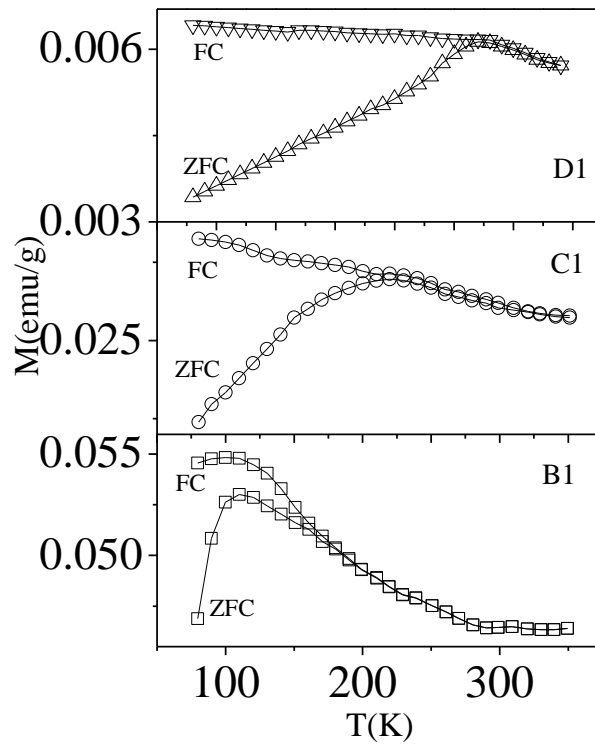


Fig. 3.17: Zero field cooled (ZFC) and field cooled (FC) magnetization ($H = 100$ Oe) vs. temperature curves of samples B1, C1, D1.

direction of H. So at low enough temperature the FC magnetization curve shows higher value and decreases with increase in temperature.

The temperature corresponding to the peak value of the ZFC curve is considered as the blocking temperature, T_B of the sample above which it behaves as a superparamagnetic material. In case of uncoated samples, T_B increases from $\sim 119\text{K}$ for sample B to $\sim 345\text{K}$ for sample D. For coated samples, it changes from $\sim 110\text{K}$ for B1 to $\sim 320\text{K}$ for D1. The lower blocking temperature of the coated samples can be attributed to the increase in the inter-particle separation (due to SiO_2 shell) that reduces the magnetic dipole-dipole interaction. The ZFC M-T curves merge with the FC curve beyond T_B . The ZFC peak broadens with the increase in particle size due to wider particle size distributions and more interactions among the particles.

3.3.3 Dynamic properties of NiFe_2O_4

The dynamic hysteresis loops of the samples C and D recorded at room temperature in the frequency range of 20 Hz - 650 Hz is shown in Figure 3.18 and 3.19.

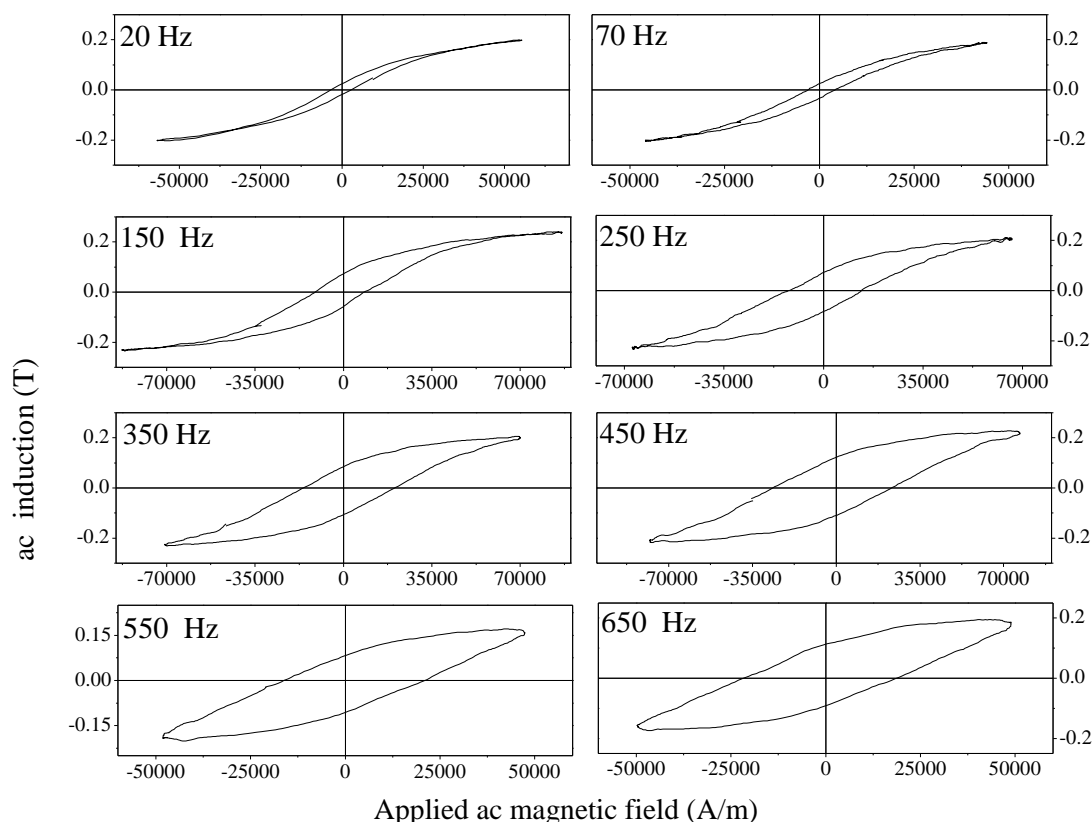


Fig. 3.18: ac hysteresis loops observed at different frequency of the nanoparticles of sample C.

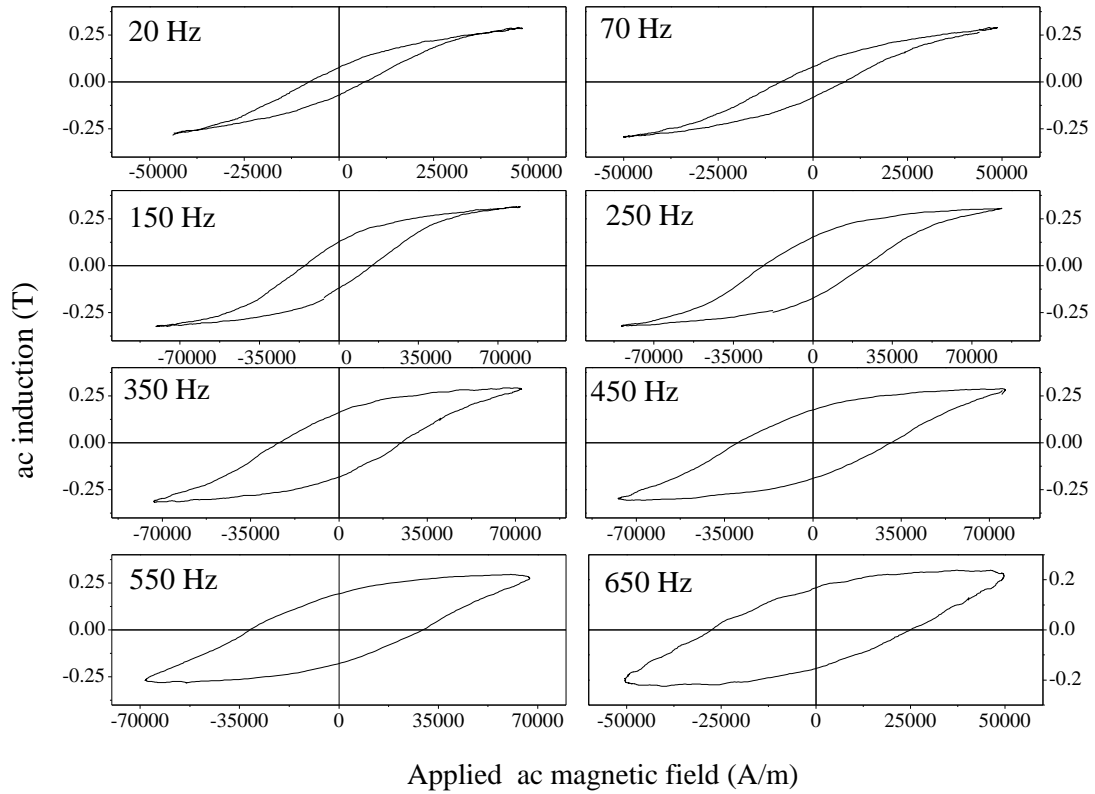


Fig. 3.19: ac hysteresis loops observed at different frequency of the nanoparticles of sample D.

In case of the coated samples and sample A, B the magnetization was so low that it was within the error bar of our home-made set up. Hence we have not presented it in this thesis. The home-made set up used for measuring the ac hysteresis loops has been described in Chapter 2.

It is observed that the hysteresis loops of sample C have smaller area than that of sample D. The particles of sample C have size of ~ 14 nm and that of D have a size of ~ 32 nm. The dc hysteresis loop of sample C at room temperature has zero coercivity whereas that of sample D shows some coercivity. Hence the relaxation time of particles of sample C is much faster than that of D. That is why the coercivity of the hysteresis loops of sample C at different frequencies is lesser than that of sample D.

It is also observed that the area of the loops increases with increase of frequency. In case of sample C the coercivity increases from 3066 A/m at 30 Hz to 20286.85 A/m at 650 Hz. In case of sample D the coercivity increases from 7318.2 A/m at 30 Hz to 26254.64 A/m at 650 Hz. For nanoparticle system with uniaxial anisotropy, the energy barrier, which separates the two easy directions of magnetization, may be smaller than the thermal energy

even at room temperature, which leads to spontaneous fluctuation of the magnetization direction having a relaxation time given by

$$\tau = \tau_0 \left(\frac{K V}{k_B T} \right) \quad (3.14)$$

where τ_0 ($10^{-9} - 10^{-10}$ s) is the inverse of the natural frequency of the gyromagnetic precession, K is the anisotropy energy constant, V is the volume of the particle, k_B is the Boltzmann constant and T is temperature in Kelvin [22]. With the increase of frequency the measuring time of the instrument decreases i.e. $\tau \gg \tau_m$ where τ_m is the measuring time of the instrument. Due to this fact ac hysteresis loops become wider and wider i.e. the coercivity increases with the increase in the applied frequency.

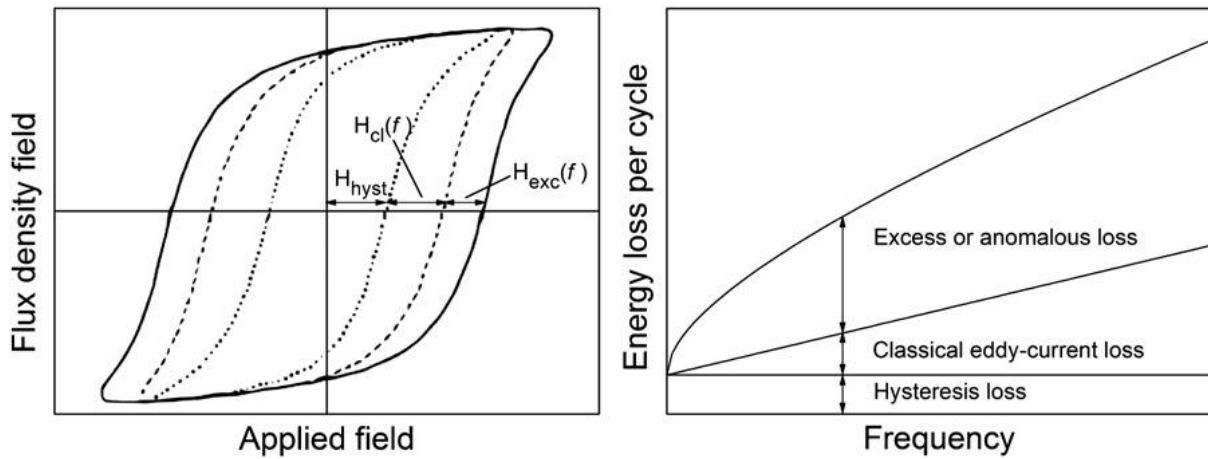


Fig.3.20: Left: contributions to the coercivity in the hysteresis loop—static hysteresis, classical eddy currents and anomalous or excess field (modified from Ref.[27]). Right: contributions to the energy loss per cycle as a function of the frequency of the magnetizing field.

Particles which are SPM at a given frequency say, 10 Hz may behave as ferrimagnetic particles at higher frequency say, 100 Hz. Thus once we increase the frequency, the number of SPM particles decreases and at the same time the number of ferrimagnetic particles increases. The coercive field or coercivity (H_c) is defined as the field at which the magnetization is reduced from remanence to zero. For a magnetization loop with peak magnetization M_{max} , $4H_c M_{max}$ gives the order of magnitude of the loop's area. Thus, H_c is a measure of the energy that is dissipated as heat in each magnetization cycle. The losses can be conventionally divided into three categories: hysteresis, classical eddy current and anomalous or excess components (Fig. 3.20) [27].

This division is artificial, since they actually do not arise from different sources, but allows treating loss mechanisms occurring on different space–time scales separately as if they were independent of each other. Hysteresis loss is due to the Barkhausen jumps between local energy minima. It is determined from the area of the static hysteresis loop and is assumed to be independent of the frequency of magnetization. The classical eddy current loss per cycle, which varies linearly with frequency, can be calculated from Maxwell’s equations for a perfectly homogeneous material with no domain structure, where the boundary conditions of the problem are given by the geometry of the specimen. The so called anomalous or excess loss increases with frequency but not linearly; it usually exhibits a rapid increase at low frequencies and then an almost constant positive slope. This component appears because the classical calculation of eddy current loss ignores the presence of domains and domain wall motion, which is damped by the eddy currents.

The continuous increase of coercivity with increasing frequency was due to the eddy currents [28]. When a magnetic field H_a is applied along a body, a flux density field B is induced in the material. If H_a varies with time, B and therefore the flux (Φ) vary as well through the cross- section of the body. Thus, according to Faraday’s law, an electromotive force (emf) will be induced in the specimen proportional to $d\Phi/dt$. If the material is a conductor, this emf will cause an eddy current. The flux rate will increase when the frequency of H_a will be increased. During each cycle, as H_a increases, the eddy currents generate a magnetic field (H_{ec}) antiparallel to H_a . The resulting field will be the sum of both fields, H_a and H_{ec} . It follows that the true field acting on the material in the interior of the specimen, where the contributions of all the eddy currents are added, becomes weaker. Hence higher the frequency, larger the eddy currents and H_{ec} . That is why the measured H_c was found to increase with increasing frequency.

To study the frequency dependence of coercivity we have plotted $\log H_c$ vs $\log f$ for both the samples in Fig. 3.21 (a) and (b). The slope of the graph (Fig. 3.22 (a) and (b)) gives the power of the frequency. In case of sample C we observe that the value of $n=0.48$ and for sample D $n=0.74$. Hence in case of sample C coercivity varies as square root of frequency. The total coercivity or loss has been sometimes approximated to one frequency dependent term f^n [29,30]. Evolution in the domain structure and the increase in the activity of domain walls with increasing frequency were observed [31,32] and are the cause for the non-linear dependence of H_c and losses with increasing frequency.

$$H_c = f^n \quad (3.15)$$

$n=0.48$ suggests domain wall damping due to eddy currents. The particles in sample C are present in an agglomerated form. Hence although they are single domain the contribution of domain wall might arise because of the agglomeration.

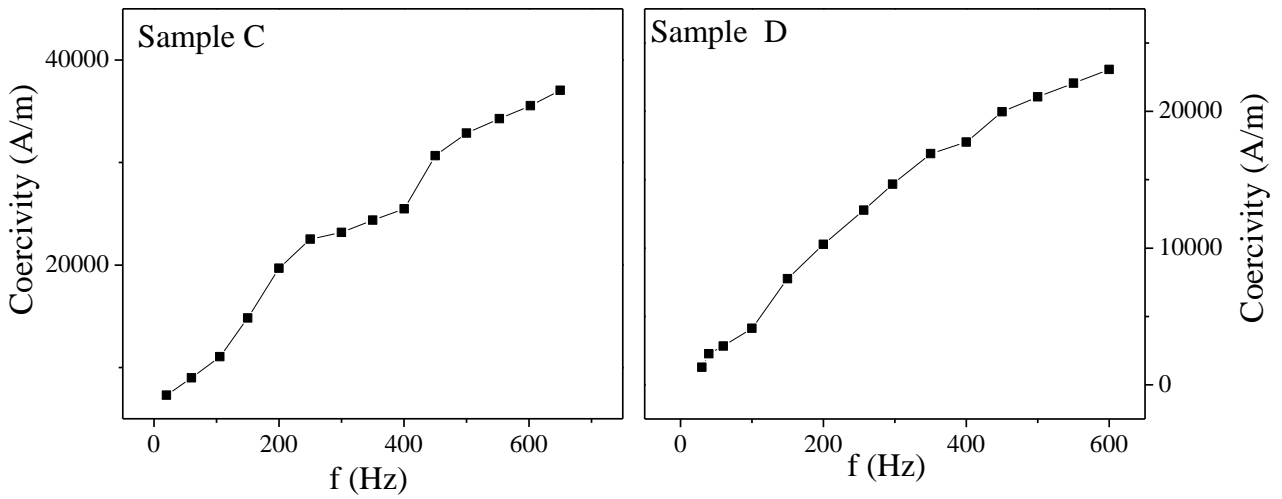


Fig. 3.21: (a) Coercivity vs f of sample C (b) Coercivity vs f of sample D

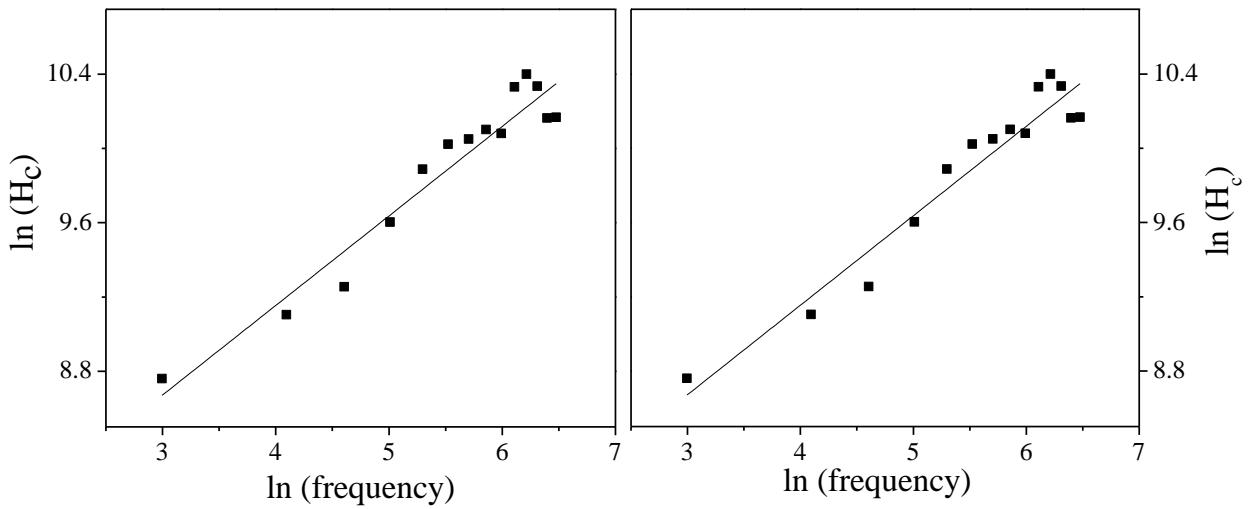


Fig. 3.22: (a) ln(Coercivity) vs. ln(f) plot of sample C with linear fitting
(b) ln(Coercivity) vs. ln(f) plot of sample D with linear fitting

3.4 Magnetic properties of nanostructured NiFe_2O_4 synthesized by solvothermal technique and its application for Gas sensing

3.4.1 Synthesis of nanostructures of NiFe_2O_4 by the solvothermal technique

All the chemicals used were analytically pure and used without further purification. $\text{NiCl}_2 \cdot 6\text{H}_2\text{O}$ and $\text{FeCl}_3 \cdot 4\text{H}_2\text{O}$ were dissolved in distilled water in stoichiometric ratio. A 5 M solution of NaOH was added drop by drop to the mixture to adjust the pH of the solution to 12 so that the reaction takes place in a basic medium. This sample was termed Sample A. In the second case (Sample B) the salts were dissolved in a mixture of Ethylene Glycol and water in the ratio of 7:2. A 5M solution of NaOH was added drop by drop to the mixture to adjust the pH of the solution to greater than 10 so that the reaction takes place in a basic medium. In both cases the mixture was transferred into a Teflon-lined steel autoclave. The autoclave was sealed and then heated at a temperature of 240°C for 12 hours. The chamber was then cooled naturally to room temperature. The product thus obtained was washed in double distilled water and dried at 60°C for 8 hours.

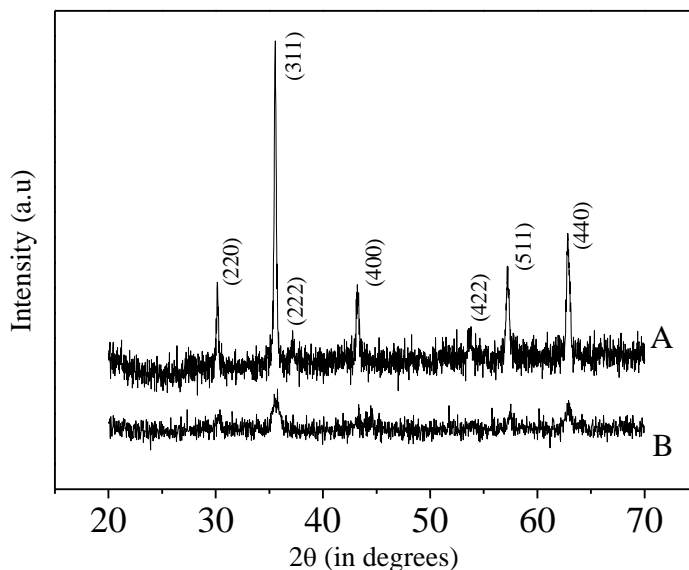


Fig. 3.22: X ray diffraction of samples A and B.

The x-ray diffraction patterns of samples A and B are shown in Fig.3.22. All the observed peaks confirmed the formation of spinel NiFe_2O_4 from the JCPDS data. The average crystallite size was calculated using the Scherrer formulae (as discussed in Chapter

2). The peaks of sample B were much broader than that of sample A implying that the particles of sample B was much smaller than that of sample A.

The Field Emission Scanning Electron Microscope images of the samples are shown in Figure 3.23 (a) and Figure 3.23(b). Figure 3.23 (a) shows the images of the particles of sample A. The particles are cubic in shape having size distribution of 60 nm to 80 nm. Water is more polar than a mixture of water and ethylene glycol in the ratio (2:7). Polar solvents are more prone to form non isotropic structures since the easy axis of growth will be less. Hence cubic structures are formed [33]. Figure 3.23 (b) shows the image of sample B and their diameter varies from 10 nm to 30 nm and were almost spherical in shape.

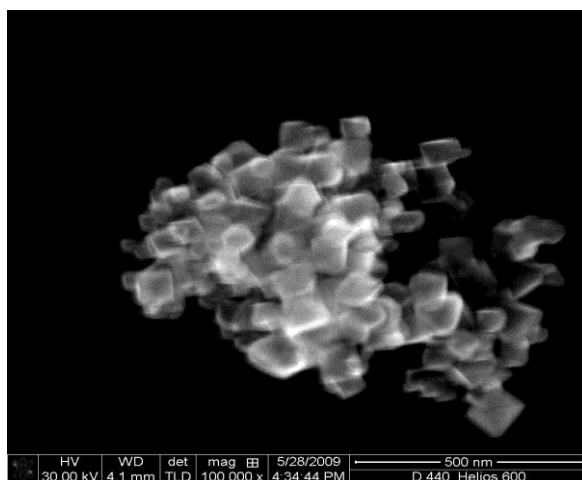


Fig. 3.23 (a): Field Emission Scanning Electron Micrographs of sample A.

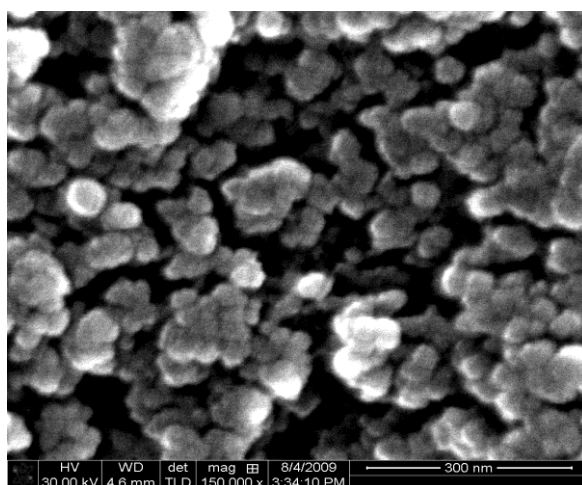


Fig. 3.23 (b): Field Emission Scanning Electron Micrographs of sample B.

In this case Ethylene Glycol acted as a capping agent. Presence of Ethylene Glycol arrested the growth of the particles and increased the nucleation rate. This resulted in the sufficient decrease in size of the particles in sample B compared to that of sample A. Since capping takes place from all sides and the growth is also arrested, spherical particles were obtained.

The M vs H loops of the samples are shown in Figure 3.24. Sample A shows Ferromagnetic hysteresis loop whereas sample B shows a loop which is nearly superparamagnetic. The coercivity of sample B is much smaller than that of sample A (60.7 Oe). It shows that as the particle size decreases the coercivity also decreases.

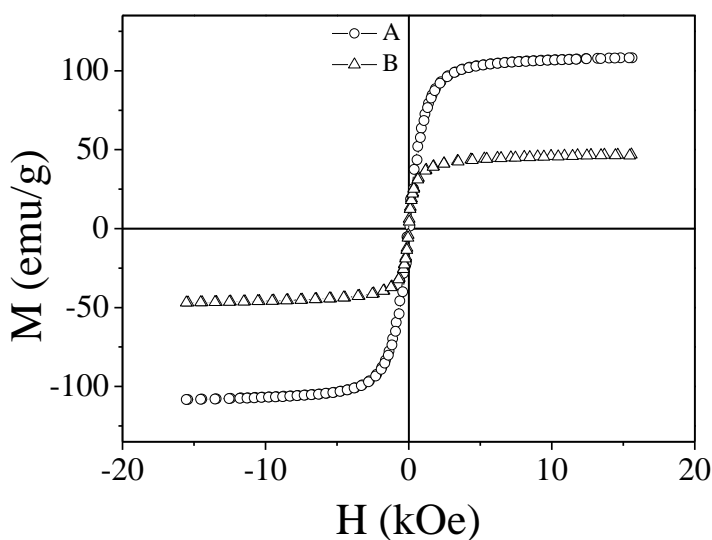


Fig. 3.24: Hysteresis loops of sample A and B.

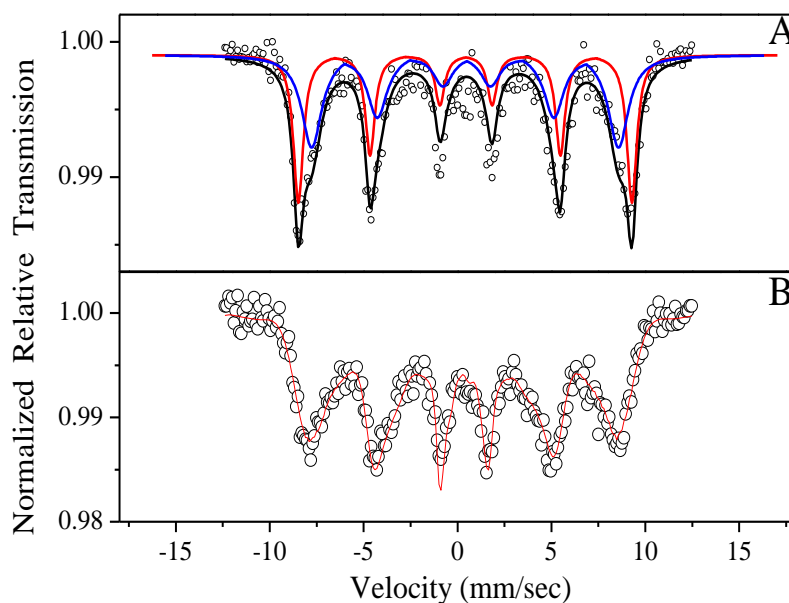


Fig. 3.25: Mossbauer spectra of sample A and B.

The Mossbauer spectra of the two samples are shown in Fig. 3.25. Sample A shows two well resolved sextets. This is consistent with a ferrimagnetic structure [34] and the two sextets signify the tetrahedral and octahedral iron sites. For exact inverse spinel the stoichiometry of $\text{Fe}^{3+}(\text{A}):\text{Fe}^{3+}(\text{B})$ is 1. But here the ratio is 1:3. This implies that Fe^{3+} is more populated in A site than in the B site. The spectrum of sample B shows relaxation in consistent with the fact that particle size of sample B is ~40 nm. This proves that the particles are nearing the superparamagnetic regime. Besides the average hyperfine field of sample B is 461 kOe which is different than that of sample A which is 507 kOe for the B site and 551 kOe for the A site.

3.4.2 Gas Sensing properties of NiFe_2O_4

Different spinel ferrites such as NiFe_2O_4 , CdFe_2O_4 , ZnFe_2O_4 and CuFe_2O_4 have been studied for various gas-sensing applications [35-38]. Nickel Ferrite (NiFe_2O_4) has been widely studied as a magnetic material [39,40] but information related to its gas-sensing properties towards reducing gases is still limited. Interestingly, nickel ferrite is reported to show sensitivity towards oxidizing gas like chlorine as well as reducing gases like hydrogen sulfide, acetone and LPG. The gas sensing is a surface phenomenon of gas–solid interaction, where the conductivity of semiconducting oxides can be altered by adsorption of gases from ambient. It is well known that depending upon the morphology and operating temperatures; the oxide surface hold various oxygen species, such as O^- , O^{2-} , O_2^- . Their number and distribution also plays an important role in the gas sensing characteristics. The literature shows that the metal oxide nanoparticles enhance the sensitivity of a gas sensing material, while the selectivity is achieved by doping on surface or in the volume. However, recently Korotcenkov [41] suggested that the shape control of the nanocrystallites can provide energetically different adsorption sites for the test gases on different crystal facets. Thus existence of large surface to volume ratio in the typical nanostructured material facilitates better response towards specific gases. Moreover, morphology and particle size of nanomaterials depend upon their method of preparation and sintering temperatures, and hence one can observe different responses towards gases for the similar composition.

The gas-sensing characteristics were recorded with reference to time at different operating temperatures and a fixed gas concentration of 1000 ppm. The change in electrical current was used as a measure of gas response at various temperatures. The gas sensitivity (S) is calculated as follows:

$$Sensitivity(S) = \left(1 - \frac{I_{gas}}{I_{air}}\right) * 100 \quad (3.25)$$

where, I_{air} = Current of the sample in air, I_{gas} = Current of the sample in the test gas.

To investigate gas-sensing properties, the crystalline nanosized $NiFe_2O_4$ powder was made in the form of pellets. The pellets of diameter 10 mm and thickness 3 mm were made under pressure of 7.5 tons using hydraulic press. These pellets were then subjected for studying their sensitivity and selectivity at the different controlled temperatures towards LPG gas in the setup which is described in Chapter 2.

Figure 3.26 shows the gas sensing measurements for LPG gas at temperatures $100^{\circ}C$, $150^{\circ}C$, $200^{\circ}C$ and $250^{\circ}C$. The gas-sensing mechanism is likely based on the changes in conductance of $NiFe_2O_4$ [42]. The oxygen adsorbed on the surface of the material influences the conductance of the $NiFe_2O_4$ based sensor. The amount of oxygen on the surface of the material depends on the particle size, morphology, and specific area of the material, and also on the operating temperature of the sensor [43]. With increasing the temperature in air, the state of oxygen adsorbed on the surface of $NiFe_2O_4$ undergoes the following reactions: $O_{2(gas)} \Rightarrow O_{2(ads)} \Rightarrow O_{2^{-}ads} \Rightarrow 2O^{-}_{(ads)} \Rightarrow 2O^{2-}_{(ads)}$. The oxygen species capture electrons from the material, leading to the changes in hole or electron concentration in the $NiFe_2O_4$ materials. Reducing gases react with the oxygen adsorbed and the electrons captured by the oxygen adsorbed, resulting in an increase in the conductance of the n-type $NiFe_2O_4$ and a decrease in conductance of the p-type $NiFe_2O_4$.

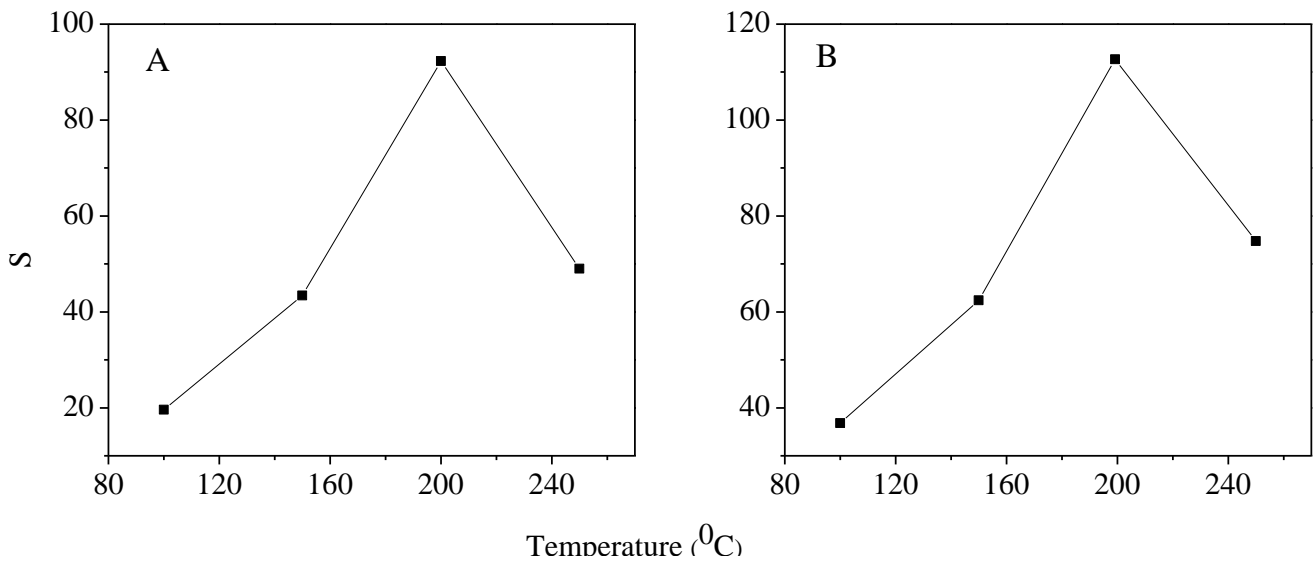


Fig.3.26: Sensitivity vs. temperature

It is observed that the NiFe₂O₄ nanoparticles A and B show good sensitivity towards LPG gas with the spherical particles being more sensitive than the cubic particles. In both cases the maximum sensitivity is obtained at 200⁰C. The spherical particles are more sensitive than the cubic shaped particles. The structural features of the nanoscale ferrite complicate the sensing activities, as it involves size, crystallite shape, phase composition, mixed valence and its surface architecture. Hence we get different sensitivities of the spherical and cubic particles.

3.5 Conclusions

NiFe₂O₄ nanoparticles with size from ~ 4 to ~32 nm have been prepared by coprecipitation method using a micelle (TX-100). The ferrite nanoparticles were coated by SiO₂ following the Stöber method. Superparamagnetic properties were observed at room temperature when the particle size of uncoated samples was around or less than 15 nm. The blocking temperatures of the coated samples were less than that of the corresponding uncoated samples. This can be attributed to the increase in the interparticle separation (due to SiO₂ shell) that reduces the magnetic dipole-dipole interaction. The hysteresis loops of the uncoated NiFe₂O₄ nanoparticles were measured in the frequency range of 20 - 650 Hz. The area of the hysteresis loops increased with the increase of frequency because of the eddy current loss. The dynamic coercivity of these nanoparticles could be well fitted as proportionality of H_c vs. f^{1/2}. The Nickel Ferrite nanoparticles with different morphologies have also been synthesized by the hydrothermal synthesis. Morphology was found to vary with the polarity of the solvent. The particles tend towards superparamagnetism with decrease in size and polarity. Mossbauer spectroscopy revealed the fluctuating nature of the spherical particles. Gas sensing measurements of differently shaped nanoparticles was performed in the presence of 1000 ppm of LPG gas. It was observed that maximum sensitivity was obtained at 200⁰C for the spherical shaped particles.

References

- [1] R.F. Service, *Science* **287**, 1902 (2000).
- [2] V.K. Babbar, J.S. Chandel, S.P. Sud, *J. Mat. Sci. Lett.* **14**, 11 (1995).
- [3] A.L. Paul, G.R. Chandra, et. al., *J. Magn. Magn. Mater.* **225**, 301 (2001).
- [4] J. Halavaara, P. Tervahartiala, et al., *Acad. Radiol.* **43**, 180 (2002).
- [5] D.-H. Chen, M.-H. Liao, *J. Mol. Catal. B Enzym.* **16**, 283 (2002).
- [6] F. Sauzedde, A. Elaissari, C. Pichat, *Macromol. Ymp.* **151**, 617 (2000).
- [7] A.R. Varlan, W. Sansen, L.A. Van, M. Hendrickx, *Biosens. Bioelectron.* **11**, 443 (1996).
- [8] F. Schüth *et al.* *Angew. Chem. Int. Ed.* **46**, 1222, (2007).
- [9] M. Mandal *et al.* *J. of Colloid and Interface Science* **286**, 187 (2005).
- [10] S. Baea, S. W. Lee, and Y.T. Ann, *Appl. Phys. Lett.* **89**, 252503 (2006).
- [11] Vijutha Sunny, Philip Kurian, P. Mohanan, P. A. Joy, M. R. Anantharaman , **489**, 297, (2010).
- [12] C.R. Vestal and Z.J. Zhang *Nano Letters* **3**, 1739 (2003).
- [13] H. Zeng , S.Sun , J.Li ,Z.L Wang and J.P. Liu *Appl.Phys. Lett.* **79**, 1501 (2001).
- [14] C.Lin , C.Wang and I.H Chen *J. Appl. Phys.* **99**, 08N707 (2006).
- [15] M. Ammar , F. Mazaleyrat , J.P Bonnet , P. Audebert ,A. Brosseau ,G. Wang and Y. Champion *Nanotechnology* **18**, 285606 (2007).
- [16] J.P. Chen, C.M. Sorensen, K.J. Klabunde, G.C. Hadjipanayis, E. Devlin, A. Kostikas, *Phys. Rev. B* **54**, 9288 (1996).
- [17] S.H. Im, T. Herricks, Y.T. Lee., Y. Xia, *Chem. Phys. Lett.* **401**, 19 (2005).
- [18] S. Zhang, D. Dong, Y. Sui, Z. Liu, H. Wang, Z. Qian, W. Su, *J. Alloys Compd.* **415**, 257 (2006).
- [19] G. Mitrikas, C.C. Trapalis, N. Boukos, V. Psyharis, L. Astrakas and G. Kordas, *J. Non-cryst. Solids* **224**, 17 (1998).
- [20] S. Chikazumi, *Theory of Ferromagnetism* (John Wiley & Sons., New York, 1964).
- [21] S. Chakraverty, K. Mandal, S. Mitra, S. Chatterjee, S. Kumar, *Jpn. J. Appl. Phys.* **43**, 7782 (2004).
- [22] L. Néél, *Ann. Geophys.* **5**, 99 (1949).
- [23] L. Néél, and C.R. Acad. Sci., Paris **228**, 66 (1949).
- [24] B. D. Cullity, *Introduction to magnetic materials* (Addison-Wesley, Reading, Massachusetts, 1972), p.385.

- [25] F.C. Fonseca, G.F. Goya, R.F. Jardim, R. Muccillo, N.L.V. Carreno, E. Longo and E.R. Leite, *Phys. Rev. B* **66**, 104406 (2002).
- [26] S. Mitra, K. Mandal, P. Anil Kumar *J. of Magnetism and Magnetic Materials* **306**, 254 (2006).
- [27] G. Bertotti, *Hysteresis in Magnetism: For Physicists, Materials Scientists, and Engineers*, Academic Press, San Diego, 1998.
- [28] S. Chakraborty, K. Mandal, D. Sarkar, V. J.Cremaschi, J. M. Silveyra *Physica B* **406**, 1915 (2011).
- [29] K. Mandal and S.K. Ghatak *Journal of Magnetism and Magnetic Materials* **118**, 315 (1993).
- [30] E.M. Gyorgy, *Metallic Glasses, Magnetic properties*, in: *Proceedings of the American Society for Metals. Seminar on Metallic Glasses*, Metals Park, Ohio, 1978.
- [31] W.J. Yuan, S.J. Pang, F.J. Liu, T. Zhang, *J. Alloys Compd.* **5045**, S142 (2010).
- [32] P. Vavassori, F. Ronconi, M. Traldi, E. Puppini, *J. Magn. Magn. Mater.* **177–181**, 127 (1998).
- [33] A. Chaudhuri, S. Mitra, M. Mandal, K. Mandal, *J. Alloys Compd.* **491**, 703 (2010).
- [34] Marco DM, Wang XW, Snyder RL, Simmins J, Bayya S, White M, and Naughton MJ *J. Appl. Phys.*, **73**, 6287 (1993).
- [35] T.S. Zhang, P. Xing, J.C. Zhang, L.B. Kong, *Mater. Chem. Phys.* **61**, 192 (1999).
- [36] C.V. Gopal Reddy, S.V. Manorama, V.J. Rao, *Sens. Actuators B* **55**, 90 (1999).
- [37] J. Azadmanjiri, S. Ebrahimi, H. Salehani, *Ceram. Int.* **33** (2007) 1623–1625.
- [38] E. Comini, M. Ferroni, V. Guidi, G. Fagila, G. Martinelli, G. Sberverglieri, *Sens. Actuators B* **84** (2002) 26–32.
- [39] S. Ziemniak, L. Anovitz, R. Castelli, W. Porter, *J. Phys. Chem. Solids* **68** (2007) 10–21.
- [40] J. Jiang, Y. Yang, *Mater. Lett.* **61** (2007) 4276–4279.
- [41] G. Korotcenkov, *Sens. Actuators B* **107** (2005) 209–232.
- [42] L. Satyanarayana et al. *Materials Chemistry and Physics* **82** (2003) 21–26.
- [43] C. Xiangfeng et al. *Sensors and Actuators B* **123** (2007) 793–797.

Chapter 4

4 Synthesis of single domain CoFe_2O_4 nanoparticles and study of the influence of micelle on its magnetic properties

4.1 Preamble

CoFe_2O_4 nanoparticles, has long been of intensive importance in the fundamental sciences and technological applications in various fields of electronics [1], photomagnetism [2], catalysis [3], ferrofluids [4], hyperthermia [5], cancer therapy [6], and molecular imaging agents in magnetic resonance imaging (MRI) [7]. The applications of CoFe_2O_4 are strongly influenced by its magnetic properties. For biomedical applications, CoFe_2O_4 nanoparticles are required to have a narrow size distribution, high magnetization values, a uniform spherical shape, and superparamagnetic behavior at room temperature. Magnetic nanoparticles because of the high surface to volume ratio have high surface energy and hence agglomerate with each other [8]. But for in vivo biomedical use these iron oxide nanoparticles must be small enough (≤ 100 nm) to avoid detection by the immune system, to be circulated through the blood stream and should be stable enough to remain in the body for a sufficient time. Hence we need to remove the agglomeration of nanoparticles so that it can be useful for biological applications. On the other hand nanoparticles below a critical size becomes single domain. If we can prepare such nanoparticles which are single domain as well as show huge coercivity then they can be very useful in memory devices which require huge amount of data to be stored in very small amount of space. The coercivity of magnetic nanoparticles depends on several parameters such as particle size and its distribution, shape, anisotropy, strain, surface spins, interaction between the particles etc. [9-12]. A number of efforts [13-16] have been made to increase the coercivity of cobalt ferrite nanoparticles as discussed in Chapter 1 Hence from many references we see that coercivity is not constant for a fixed size and critical single domain size also differ. Hence size is not only a crucial point, there are some other parameters too influencing the magnetic properties in case of nanoparticles. We have

synthesized CoFe_2O_4 nanoparticles by wet chemical route using micelles as capping agent and obtained a high coercivity of ~ 4.4 kOe at room temperature (RT) for the as synthesized particles of diameter ~ 16 nm. We have also investigated the reason behind the huge coercivity.

4.2 Synthesis of nonagglomerated CoFe_2O_4 nanoparticles

$\text{FeCl}_3 \cdot 6\text{H}_2\text{O}$ and $\text{CoCl}_2 \cdot 6\text{H}_2\text{O}$ taken in stoichiometric ratio were dissolved in a solvent composed of 40 ml of distilled water and 20 ml of ethanol. Now 4 gm of Sodium Oleate and 4 ml of Olyl Amine were added into the above solution with stirring for 2 hours. The precursor solution was then added into a Teflon lined steel autoclave of capacity 80 ml. The Teflon chamber was kept at 180°C for 12 hours to crystallize the particles. After that the autoclave was cooled to room temperature naturally. The products were separated from the final reaction solution by the addition of hexane [17]. The as prepared cobalt ferrite could be deposited by adding ethanol and obtained by centrifugating at a high speed without any size-selection process. Concentration of Olyl amine and Sodium Oleate were varied to obtain particles of different size. We have prepared three sets of samples and named them as follows. Sample A was prepared using 4 gm of Sodium Oleate, 4ml of Olyl Amine. Sample B was prepared using 2 gm of Sodium Oleate, 2 ml of Olyl Amine. Sample C was prepared using 1 gm of Sodium Oleate and 1 ml of Olyl Amine.

4.3 Synthesis of micelle coated CoFe_2O_4 nanoparticles

Cobalt-ferrite nanoparticles were prepared by wet-chemical route in micellar medium of TX-100 using sodium hydroxide as co-precipitating agent. Cobalt chloride and Ferric ammonium sulfate salts were used as sources of Co^{+2} and Fe^{+3} respectively. These salts were taken in 1:2 molar ratios and were dissolved in TX-100 micellar medium. The mixture was heated and stirred. The temperature of the mixture was controlled by thermostat and was observed by a thermometer and when the temperature reached at 65 to 70°C , the sodium hydroxide was added to it drop by drop keeping the flow rate constant under the same stirring and heating condition [18]. Initially the solution turned into reddish brown color and became black after boiling the solution for 1 hr. The particles were separated from the mixture by the method of centrifugation and purified by washing the particles several times by water. The as-prepared

sample was annealed at different temperatures varying from 523 to 1473K for 2 hours each to obtain the particles of various grain sizes.

4.4 Results and Discussions

The X Ray Diffraction (XRD) of the CoFe_2O_4 samples A, B and C is shown in Fig. 4.1. All the observed peaks showed the formation of pure phase CoFe_2O_4 . As the quantity of Olyl amine and sodium oleate decreases the particle size increases. It also shows that the peaks obtained are very broad which is a signature of nanocrystallinity. The average grain size as calculated from the scherrer formulae for sample A, B and C are $\sim 8 \pm 2\text{nm}$, $\sim 16 \pm 2\text{ nm}$ and $\sim 24 \pm 2\text{ nm}$ respectively.

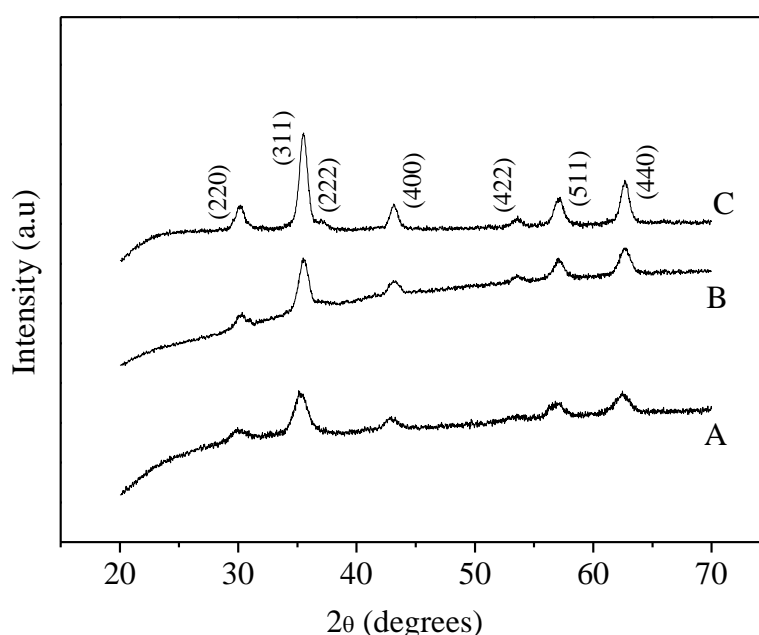


Fig. 4.1: X Ray Diffraction of sample A,B and C.

The X-ray diffraction pattern of the as prepared micelle coated CoFe_2O_4 and the corresponding annealed powder samples of CoFe_2O_4 are shown in Figure 4.2, which confirms crystalline CoFe_2O_4 with the expected inverse spinel structure. No other phase/impurity was detected. From these curves it has been observed that with the increase of annealing temperature from 873K and above, the FWHM of the peaks decreases, which indicate the increase of particle size with annealing temperature. The size of the particles was determined by Scherrer formula considering the first two strongest peaks. The estimated particle size of the as synthesized sample and the sample annealed at 623K is $16 \pm 3\text{ nm}$ and that after

annealing at 873 K, 1073 K, 1273 K, and 1473 K for 2 h, are 23 ± 2.5 nm, 32 ± 2.5 nm, 58 ± 2.2 nm and 97 ± 2 nm, respectively.

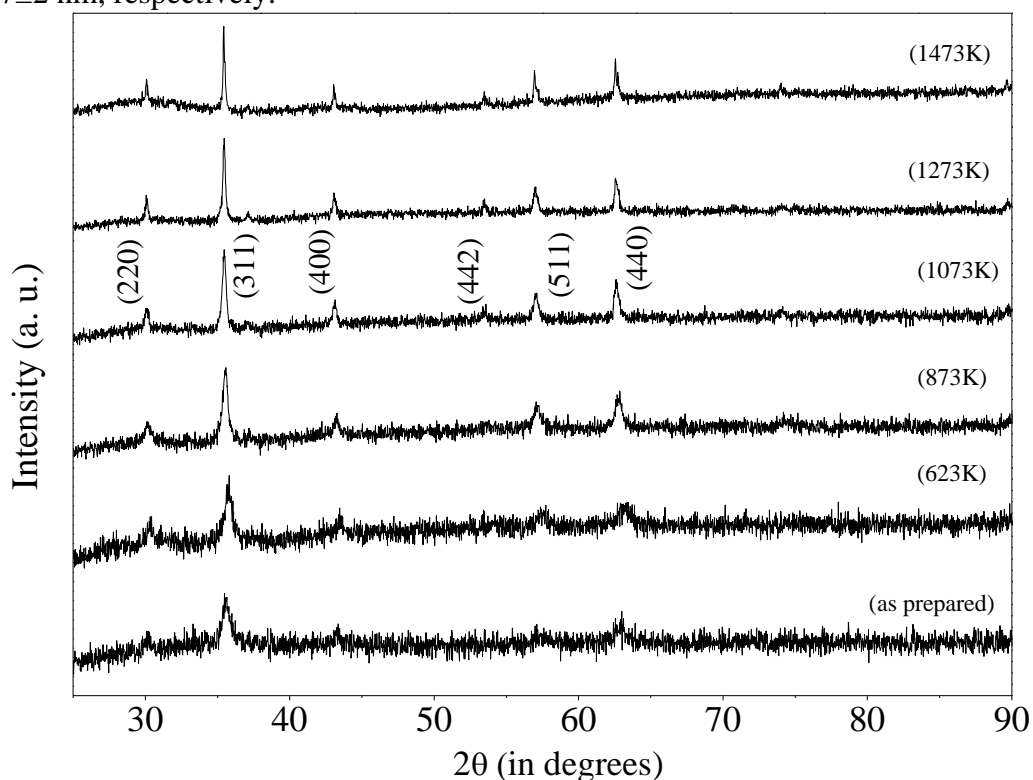


Fig. 4.2: X-ray diffraction pattern of as prepared micelle coated cobalt ferrite sample (a) and annealed at 623K (b), 873K (c), 1073K (d), 1273K (e), 1473K (f) for 2 hrs.

Figure 4.3 shows the Transmission Electron Microscope (TEM) images of sample A, B and C. The TEM images reveal that the particles were nearly spherical and monodisperse. The average particle size of sample A obtained from TEM micrograph is ~ 8 nm which is in agreement with that obtained from the XRD study. We observe that the particle size as well as shape varied with the variation in concentration of Oyl Amine and Sodium Oleate.

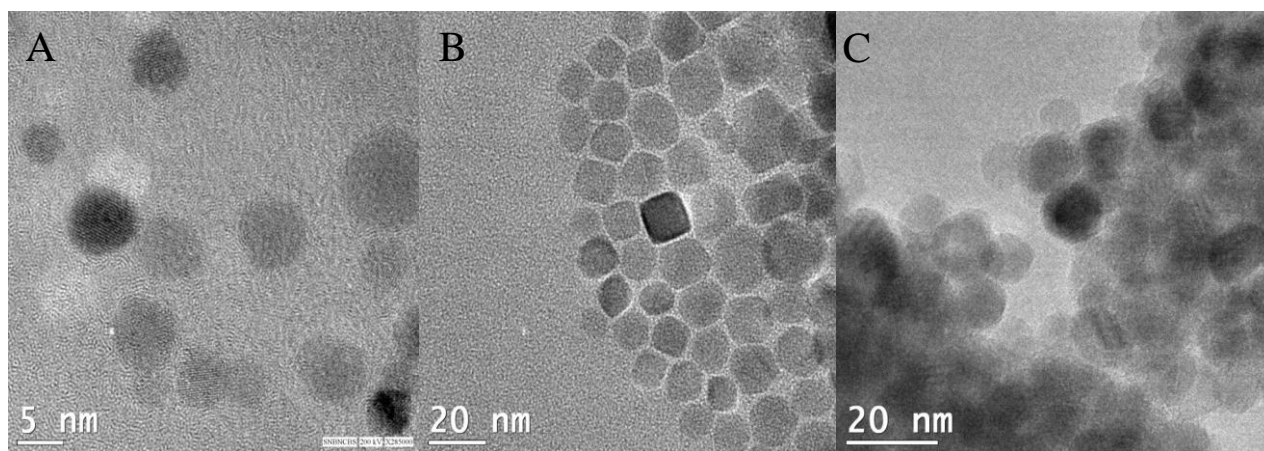


Fig. 4.3: HRTEM images of sample A, B and C

The variation of particle size with the concentration of Oleic acid and Olyl Amine is shown in the Table 4.1.

Table 4.1: Size of the particles at different concentrations

Sample Name	Concentration of Olyl Amine and Sodium Oleate	Size of particle from XRD (nm) with standard deviation
A	4 ml, 4 gm	8 (0.5)
B	2 ml, 2 gm	16 (1.2)
C	1 ml, 1 gm	24 (2)

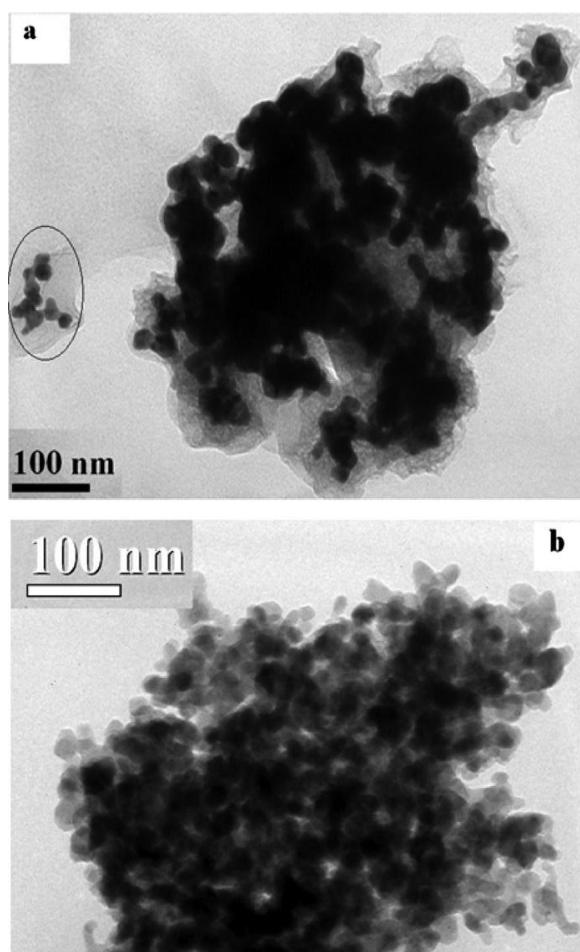


Fig. 4.4: HRTEM images of as synthesized micelle coated particles (a) and annealed at 623K (b).

The TEM images taken for as-prepared micelle (TX 100) coated samples and annealed at 623K, is shown in Figs. 4.4(a) and (b), respectively. Due to the magnetic force of attraction between the particles it becomes very difficult to get image of well dispersed region of particles. However we obtained a smaller region marked by oval in Fig. 4.4 (a) from where we calculated the particle size of 17 ± 3 nm, which is in consistence with that obtained from XRD data. In Fig. 4.4(b) we can see the particle sizes are almost same as is observed in Fig. 4.4(a).

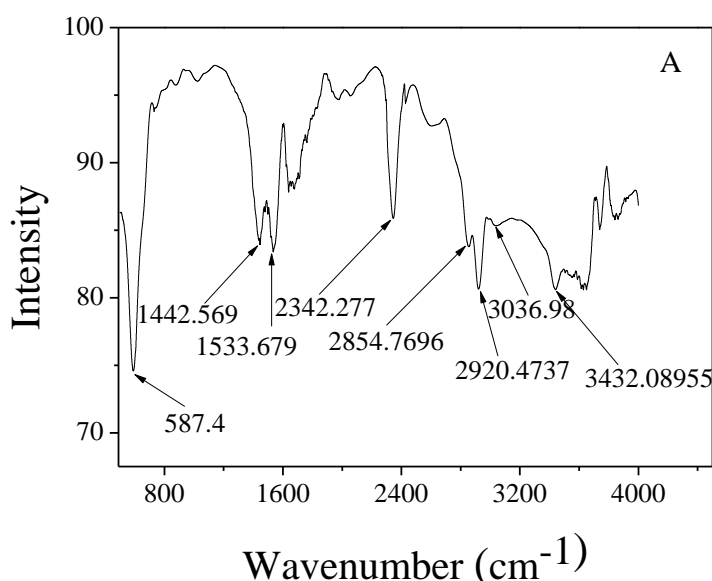


Fig. 4.5: FTIR spectra of the as-synthesized CoFe_2O_4 nanoparticles Sample A

The FTIR spectra of sample A performed in the range of 500 cm^{-1} to 4000 cm^{-1} has been shown in Fig. 4.5. The peak at 587.4 cm^{-1} is due to the ferrite nanoparticles. The peaks at 1443 cm^{-1} and 1534 cm^{-1} correspond to COO^- asymmetric and COO^- symmetric stretch. Oleic acid shows vibration bands at 2920 and 2855 cm^{-1} that are attributed to the CH_2 asymmetric and CH_2 symmetric stretch. The sharp peaks are due to the long hydrocarbon chain of oleic amine. [19]. The peak at $3,037 \text{ cm}^{-1}$ is assigned to the stretching of the vinyl group. The peak at $3,432 \text{ cm}^{-1}$ is ascribed to the $-\text{NH}_2$ group on the surface of CoFe_2O_4 . Thus the above results proved that oleic acid and oyl amine combined with the surface of CoFe_2O_4 nanoparticles.

4.4.1 Magnetic properties

The hysteresis loops of sample A, B and C at 300K are shown in Figure 4.6. The particles of sample A exhibit superparamagnetism with almost zero coercivity and

remanance. With the increase in particle size the coercivity also increases for particle B and C. The M_s value is $\sim 55 \text{ emu/g}$ which is less than the bulk value of 75 emu/g . For nanoparticles, the loss of the M_s value is due to surface spin canting effect and the presence

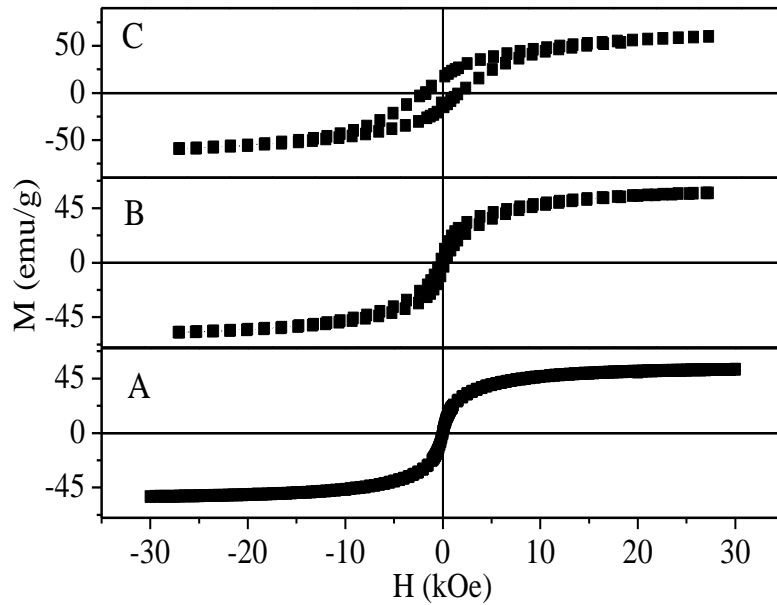


Fig. 4.6: Room temperature hysteresis loops of sample A,B and C.

of a magnetic dead or antiferromagnetic layer on the surface which is caused by finite-size effect of the small magnetic nanoparticles [20]. H_c of sample A at temperatures 4 K, 50 K, 150 K, 250 K and 300 K are $\sim 9084 \text{ Oe}$, $\sim 4490 \text{ Oe}$, $\sim 1082 \text{ Oe}$, $\sim 9.35 \text{ Oe}$ and $\sim 0 \text{ Oe}$ respectively. It is shown in Fig. 4.7. The M_s value measured at 4K is $\sim 71.2 \text{ emu/g}$ which is close to that of the bulk value.

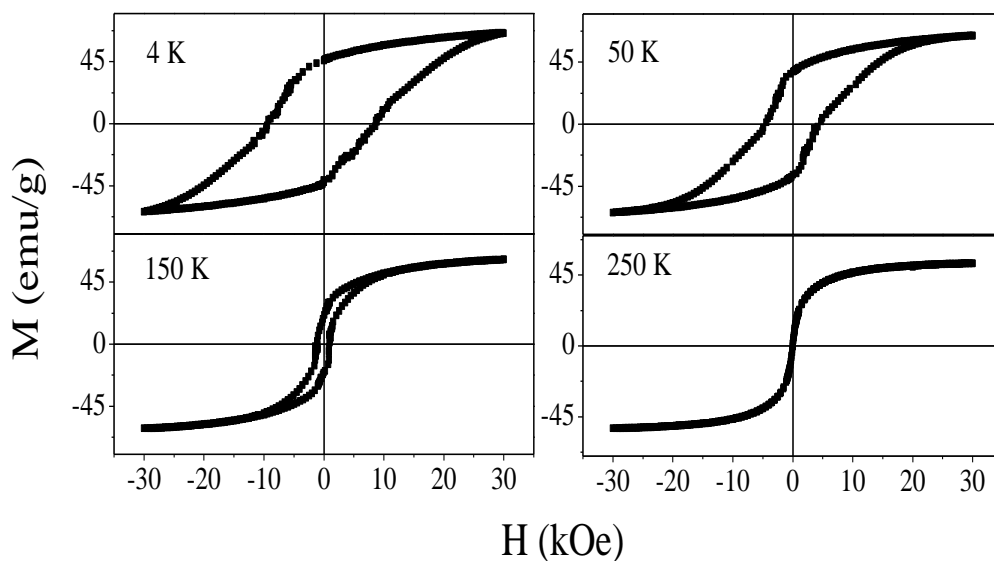


Fig. 4.7: Hysteresis loops of sample A at 4K, 50K, 150K and 250 K.

The Zero Field Cooled (ZFC) and Field Cooled (FC) curves of sample A, B and C are shown in Figure 4.8. In case of sample A the measurement is done from 3K to 310K. In case of sample B and C it is done from 80K to 400K. It is observed that the blocking temperature of sample A is 230 K and it increases with the increase in particle size to 340K and 400K for sample B and C respectively.

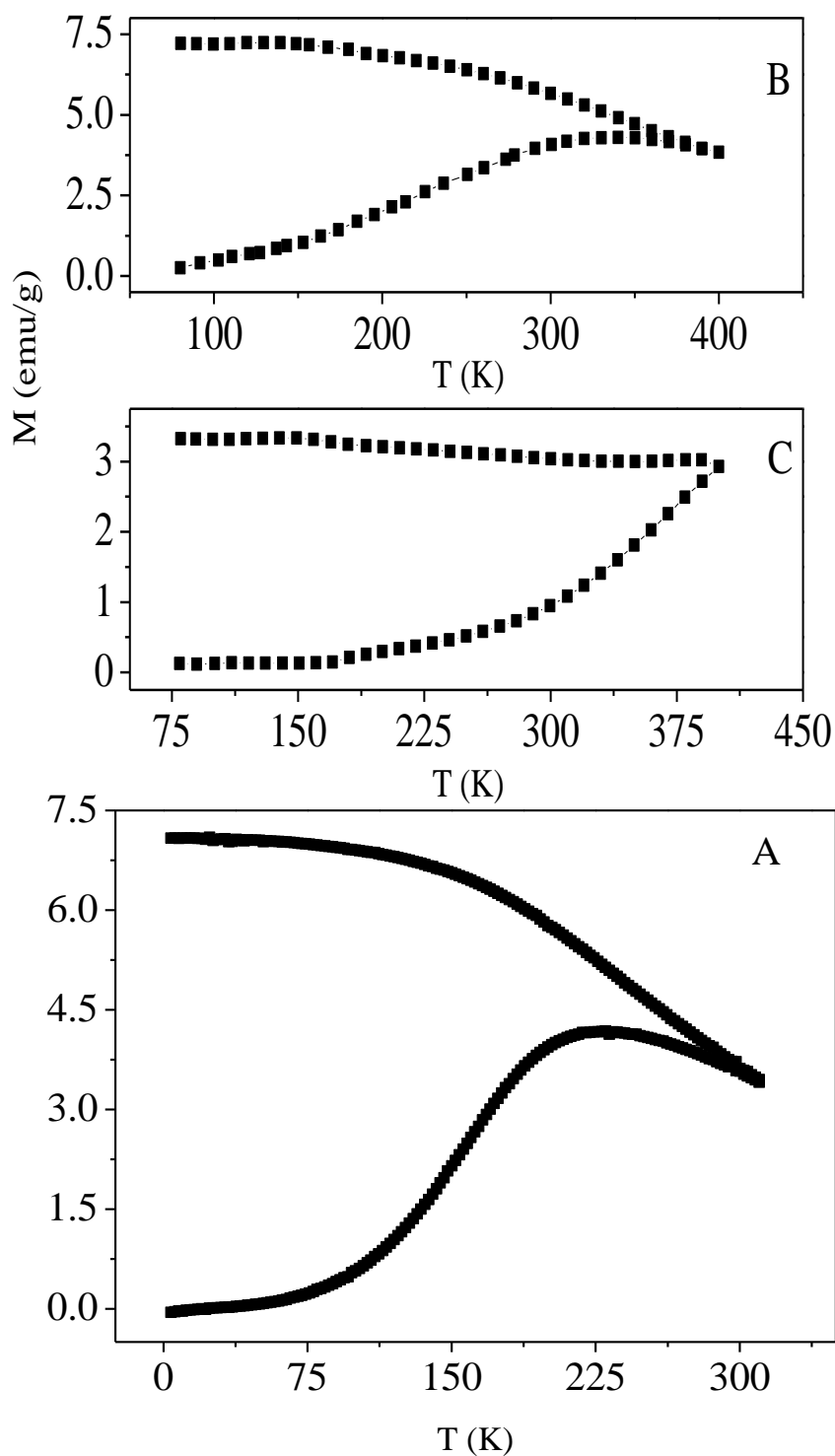


Fig. 4.8 : Zero Field Cooled (ZFC) and Field Cooled (FC) curves of sample A,B and C

The hysteresis loops of as prepared samples of the micelle coated CoFe_2O_4 nanoparticles taken at 300K, 77K and 2.5K are depicted in Figure 4.9. The H_c value at 300K was ~ 4.4 kOe and it increases with decreasing the measuring temperature. This is attributed to the increase of magnetocrystalline anisotropy with decreasing temperature [20]. The saturation magnetization M_S and remanent magnetization M_R obtained at 300K was ~ 23.14 emu/g and ~ 11.02 emu/g, respectively. The value of squareness ratio M_R/M_S increases with the decrease in temperature and reaches a maximum value of 0.60 at 2.5 K. According to the Stoner–Wohlfarth model, H_C and M_R/M_S for an assembly of noninteracting three-dimensional random particles are given by $H_C=0.985 K_1 /M_S$, $M_R/M_S=0.5$ for uniaxial anisotropy, and $H_C=0.64 K_1 /M_S$, $M_R/M_S=0.832$ for cubic anisotropy ($K_1 > 0$). For both the cases thermal agitation has been ignored. In our case since squareness ratio M_R/M_S is 0.60 at 2.5 K hence it can be interpreted that these particles have equiaxial cubic magnetocrystalline anisotropy as observed by Chinnasamy *et al* [21].

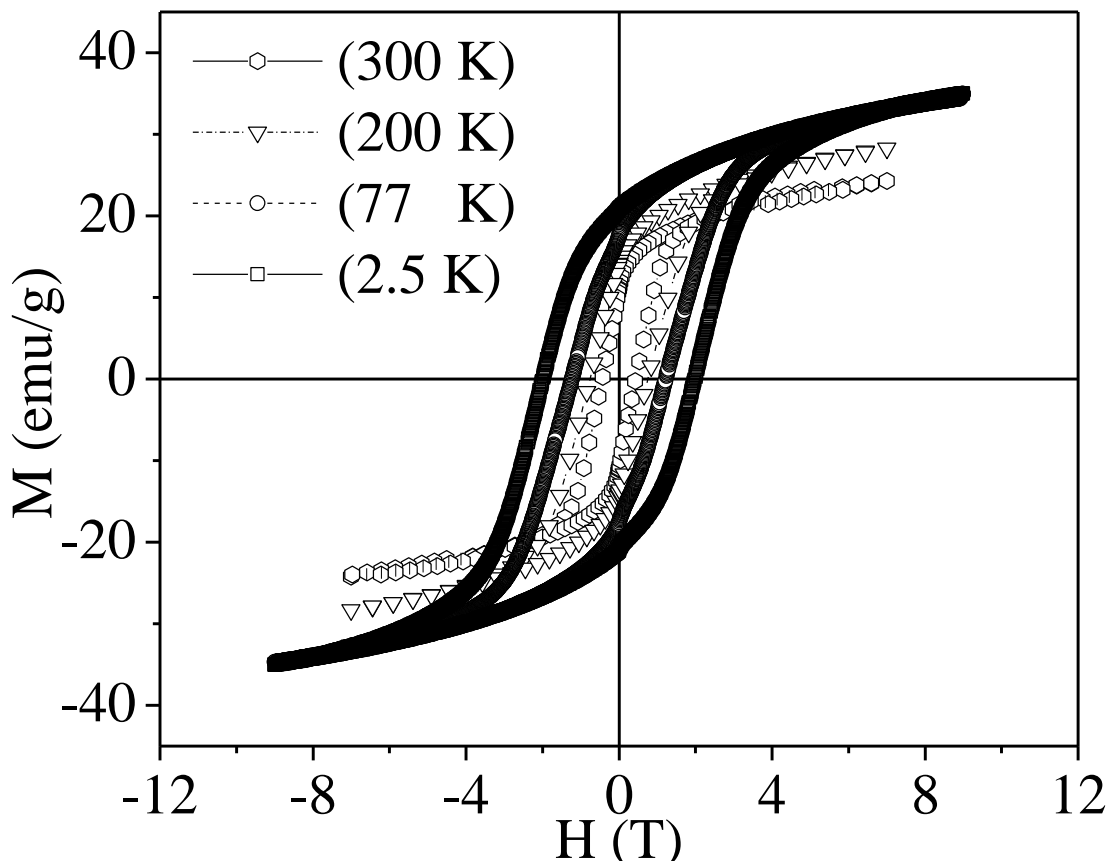


Fig. 4.9: Magnetic hysteresis loops of as prepared samples at temperature 2.5K (a), 77K (b), 200K (c), 300K (d).

A linear behavior was found while H_C is plotted with square root of the temperature (\sqrt{T}) as shown in Figure 4.10. The saturation magnetization (M_S) and remanent magnetization (M_R) obtained at room temperature was ~ 23.14 emu/g and ~ 11.02 emu/g respectively. Linear

dependency of H_C with \sqrt{T} is also an evidence of mono-dispersed non-interacting, ferromagnetically ordered single domain particles [22-25].

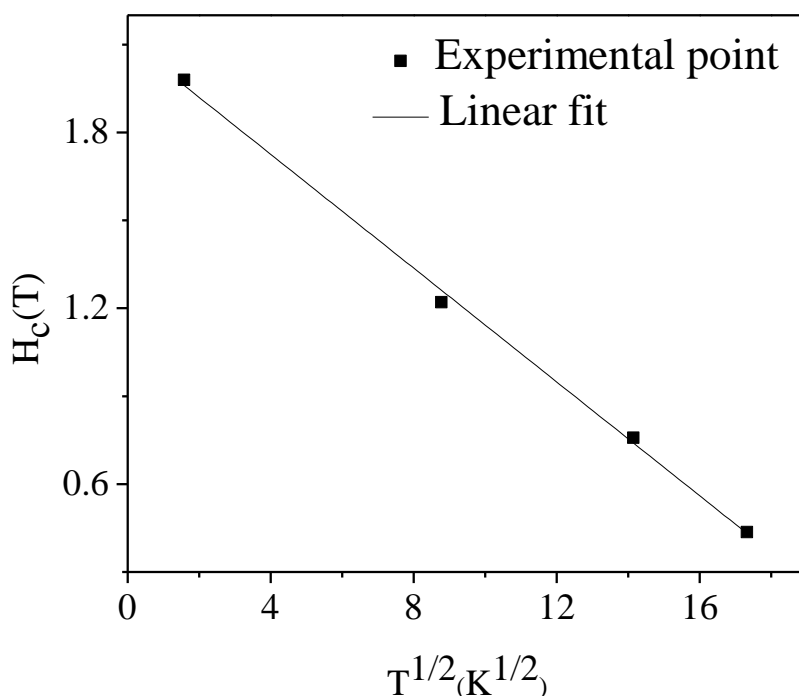


Fig. 4.10: Coercivity vs. $T^{1/2}$ plot of micelle coated $CoFe_2O_4$.

Figure 4.11 shows the hysteresis loops of as prepared micelle coated $CoFe_2O_4$ sample as well as the samples annealed at 523K, 623K, 873K, 1073K, 1273K, 1473K. From these curves we have measured the coercivity (H_C) for as-prepared samples and annealed samples. We have plotted coercivity as well as particle size with respect to annealing temperature in the same Fig.4.12. The particle size was obtained from the Scherrer formulae from Fig. 4.2. Fig. 4.12 shows that the, average particle size of the as prepared sample (16 ± 3 nm) remains almost the same upto the annealing temperature of 623K, beyond which the particle size increases to ~ 23 , ~ 32 , ~ 58 and ~ 97 nm respectively on annealing the as synthesized particles at 873, 1073, 1273 and 1473K for 2 h, respectively.

It is interesting to note that though the particle size remains same up to an annealing temperature of 623K but the coercivity decreased drastically from ~ 4.4 kOe to ~ 870 Oe when the sample was annealed at 523K and to ~ 350 Oe when annealed at 623K. From these results it is evident that not only the particle size, but also some other factors influences the coercivity of these nanoparticles. To investigate this we also annealed the sample at 373K for 2 h and then measured the coercivity. In this case, coercivity is the same as that in the case of

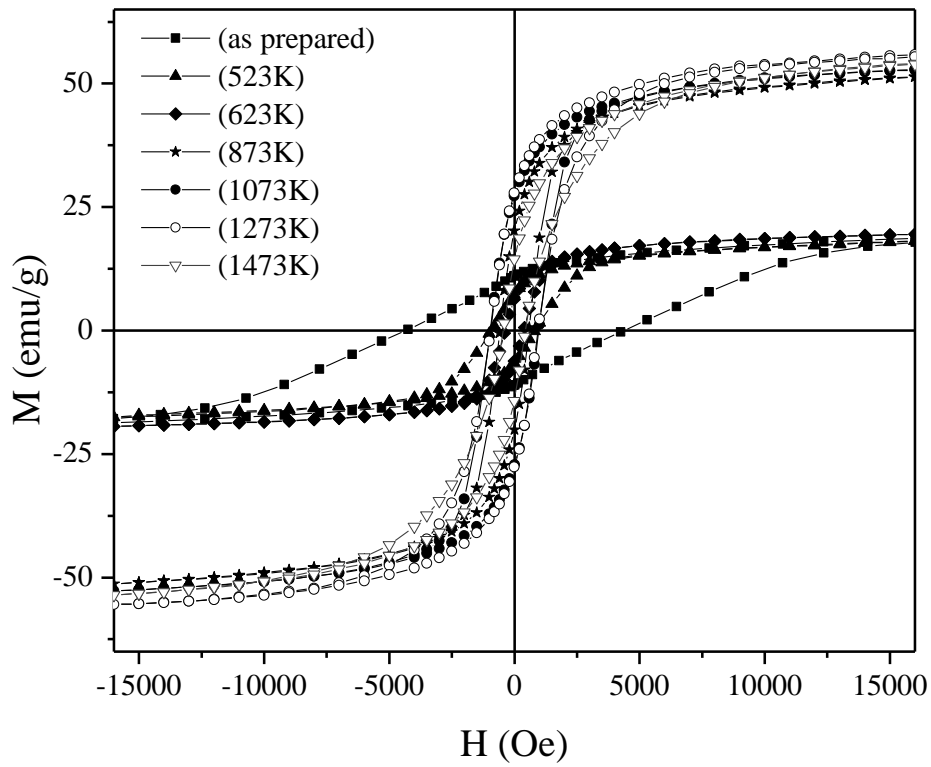


Fig. 4.11: Magnetic hysteresis loops of as prepared micelle coated CoFe_2O_4 (a) and annealed samples at different temperatures: (b) 523K, (c) 623K, (d) 873K, (e) 1073K, (f) 1273K, (g) 1473K.

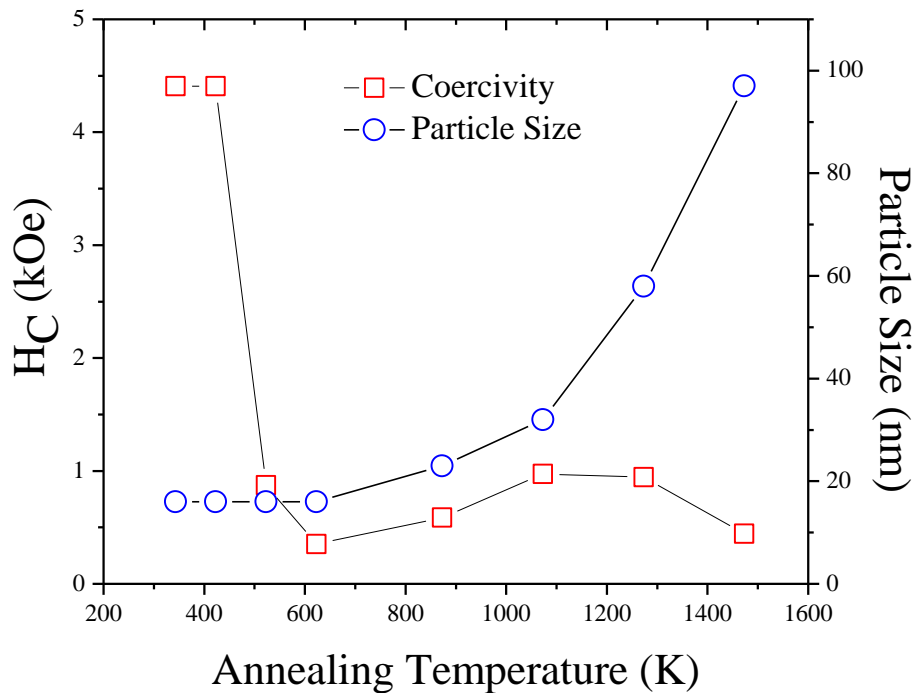
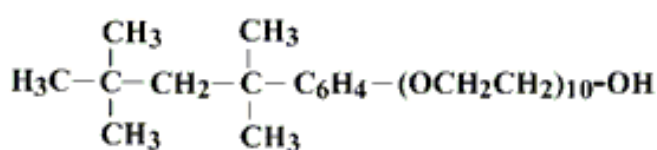


Fig. 4.12: Variation of particle size and coercivity (H_C) with annealing temperature of micelle coated CoFe_2O_4 .

as-prepared sample. On analyzing these results we reach to the conclusion that upto 373K the micelles remain as capping agent on the particle surface but at 523K the micelles start to evaporate and at 623K they are totally removed.

This is also evident from TEM images taken for as-prepared samples and those annealed at 623K as shown in Figs. 4.5(a) and (b), respectively. In Fig. 4.5 (b) we can see the particle sizes are almost the same as is observed in Fig. 4.5 (a). We have also observed that if particles are annealed at 423K for 2 h the coercivity remains same as that for as-prepared particles. Because this temperature is not high enough to remove the micelles from the surface of the particles surface as the boiling point of TX-100 is about 523K. From these results we reach to the conclusion that as micelles remain on particle surface, they form a cage like structure around the particles which in turn produce a steric hindrance, and restrict free movement or rotation of surface spin of the magnetic particles. The coercivity of a magnetic material is the magnetic field required to change the direction of magnetization. For a single domain particle system, domain walls are necessarily absent, so magnetization takes place by rotation of M_S vector of particles. For nanoparticles, M_S vector is dominated by surface spin. When a field is applied, it rotates the M_S vector of a single domain particle out of the easy direction; the rotation takes place against the restoring force of some anisotropy, usually the anisotropy of surface, or crystal. In our case the as prepared CoFe_2O_4 particles of diameter 16 nm shows a high coercivity of 4.4 kOe.

Surfactants:



(TX-100)

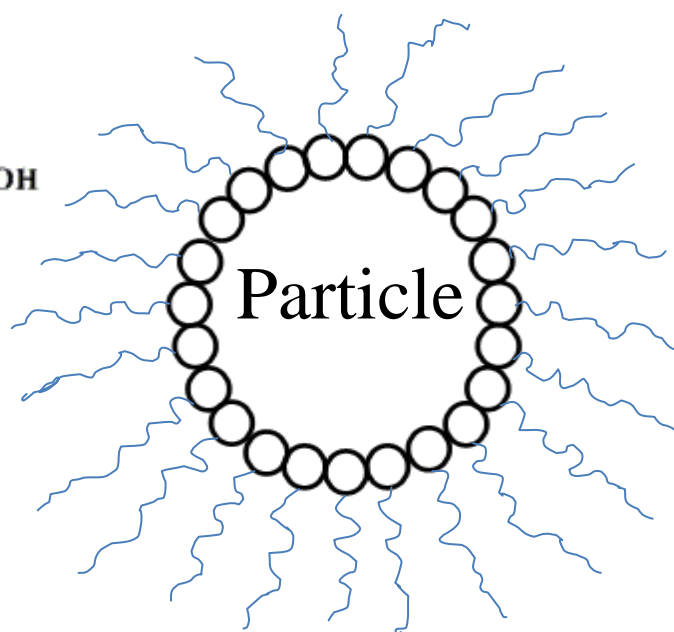
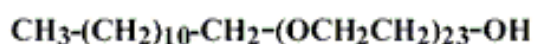


Fig. 4.13: Chemical formulae of TX 100 and cage like structure formed by the micelle

For as synthesized sample as the micelles are strongly bound to surface atoms of the CoFe_2O_4 particles, that creates a substantial surface anisotropy and hence a large H_C . The micelles, strongly bound to the surface of the particles, arrest the surface spin introducing a sterical hindrance forming a cage like structure around the particles. Thus the surface spin motions are hindered and hence higher magnetic field is required to align the magnetic spin in applied magnetic field direction which leads to high coercivity [26, 27]. When the particles are annealed at comparatively low temperature (up to 623K), the particle size remains same but the coercivity value drops to about 350 Oe. It is because of the fact that at this temperature micelles are removed, surface spins can rotate freely and at lower magnetic field they can align easily in applied magnetic field direction leading to lower coercivity value for the particles. In addition to that, the micelles can separate the particles from one another as a result of which the interaction between the particles becomes weaker, which may increase the coercivity [9].

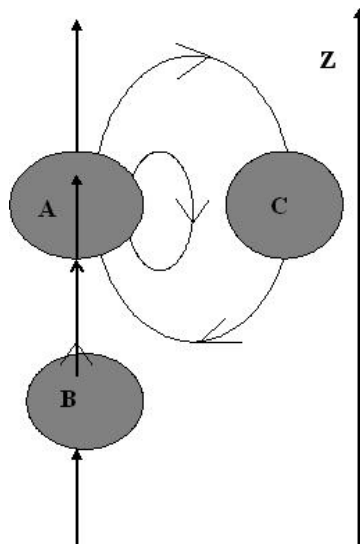


Fig. 4.14: Schematic diagram of three single domain particles, showing how interparticle separation influences the coercivity.

To illustrate this point we present a schematic diagram in Figure 4.14. Here A, B and C are three single domain particles. The arrow represents the external field lines of these particles. The external field generated by particle 'A' acts in the +Z direction on particle 'B', but in -Z direction on particle 'C'. Now let the M_S vectors of these particles had all been turned upward by a strong magnetic field in the +Z direction. If the field is reduced to zero and increased in the -Z direction, the field of 'A' at 'C' now aids the applied field and 'C' would reverse its magnetization at a lower applied field than if 'A' were absent and the coercivity would therefore lowered. However an opposite conclusion would be reached if we

consider ‘A’ and ‘B’. A quantitative study of the interaction of three particles would lead to many body problem whose exact solution is virtually impossible, but it has been proved that when the particles come closer, the interaction becomes stronger and the coercivity continues to be decreased. So the micelles play an important role to enhance the coercivity. When the as-prepared samples are annealed, the micelles start to be decomposed and are evaporated from the surface which is evident from the DSC curves shown in Figure 4.15.

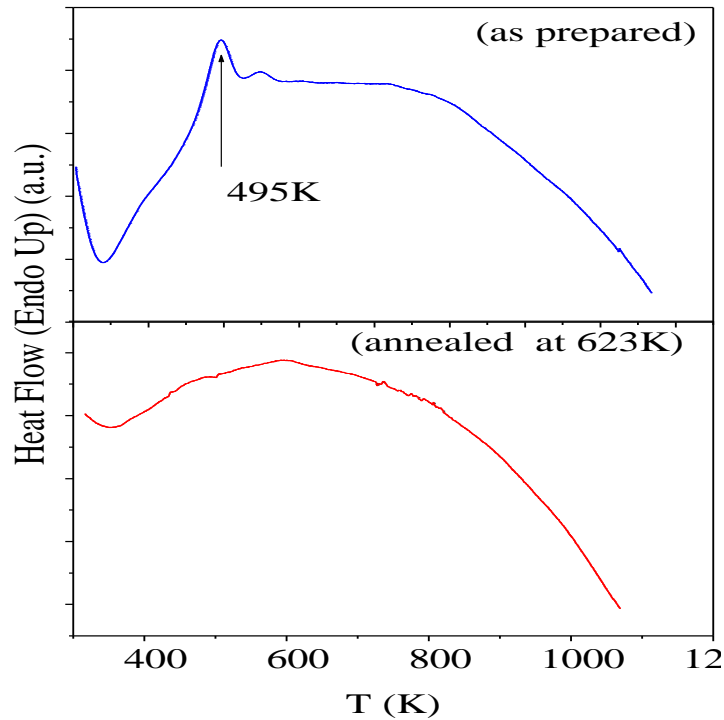


Fig. 4.15: DSC curves of (a) as prepared micelle coated CoFe_2O_4 samples and (b) annealed at 623K.

The endothermic peak at about 495K of as-prepared sample (Figure 4.16 (a)) indicates initiation of evaporation of micelles from the surface of CoFe_2O_4 particles whereas there is no such peak for the sample annealed at 873K (Figure 4.16 (b)). For the samples annealed at 623K, though the particle size remains the same ($\sim 16\text{nm}$), the coercivity falls to a low value because the micelles are decomposed completely from the surface of the particles. On further increase of annealing temperature, H_C increases and reaches a maximum value of 972 Oe for a particle size of $\sim 40\text{nm}$ and then again decreases with the increase of particle size (Figure 4.12). This behavior is due to the expected crossover from single domain to multidomain behavior with increasing particle size. From Figure 4.11 we have observed that with the increase of annealing temperature from 873K and above, the saturation

magnetization value increases due to the increase of the particle size which is a general trend [28]. But in case of samples annealed at 523 and 623K saturation magnetization remains almost same (the little change is due to experimental error). This result again authenticates no increase of particle size takes place at these low annealing temperatures.

4.4.2 Magnetic relaxation

Magnetic relaxation behaviors that are a dynamic property of the samples were studied. The relaxation phenomenon of samples A, B and C was studied at different temperatures after magnetizing the samples by a magnetic field of 2000 Gauss and then switching off the field. After waiting for 5 second the measurements were performed during a time period of 400 seconds.

After the removal of a field of 2000 Gauss, magnetizations of all samples evolve with time towards a demagnetized state which is shown in Fig. 4.18 (a), Fig. 4.19 (a) and Fig. 4.20 (a). Experiments were carried out for different temperatures from 80 K to 100K. Relaxation time for a non-interacting single domain particle is given by Neel's theory [29,30]. According to Eq. 3.6 in Chapter 3 relaxation rate for a single domain particle is a very sensitive function of particle size. The M vs $\ln t$ curves for samples of average particle sizes 8 nm(± 0.5) (A), 16 nm (± 1.2) (B), 21 nm(± 2) (C) measured at different temperatures are shown in Fig.4.18 (b), Fig. 4.19 (b) and Fig. 4.20 (b). For each sample the plots apparently show a linear behavior, which would be expected from the following logarithmic approximation [31-33]

$$M(t) = M(0) - S \ln(t) \quad (4.1)$$

where S is the classical rate of relaxation or the classical viscosity and according to Eq. (4.1) it is defined as,

$$S = - \frac{1}{M_0} \frac{\partial M}{\partial (\ln t)} \quad (4.2)$$

The use of the word "apparent" is justified if we try to analyze a single temperature dependent curve. It would clearly show a deviation from the linear behavior at very small starting measurement time as suggested by the Eq. (4.1). The relaxation for different particle sizes differ significantly from each other. As a result what we obtained was originally an average behavior of the relaxations of the particles at the initial measurement time. It is also observed that for highest measuring temperature T the starting value of M is lowest and vice

versa. This happens because for each sample for higher value of temperature T , greater is the proportion of M that relaxes before the VSM is able to start measurement following Eq. 3.6. Hence for higher T , the starting value of M is lowest. Thus for this type of thermally activated samples by changing T , we can change the part of relaxation process that falls within the measurement time window. In Fig. 4.19 (a), 4.20 (a) and 4.21 (a) the M versus time (t) data were plotted at temperatures 80K, 85K, 90K, 95K and 100K for samples A, B and C. The value of M at the starting point of the measurement is found to be much smaller in case of A compared to B for all the temperatures. The reason behind this is increased disordered surface effect, which decreases the M value in case of A comprised of smaller particles [34].

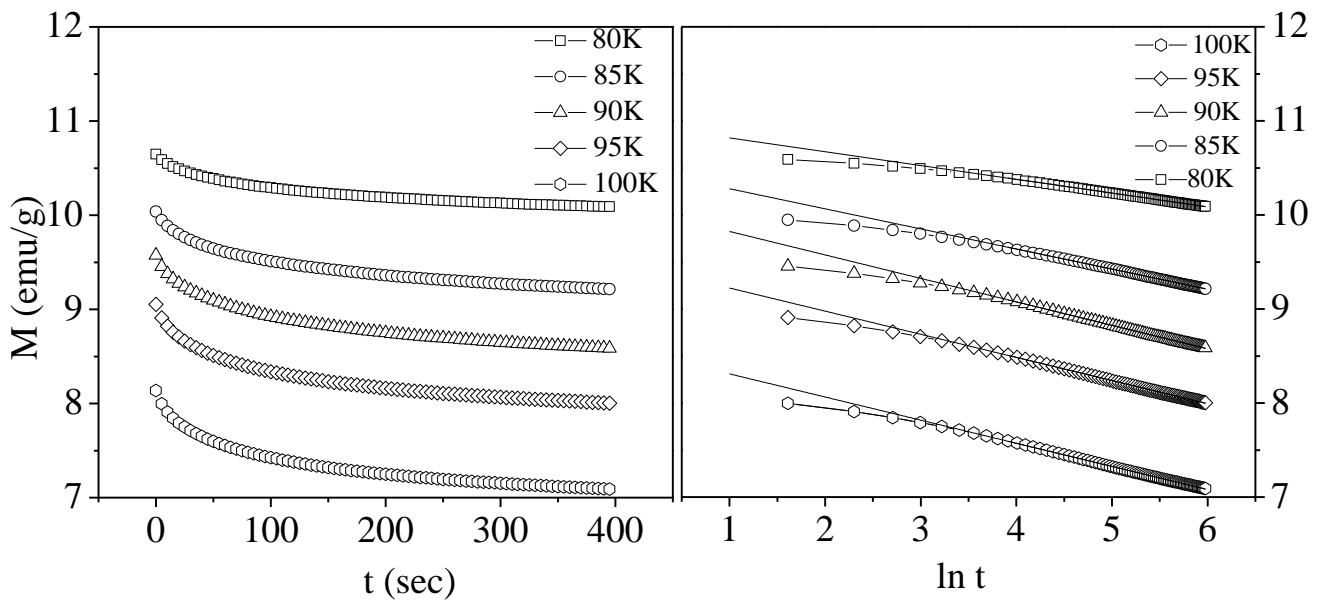


Fig. 4.18 (a) Time evolution of M for sample A **(b)** M vs. $\ln t$ curve of sample A

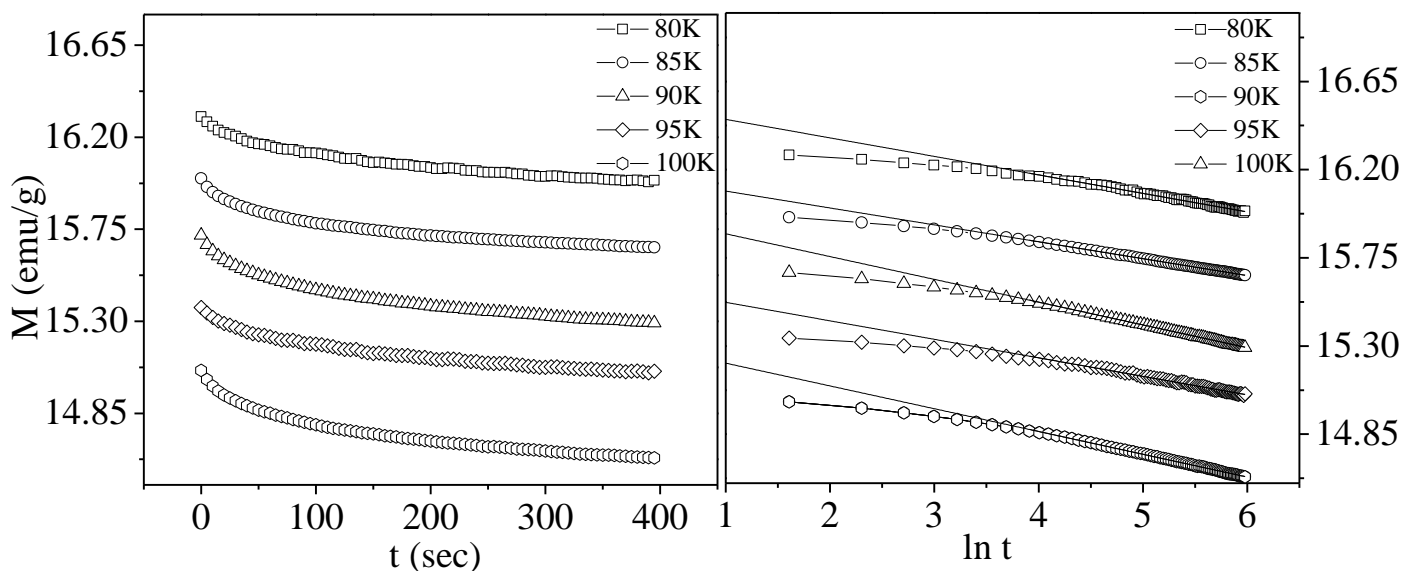


Fig. 4.19 (a) Time evolution of M for sample B **(b)** M vs. $\ln t$ curve of sample B

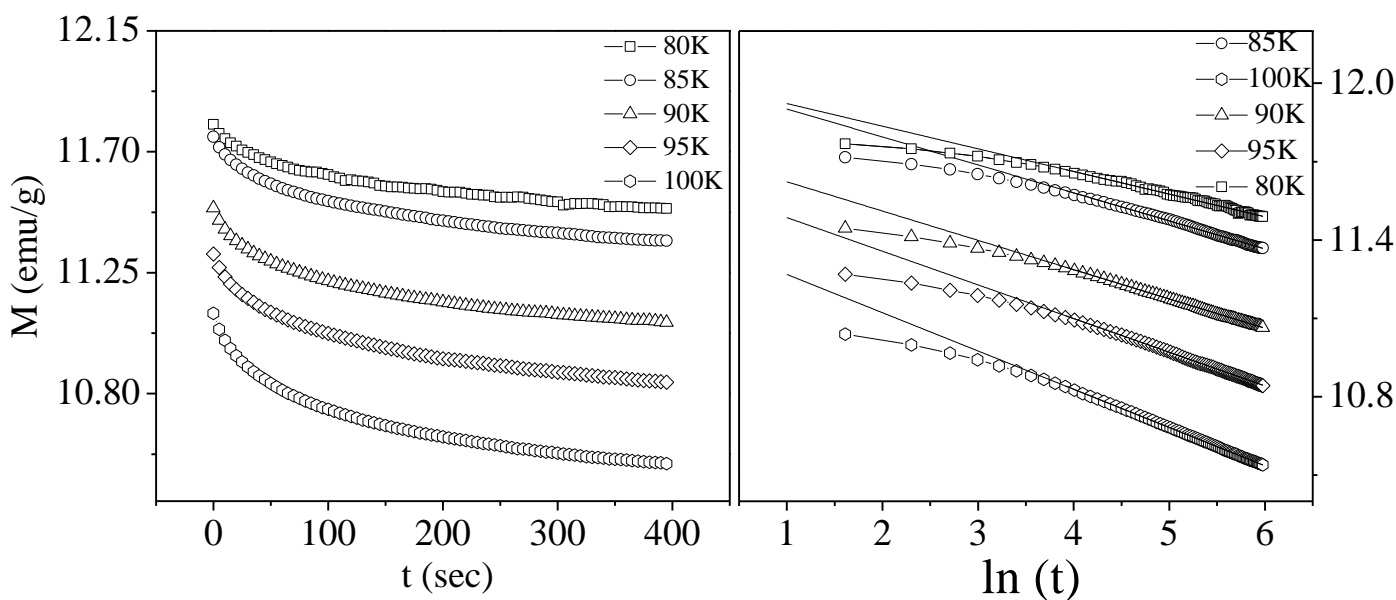


Fig. 4.20 (a) Time evolution of M for sample C **(b)** M vs. $\ln t$ curve of sample C

4.5 Conclusions

We have successfully synthesized unagglomerated, monodisperse CFO nanoparticles by a simple hydrothermal technique using Olyl amine and Sodium oleate as capping agents. The particle size changed with the change in concentration of Olyl amine and Sodium oleate. The Hysteresis curve showed that the particles prepared with the lowest concentration of the capping agents were superparamagnetic. Blocking temperature (T_B) increased with the increase in particle size. The time evolution of the magnetization of the superparamagnetic

particles was also discussed. We have also successfully synthesized single domain cobalt ferrite nanoparticles by coprecipitation method using a micelle as capping agent. Here we have observed micelles remaining as capping agent around the particles enhance the coercivity of the particles to a large extent. This is a new phenomenon we have observed here. By extensive analysis of the results obtained, we have concluded how micelles play the role to induce the high coercivity in these particles. The micelles form a cage-like sterically hindered structure around the particles which restricts the surface spin and hence enhances the surface anisotropy of the particles which enhances the coercivity. We have shown that particle size is also another parameter to change the coercivity of nanoparticles. Such a small single domain magnetic nanoparticles with a high coercivity will be useful for data storage device in near future. We have also studied the magnetic relaxation phenomenon of the unagglomerated CFO nanoparticles.

References

- [1] M. Sugimoto, J. Am. Ceram. Soc. **82**, 269 (1999).
- [2] A.K. Giri, E.M. Kirkpatrick, P. Moongkhamklang, S.A. Majetich, Appl. Phys. Lett. **80**, 2341 (2002).
- [3] T. Mathew, S. Shylesh, B.M. Devassy, M. Vijayaraj, C.V.V. Satyanarayana, B.S. Rao, C.S. Gopinath, Appl.Catal. A-Gen. **273**, 35 (2004).
- [4] G.V.M. Jacintho, A.G. Brolo, P. Corio, P.A.Z. Suarez, J.C. Rubim, J. Phys. Chem. C **113**, 7684 (2009).
- [5] P. Pradhan, J. Giri, G. Samanta, H.D. Sarma, K.P. Mishra, J. Bellare, R. Banerjee, D. Bahadur, J. Biomed. Mater. Res. Part B Appl. Biomater. **81B**, 12 (2007)
- [6] M. Sincai, D. Ga[^]nga[˘], D. Bica, L. Ve[^]ka[˘]s, J. Magn. Mater. **225**, 235 (2001)
- [7] J.H. Lee, Y.M. Huh, Y.W. Jun, J.W. Seo, J.T. Jang, H.T. Song, S. Kim, E.J. Cho, H.G. Yoon, J.S. Suh, J. Cheon, Nat. Med. **13**, 95 (2007).
- [8] D. L. Huber, Small **1**, 482 (2005).
- [9] B. D. Cullity, *Fine Particles and Thin Films: Introduction to Magnetic Material* Addison-Wesley, London, 1972, p. 385.
- [10] B. H. Liu, J. Ding, Z. L. Dong, C. B. Boothroyd, J. H. Yin, and J. B. Yi, Phys. Rev. B **74**, 184427 (2006).
- [11] N. Chinnasamy, B. Jeyadevan, K. Shinoda, K. Tohji, D. J. Diayaprawira, M. Takahashi, R. J. Joseypphus, and A. Narayanasamy, Appl. Phys. Lett. **83**, 2862 (2003).
- [12] C. P. Bean, J. Appl. Phys. **26**, 1381 (1955).
- [13] B. H. Liu, J. Ding, Z. L. Dong, C. B. Boothroyd, J. H. Yin, and J. B. Yi, Phys. Rev. B **74**, 184427 (2006).
- [14] C. N. Chinnasamy, B. Jeyadevan, K. Shinoda, K. Tohji, D. J. Diayaprawira, M. Takahashi, R. J. Joseypphus, and A. Narayanasamy, Appl. Phys. Lett. **83**, 2862 (2003).
- [15] V. Kumara, A. Ranaa, M. S. Yadav and R. P. Pant, J. Magn. Mater. **320**, 1729 (2008).
- [16] B. G. Toksha, E. S. Sagar, S. M. Patange, and K. M. Jadhav, Solid State Commun. **147**, 479 (2008).
- [17] S. Gyergyek, D. Makovec, A. Kodre, I. Arcon, M. Jagodic, M. Drogenik, J. Nanopart Res **12**, 1263 (2010).

- [18] D. Pal, M. Mandal, A. Chaudhuri, B. Das, D. Sarkar and K. Mandal J. of App. Phys. **108**, 124317 (2010).
- [19] Wu N, Fu L., Aslam M, Wong K. C., Dravid V. P. Nano Lett. **4**, 383 (2004).
- [20] R. M. Bozorth, E. F. Tilden, and A. Williams, J. Phys. Rev. **99**, 1788 (1955).
- [21] C. N. Chinnasamy, B. Jeyadevan, K. Shinoda, K. Tohji, D. J. Diayaprawira, M. Takahashi, R. J. Joseypphus, and A. Narayanasamy, Appl. Phys. Lett. **83**, 2862 (2003).
- [22] M. Mandal, D. Pal, and K. Mandal, Colloids Surf., A **348**, 35 (2009).
- [23] S. Mitra, K. Mandal, and P. A. Kumar, J. Magn. Magn. Mater. **306**, 254 (2006).
- [24] G. I. Frolov, Bull. Russ. Acad. Sci. Phys. **71**, 1629 (2007).
- [25] X. Batlle, M. Garcia del Muro, J. Tejada, H. Pfeiffer, and G. E. Sinn, J. Appl. Phys. **74**, 3333 (1993).
- [26] A. E. Berkowitz, J. A. Lahut, I. S. Jacobs, L. M. Levinson, and D. W. Forester, Phys. Rev. Lett. **34**, 594 (1975).
- [27] R. H. Kodama, A. E. Berkowitz, E. J. McNiff, and S. Foner, Phys. Rev. Lett. **77**, 394 (1996).
- [28] K. Maaz, A. Mumtaza, S. K. Hasanaina, and A. Ceylan, J. Magn. Magn. Mater. **308**, 289 (2007).
- [29] L. Néel, Ann. Geophys. **5**, 99 (1949).
- [30] L. Néel and C. R., Acad. Sci., Paris **228**, 664 (1949).
- [31] A.J. Moses, *Nonlinear Electromagnetic Systems*, A. Basak, ed., (IOS press, Amsterdam, 1996), p.489.
- [32] A. Robinson, P. Southern and W. Schwarzacher, J. Phys.: Conference series **17**, 16 (2005).
- [33] R. Prozorov, Y. Yeshurun, T. Prozorov and G. Gedanken, Phys. Rev. B **59**, 6956 (1999).
- [34] *Surface Effects in Magnetic nanoparticles*, D. Fiorani, ed., (Springer, New York, 2005).

Chapter 5

5 Synthesis and study of nanostructured Bismuth Ferrites

5.1 Preamble

Some of the iron oxides show two or more ferroic properties simultaneously, such as ferroelectricity, ferromagnetism and ferroelasticity. They are called Multiferroics. By tuning one property we can change another one which can be utilized for information storage like spintronic devices and sensors [1-4]. But very few single phase materials are found to exhibit multiferroicity. In recent years Bismuth Ferrite (BiFeO_3) has come up as a very interesting single phase multiferroic material. It has a rhombohedrally distorted perovskite structure with space group $R3c$ at room temperature. It is unique in the sense that its Néel temperature and Curie temperature are 370°C and 830°C respectively. We have synthesized various nanostructures of BiFeO_3 by the hydrothermal synthesis route and studied its magnetic as well as dielectric properties. We have also investigated the formation mechanism of the different morphologies [5]. But Bismuth Ferrite at room temperature does not show the multiferroic properties, i.e., both the ferroelectric and ferromagnetic properties simultaneously. There is a spin cycloid structure of wavelength ~ 62 nm present in the BiFeO_3 lattice which leads to the cancellation of the magnetization. There is also a problem of high leakage current in undoped BFO. Preparing nanostructured materials might result in breaking of the spin cycloid thereby enhancing the magnetization. Doping of various elements like rare earth, transition in the Bi site and the Fe site can overcome this problem since due to doping some distortion takes place which breaks the spin cycloid [6-9]. Doping of rare earth elements in the Bi site can stabilize the structure and reduce the leakage current. This motivated us to dope Lanthanum as well as Barium in the Bi site separately and study its magnetic and dielectric properties in details [10]. Synthesis and characterization of various nanostructures of lanthanum, barium doped bismuth ferrite have

rarely been done and change in the ferromagnetic and dielectric properties with change in morphology have also been rarely investigated.

5.2 Experimental

Equimolar mixture of $\text{Bi}(\text{NO}_3)_2 \cdot 5\text{H}_2\text{O}$ and $\text{Fe}(\text{NO}_3)_2 \cdot 9\text{H}_2\text{O}$ were dissolved in 50 ml of distilled water. A 10ml solution of NaOH of 5M concentration was added drop by drop to the above mixture to adjust the pH of the solution to 12 so that the reaction takes place in a basic medium. Due to the addition of NaOH, precipitation of $\text{Bi}(\text{OH})_3$ and $\text{Fe}(\text{OH})_3$ took place. The mixture was stirred for 20 min and then transferred into a Teflon-lined steel autoclave. The autoclave was sealed and then heated at different temperatures for a certain period of time. After a stipulated time, the chamber was cooled naturally to the room temperature. The product thus obtained was washed successively in double distilled water and ethanol (EtOH) and dried at 60°C overnight. The reaction time was kept constant for 12 hours. The reaction temperature was varied to get particles of different morphology. We prepared four sets of samples, three of them with water as solvent and by heating the solution at 180°C (Sample A), 210°C (Sample B), 240°C (Sample C) and the fourth one using a solvent of mixture of ethyl alcohol (EtOH) and water in the ratio 2:7 by volume and heating at 240°C (Sample D). In case of Lanthanum doping and Barium doping, $\text{La}(\text{NO}_3)_3 \cdot 4\text{H}_2\text{O}$ and $\text{Ba}(\text{NO}_3)_2$ were taken as the source of Lanthanum and Barium respectively and the hydrothermal temperature was 240°C ; water was taken as the solvent and the reaction was continued for 12 hours. In case of Lanthanum doped BFO three sets of samples were prepared $\text{Bi}_{(1-x)}\text{La}_x\text{FeO}_3$ $x=0.05$ (Dop1), $x=0.1$ (Dop2) and $x=0.15$ (Dop3). In case of Barium doped BFO two sets of sample were prepared $\text{Bi}_{(1-x)}\text{Ba}_x\text{FeO}_3$ $x=0.1$ (Dop4), $x=0.2$ (Dop5). X-ray diffraction was performed using a PANalytical X-ray diffractometer with high intensity Cu $K\alpha$ radiation. The morphology of the particles was studied with the help of a field emission scanning electron microscope (JEOL) and Transmission Electron Microscope (FEI). Thermal analysis of the samples was carried out to study the phase transition behaviour, using a differential thermal analyzer (DTA, PerkinElmer). The magnetization M as a function of applied field H was measured using a vibrating sample magnetometer (Lake Shore Cryotronics). The powder samples were pressed into pellets of 10 mm diameter and 1 mm thickness at a pressure of 60 MPa in a hydraulic press with Polyvinyl Alcohol as a binder. For the measurements of dielectric

properties, these pellets were carefully polished and subsequently pasted with Ag paste on both sides as electrodes. The dielectric constant versus frequency and Dissipation factor versus frequency measurements were performed with the help of Precision Impedance Analyzer (Agilent, 4294A). The Polarization vs Electric Field measurements were performed in a PE Loop Tracer (Marine India Ltd.). The electron spin resonance studies of all the samples were carried out at 300 K using an X-band spectrometer of JEOL-make operating at 9440.9 MHz.

5.3 Results and Discussions

5.3.1 Structural properties

The XRD of sample A, B, C and D is shown in Fig. 5.1 (a). The peaks of sample A correspond to the Sillennite phase of Bismuth Ferrite having chemical formulae $\text{Bi}_{12}(\text{Bi}_{0.5}\text{Fe}_{0.5})\text{O}_{19.5}$.

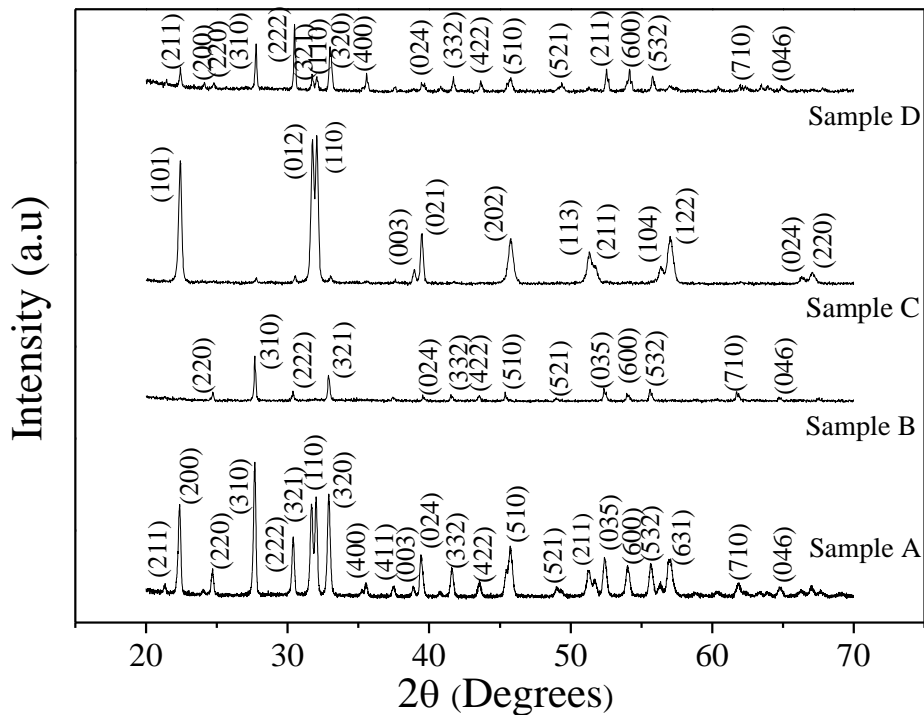


Fig. 5.1 (a): X-ray diffraction of sample A, B, C and D.

Peaks of sample B correspond to the phase of Bismuth Ferrite having chemical formulae $(\text{Bi}_{24}\text{Bi}_{1.04}\text{Fe}_{0.84}\text{O}_{40})$. The XRD of sample C shows single phase Bismuth Ferrite (BiFeO_3) with a rhombohedrally distorted perovskite structure belonging to R3c space group, which match well with the literature data (JCPDS:86-1518). This means that well-crystallized Bismuth Ferrite

crystals could be obtained by the present solvothermal process. The XRD of sample D is found to be the same as that of sample A proving that the same phase was obtained in both cases.

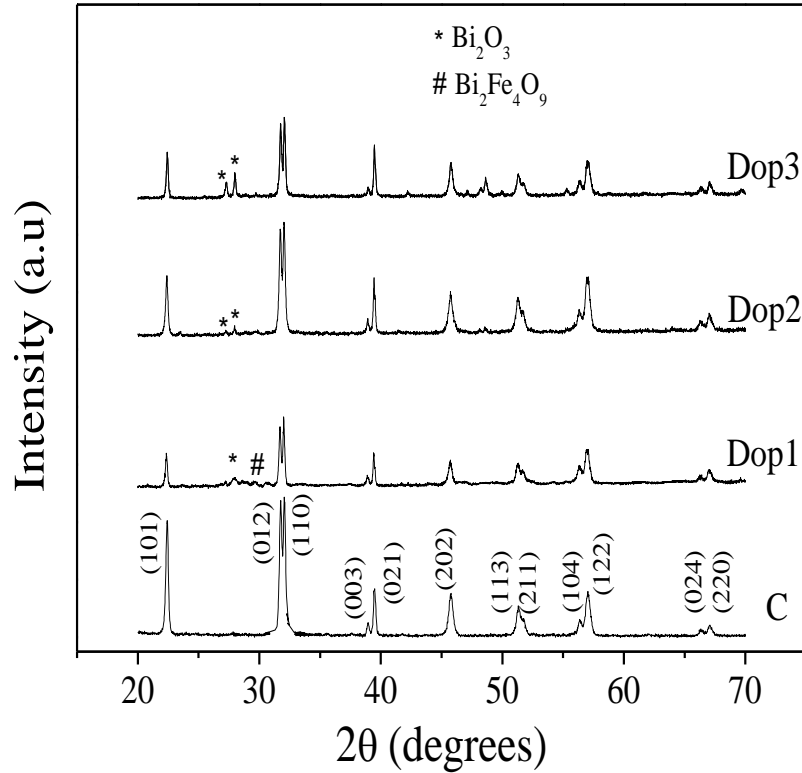


Fig. 5.1 (b): X Ray diffraction of samples $x=0.0$ (C), $x=0.05$ (Dop1), $x=0.1$ (Dop2) and $x=0.15$ (Dop3) of $\text{Bi}_{(1-x)}\text{La}_x\text{FeO}_3$.

Figure 5.1 (b) shows the XRD pattern of the $\text{Bi}_{1-x}\text{La}_x\text{FeO}_3$ crystallites with $x=0.0$ (C), 0.05 (Dop 1), 0.1 (Dop 2) and 0.15 (Dop 3). All the observed peaks of the $x=0.0$ (C) sample confirmed the formation of BiFeO_3 which has a rhombohedrally distorted perovskite structure belonging to $R3c$ space group. No impurity phase was found in the undoped BFO. Some low intensity peaks of $\text{Bi}_2\text{Fe}_4\text{O}_9$ and Bi_2O_3 are obtained as the doping concentration was increased in case of La doped BFO. However the crystalline structure does not change and remains rhombohedral in all the cases. In solid state synthesis, the crystalline structure usually changes from rhombohedral to orthorhombic after doping [11]. But in our hydrothermal synthesis no such change in the crystalline structure is observed. The reason behind this might be the different ambient conditions created in two different synthesis methods.

X Ray Diffraction graph of the $\text{Bi}_{1-x}\text{Ba}_x\text{FeO}_3$ crystallites with $x=0.0$ (C), $x=0.1$ (Dop 4) and $x=0.2$ (Dop 5) samples is shown in Figure 5.1 (c). All the observed peaks confirmed the formation of BiFeO_3 which has a rhombohedrally distorted perovskite structure belonging to $R3c$ space group. All the samples were phase pure. No impurity phase is obtained in case of all the samples which is unlike the Lanthanum doped case.

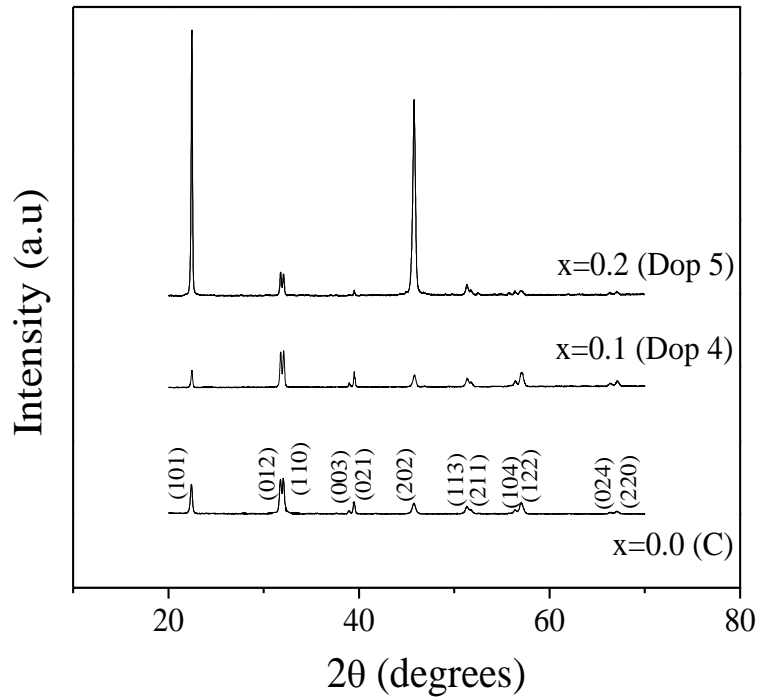


Fig. 5.1 (c):- X ray diffraction of samples $x=0.0$, $x=0.1$ and $x=0.2$.

In case of Dop 5 the maximum intensity peaks are that of the (101) and (202) planes instead of the (012) and (110) planes which is not the case for the other samples. This implies that in this sample maximum particle growth takes place along this direction. Hence we can conclude that the morphology of the particles change with doping [12].

Figure 5.2 show the Field Emmission Scanning Electron Micrographs (FESEM) of samples A, B, C and D respectively. It shows that the particles obtained for Sample A were spindle shaped having average diameter ~ 450 nm and length $\sim 1\mu\text{m}$. Sample B is composed of tile shaped particles having each side $\sim 600\text{nm}$ and average width ~ 115 nm. Sample C shows cylindrical shaped particles having average length ~ 400 nm and diameter ~ 450 nm. Hexagonal structure with average side of ~ 300 nm are observed for sample D.

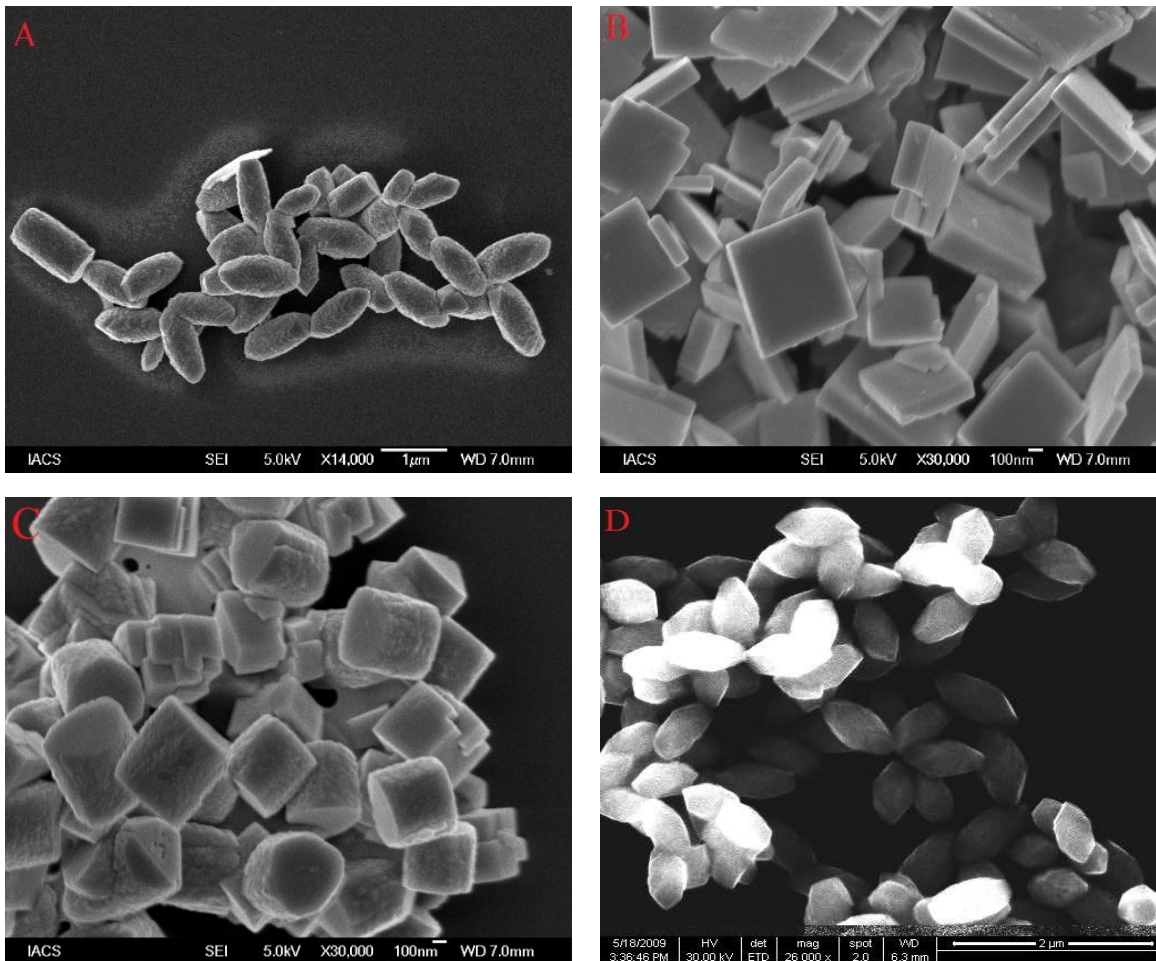


Fig. 5.2 (a): Scanning Electron Micrographs of sample A, B, C and D.

Therefore, with the change in solvothermal conditions such as temperature and solvent, the rate of nucleation and growth becomes different which leads to different shaped particles [13]. The possible growth processes at different temperatures are shown with the help of a schematic diagram in Fig. 5.2 (b). With the increase of temperature the collision probability of the particles increases. At the beginning of the crystal growth process, very small particles (~a few nm) are formed which are usually spherical in shape. These spherical nanoparticles further grow to form spindle shaped particles (sample A) which we observe when the solvothermal process is performed at 180°C. When the synthesis temperature is increased further, i.e. at 210°C, the elongated particles collide to form plate like particles (sample B). When prepared at 240°C, the plates agglomerate to form cylindrical (sample C) or hexagonal (sample D) structures depending on the solvent used. In case of sample C only water is used as solvent

which is more ionic than a mixture of ethyl-alcohol (EtOH) and water used for sample D. Less ionic solvents are more prone to form more isotropic structure. This might have led to the formation of hexagonal shaped particles in sample D.

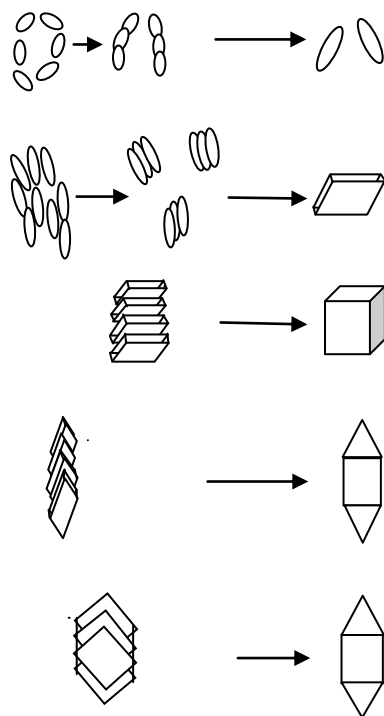


Fig. 5.2 (b): The possible schematic diagram of the growth process of the BiFeO_3 nanostructures.

Figure 5.3 (a) shows the Transmission Electron Micrograph of the La doped BFO ($x=0.1$ Dop2) sample. Undoped BFO (C) (Fig. 5.2) consists of cylindrical shaped particles with an average length ~ 400 nm and diameter ~ 450 nm. The diameter of the particles gradually reduces on doping lanthanum. For the sample with $x=0.1$ (Dop 1) [Fig. 5.3 (a)] the average length and diameter of the rod-shaped particles are ~ 600 nm and ~ 100 nm respectively. Selected Area Electron Diffraction (SAED) pattern of sample Dop2 taken in a direction perpendicular to the length is shown in Fig.5.3 (b). It indicates the particles to be single crystalline. The same kind of electron diffraction pattern is obtained throughout the length of the sample confirming the single crystalline and oriented nature of the nanorods. The estimation of d value from the micrograph indicates that the nanorods grow along the (110) plane.

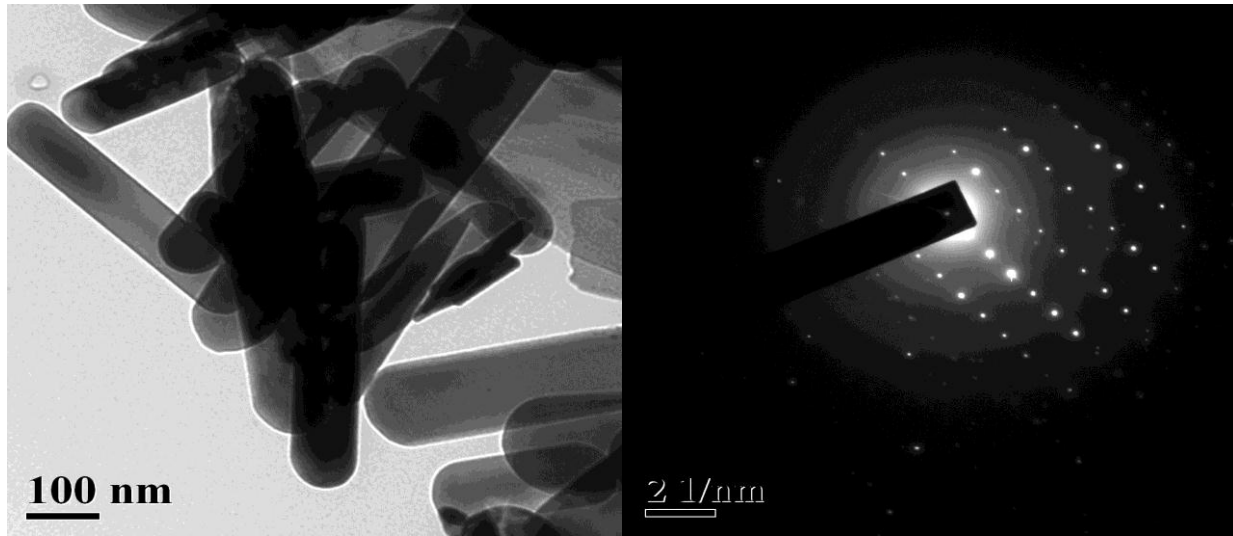


Fig. 5.3: (a) Transmission Electron Micrograph of $\text{Bi}_{(1-x)}\text{La}_x\text{FeO}_3$ $x=0.1$ (Dop2). (b) Small area electron diffraction pattern of Dop2.

The formation mechanism of rod-like BLFO could be understood based on a “dissolution and crystallization” mechanism of hydrothermal synthesis, in which Bi^{3+} , La^{3+} and Fe^{3+} hydroxides dissolved in alkali solution at a high temperature and pressure. The formation of BLFO crystallites took place through nucleation, precipitation, dehydration and growth between the ions and ion groups on the interfaces of the nuclei. An anisotropy of grain growth could be favored, making grain grow along a preferential orientation [14], such as along (110) plane in our case. La entered into the BFO lattice offering additional energy for a certain crystal plane to grow fast. As a result, the morphology of BLFO crystallites became rod like.

Figure 5.4 shows the FESEM images of all the samples of $\text{Bi}_{(1-x)}\text{Ba}_x\text{FeO}_3$ $x=0.1$ (Dop 4), $x=0.2$ (Dop 5). The particles of the sample $x=0.1$ (Dop 4) are cube shaped. The sample with $x=0.2$ (Dop 5) show hexagonal shaped morphology having thickness of ~ 100 nm and length, breadth of ~ 500 nm. This indicates that as the doping concentration increases the morphology of the particles changes [12]. The size of Barium ion (1.42 \AA) is quite larger than Bismuth ion (1.03 \AA). As a result of doping there might occur a change in the rate of nucleation and growth. This might be the result of obtaining cube as well as hexagonal particles.

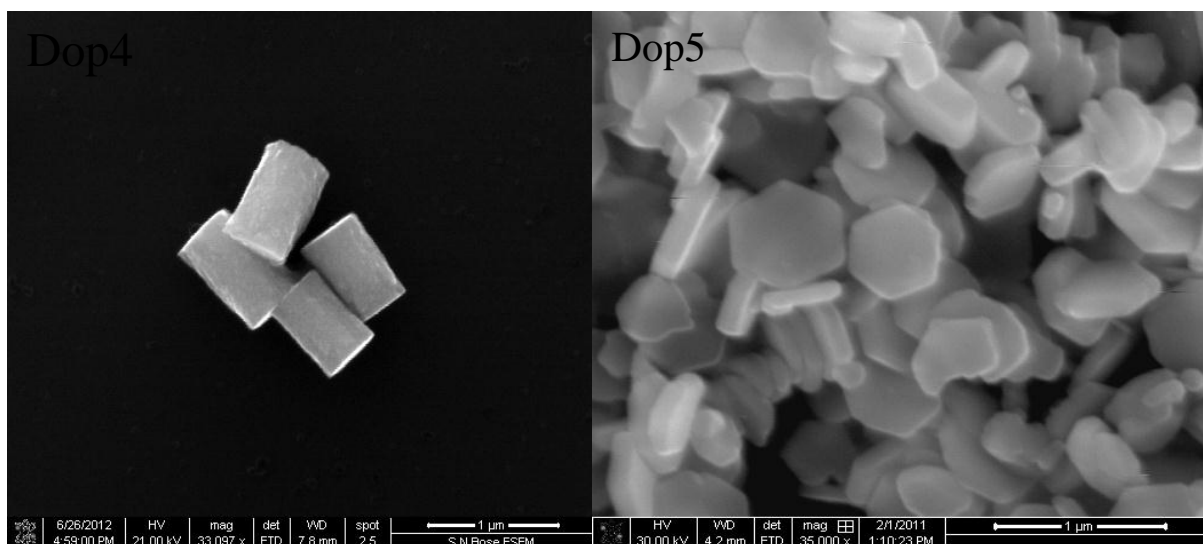


Fig. 5.4:- Field Emission Scanning Electron Micrographs of samples $\text{Bi}_{(1-x)}\text{Ba}_x\text{FeO}_3$ $x=0.1$ (Dop4) and $x=0.2$ (Dop5).

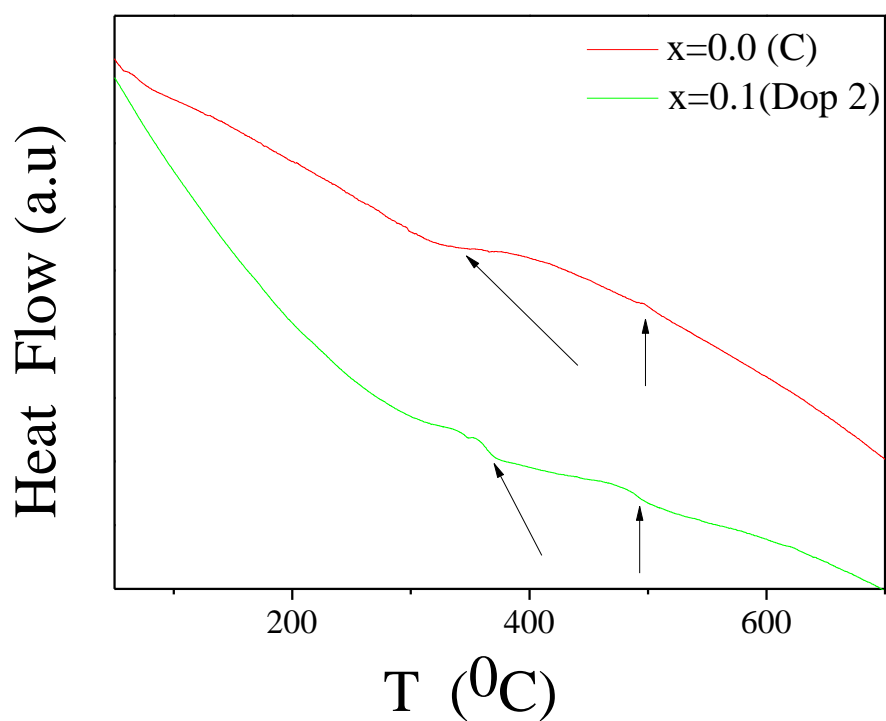


Fig. 5.5: Differential Thermal Analysis of Lanthanum doped sample $x=0.0$ (C) and $x=0.1$ (Dop 2).

Differential Thermal Analysis of Sample C and Dop 2 are studied with a scan rate of 5⁰C per minute and it is shown in Fig.5.5. It shows that the Neel Temperature (T_N) of Sample C is 328⁰C and that of Dop2 is 367⁰C. T_N increases with La-doping. Neel temperature of lanthanum ferrite (LaFeO_3) is 465⁰C which is a G type antiferromagnetic material [15]. Hence with La-doping the T_N increases towards the Neel temperature of lanthanum ferrite. Similar results were also obtained by Cheng et al. [16]. Another transition is also observed at the vicinity of 500⁰C for both the samples which is corroborated from peaks in similar position in Fig. 5.8 (a).

5.3.2 Magnetic properties

The variation of the magnetization of samples A, B, C and D at room temperature with an applied magnetic field varying from 0 T to $\pm \sim 1.6$ T is shown in Fig. 5.6(a). The magnetic hysteresis loops of all the samples show almost linear field dependence [16] which is an indication of antiferromagnetic (AF) order at room temperature. The antiferromagnetic order is developed due to the superexchange interaction between the Fe ions in two adjacent lattice mediated by an Oxygen ion. Fig. 5.6 (b) shows the M vs. H curves of the same samples at 80K. Sample D shows the maximum coercivity of ~ 1.68 kOe.

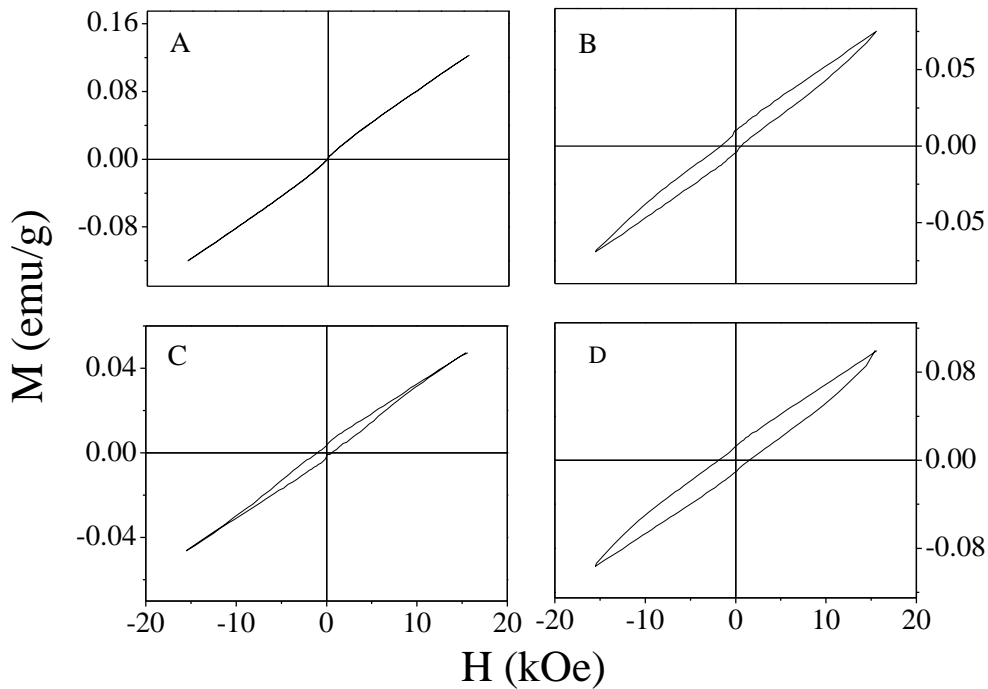


Fig. 5.6 (a): Room Temperature magnetic hysteresis loops of sample A, B, C and D

Except for the sample C all of the samples show substantial coercivity. In case of sample C both the room temperature and 80K hysteresis loops shows negligible coercivity. In case of sample B at 80K a small hysteresis is observed. This might be because particularly for this structure the spin cycloid is breaking.

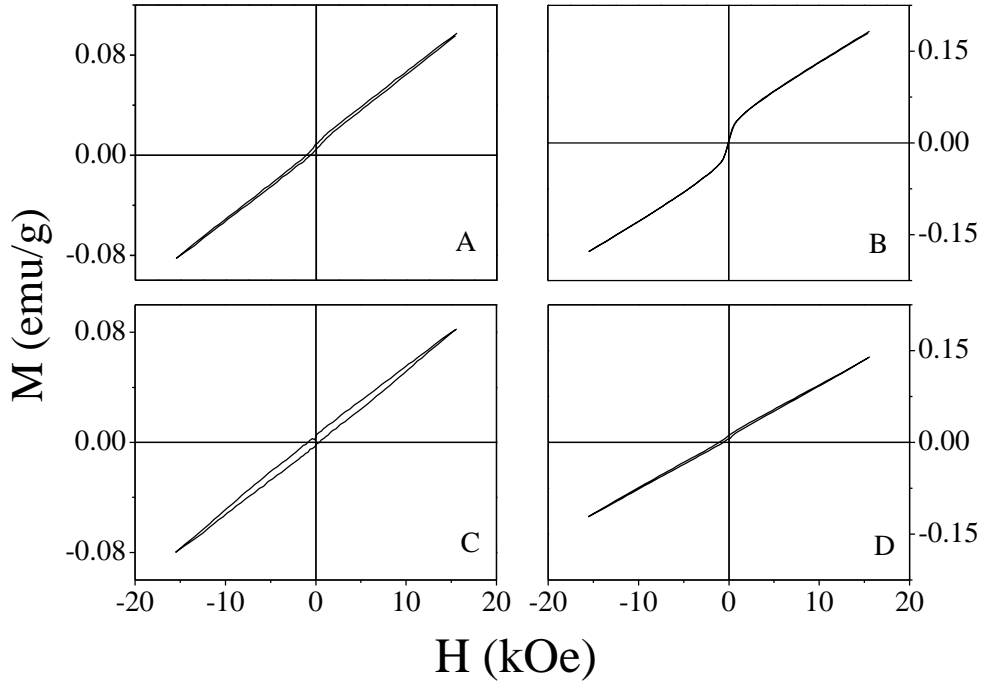


Fig. 5.6 (b): Magnetic hysteresis loops of sample A, B, C and D at 80K.

Figure 5.7 (a) shows the room temperature Magnetic Hysteresis loops of the La doped BFO samples with $x=0.0$ (C), 0.05 (Dop 1), 0.1 (Dop 2) and 0.15 (Dop 3). The M - H curve of the $x=0.0$ sample is almost a straight line passing through the origin [17]. Sigmoid shaped hysteresis loop appears on doping lanthanum and hysteresis effect increases on increasing the lanthanum content. Magnetic moment at the maximum field (~ 1.6 T) increases from ~ 0.05 emu/g for C to ~ 0.2 emu/g for Dop3. Coercivity increases from ~ 79 Oe for C to ~ 291 Oe for Dop3. Doping leads to the release of the potential magnetization locked in the spin cycloid of the undoped bismuth ferrite ($x=0.0$) [18]. This results in enhancement of the magnetization. Since the materials (such as Bi_2O_3 , $\text{Bi}_2\text{Fe}_4\text{O}_9$) corresponding to low intensity peaks obtained in the XRD of La-doped BFO do not have any magnetic order, we can conclude that the enhancement of magnetization is due to the increase in lanthanum concentration.

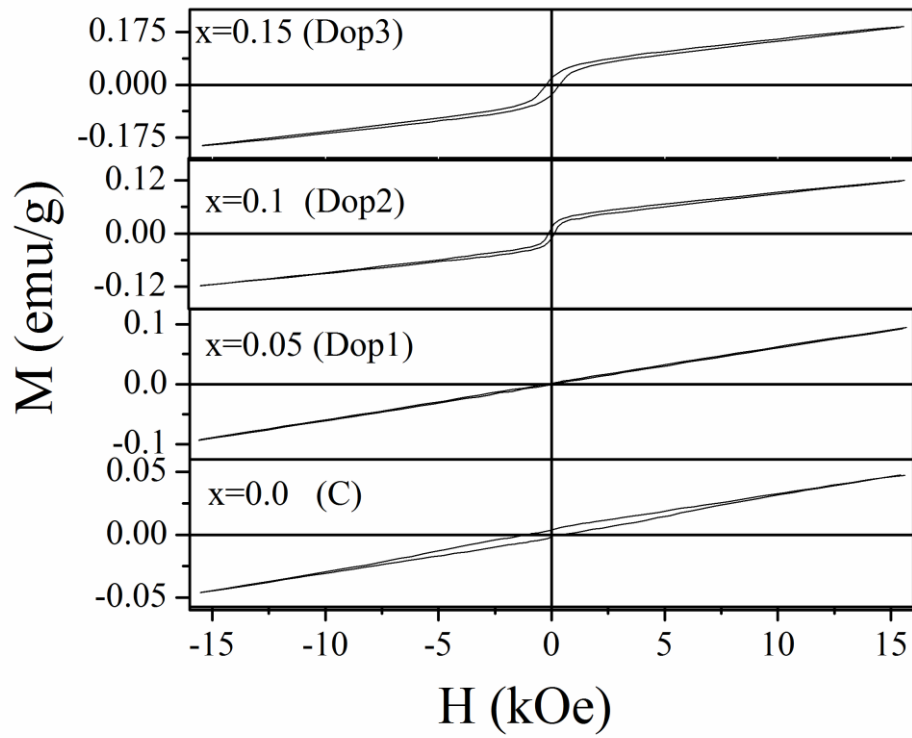


Fig. 5.7 (a): Magnetic hysteresis loops of $\text{Bi}_{(1-x)}\text{La}_x\text{FeO}_3$ $x=0.0$ (C), $x=0.05$ (Dop1), $x=0.1$ (Dop2), $x=0.15$ (Dop3) at 300K.

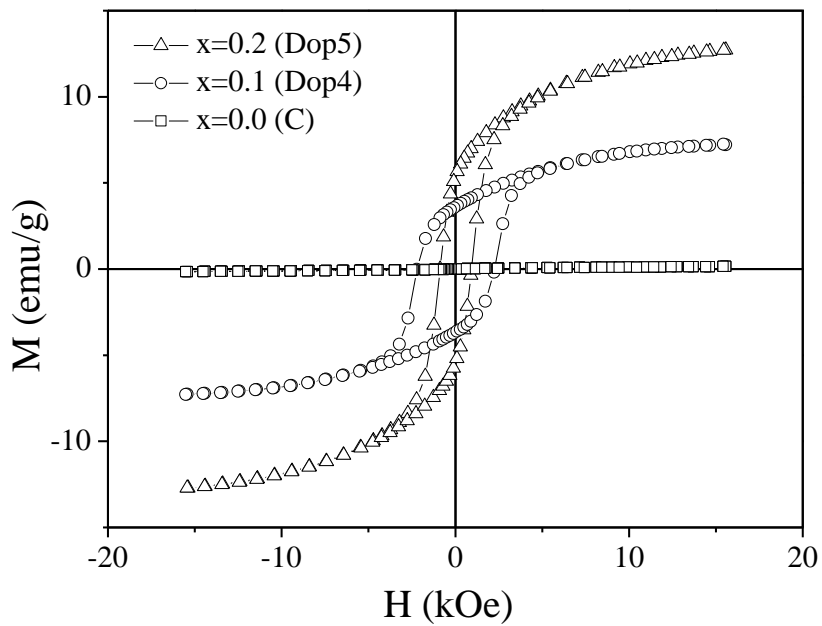


Fig. 5.7 (b):- Magnetic hysteresis loops of $\text{Bi}_{(1-x)}\text{Ba}_x\text{FeO}_3$ $x=0.0$, 0.1 and 0.2 at 300K.

Figure 5.7 (b) shows the Hysteresis loops of the samples $\text{Bi}_{(1-x)}\text{Ba}_x\text{FeO}_3$ $x=0.0$ (C), $x=0.1$ (Dop 4) and $x=0.2$ (Dop 5) at room temperature. Ferromagnetic hysteresis loop having a coercivity of ~ 2.24 kOe and a magnetization of ~ 7.24 emu/g at the maximum field of ~ 1.6 kOe appears in case of the sample Dop4. Coercivity decreases to ~ 0.9 kOe for Dop5 but magnetic moment at the maximum field increases to ~ 12.74 emu/g. The increase in magnetization might be due to two reasons. Firstly the distortion of the perovskite structure resulting in a smaller bond angle of Fe-O-Fe and a significant magnetization of $\text{Bi}_{(1-x)}\text{Ba}_x\text{FeO}_3$. Secondly the valency of Bismuth is $3+$ whereas that of Barium is $2+$. Hence incorporating Barium in the Bismuth site will require charge compensation. This may result in the formation of Fe^{4+} or oxygen vacancies; the former may distribute statistically with Fe^{3+} in the octahedron in BBFO and lead to a net magnetization and ferromagnetism [19]. In addition, for both the La doped and Ba doped case the modified size and morphology of the agglomerated particles after doping might also contribute to the enhancement in the magnetic moment through destroying the cycloid magnetic structure. As we know, the period of spiral spin magnetic structure in BiFeO_3 is 62 nm. Therefore nano $\text{Bi}_{1-x}\text{La}_x\text{FeO}_3$ and $\text{Bi}_{1-x}\text{Ba}_x\text{FeO}_3$ grains that agglomerate into bigger sized nanoparticles might break this period and induce enhanced magnetic property.

The magnetization versus temperature plot of sample C, Dop2 in presence of an applied field of 6000 Oe in the temperature range of 30°C to 650°C is shown in Fig. 5.8 (a). Figure 5.8 (b) shows the similar plot of sample C at an applied field of 6000 Oe and Dop 5 at an applied field of 100 Oe in the temperature range of 30°C to 650°C . In case of samples C and Dop 2 the magnetization value was so low that it was within the error bar of our VSM instrument. Hence a large field of 6000 Oe was applied in these two cases. It shows that the magnetization remains constant up to a temperature, $\sim 400^\circ\text{C}$. The magnetization then starts increasing with temperature and a peak is observed at $\sim 550^\circ\text{C}$ (in case of C and Dop 2) beyond which the magnetization starts decreasing. In case of Dop 5 the peak is obtained at $\sim 610^\circ\text{C}$. Beyond 610°C magnetization starts decreasing. Spin canting due to lattice distortion or increase in thermal energy [20] might be the reason for enhancement in magnetization.

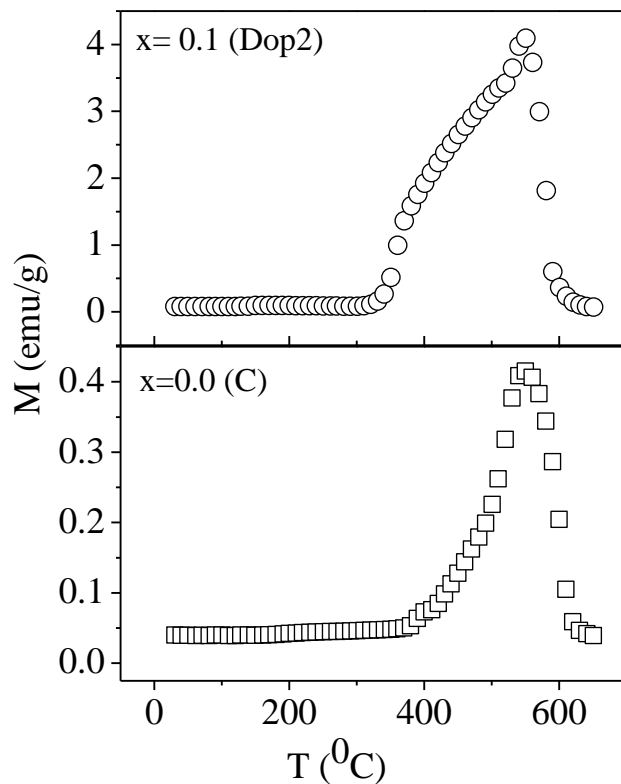


Fig. 5.8 (a) High temperature magnetization vs temperature of samples $x = 0.0$ (C) and $x = 0.1$ (Dop2) of $\text{Bi}_{(1-x)}\text{La}_x\text{FeO}_3$ at an applied field of 6000 Oe.

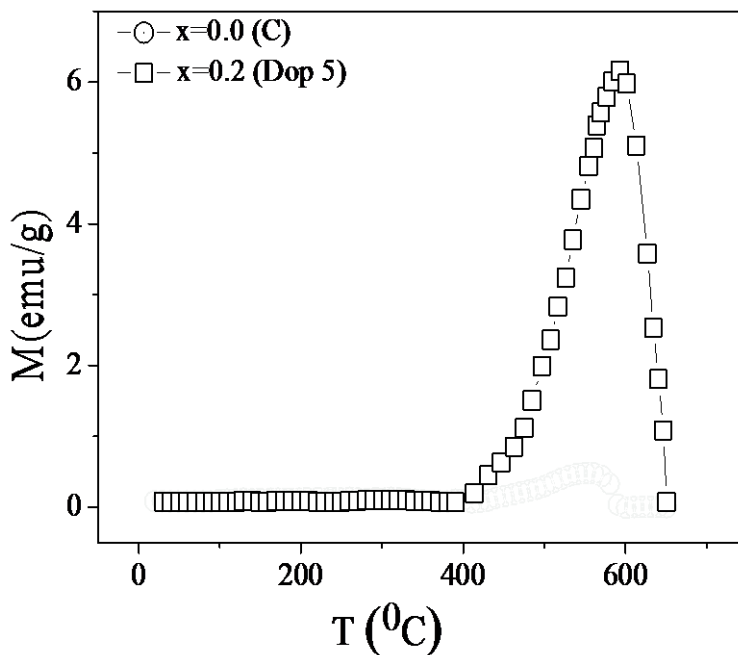


Fig. 5.8 (b) High temperature magnetization vs. temperature of samples $x = 0.0$ (Sample C) at an applied field of 6000 Oe and Sample Dop5 at an applied field of 100 Oe.

We have further measured the hysteresis loops at temperatures 100°C , 400°C , 500°C , 560°C for samples C, Dop 2 and 100°C , 550°C , 600°C , 650°C , 670°C for sample Dop 5 to vindicate the fact and they are shown in Fig.5.9 (a), (b) and (c) respectively. As the temperature is increased above room temperature the sample becomes ferromagnetic and the best magnetic property is observed around the peak. Beyond 550°C the sample again becomes paramagnetic. In case of $x=0.2$ (Dop5) the hysteresis loop at 100°C shows that the sample is highly ferromagnetic with a coercivity of ~ 1.57 kOe. Its magnetic moment at the maximum field of 1.6 kOe is ~ 1.03 emu/g. The loop at 550°C shows that the coercivity becomes very small ~ 0 but the magnetic moment at the maximum field increases to ~ 4.24 emu/g. The magnetic moment increases to ~ 6.37 emu/g at 600°C . Magnetic moment gradually decreases after 600°C and at 670°C the sample becomes paramagnetic.

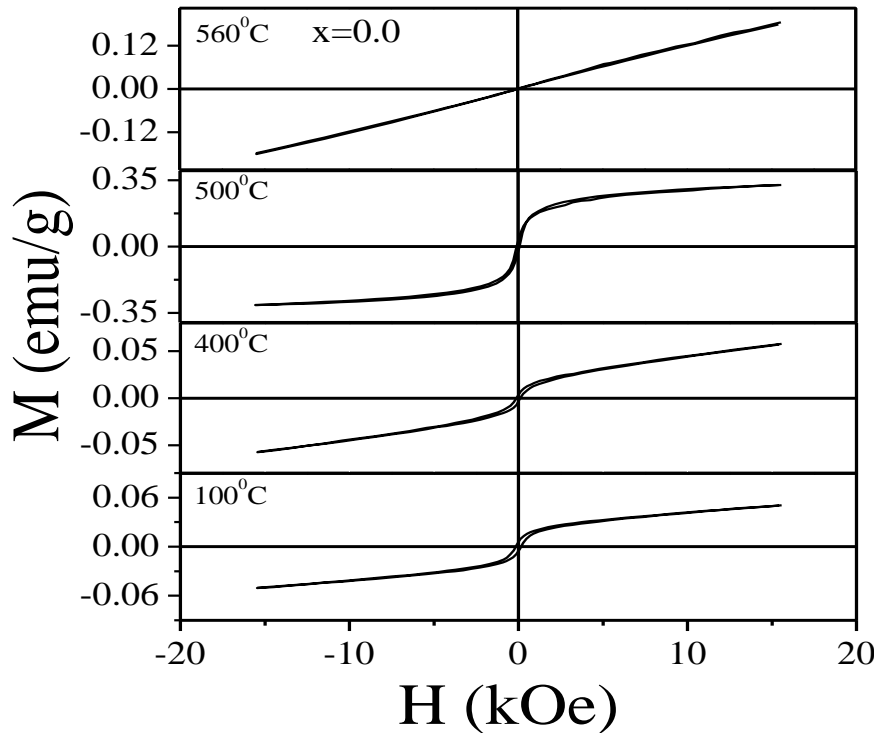


Fig. 5.9 (a):- High Temperature hysteresis loops of sample $x=0.0$ (C) at temperatures 100°C , 400°C , 500°C and 560°C .

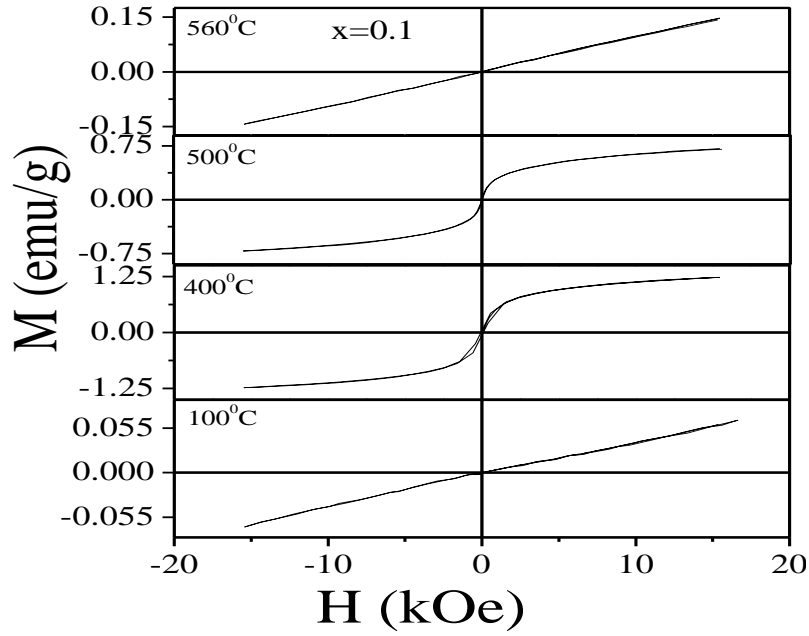


Fig. 5.9 (b) High Temperature hysteresis loops of Lanthanum doped sample $x=0.1$ (Dop1) at temperatures 100°C , 400°C , 500°C and 560°C

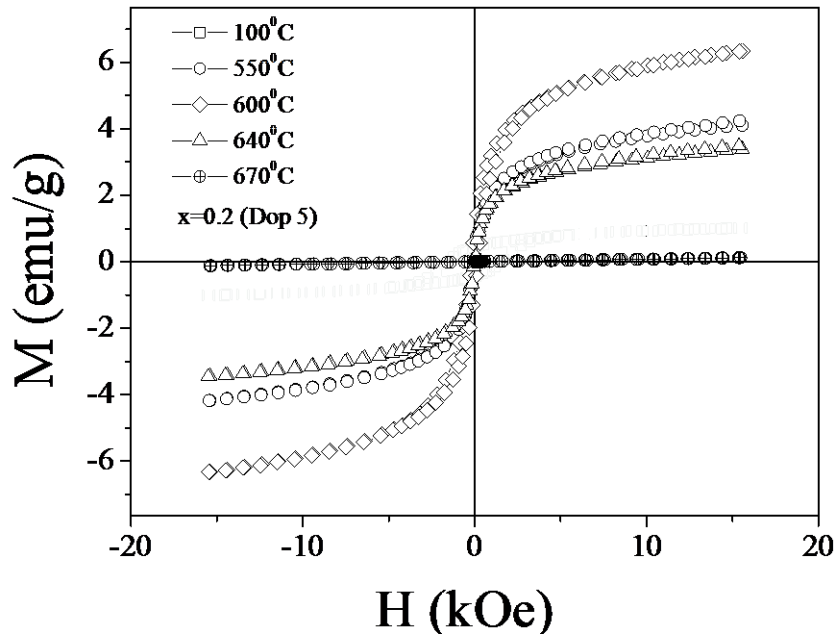


Fig. 5.9 (c) High Temperature hysteresis loops of sample $x=0.2$ (Dop5) of Ba doped BFO at temperatures 100°C , 550°C , 600°C , 640°C and 670°C .

5.3.3 Dielectric properties

A dielectric is considered to be a material with no free charges and under an applied ac field the dielectric properties can be represented by a complex quantity given by

$$\varepsilon^*(\omega) = \varepsilon'(\omega) - j\varepsilon''(\omega) \quad (5.1)$$

The dielectric loss tangent ($\tan \delta$) or dissipation factor (D) is given by

$$\tan \delta = \frac{\varepsilon''}{\varepsilon'} \quad (5.2)$$

Here ω is the angular frequency of the ac voltage field, ε' and ε'' are respectively the dielectric constant and loss, and δ is the phase by which the electric displacement lags behind the applied field. During the dielectric measurements, the electrical equivalent of a composite ceramic can be represented by a parallel combination of capacitance (C_p), and a frequency dependent resistance due to short range polarization $R_{ac}(\omega)$ and a dc resistance R_{dc} due to a long range transport of charge carriers (as shown in Fig. 5.10). C_p and R_p are the equivalent capacitance and resistance measured in the experiment for evaluating the dielectric constant and the loss tangent ($\tan \delta$).

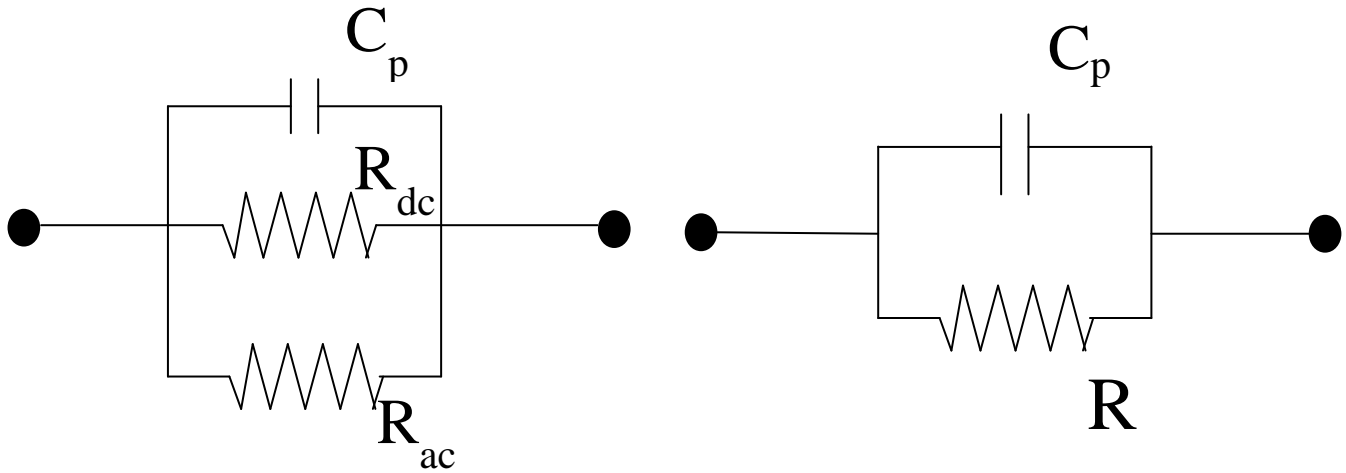


Fig. 5.10: Simplified equivalent circuit of a dielectric ceramic (a) a parallel combination of C_p , R_{dc} and R_{ac} (b) the parallel combination of R_{dc} and R_{ac} replaced by an equivalent resistance R_p .

It may be noted that the resistance R_p in parallel arises due to a combination of both ac and dc conductivity [$\sigma_{ac} + \sigma_{dc}$] in the sample [21]. While making the frequency dependent dielectric measurements using an Impedance Analyzer at a given frequency ω , two quantities are

measured in the balanced condition, C_p the capacitance in the parallel mode, and the dielectric dissipation factor $\tan \delta$, and the measured:

$$\tan \delta = \frac{1}{\omega C_p R_p} \quad (5.3)$$

The measured dielectric loss ε''_{meas} at a given frequency ω is given by;

$$\varepsilon''_{meas} = \varepsilon' \tan \delta \quad (5.4)$$

And (ε') the dielectric constant is calculated from measured C_p by the formulae

$$C_p = \frac{\varepsilon' \varepsilon_0 A}{d} \quad (5.5)$$

where ε_0 = permittivity of free space

A = area of the pellet

d = thickness of the pellet

A schematic representation of the real part of the dielectric constant is shown in Figure 5.11. At high frequencies ($>10^{14}$ Hz), the contribution comes solely from electronic polarization (optical polarization). It arises due to slight displacement of the electron cloud with respect to the positive nucleus because of the application of an electric field. The relaxation time is very fast and of the order of $10^{-15} \sim 10^{-16}$ s. At frequencies ($10^{10} - 10^{14}$ Hz) the contribution comes from the atomic or ionic polarization (Vibrational polarization). It arises because the arrangement of atomic nuclei in a molecule can be distorted by the application of an electric field. While in ionic crystals the positive ions shift with respect to the negative ones. The relaxation time is of the order of $10^{-12} \sim 10^{-13}$ s. At frequencies ($10^4 - 10^{10}$ Hz) the contribution comes from the dipolar or orientation polarization. This arises because molecules having a permanent dipole moment tend to align in the direction of the applied field, giving a net polarization in that direction. The relaxation time is very slow of the order of $10^{-6} \sim 10^{-2}$ s.

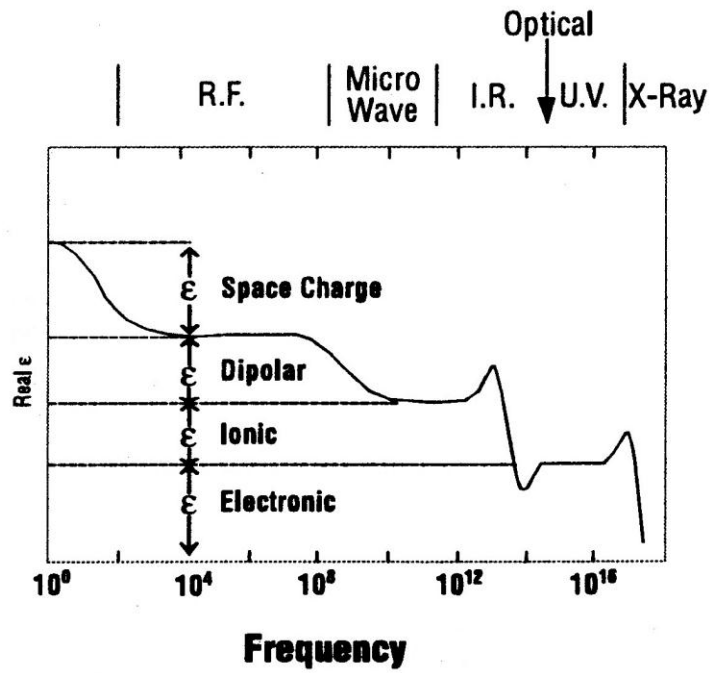


Fig. 5.11: Contributions to the frequency-dependent dielectric constant from the different charge configurations.

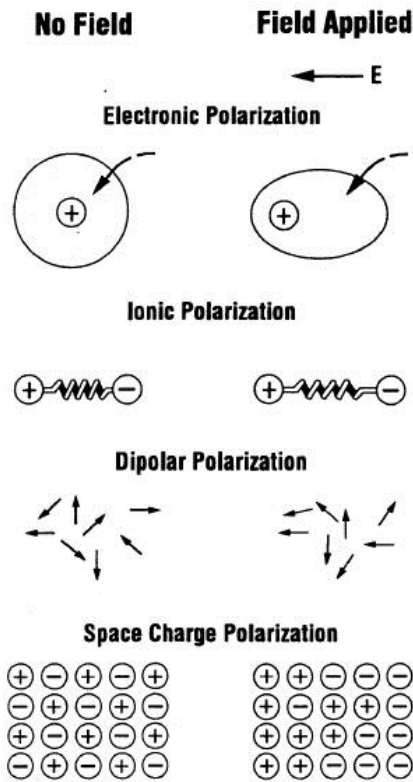


Fig.5.12: Schematic representation of different mechanisms of polarization.

The maximum contribution to the dielectric constant comes from the space charge or interfacial polarization which are present in the grain boundaries or interfaces and can migrate an appreciable distance through a dielectric but become trapped or cannot discharge at an electrode. Its relaxation time is extremely slow.

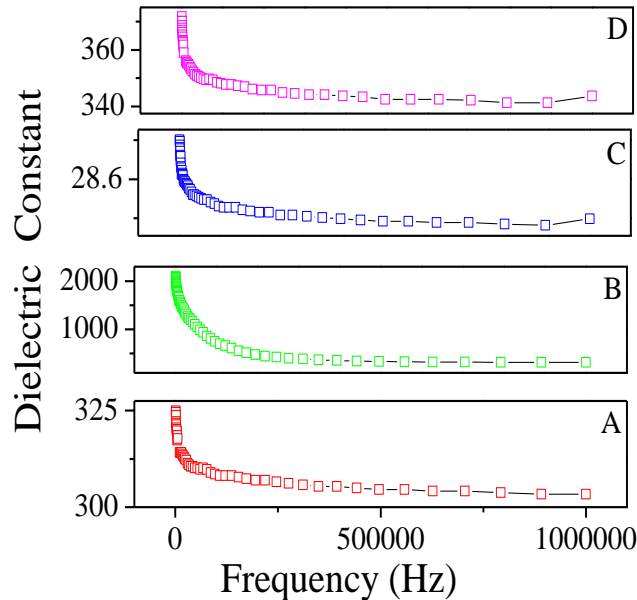
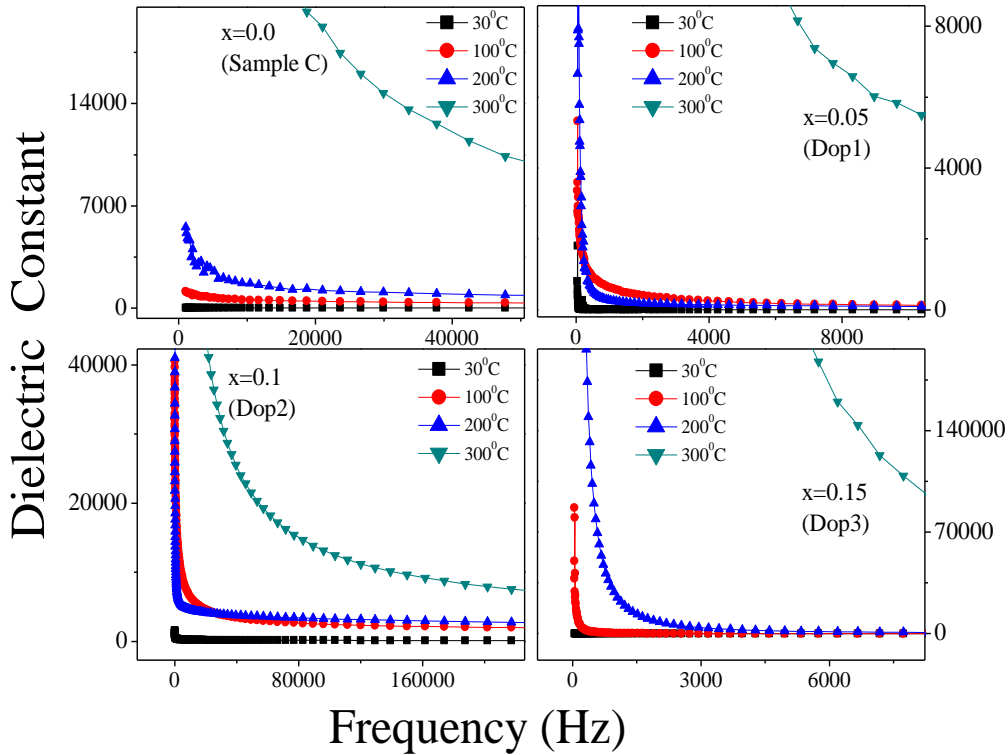


Fig. 5.13 (a):- Dielectric constant of sample A,B,C and D

Fig. 5.13 (a) shows the frequency dependence of dielectric constant of samples A, B, C and D at room temperature. At low frequency the dipoles can follow the applied field. Hence the dielectric constant is high. But after around 1 kHz the dipoles cannot follow the applied field and the dielectric constant remains almost constant. It shows that the dielectric constant is very high for the tile shaped samples compared to the other shapes.

Frequency dependence of the dielectric constant of samples C, Dop1, Dop 2, Dop 3 and C, Dop 4, Dop 5 at temperatures 30°C, 100°C, 200°C, 300°C are shown in Figure 5.13 (b) and Figure 5.13 (c) respectively. Dielectric constant followed Debye law of frequency dispersion, i.e., it remained fairly constant at high frequencies and increased at low frequency [22]. The increase in dielectric constant with decrease in frequency (below 1 kHz) can be explained by the phenomenon of space charge (mostly residing in grain boundaries) relaxation. These space charge forms defect dipoles which can only follow the applied field at lower frequencies. At high frequencies, they may not have the time to build up and undergo relaxation.



5.13 (b):- Dielectric constant vs. Frequency plot of samples C, Dop 1, Dop 2 and Dop 3 at temperatures 30^oC, 100^oC, 200^oC and 300^oC.

For each composition, the dielectric constant increases with temperature. With the increase in temperature dipole-dipole interaction reduces resulting in more dipoles aligning towards the applied field. Hence this increase in dielectric constant took place. The incorporation of La³⁺ (ionic radii. 1.16 Å) and Ba³⁺ (ionic radii 1.42 Å) in the Bi (ionic radii 1.03 Å) site of BFO lattice might cause an off-centre movement of Fe³⁺ ions in the octahedra since the ionic size of Lanthanum and Barium are bigger than that of Bismuth. This will lead to an increase in polarization ability in the form of dielectric constant. The dielectric loss (D) decreases in the whole frequency range and decreases along with the doping level, as shown in Fig. 5.14. Decrease of dielectric loss imply that the conductive property of undoped BFO is decreasing with doping.

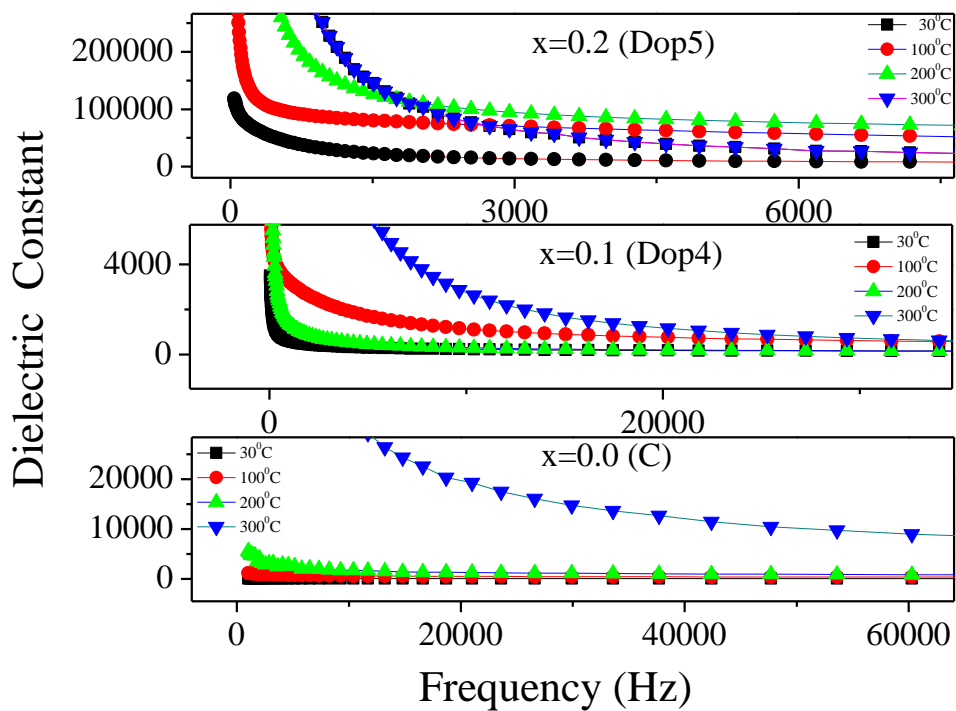


Fig. 5.13 (c):- Dielectric Constant vs. Frequency graphs of samples C, Dop 4 and Dop 5 at temperatures 30°C, 100°C, 200°C, 300°C.

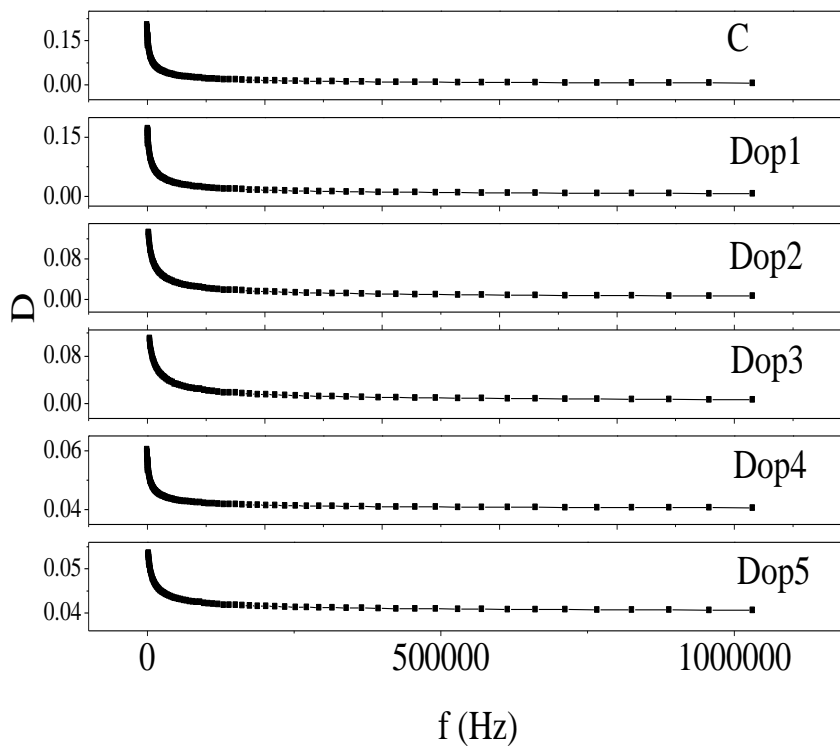


Fig. 5.14: Dielectric Loss (D) vs frequency of all the samples

Fig.5.15 (a) represents the Complex Impedance Cole-Cole [23] (imaginary part of the complex impedance: Z'' vs. real part of the complex impedance: Z') plot for undoped BFO (C) and Lanthanum $x=0.05$ (Dop1), $x=0.1$ (Dop2), $x=0.15$ (Dop3) Barium $x=0.1$ (Dop4), $x=0.2$ (Dop5) doped BFO pellets at temperatures 30°C , 100°C , 150°C , 200°C and 250°C in the frequency range of 40 Hz to 110 MHz. The peak of the curve corresponds to the largest value of Relaxation and the corresponding frequency can be obtained from the measured data [24]. Now multiplying frequency with $2*\pi$ we get the corresponding ω (angular frequency). We know that $\omega*\tau=1$, where τ = Relaxation time and by calculating the relaxation time from the values of angular momentum we can get different values of τ corresponding to different Temperatures. Now we can plot a graph between (Fig.5.15 (b)) $\ln(\tau)$ vs. $1/T$ (T =Temperature in Kelvin). From the slope of these graphs and using the equation:

$$\tau = \tau_0 \exp\left(\frac{-E_r}{k_B T}\right) \quad (5.6)$$

where, τ_0 =Pre exponential constant which equals to the relaxation time at infinitely high Temperature,

k_B =Boltzmann Constant,

T =Temperature in Kelvin

we can obtain the values of E_r =Activation energy for Dielectric Relaxation.

The straight line confirms the Debye like behavior [25,26]. A decrease of relaxation time with Temperature can be noted here. The possibility of existence of multiple equilibrium states with a distribution of relaxation time in the nanosystem is thus evident here. The hopping depends on the Activation energy for Dielectric Relaxation which is associated with the electrical energy barrier experienced by the electrons during hopping.

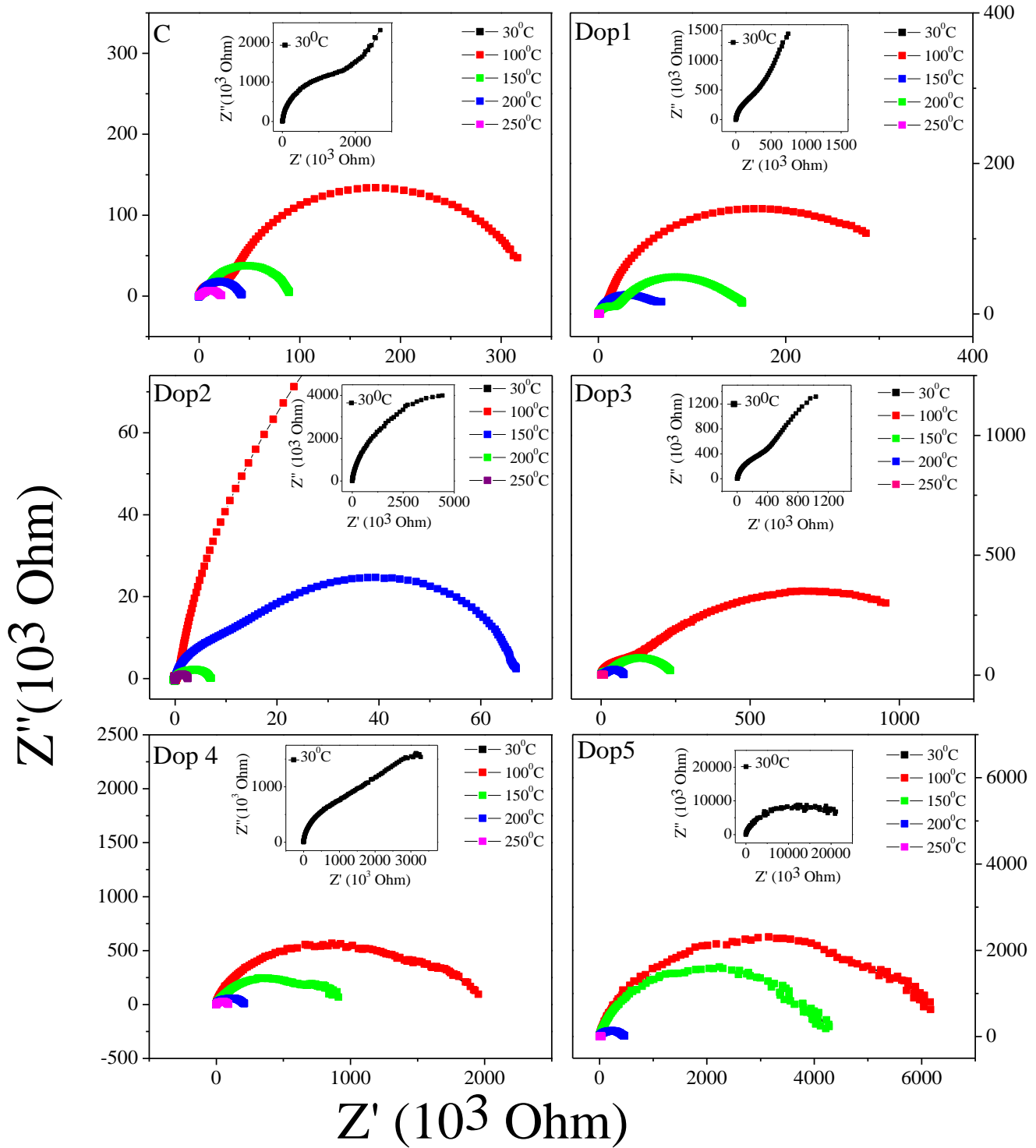


Fig.5.15 (a): Cole Cole plot of samples $\text{Bi}_{(1-x)}\text{La}_x\text{FeO}_3$ $x=0.0$ (C) $x=0.05$ (Dop1) $x=0.1$ (Dop 2) and $x=0.15$ (Dop3) $\text{Bi}_{(1-x)}\text{Ba}_x\text{FeO}_3$ $x=0.1$ (Dop4) $x=0.2$ (Dop5).

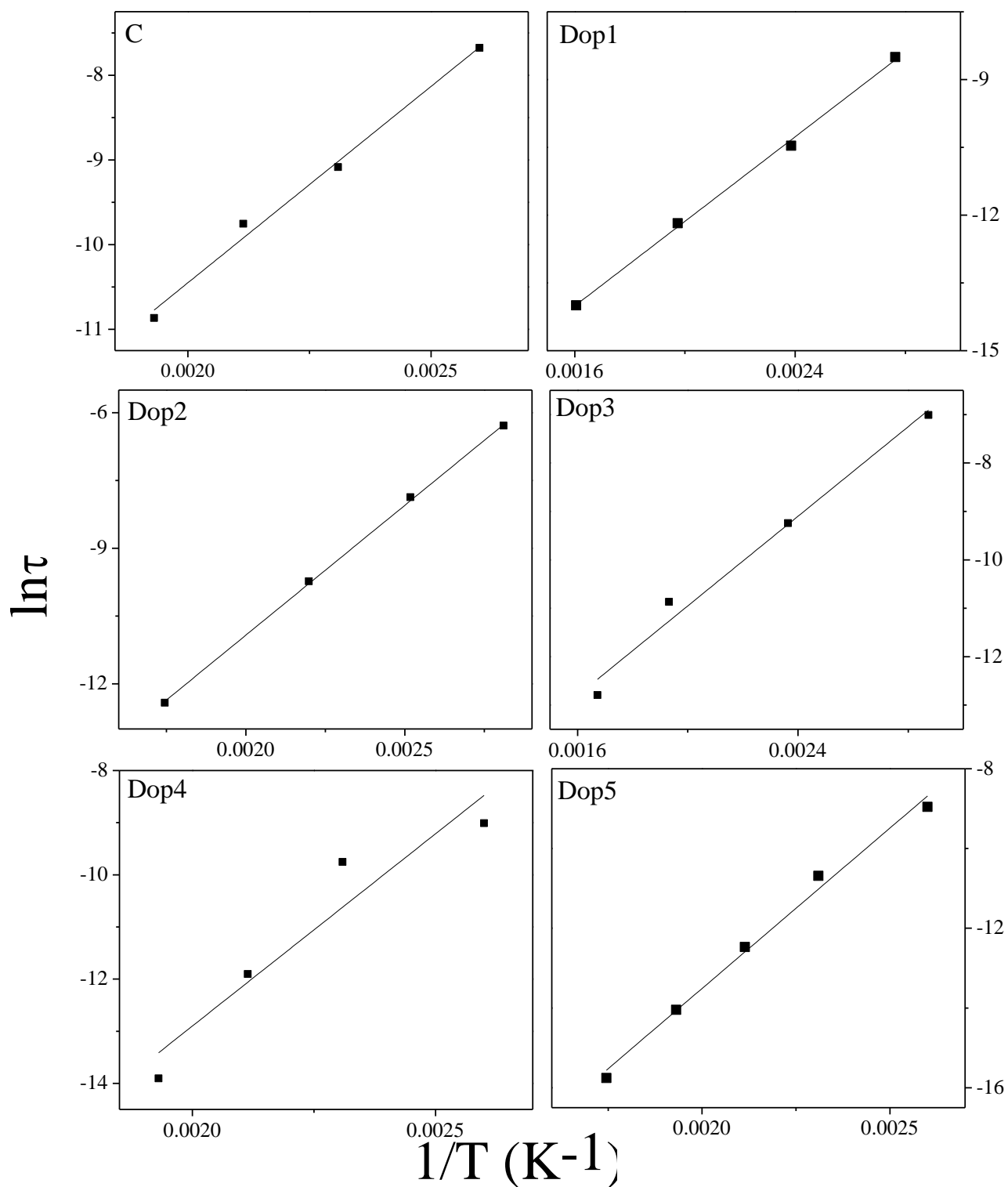


Fig.5.15 (b): $\ln \tau$ vs $1/T$ plot of samples $\text{Bi}_{(1-x)}\text{La}_x\text{FeO}_3$ $x=0.0$ (C) $x=0.05$ (Dop1) $x=0.1$ (Dop2) and $x=0.15$ (Dop3) $\text{Bi}_{(1-x)}\text{Ba}_x\text{FeO}_3$ $x=0.1$ (Dop4) $x=0.2$ (Dop5).

Figure 5.16 (a) shows the ac conductivity plotted as a function of frequency at varying temperatures in the range of 30–250°C. We have calculated the conductivity from the conductance from the relation

$$\sigma = Gl/A \quad (5.7)$$

where, σ =Conductivity

G =Conductance

l =Thickness of the pellet

A =Area of cross section of pellet

The plots tend to flatten with increasing temperature in the low frequency region, and the flattened region becomes wide and is shifted toward higher frequencies with increasing temperature. The low frequency flat (frequency independent) region is due to dc conductivity, while the frequency dependent region is due to ac conductivity of the nonconductive region. With the increase in temperature the conductivity of these pellets increases, due to the increase in oxygen vacancy mobility, and the flattened region shifts upwards and dominates over a larger range of frequencies [27,28]. The σ_{ac} becomes frequency independent at these frequencies, suggesting a dc conduction behavior. Figure 5.12 (b) shows the dc conductivity versus $1/T$ at different frequencies. The temperature dependence of dc conductivity can be described by the Arrhenius equation

$$\sigma_{dc} = \sigma_0 \exp\left(\frac{E_a}{k_B T}\right) \quad (5.8)$$

where σ_0 = pre-exponential constant which is the ac conductivity at infinitely high temperature and k_B are constant and E_a is the electrical activation energy of conduction, which can be calculated at different frequencies from the line slopes in Fig. 5.16 (b). From Eq.5.8, the activation energy of conduction for all the samples were calculated which is shown in Table 5.1.

Oxygen vacancies are mobile charges and often play an important role in the conduction process of Bismuth Ferrite pellets. The calculated value of activation energy suggests that the involvement of oxygen vacancies at high temperatures in the pellets. It is observed that the activation energy increases with the increase in the doping concentration [29]. It proves that the dielectric performance of BFO enhances with doping. It was also observed that the value of E_f is

close to that of E_a , confirming the same type of charge carriers that are responsible for dielectric relaxation and conduction of the BFO and doped BFO pellets.

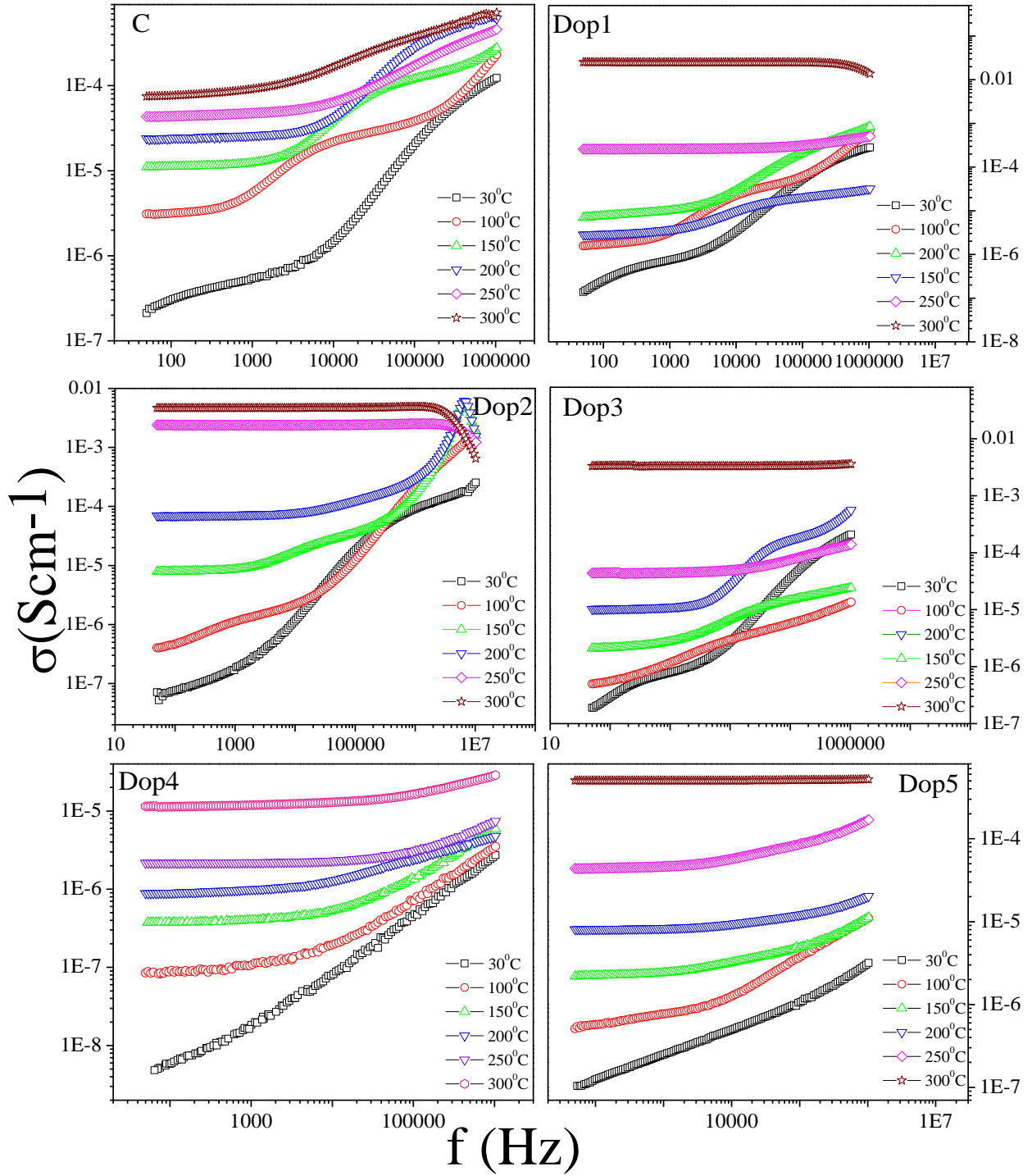


Fig.5.16 (a) : Ac conductivity vs Frequency plot of samples $\text{Bi}_{(1-x)}\text{La}_x\text{FeO}_3$ $x=0.0$ (C), $x=0.05$ (Dop1), $x=0.1$ (Dop2), $x=0.15$ (Dop3) and $\text{Bi}_{(1-x)}\text{Ba}_x\text{FeO}_3$ $x=0.1$ (Dop4) $x=0.2$ (Dop5).

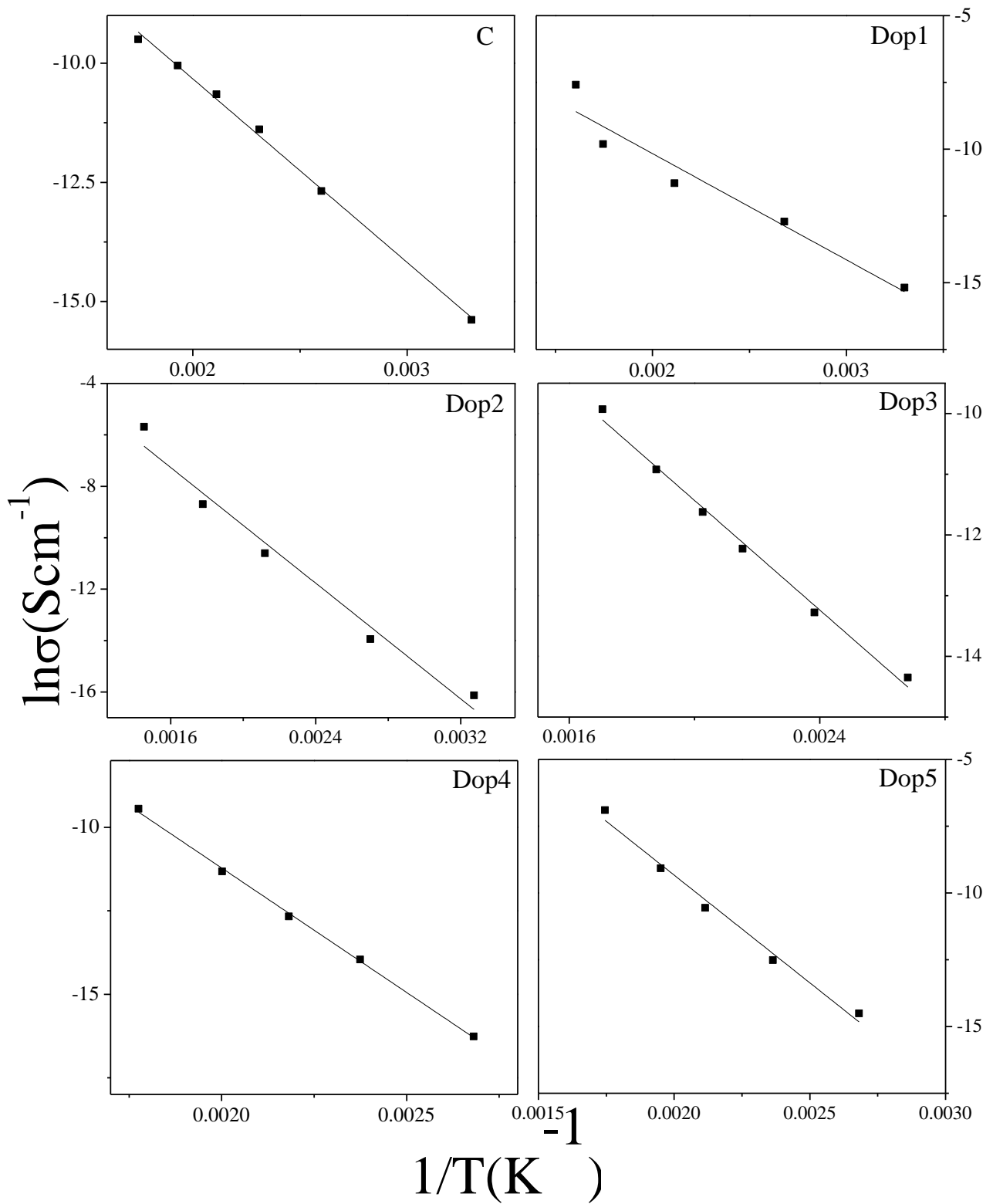


Fig. 5.16 (b) $\ln\sigma$ vs $1/T$ of samples $\text{Bi}_{(1-x)}\text{La}_x\text{FeO}_3$ $x=0.0$ (C) $x=0.05$ (Dop1) $x=0.1$ (Dop2) $x=0.15$ (Dop3) and $\text{Bi}_{(1-x)}\text{Ba}_x\text{FeO}_3$ $x=0.1$ (Dop4), $x=0.2$ (Dop5).

Table 5.1: Activation Energy for conduction (E_a) and Activation Energy for relaxation(E_r) for all the samples

Sample	E_a (eV)	E_r (eV)
BFO (C)	0.3317	0.39936
$\text{Bi}_{0.95}\text{La}_{0.05}\text{FeO}_3$ (Dop1)	0.3428	0.3834
$\text{Bi}_{0.9}\text{La}_{0.1}\text{FeO}_3$ (Dop2)	0.4847	0.4952
$\text{Bi}_{0.85}\text{La}_{0.15}\text{FeO}_3$ (Dop3)	0.3891	0.3987
$\text{Bi}_{0.9}\text{Ba}_{0.1}\text{FeO}_3$ (Dop4)	0.6428	0.6352
$\text{Bi}_{0.8}\text{Ba}_{0.2}\text{FeO}_3$ (Dop5)	0.6950	0.6933

Figure 5.17 shows the Polarization (P) versus Electric Field (E) loops of the Barium doped BFO samples having $x=0.0$ (C), $x=0.1$ (Dop4) and $x=0.2$ (Dop5). The P vs. E loop of sample C is just a straight line passing through the origin having zero remnant polarization. Unsaturated hysteresis loops were obtained for the samples having $x=0.1$ (Dop4) and $x=0.2$ (Dop5). The remnant polarization of the sample Dop4 is $\sim 0.07 \mu\text{C}/\text{cm}^2$ and that of the sample Dop5 is $\sim 0.03 \mu\text{C}/\text{cm}^2$ [30]. Hence polarization is enhanced with doping.

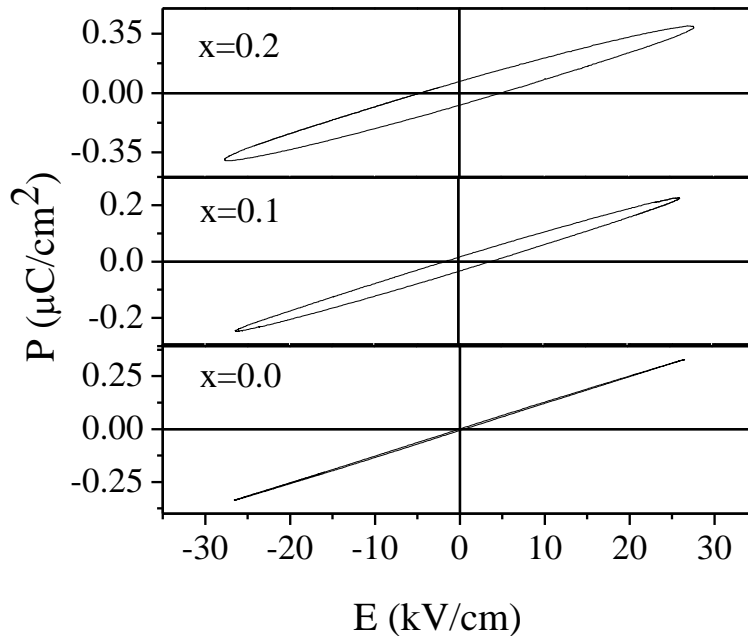


Fig. 5.17 :- Polarization vs Electric Field hysteresis loop of samples $\text{Bi}_{(1-x)}\text{Ba}_x\text{FeO}_3$ $x=0.0$ (C), $x=0.1$ (Dop4) and $x=0.2$ (Dop5).

The electron spin resonance (ESR) spectra at 9440.9 MHz of $\text{Bi}_{(1-x)}\text{La}_x\text{FeO}_3$ with $x = 0.0$ (C), 0.05 (Dop1), 0.1 (Dop2) and 0.15 (Dop 3) are shown in Fig. 5.18. The g-value was obtained from the formulae

$$h\nu = g\mu_B H \quad (5.9)$$

where h was Planck's constant, ν the operating frequency and μ_B , the Bohr Magneton.

Fig. 5.18 corresponding to $x = 0.0$, shows only a single absorption spectrum with $g = 2.16$ due to the resonance absorption in the cycloidal spin structure, marked as R_{cyc} . On doping La, more than one peaks are observed which indicated the presence of more absorption lines [31,32]. This means that with doping free spins are developed. The reason for the development of free spins must be the breakage of the spin cycloid. The ESR line with narrow line width is associated with the defect induced free spins (R_{def}) while the other one with relatively wider line width is the resonant absorption in the cycloidal spin structure (R_{cyc}) as mentioned earlier. The g-value obtained from R_{cyc} of the La-doped samples increases from 2.14 to 2.72 whereas that obtained from R_{def} decreases from 2.17 for $x = 0.0$ to 2.03 for $x = 0.1$ and then increases to 2.11 for $x = 0.15$. g-values obtained from all the samples are shown in the Table 5.2.

Table 5.2: Calculated g values of all the samples

Sample	g value from R_{cyc}	g value from R_{def}
BiFeO_3	2.1668	
$\text{Bi}_{0.95}\text{La}_{0.05}\text{FeO}_3$	2.462	2.0907
$\text{Bi}_{0.9}\text{La}_{0.1}\text{FeO}_3$	2.521	2.0271
$\text{Bi}_{0.85}\text{La}_{0.15}\text{FeO}_3$	2.7284	2.1145

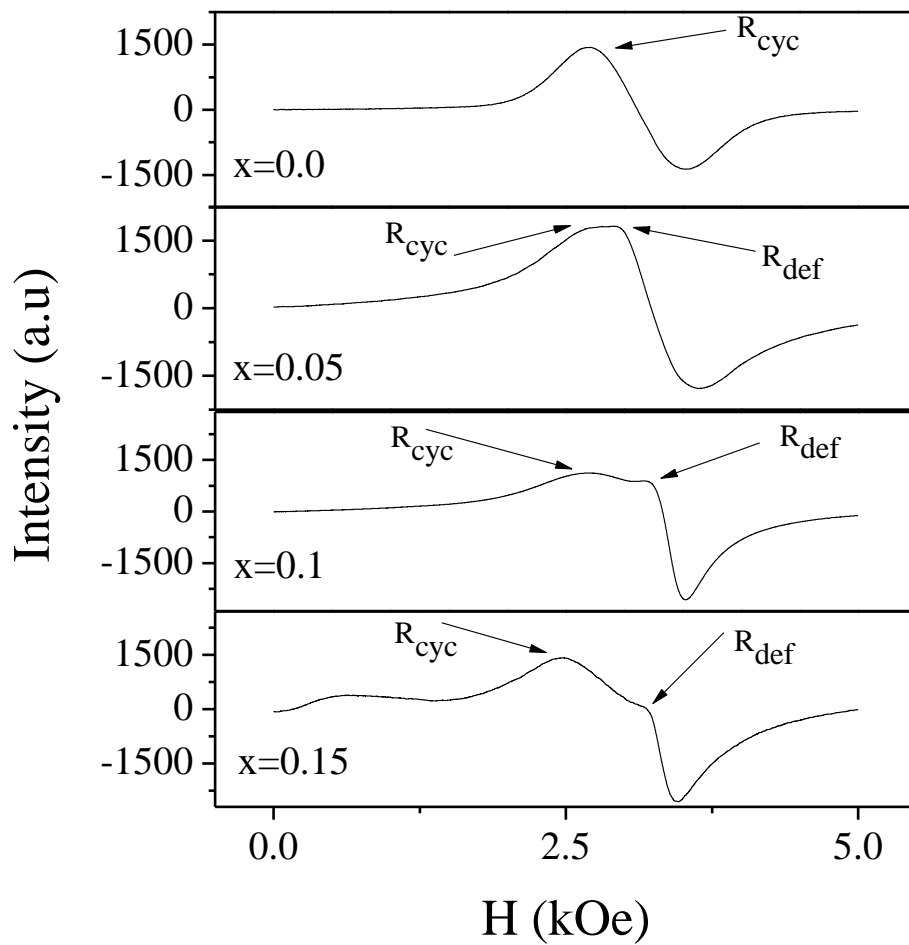


Fig. 5.18: Electron spin resonance spectra (ESR) of samples $\text{Bi}_{(1-x)}\text{La}_x\text{FeO}_3$ $x = 0.0$ (C), $x = 0.05$ (Dop1), $x = 0.1$ (Dop2) and $x = 0.15$ (Dop3) at 300 K.

5.4 Conclusions

Nanostructured BiFeO_3 was prepared by solvothermal process. Spindle, plate, cylindrical and hexagonal particles are grown by changing the preparation temperature and solvent. All the samples show antiferromagnetic ordering within the measured temperature range of $80\text{K} \leq T \leq 300\text{K}$. The plate shaped samples show the best magnetic as well as dielectric properties. The cylindrical shaped BFO nanoparticles were doped with different concentration of Lanthanum and Barium by the hydrothermal technique. For the La 0.1 doped sample we obtain rod shaped nanoparticles. In case of Barium doping also morphology of the particles changed with doping which is proved from the XRD and FESEM analysis. Both magnetization and dielectric constant increase with the increase in doping concentration with the maximum enhancement occurring in Barium doped samples. The difference in ionic radius of Lanthanum and Barium ions in comparison to Bismuth ion might be one of the reasons for the distortion in the oxygen octahedra which leads to polarization ability in the form of dielectric constant. The dielectric loss decreases with the increase in doping concentration with the minimum loss occurring for the Ba 0.2 doped BFO sample. The activation energy for conduction and activation energy for relaxation has been calculated from the cole-cole plot and the plot of log of ac conductivity vs. frequency. The activation energy increases with the increase in doping indicating the better performance as a dielectric of BFO after doping. An abrupt increase in magnetization is observed from 400°C which has been attributed to the spin canting due to lattice distortion and the increase in thermal energy. Electron spin resonance study of the La doped BFO proves the breakage of spin cycloid with doping.

References

- [1] R. Ramesh, N.A. Spaldin, *Nat. Mater.* **6**, 21 (2007).
- [2] S.-W. Cheong, M. Mostovoy, *Nat. Mater.* **6**, 13 (2007).
- [3] C.-L. Jia, N. Nagaranjan, J.Q. He, L. Houben, T. Zhao, R. Ramesh, K. Urban, R. Waser, *Nat. Mater.* **6**, 64 (2007).
- [4] P. Muralt, *Nat. Mater.* **6**, 8 (2007).
- [5] A. Chaudhuri, S. Mitra, M. Mandal, K. Mandal *J. Alloys and Compd.* **491**, 703 (2010).
- [6] P. Fischer, M. Polomska, I. Sosnowska, M. Szymanski, *J. Phys. C Solid State Phys.* **13**, 1931 (1980).
- [7] V.A. Khomchenko et al. *J. Magn. Magn. Mater.* **321**, 1692 (2009).
- [8] M. Kumar and K. L. Yadav *Appl. Phys. Lett.* **91**, 242901 (2007).
- [9] B. Bhushan, A. Basumallick, S. K. Bandopadhyay, N. Y. Vasanthacharya and D Das, *J. Phys. D: Appl. Phys.* **42**, 065004 (8pp) (2009).
- [10] A. Chaudhuri, K. Mandal *Materials Research Bulletin* **47**, 1057 (2012).
- [11] Y.H. Lin, Q. Jiang, Y. Wang, C.W. Nan, L. Chen, J. Yu, *Appl. Phys. Lett.* **90**, 172507 (2007).
- [12] Y. Du, Z. X. Cheng, M. Shahbazia, E. W. Collings, S. X. Doua, X. L. Wang *J. of Alloys and Compounds* **490**, 637 (2010).
- [13] J.T. Han, Y. H. Huang, X.J. Wu, C.L. Wu, W. Wei, B. Peng, W. Huang and J. B. Goodenough *Adv. Mater.* **18**, 2145 (2006).
- [14] S. Mitra, S. Das, K. Mandal, S. Chaudhuri, *Nanotechnology* **18**, 275608 (9pp.) (2007).
- [15] H. G. Jonker, *Physica*, **22**, 707 (1956).
- [16] A.K. Pradhan, K. Zhang, D. Hunter, J.B. Dasdon, G.B. Loutts, *J. Appl. Phys.* **97**, 093903 (2005).
- [17] S.R. Das, R.N.P. Choudhary, P. Bhattacharya, R.S. Katiyar, *J. Appl. Phys.* **101**, 034104 (2007).
- [18] Jinrong Cheng et al. *J. of the European Ceramic Society* **30**, 265 (2010).
- [19] Meiya Li, Min Ning, Yungui Ma, Qibin Wu and C K Ong, *J. Phys. D: Appl. Phys.* **40**, 1603 (2007).
- [20] S. Mitra, S. Das, S. Basu, P. Sahu, K. Mandal, *J. Magn. Mag. Mater.* **321**, 2925 (2009).

- [21] A. Mansingh Bull. Mater. Sci. **2**, 325 (1980).
- [22] P Uniyal and K L Yadav J. Phys.: Condens. Matter **21**, 405901 (6pp) (2009).
- [23] J. Wu and J. Wang J. of App. Phys. **105**, 124107 (2009).
- [24] Y. Z. Wei and S. Sridhar J. Chem. Phys., **99**, 3119 (1993).
- [25] E. R. Losilla, M. A. G. Aranda, S. Bruque, M. Paris, J. Sanz, and A. R. West, Chem. Mater. **10**, 665 (1998).
- [26] S. R. Elliott, Solid State Ionics **70–71**, 27 (1994).
- [27] D. P. Almond, C. R. Bowen, and D. A. S. Rees, J. Phys. D: Appl. Phys. **39**, 1295 (2006).
- [28] C. R. Bowen and D. P. Almond, Mater. Sci. Technol. **22**, 719 (2006).
- [29] J. G. Wu, G. Q. Kang, H. J. Liu, and J. Wang, Appl. Phys. Lett. **94**, 172906 (2009).
- [30] D. H. Wang, W. C. Goh, M. Ning, C. K. Ong, Appl. Phys. Lett. **88**, 212907 (2006).
- [31] J. W. Lin, Y. H. Tang, C. S. Lue, and J. G. Lin App Phys. Lett. **96**, 232507 (2010).
- [32] B. Ruetter *et. al.* Phys. Rev. B **69**, 064114 (2004)

Chapter 6

6 Magnetolectric properties in $\text{CoFe}_2\text{O}_4/\text{BaTiO}_3$ core shell nanocomposites

6.1 Preamble

Magnetolectric (ME) effect is the phenomenon of inducing magnetization by applying an external electric field and vice versa due to coupling of the two ferroic orders. According to the original definition by, van Suchtelen in 1972 [1] the composite ME effect is a result of the product of the magnetostrictive effect (magnetic/mechanical effect) in the magnetic phase and the piezoelectric effect (mechanical/electrical effect) in the ferroelectric phase,

$$ME\ effect = \frac{\text{Magnetic}}{\text{Mechanical}} * \frac{\text{Mechanical}}{\text{Electric}} \quad (6.1)$$

The application of a magnetic field in the magnetostrictive phase will induce a strain in it which in turn will induce a strain in the piezoelectric phase resulting in the generation of ferroelectricity. ME materials find applications as smart materials in actuators, sensors, magnetic probes, phase inverters, rectifiers, modulators, and transducers in solid state microelectronics and microwave devices [2-3]. This effect can be realized in single phase as well as composite materials. But in single phase materials it is difficult to obtain magnetolectric effect for the simple reason that magnetic and electric dipoles have to coexist in an assymetric structure. These limitations can be overcome by the synthesis of composites of magnetostrictive and piezoelectric phases. Some Iron Oxides like CoFe_2O_4 are highly magnetostrictive. BaTiO_3 is also highly piezoelectric. Composites also do not solve the problem completely. In composites the particles are present in an agglomerated state with an irregular distribution. This increases the conductivity of the sample and hence it becomes very lossy. This problem can be overcome by

preparing core shell particles. This motivated us to synthesize nanostructured core shell $\text{CoFe}_2\text{O}_4:\text{BaTiO}_3$ nanocomposites. We have also prepared a mixture of $\text{CoFe}_2\text{O}_4:\text{BaTiO}_3$ nanoparticles for comparison with the core shell nanoparticles. We have shown that the magnetoelectric coupling in the core shell nanocomposites is higher than in the mixture of the two phases. Studies by Van den Boomgaard et al. [4] have first demonstrated that the effective magnetoelectric coupling effect in the composite materials relies on the chemical equilibrium of the phases, the magnetostriction and piezoelectric coefficient of the ferrite and ferroelectric phases, the mechanical coupling between the grains of the constituent phases, the resistivity, and the molar percentage of the constituent phases.

6.2 Experimental

6.2.1 Synthesis of CoFe_2O_4

Synthesis of CoFe_2O_4 nanoparticles was performed by the hydrothermal technique. All the chemicals obtained were of analytical grade. $\text{Co}(\text{NO}_3)_2 \cdot 6\text{H}_2\text{O}$; $\text{Fe}(\text{NO}_3)_3 \cdot 9\text{H}_2\text{O}$ were used as precursors. Polyvinylpyrrolidone (PVP) was used as capping agent. Sodium Borohydride (NaBH_4) was used as a reducing agent. $\text{Co}(\text{NO}_3)_2 \cdot 6\text{H}_2\text{O}$ and $\text{Fe}(\text{NO}_3)_3 \cdot 9\text{H}_2\text{O}$ were mixed in stoichiometric ratio. A clear solution of them in 60 ml of distilled water was prepared. NaBH_4 and PVP were added. The precursor solution was then transferred to a Teflon lined steel autoclave of capacity 80 ml [5]. The Teflon chamber was kept at 120°C for 12 hours to crystallize the particles. After that the autoclave was cooled to room temperature naturally. The as obtained CoFe_2O_4 nanoparticles were washed in a centrifuge to remove the impurities.

6.2.2 Synthesis of $\text{CoFe}_2\text{O}_4:\text{BaTiO}_3$ core shell

A solution of $\text{CoFe}_2\text{O}_4:\text{BaTiO}_3$ core shell in the weight ratio of 1:1 was prepared following the sol gel route using citric acid as a functionalizing agent and ethanol as a solvent. A solution of BaCO_3 was prepared in distilled water. Citric Acid was added to dissolve the BaCO_3 . Then a solution of Titanium Isopropoxide was prepared in Ethanol and Citric Acid was also added here [6]. Then these two solutions were mixed with each other to form a sol. A dispersed solution of CoFe_2O_4 in Ethanol was prepared by ultrasonication of the solution in an ultrasonication bath. The weight of CoFe_2O_4 was so calculated that the weight ratio of CFO:BTO be 1:1. This solution was

then added to the sol and the mixture was heated at 90⁰C to form a gel. The gel was then dried at 80⁰C overnight in an oven. The dried gel was then annealed at 750⁰C for 5 hours.

The powder was pressed into discs of 5 mm diameter and 1 mm thickness at a pressure of 60 MPa in a hydraulic press with polyvinyl alcohol as a binder. The pellets were sintered at a high temperature of 600⁰C for 3 h. For the measurements of electrical properties, the ceramic discs were carefully polished and subsequently pasted with Ag paste on both sides as electrodes [7]. To enable the ME effect, composites need to be poled both electrically and magnetically. During the electric poling the samples were heated above the ferroelectric Curie temperature T_C ie. 120⁰C (in silicon oil) and cooled under the influence of an external electric field of 6 kV/cm to room temperature. The samples were poled magnetically by applying the static dc magnetic field of 4.0 kOe at room temperature. For comparison, a sample with similar composition was produced by mixing the CoFe₂O₄ and BaTiO₃ powders following the same heat treatment and poling procedure. The crystalline structure of composite materials was investigated by X-ray diffractometer (XRD) using Cu-K_α radiation. The hysteresis loops were measured at room temperature using a Vibrating Sample magnetometer (Lake Shore Cryotronics) which generates field up to 1.6 T. The core shell structure was investigated by High Resolution Transmission Electron Microscope (HRTEM). The dielectric constant was measured by the Impedance Analyzer (Agilent 4294A). The ME coefficient was measured using lock-in technique which is described in Chapter 2. We have employed an AC field of 20 Oe superimposed onto a DC magnetic field (generated by an electromagnet) up to ~5 kOe.

When ME materials are exposed to a magnetic field H , a voltage V appears. Assuming

$$V = f(H) = Const + \alpha H + \beta H^2 + \gamma H^3 + \delta H^4 + \dots \quad (6.2)$$

$$\Rightarrow \frac{dV}{dH} = \alpha + \beta H + 3\gamma H^2 + 4\delta H^3 + \dots \quad (6.3)$$

When a small AC field $h = h_0 \sin \omega t$ is superimposed onto a DC bias field H , the total field:

$$H_{total} = H + h_0 \sin(\omega t). \quad (6.4)$$

Then

$$V = \text{const} + \alpha(H + h_0 \sin \omega t) + \beta(H + h_0 \sin \omega t)^2 + \gamma(H + h_0 \sin \omega t)^3 + \delta(H + h_0 \sin \omega t)^4 + \dots$$

$$\begin{aligned} V_{out} = & \frac{1}{8} [(Const + 4\beta h_0^2 + 3\delta h_0^4 + 8\alpha H + 12\gamma h_0^2 H + 8\beta H^2 + 24\delta h_0^2 H^2 + 8\gamma H^3 + 8\delta H^4) \\ & + (8\alpha h_0 + 6\gamma h_0^3 + 16\beta h_0 H + 24\delta h_0^3 H + 24\gamma h_0 H^2 + 32\delta h_0 H^3 \sin \omega t) + \\ & (-4\beta h_0^2 - 4\delta h_0^4 - 12\gamma h_0^2 H - 24\delta h_0^2 H^2) \cos 2\omega t + (-2\gamma h_0^3 - 8\delta h_0^3 H) \sin 3\omega t \\ & + \delta h_0^4 \cos 4\omega t + \dots] \end{aligned}$$

The lock-in amplifier output voltage V_{out} is

$$\begin{aligned} V_{out} = & \frac{1}{8} (8\alpha h_0 + 6\gamma h_0^3 + 16\beta h_0 H + 24\delta h_0^3 H + 24\gamma h_0 H^2 + 32\delta h_0 H^3) \\ = & \frac{H^4}{8} \left[\frac{8\alpha}{H^3} \left(\frac{h_0}{H} \right) + \frac{6\gamma}{H} \left(\frac{h_0}{H^3} \right) + \frac{16\beta}{H^2} \left(\frac{h_0}{H} \right) + 24\delta \left(\frac{h_0}{H} \right)^3 + \frac{24\gamma}{H} \left(\frac{h_0}{H} \right) + 32\delta \left(\frac{h_0}{H} \right) \right] \end{aligned}$$

Neglecting high order terms in $\left(\frac{h_0}{H} \right)$ when $\left(\frac{h_0}{H} \right)$ is $\ll 1$

$$\begin{aligned} V_{out} = & \frac{H^4}{8} \left(\frac{8\alpha}{H^3} + \frac{16\beta}{H^2} + \frac{24\gamma}{H} + 32\delta \right) \left(\frac{h_0}{H} \right) \\ = & h_0 (\alpha + 2\beta H + 3\gamma H^2 + 4\delta H^3) \\ = & h_0 \frac{dV}{dH} \end{aligned}$$

$$\text{ME coefficient} = \frac{dE}{dH} = \frac{1}{d} \frac{dV}{dH} = \frac{V_{out}}{h_0 d} \quad (6.5)$$

where d is the effective thickness of the piezoelectric phase.

Looking in the equations above one can recognize that the philosophy of this technique is to measure the effective value of the small AC ME voltage (V_{out}) appearing across the sample when applying a small AC magnetic field instead of measuring the ME charge or voltage as in the static method. This method also allows one to measure the phase shift of the signal. However, this phase shift is approximately constant during varying the bias field measurements. By changing the DC magnetic bias field, one can explore the ME effect at different working points of the sample. And by changing the frequency of the AC field, one can study the response

of the sample under different time scale. Since the ME signal in this method has a well-defined frequency (determined by the driving current) and is measured by a lock-in amplifier, the noise is dramatically reduced and the problem of charge accumulation is avoided. These are the advantages of this method. However, due to the assumption that the AC field is much smaller than the DC one ($\frac{h^0}{H} \ll 1$), this method will give information about the ME effect at low-AC magnetic field but at different working points of the magnetostrictive component. Since an AC magnetic field is employed, an induction voltage always exists, contributing as zero signal. To avoid it, the lock-in amplifier has to work in differential mode to subtract the common-mode induction contribution. Using this mode, not only the zero-signal problem is solved, but also the calibration is not needed, since with good cable (well shielded, low capacity) and good connection, the ME signal is zero without sample or with a non-ME samples. The sample is placed in the magnetic field with its surface perpendicular to the field direction.

6.3 Results and Discussions

The X ray diffraction pattern of the CoFe_2O_4 nanoparticles and the $\text{CoFe}_2\text{O}_4:\text{BaTiO}_3$ core shell nanoparticles is shown in Fig.6.1 (a) and 6.1 (b).

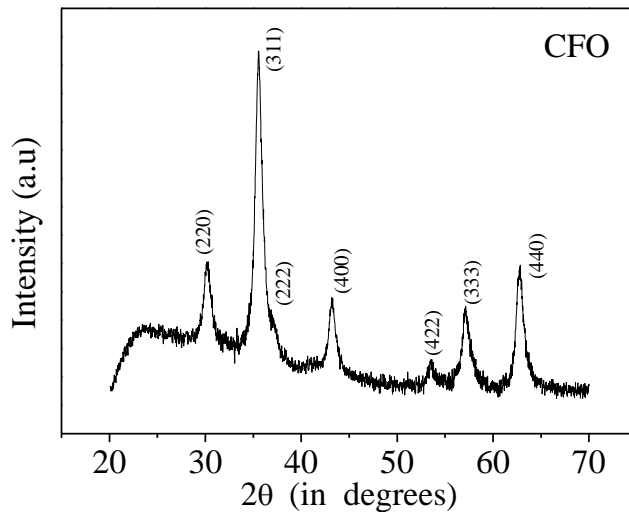


Figure 6.1(a): X ray diffraction of CoFe_2O_4

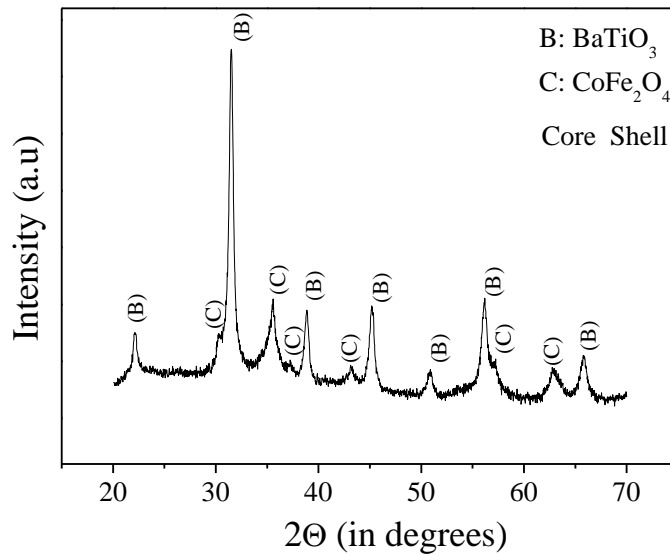


Figure 6.1(b): X ray diffraction of $\text{CoFe}_2\text{O}_4:\text{BaTiO}_3$

The X ray diffraction pattern of the core shell particles show the presence of the both ferrite and ferroelectric phases without any additional impurity phase peak. The ferrite phase has a cubic spinel structure and ferroelectric phase has perovskite tetragonal structure. The average particle diameter as measured from scherrer formulae from Fig. 6.1(a) for the full width at half maxima is 21 nm (± 3) for the CFO particles.

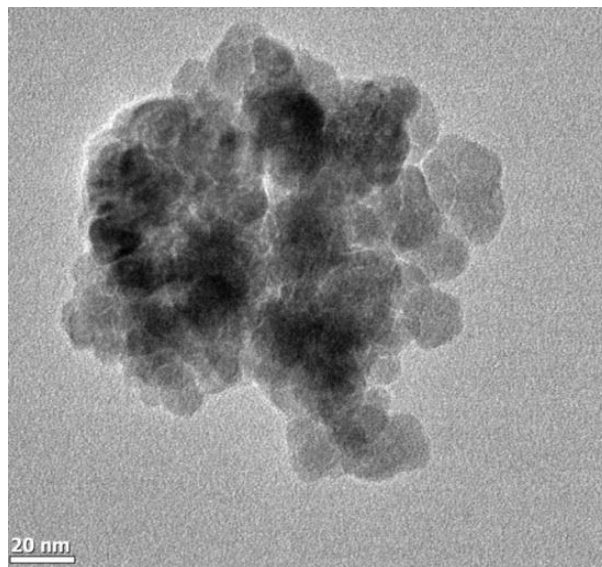


Figure 6.2 (a) TEM image of CoFe_2O_4

The TEM image of the as prepared CoFe_2O_4 nanoparticles is shown in Fig.6.2 (a). The TEM image of the CoFe_2O_4 nanoparticles show that they were nearly spherical and ~ 20 nm diameter which matches well with the XRD data. The selected area electron diffraction (SAED) pattern of the CoFe_2O_4 nanoparticles is shown in Fig. 6.2(b). It shows that the particles obtained are polycrystalline in nature.

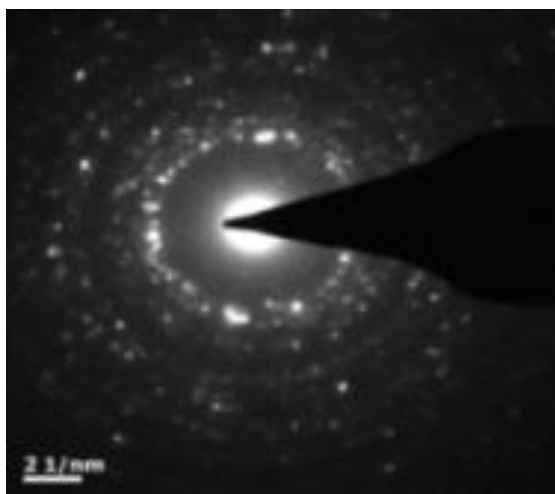


Figure 6.2 (b) SAED pattern of CoFe_2O_4

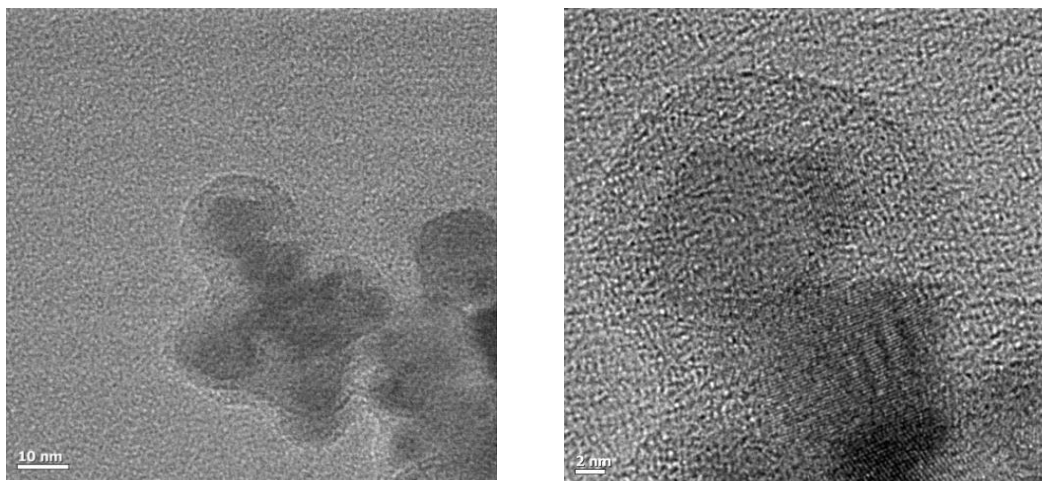


Figure 6.2 (c) TEM image of $\text{CoFe}_2\text{O}_4:\text{BaTiO}_3$ core shell

The TEM image of the $\text{CoFe}_2\text{O}_4:\text{BaTiO}_3$ core shell nanoparticles prepared by the sol-gel technique are shown in Fig. 6.2 (c). It shows that nearly core shell nanoparticles have been

obtained. The diameter of these core shell nanoparticles is between 30 nm and 40 nm with the ferrite particles at the core and the average thickness of the BaTiO₃ shell being 18 nm.

The Magnetization vs Magnetic Field plot of the CoFe₂O₄ (CFO) sample as well as the CoFe₂O₄:BaTiO₃ core shell and mixture sample at room temperature has been depicted in Fig. 6.3. The value of saturation magnetization (M_s), Coercivity (H_c) for the CFO particle is ~50 emu/g, ~656 Oe and for the CFO: BTO core shell particle is ~2.71 emu/g, ~1000 Oe respectively. Coercivity of the core shell increases since the BTO coating arrests the movement of the spins [9]. The M_s value decreases because of the presence of the BaTiO₃ coating which is non-magnetic. We also observe that in case of the mixture of CFO:BTO the coercivity is of the same value as in the as prepared CFO sample whereas the M_s value decreases to ~2.2 emu/g. Hence increase of coercivity and decrease of M_s is also an indication of the coating of BTO on CFO.

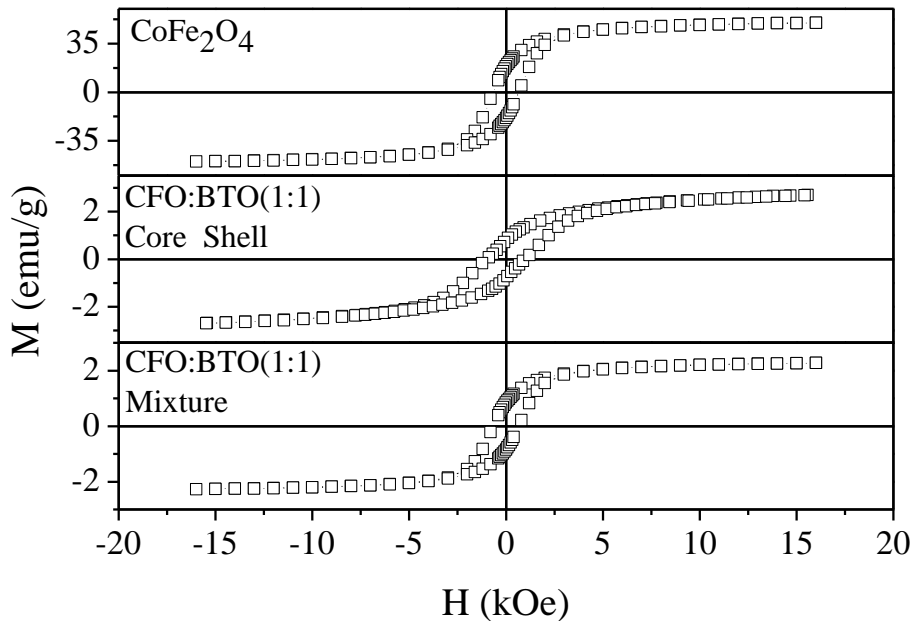


Figure 6.3 (a) M vs H of CoFe₂O₄ (b) CFO:BTO (1:1) core shell (c) CFO:BTO (1:1) mixture

The Zero Field Cooled (ZFC), Field Cooled (FC) magnetization data of all the samples was taken from 80K to 400K in an applied field of 100Oe and it is shown in Fig. 6.4 (a), (b) and (c). We observe that all the samples show a large divergence between field cooled FC and zero

field cooling ZFC magnetization data the divergence increasing with decreasing temperature. The blocking temperature of the as prepared CFO and CFO:BTO mixture sample is nearly similar ie. $\sim 390\text{K}$. But it decreases to $\sim 345\text{K}$ in case of the core shell sample. This is an interesting result.

The lower blocking temperature of the coated samples can be attributed to the increase in the inter-particle separation (due to BTO shell) that reduces the magnetic dipole-dipole interaction [10]. Due to the reduction of the magnetic dipole-dipole interaction the thermal energy will overcome the anisotropy energy at lower temperature. Hence the blocking temperature will be less. But in the mixture sample there is no coating of BTO on CFO. Hence in this case the blocking temperature is similar to that of the as prepared CFO nanoparticles.

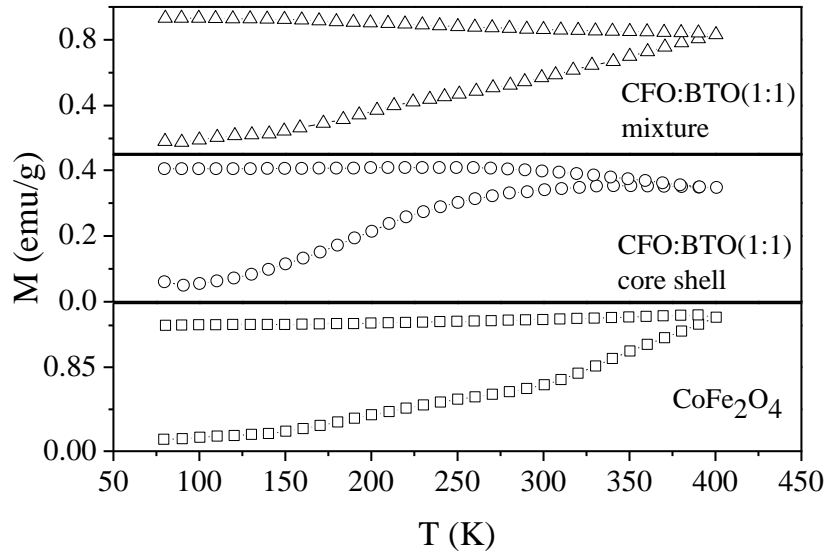


Fig. 6.4: ZFC FC plot of (a) as prepared CFO (b) CFO:BTO (1:1) core shell (c) CFO:BTO (1:1) mixture

Fig. 6.5 shows the ME co-efficient variation as a function of the dc magnetic bias. The magnetoelectric voltage coefficient, α_E , initially increases with the bias field and then saturates at about ~ 1200 Oe with the maximum ME sensitivity reaching $\sim 1130 \mu\text{V}/\text{cm.Oe}$. Further increasing the bias field results in a decrease in magnetoelectric voltage coefficient, (according to Eq. 6.1) since the induced electric field has been saturated. This trend of the ME sensitivity variation as a function of the dc magnetic bias is consistent with previous studies [11]. The BaTiO₃/CoFe₂O₄ particulate composite systems prepared by mixing and sintering BaTiO₃ and

CoFe₂O₄ powders inevitably form aggregates with irregular morphology, which act as the conductive channels to disable the poling effort. Therefore, the electric dipoles in the BaTiO₃ matrix remain largely unaligned. Hence the magnetoelectric coupling is also very less in this sample as proved by Fig. 6.5. The magnetoelectric coefficient in the core shell structure is 11 times more than that in the mixed structure.

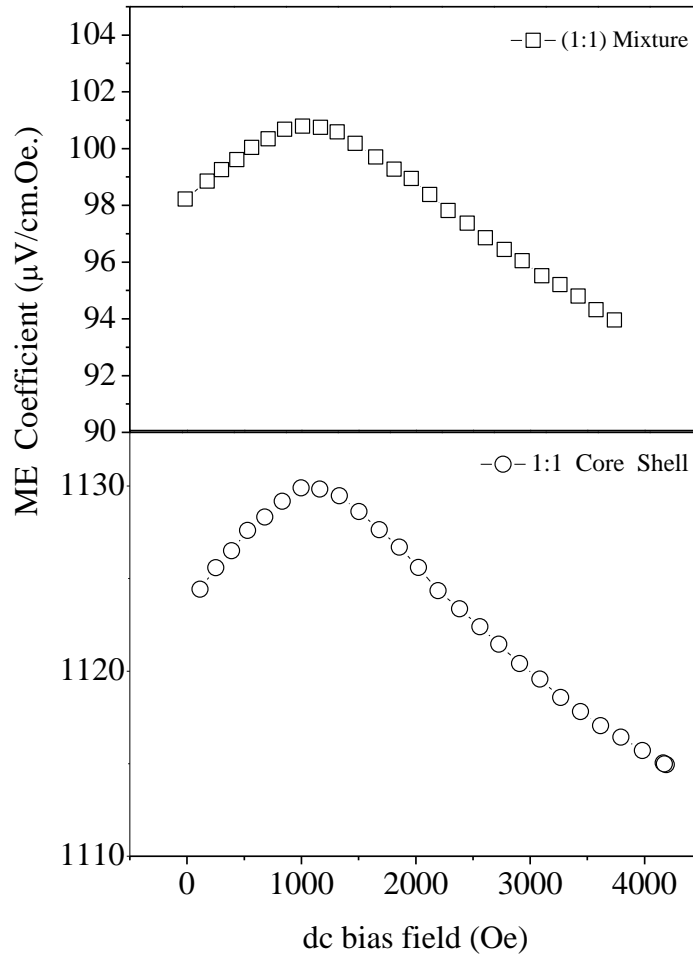


Figure 6.5: α_{ME} vs dc bias field

Fig. 6.6 (a) and (b) depict the frequency dependence of dielectric constant of the mixture and the core shell sample respectively. The dielectric constant was measured in the presence and absence of a magnetic field of 1 Tesla. It is observed that the difference in $\epsilon(H)$ and $\epsilon(0)$ is ~ 3000 in case of the core shell sample whereas it is just 514 in case of the mixture sample. Hence this measurement is also an indication of the enhanced magnetoelectric effect in the core shell sample.

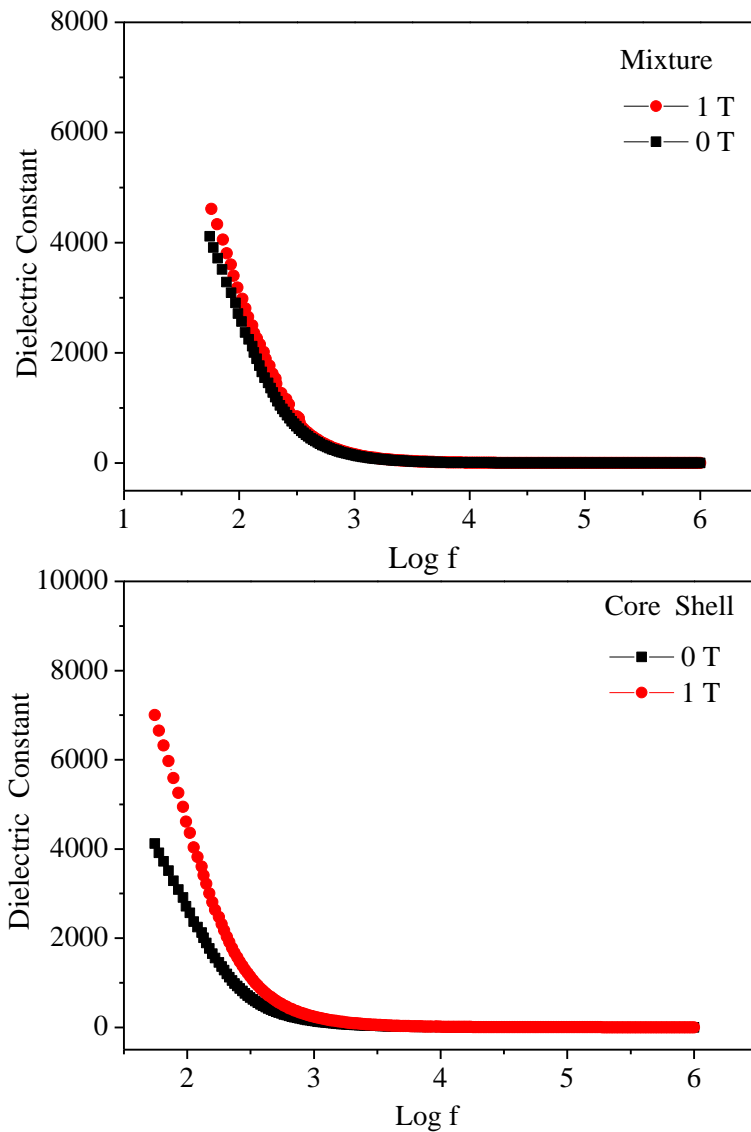


Figure 6.6: Dielectric constant vs frequency

Figure 6.7 shows the frequency dependence of the dielectric loss of the core shell CFO:BTO (1:1) sample. The dielectric loss as shown in Fig. 6.7 decreases in the whole frequency range. Its value is also very small. Hence it proves that because of the core shell composite the dielectric loss of the sample is also low.

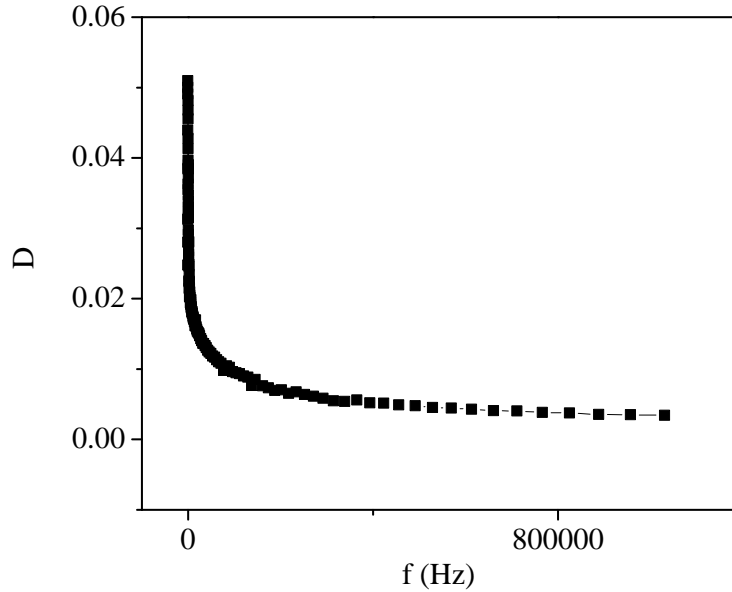


Fig. 6.7: Dielectric loss vs frequency of CFO:BTO (1:1) core shell

6.4 Conclusions

We have successfully synthesized the core shell nanocomposites of $\text{CoFe}_2\text{O}_4:\text{BaTiO}_3$ having (1:1) weight ratio. The TEM image proved the formation of core shell structure. The hysteresis loop and the ZFC FC curve also proved the formation of core shell. We have also proved from the magnetoelectric co-efficient plot that the coupling between the magnetostrictive and piezoelectric phases in the core shell structure is much better than in the mixed structure.

References

- [1] J. van Suchetelene, Philips Res. Rep. **27**, 28 (1972).
- [2] K. Zhao, K. Chen, Y. R. Dai, J. G. Wan, and J. S. Zhu Appl. Phys. Lett. **87**, 162901 (2005).
- [3] S. R. Kulkarni, C. M. Kanamadi, and B. K. Chougule, Mater. Res. Bull. **40**, 2064 (2005).
- [4] J. V. Boomgaard and R. A. J. Born, J. Mater. Sci. **13**, 1538 (1978).
- [5] A. Chaudhuri, S. Mitra, M. Mandal and K. Mandal, Journal of Alloys and Compounds, **491**, 703 (2010).
- [6] V. Corral-Flores, D. Bueno-Baque's, R.F. Ziolo Acta Materialia **58**, 764 (2010).
- [7] A. Chaudhuri , K. Mandal Mater. Res. Bull. **47**, 1057 (2012).
- [8] G. V. Duong, R. Groessinger, M. Schoenhart, D. Bueno-Basques J. of Magn. and Magn. Mater. **316**, 390 (2007).
- [9] D. Pal, M. Mandal, A. Chaudhuri, B. Das, D. Sarkar, and K. Mandal J. of App. Phys. **108**, 124317 (2010).
- [10] A. Chaudhuri, M. Mandal, K. Mandal J. of Alloys and Compounds **487**, 698 (2009).
- [11] G. V. Duong, R. S. Turtelli, R. Groessinger, J. of Magn. and Magn. Mater. **322**, 1581 (2010).

Chapter 7

Conclusion and scope for future study

We present an overall summary of the work done in the present thesis.

NiFe₂O₄:SiO₂ core shell nanocomposites were successfully synthesized following the Stöber method. The magnetic properties of the coated and uncoated particles were investigated. The particles were proved to be single domain. The blocking temperatures of the coated samples were less than that of the corresponding uncoated samples. This was attributed to the increase in the interparticle separation (due to SiO₂ shell) that reduces the magnetic dipole-dipole interaction. Because of the SiO₂ coating the agglomeration could be overcome to some extent. These core shell nanoparticles can be very useful for biomedical applications. To throw light on the high frequency application of ferrites; the hysteresis loops of the uncoated NiFe₂O₄ nanoparticles were measured in the frequency range of 20 - 650 Hz. It was observed that the area of the hysteresis loops increased with the increase of frequency which was attributed to the eddy current loss. Coercivity varied as ½ power of frequency. Nickel Ferrite nanoparticles with different morphologies were also synthesized by the hydrothermal route. Morphology was found to vary with the polarity of the solvent. The particles tend towards superparamagnetism with decrease in size. Gas sensing measurements of differently shaped nanoparticles was studied and it was observed that gas sensitivity changed with the change in morphology.

Unagglomerated, monodisperse CFO nanoparticles were successfully synthesized by a simple hydrothermal technique using capping agents. Blocking temperature (T_B) increased with the increase in particle size. The time evolution of the magnetization of the superparamagnetic particles was also discussed. Micelle coated single domain cobalt ferrite nanoparticles were also successfully synthesized by coprecipitation method. A high coercivity of 4.4 kOe was obtained for the as synthesized particles; which is quite unusual since the particles are single domain

nanoparticles. By extensive analysis of the results obtained, we have concluded that micelles form a cage like structure resulting in the high coercivity of these particles. Such small single domain magnetic nanoparticles with a high coercivity can be useful for data storage device in near future.

Spindle, plate, cylindrical and hexagonal shaped nanostructured BiFeO₃ particles were synthesized by the solvothermal technique by playing with the temperature and solvent of the solvothermal synthesis. The role of temperature and solvent in determining the morphology was investigated. All the samples show antiferromagnetic ordering at room temperature. The plate shaped samples show the best magnetic as well as dielectric properties. The cylindrical shaped BFO nanoparticles were doped with different concentration of Lanthanum and Barium by the hydrothermal technique. For the La 0.1 doped BFO sample we obtain rod shaped nanoparticles. Also in case of Barium doped BFO; doping led to the change in morphology which is proved from the XRD and TEM analysis. Both magnetization and dielectric constant increase with the increase in doping concentration with the maximum enhancement occurring in Barium doped samples. The difference in atomic radius of Lanthanum and Barium in comparison to Bismuth atom is the main reason for the distortion in the oxygen octahedral which leads to some dipole moment and hence increase in dielectric constant. We obtained an interesting and new result where an abrupt increase in magnetization is observed from 400⁰C which has been attributed to the spin canting due to lattice distortion and the increase in thermal energy. Electron spin resonance study of the La doped samples proves the breakage of the spin cycloid due to doping.

Successful synthesis of core shell nanocomposites of CoFe₂O₄:BaTiO₃ having (1:1) weight ratio have been done. The TEM image proved the formation of core shell structure. The hysteresis loop and the ZFC FC curve also proved the formation of core shell. We have also proved from the magnetoelectric co-efficient graph that the coupling between the magnetostrictive and piezoelectric phases in the core shell structure is much better than in the mixed structure.

Scope for future work in different areas

NiFe₂O₄:SiO₂ core shell nanoparticles can be very useful in biomedical applications. Besides instead of SiO₂; coating of any polymer, organic ligands can also be done and the thereby applied for different biomedical purposes. The agglomeration of the particles can be further

overcome by using different capping agents. Non agglomerated particles are more suitable for biomedical applications. NiFe_2O_4 is a very good gas sensor which we have proved in Chapter 3 of this thesis. We can further observe the gas sensing capability of NiFe_2O_4 in gases like Cl_2 , H_2S , Acetone etc. $\text{NiFe}_2\text{O}_4:\text{SiO}_2$ core shell can find application in telecommunication system. NiFe_2O_4 nanoparticles can be used further in high frequency applications in transformer core, electronic inductors, ferrite beads etc.

Non-agglomerated CoFe_2O_4 nanoparticles find extensive application in photomagnetism, catalysis, ferrofluids, hyperthermia, cancer therapy and molecular imaging agents in magnetic resonance imaging (MRI). Single domain CoFe_2O_4 nanoparticles having high coercivity can be very useful in data storage devices. We have enhanced the coercivity of CoFe_2O_4 by coating with the micelle TX 100 which is a neutral micelle. It can be very interesting if we can investigate the effect of coating it with other micelles like SDS (negatively charged), CTAB (positively charged).

The doped Bismuth Ferrite offers a wide opportunity for potential applications in ferroelectric memories, spintronics, storage devices, spin valves, sensors etc. We have prepared La doped BFO and Ba doped BFO separately. It can be very interesting if Lanthanum and Barium are simultaneously doped in the Bismuth site and the Iron site and vice versa. The magnetoelectric coupling is usually very low in Bismuth Ferrite and doped Bismuth Ferrite. Hence different kinds of doping, preparing thin films can be done to enhance the magnetoelectric coupling.

In $\text{CoFe}_2\text{O}_4:\text{BaTiO}_3$ nanocomposites CoFe_2O_4 and BaTiO_3 in different weight ratio can be prepared to enhance the magnetoelectric co-efficient. Doping of certain Jahn teller ions like Copper, Nickel etc. in the Cobalt site will lead to the enhancement of magnetostriction resulting in high magnetoelectric coupling. Hence doping of Copper, Nickel in Cobalt site of CoFe_2O_4 can be a good prospect.